Cosmic-ray ionisation of dense molecular clouds

Solenn Vaupré

To cite this version:

Solenn Vaupré. Cosmic-ray ionisation of dense molecular clouds. Astrophysics [astro-ph]. Université Grenoble Alpes, 2015. English. NNT : 2015GREAY049 . tel-01273899

HAL Id: tel-01273899
https://theses.hal.science/tel-01273899

Submitted on 14 Feb 2016

UNIVERSITÉ DE GRENOBLE

THÈSE

Pour obtenir le grade de

DOCTEUR DE L'UNIVERSITÉ DE GRENOBLE

Spécialité : **Astrophysique**

Arrêté ministériel : 7 août 2006

Présentée par

Solenn Vaupré

Thèse dirigée par **Cecilia Ceccarelli**
et codirigée par **Pierre Hily-Blant**

préparée au sein **de l'Institut de Planétologie et d'Astrophysique de Grenoble**
et de **l'École doctorale de Physique de Grenoble**

Ionisation des nuages moléculaires par les rayons cosmiques

Cosmic-ray ionisation of dense molecular clouds

Thèse soutenue publiquement le **10 juillet 2015**,
devant le jury composé de :

Mme Claudine Kahane
Professeur à l'Université Joseph Fourier (Grenoble I), Présidente
M. Jacques Le Bourlot
Professeur à l'Université Paris-Diderot, Rapporteur
M. Claudio Codella
Chercheur à l'Osservatorio Astrofisico di Arcetri, Firenze, Rapporteur
M. Dariusz C. Lis
Professeur à l'Université Paris 6, Examinateur
M. Alexandre Marcowith
Directeur de Recherche au Laboratoire Univers et Particules de Montpellier, Examinateur
Mme Cecilia Ceccarelli
Astronome à l'Institut de Planétologie et d'Astrophysique de Grenoble, Directrice de thèse
M. Pierre Hily-Blant
Maître de conférence à l'Université Joseph Fourier (Grenoble I), Co-Directeur de thèse

Remerciements

Je remercie les membres du jury qui ont accepté de juger mon travail de thèse, ce vendredi 10 juillet 2015 à Grenoble. Je remercie particulièrement M. Jacques Le Bourlot et M. Claudio Codella pour avoir accepté de juger du présent manuscrit, et pour avoir proposé des corrections qui ont permis d'en améliorer la qualité scientifique.

Je souhaite remercier très chaleureusement Cecilia Ceccarelli et Pierre Hily-Blant, qui ont su diriger cette thèse avec une énergie et un enthousiasme indéfectibles et contagieux. Cela a été pour moi un plaisir sans cesse renouvelé que de travailler avec eux pendant ces trois années. J'ai pu pleinement profiter de cette double tutelle, apprenant de leurs expertises complémentaires et de leurs différentes approches. Ils ont su tout mettre en oeuvre pour la réussite de cette thèse et mon épanouissement professionnel : ensemble, nous avons obtenu suffisamment de temps de télescope (au 30m de l'IRAM, dans la Sierra Nevada) pour à la fois explorer et modéliser en détail une région d'intérêt et élargir l'étude à des régions similaires ; ils m'ont également offert l'opportunité de candidater à de nombreuses conférences, où j'ai pu présenter mes travaux au niveau national et international. Pierre, Cecilia, je n'aurais pas imaginé de meilleures conditions d'encadrement et je vous remercie beaucoup.

Je remercie également nos collaborateurs : Mme Gaëlle Dumas (IRAM), M. Guillaume Dubus (IPAG), M. Stefano Gabici (APC), M. Thierry Montmerle (IAP), M. Marco Padovani (LUPM) et M. Julian Krause (APC). Notre collaboration a permis une approche pluridisciplinaire du travail de thèse, en réunissant des experts de la physico-chimie du milieu interstellaire d'une part et des processus de haute énergie d'autre part.

Cette thèse s'est déroulée au sein de l'Institut d'Astrophysique et de Planétologie de Grenoble, où j'avais déjà eu l'occasion d'accomplir un stage de recherche en Licence (2008) dans l'équipe instrumentale, puis ma deuxième année de Master (2011-2012). Je tiens à remercier l'ensemble des personnels et équipes du laboratoire, que j'ai croisés avec plaisir toutes ces années, et qui participent à l'ambiance joyeuse de ce laboratoire. Je remercie le service administratif pour la qualité du suivi des doctorants et le Groupe d'Accompagnement des Doctorants pour sa volonté de voir des doctorants sereins et sains d'esprit, dans la mesure du possible.

Je remercie tous ceux qui, Parisienne, Jurassien, Toulousains, Bavarois, Lyonnais ou Grenoblois, m'ont permis de profiter pleinement de ces dernières années d'études en ville et en montagne, en été comme en hiver, tôt le matin et tard le soir.

Enfin, je pense bien sûr à ma famille, proche et élargie, ceux qui ont fait le déplacement et ceux qui étaient là par la pensée, pour faire de ce 10 juillet cinq jours mémorables...

Acknowledgments

I would like to thank the members of the jury who accepted to examine my work, and especially M. Jacques Le Bourlot and M. Claudio Codella who accepted to review the manuscript, and who suggested corrections that helped improve its scientific quality.

I would like to warmly thank Cecilia Ceccarelli and Pierre Hily-Blant who were tremendous supervisors. I highly recommend them to future possible PhD candidates.

I also recommend the Institut de Planétologie et d'Astrophysique de Grenoble, where both the people and the scientific environment make it a perfect place to do research.

Finally, I thank our collaborators from both Molecular Astrophysics and High Energy Astrophysics, who helped make this research interdisciplinary: Mme Gaëlle Dumas (IRAM), M. Guillaume Dubus (IPAG), M. Stefano Gabici (APC), M. Thierry Montmerle (IAP), M. Marco Padovani (LUPM) and M. Julian Krause (APC).

Contents

Goals of the thesis

Cosmic rays (CR) are relativistic charged particles. Their acceleration is likely associated with one of the most energetic phenomena in the Universe: the final explosion of massive stars. The importance of CRs is huge in the interstellar medium. They can travel long distances through gas and dust and are a major source of ionisation in the coldest environments of the Galaxy. Namely, they influence the dynamics, evolution and chemistry of the gas, in the very place where stars and planets form.

Yet, our knowledge of the origin and the acceleration process of CRs is still very limited, since they are efficiently scattered along the way by interstellar magnetic fields, and low-energy CRs are even prevented from entering the Heliosphere. Finally, the atmosphere fortunately shields us from most of the CR irradiation, but this makes their ground-based observations difficult. All direct information about the acceleration sites is lost, and other means have to be developed to explore them.

The long-held hypothesis of a CR origin in the expanding shells of supernova remnants (SNR) relies on energetic arguments, and additional evidence is brought by new observations. The relative contributions of radio, X-ray, and gamma-ray emission to the spectral energy distribution of a SNR can indeed be attributed to relativistic electrons or protons. Further evidence is needed to determine the dominant contributor in each case. In old remnants though, protons are usually dominant, and can also explain gamma-ray emission from molecular clouds nearby, due to pion-decay.

Several molecular-clouds/old-SNR associations are strong gamma-ray sources. This constitutes the first piece of evidence of a possible interaction between the two objects, *via* CRs. These molecular clouds probably experience an enhanced irradiation of freshly accelerated particles in the close remnant, with respect to the Galactic average. One expects then that other CR induced effects could be observed in those clouds.

The enhanced ionisation of the gas in interacting clouds is one of those expected effects. When entering the gas, CRs will liberate electrons from H and H_2, thereby forming H^+ and H_2^+. These initial ions form at a rate that depends on the incoming CR flux and energy distribution, and which is described in a given environment by the CR ionisation rate ζ. They will rapidly react with the dominant species in the gas, such as H_2 or CO, and lead to the formation of a series of other species, including molecular ions, whose abundance will be highly dependent on ζ. These CR induced species are called tracers of the ionisation. By observing H_3^+ absorption in the infrared, Indriolo et al. (2010) brought observational evidence of a CR ionisation rate in diffuse molecular clouds near the SNR IC443 about five times larger than toward average diffuse clouds. In dense molecular clouds, where transitions of H_3^+ cannot usually be observed, Ceccarelli et al. (2011) derived the DCO^+/HCO^+ abundance ratio and found for the first time a CR ionisation rate at least a hundred times higher than the standard value, toward a position near the SNR W51C. Such observations are very promising to reveal unusually high fluxes of incoming CRs. My PhD work started in 2012 and contributed to the very beginnings of the investigation of enhanced CR ionisation in dense molecular clouds next to SNRs. At the time, the goals of my work were as follows:

1. First, studying the ionisation in Galactic molecular clouds close to supernova remnants, starting with W28. At this scope, I used the DCO^+/HCO^+ abundance ratio by combining observations and modeling. The generalisation of an enhanced ionisation in these associations would support the hypothesis of an enhanced CR flux freshly accelerated in the shell of the remnant, namely the origin of CRs in the shocks created by the explosion.

2. Studying the chemistry in such associations: this could demonstrate the presence of CRs close to SNRs, and bring information about the low-energy tail of their initial energy distribution, information that

no other observations can provide at these energies. In particular, this would bring constraints on the extrapolation of the CR spectrum at energies below 1 GeV.

3. Proving the existence of an ionisation gradient in the cloud, away from the expanding shock of the remnant: this would give precious observational constraints on the propagation properties of low-energy CRs ($\lesssim$ 1 GeV). Combining with observations at higher energies from gamma-ray observations, we could better describe the energy dependence of CR propagation.

These three initial goals have been partly achieved by the study of W28, follow-up observations of W51C, and observations of W44. The associated results are presented in Chapters 9 and 10. These first works have led me to demonstrate the limitations of the DCO^+/HCO^+ method, which is commonly used to measure the CR ionisation rate in "standard" molecular clouds. These limitations are even more crucial at high ionisation, and beg for the identification of a new set of molecular tracers of the CR ionisation. Therefore, during the thesis, I added the following new objective:

4. Identifying alternative tracers to DCO^+ and HCO^+: this which would allow a more accurate determination of the CR ionisation rate in dense molecular clouds, especially in highly-ionised regions. I would then determine the applicability of these new tracers to other environments.

The efforts regarding this last objective are presented in Chapter 11, and rely on follow-up observations of W28. Finally, when studying W44, I unexpectedly derived constraints on the elemental abundances in the cloud, as presented in Chapter 12.

The thesis manuscript is organised in three parts. In the first part, I will introduce the context of my PhD work. In Chapter 1, I present the interstellar medium, which hosts the chemical evolution of the gas. Chapter 2 is dedicated to the presentation of CRs and their influence on the ISM, and Chapter 3 emphasises their effect on the molecular cloud chemistry. In Chapter 4, I present supernova remnants and the observational evidence for their interaction with molecular clouds, aside from chemistry. In Chapter 5, I introduce the astrophysical objects I investigated and the methods.

My work combines radio observations and chemical modeling to give an interpretation of the physics and chemistry at play in molecular clouds. I present the details of these methods in Part II.

Results are gathered in Part III.

Objectifs de la thèse

Les rayons cosmiques (RC) sont des particules chargées relativistes. Leur accélération est probablement liée à l'un des phénomèmes les plus énergétiques existant dans l'Univers : l'explosion des étoiles massives en fin de vie, les supernovæ. Les RC ont un rôle primordial dans le milieu interstellaire : ils peuvent se propager sur de longues distances à travers le gaz et la poussière et constituent une source majeure d'ionisation dans les environnements les plus froids de la Galaxie. En particulier, les RC influencent la dynamique, l'évolution et la chimie du gaz, dans les lieux de formation stellaire et planétaire.

Pourtant, nos connaissances sur l'origine et les processus d'accélération des RC restent limitées. En effet, les RC sont déviés par les champs magnétiques interstellaires lors de leur propagation. De plus, l'Héliosphère maintient les RC de basse énergie hors du système solaire. Enfin, l'atmosphère terrestre nous protège – heureusement – de la majeure partie des RC, ce qui rend leur observation depuis le sol d'autant plus difficile. Toute l'information directe sur les sources d'accélération des RC est perdue et d'autres méthodes d'exploration doivent être mises en place.

L'hypothèse, longuement soutenue, que les RC trouvent leur origine dans les enveloppes en expansion des rémanents de supernova (SNR), repose sur des arguments énergétiques et tend à être confirmée par les observations récentes. Les contributions relatives de l'émission radio, des rayons X et des rayons gamma dans la distribution spectrale d'énergie d'un SNR peut en effet être attribuée à la présence de protons et/ou d'électrons relativistes. Des indices plus précis sont nécessaires pour déterminer quel est le type de particule dominant l'émission pour chaque objet. Pour les rémanents les plus vieux, l'émission est cependant souvent dominée par les protons, qui permettent aussi d'expliquer, *via* la désintégration de pions, l'éventuelle émission gamma provenant de nuages moléculaires voisins.

Un certain nombre d'associations constituées d'un vieux SNR et de nuage(s) moléculaire(s) à proximité sont des sources intenses de rayons gamma. Cela présente un premier indice d'une possible interaction entre les deux types d'objets, *via* les RC. Ces nuages moléculaires sont probablement irradiés par un flux, plus intense que la moyenne Galactique, de particules fraîchement accélérées par le SNR à proximité. On s'attend ainsi à ce que ce flux intense de RC induise d'autres effets observables dans ces nuages.

Parmi ces effets, les RC peuvent provoquer une ionisation du gaz moléculaire plus importante que dans des nuages isolés. Lorsqu'ils rencontrent le gaz, les RC arrachent des électrons à H et H_2, formant ainsi H^+ et H_2^+. Le taux de formation de ces premiers ions dépend du flux incident de RC et de leur distribution énergétique et est décrit, dans un environnement donné, par le taux d'ionisation ζ. Ces ions vont ensuite rapidement réagir avec les espèces dominantes dans le gaz, par exemple H_2 ou CO, pour former d'autres espèces, notamment des ions moléculaires, dont les abondances dépendent fortement de ζ. Ces espèces formées par la présence de RC sont appelées des traceurs de l'ionisation. Dans des nuages moléculaires diffus, Indriolo et al. (2010) ont utilisé l'absorption infrarouge de H_3^+ pour apporter une preuve observationnelle d'un taux d'ionisation près du SNR IC443 cinq fois plus élevé que dans les nuages diffus isolés. Dans les nuages moléculaires denses, où H_3^+ ne peut généralement pas être observé, Ceccarelli et al. (2011) ont mesuré le rapport d'abondances DCO^+/HCO^+ dans un nuage près du SNR W51C et ont déterminé un taux d'ionisation inédit, au moins cent fois plus élevé que la valeur standard. De telles observations sont encourageantes pour la révélation de taux d'ionisation par le RC anormalement élevés dans la Galaxie.

Mon travail de thèse a commencé en 2012 et a contribué aux toutes premières recherches sur la détection d'une forte ionisation par les RC dans des nuages moléculaires denses proches des SNR. À cette époque, les objectifs de mon travail de thèse étaient les suivants :

1. Étudier l'ionisation dans les nuages moléculaires proches des SNR, dans la Galaxie, en commençant par le SNR W28. Pour cela, j'ai utilisé le rapport d'abondances DCO^+/HCO^+ en combinant observations

et modélisation. La généralisation d'un taux d'ionisation élevé dans ce type d'associations appuierait l'hypothèse d'un flux de RC intense, fraîchement accélérés dans l'enveloppe du rémanent, et notamment l'hypothèse de l'origine des RC dans les chocs générés par l'explosion de l'étoile.

2. Étudier la chimie dans ces associations : cela pourrait démontrer la présence de RC à proximité des SNR et apporter des informations sur les RC de basse énergie ($\lesssim$ 1 GeV) et le spectre initial des RC. De telles informations sont inaccessibles à l'heure actuelle par d'autres méthodes d'observation, dans ce domaine d'énergies. En particulier, cela apporterait des contraintes pour l'extrapolation à basse énergie du spectre des RC.

3. Prouver l'existence d'un gradient d'ionisation dans le nuage, en s'éloignant du choc en expansion du rémanent : cela apporterait des contraintes observationnelles précieuses sur les propriétés de propagation des RC de basse énergie ($\lesssim$ 1 GeV). En associant ces contraintes à celles à haute énergie provenant des observations gamma, il serait possible de mieux décrire la dépendance en énergie de la propagation des RC.

Ces objectifs initiaux ont été réalisés en partie, grâce à l'étude de la région du SNR W28, d'observations complémentaires vers le SNR W51C et d'observations de la région du SNR W44. Les résultats correspondants sont présentés dans les chapitres 9 et 10. Ces premiers travaux m'ont permis de faire émerger des limitations dans la méthode DCO^+/HCO^+, communément utilisée pour mesurer les taux d'ionisation dans les nuages moléculaires "standards". Ces limitations sont encore plus déterminantes à haute ionisation et suggèrent fortement l'identification d'autres traceurs moléculaires de l'ionisation par les RC. Ainsi, durant ma thèse, j'ai ajouté un nouvel objectif :

4. Identifier des traceurs de l'ionisation alternatifs à DCO^+ et HCO^+ : cela permettrait d'obtenir une mesure plus précise du taux d'ionisation par les RC dans les nuages denses, en particulier dans des régions de forte ionisation. Je serais ensuite amené à déterminer l'applicabilité de ces nouveaux traceurs à d'autres environnements.

Le travail effectué dans le cadre de ce dernier objectif est détaillé chapitre 11 et s'appuie sur des observations complémentaires de la région W28. Enfin, en étudiant la région W44, j'ai identifié des contraintes, de manière inattendue, sur certaines abondances volatiles dans le nuage. Ces résultats sont présentés chapitre 12.

Ce manuscrit est organisé en trois parties.

Dans la première partie, j'introduis le contexte de mon travail de thèse. Dans le chapitre 1, je présente le milieu interstellaire, où l'évolution chimique du gaz prend place. Le chapitre 2 est dédié à la présentation des RC et à leur influence sur le milieu interstellaire et le chapitre 3 précise leur effet sur la chimie du nuage moléculaire. Dans le chapitre 4, je présente les rémanents de supernova et liste les preuves observationnelles de l'existence d'une interaction avec les nuages moléculaires voisins, mis à part les effets sur la chimie. Dans le chapitre 5, je présente les objets astrophysiques que j'ai étudiés pendant ma thèse et la méthode utilisée.

Mon travail repose sur des observations radio et une modélisation chimique du nuage, afin d'interpréter les processus physico-chimiques mis en jeu dans les nuages moléculaires. Je présente ces méthodes en détails dans la Partie II.

Les résultats sont regroupés dans la Partie III.

Part I

Context: CR irradiated molecular clouds

Chapter 1

The interstellar medium (ISM)

Contents

This work deals with the dense regions of the interstellar medium (ISM). Interstellar space is filled with gas and dust that are often too cold to emit visible light and were only discovered in the last century. ISM both receives rich material from dying stars and gives birth to new generations of stars. The densest and coldest parts of the ISM are those shielded from UV radiation and where a complex organic chemistry takes place. Cosmic rays (CR) are the main source of ionisation in these parts, and are of tremendous importance in their evolution.

In this chapter, I describe the structure of the ISM, with an emphasis on dense molecular clouds.

1.1 Structure of the ISM

1.1.1 Discovery

On a clear starry night, we can look at our own Galaxy from inside. There are stars everywhere, but many of them are gathered in a light narrow band across the sky: the Milky Way, named by ancient greek astronomers. The Milky Way, first looked on closely by Galileo in the early 1600's, revealed thousands of stars within the field of view of his telescope.

Yet, the Galaxy is not composed solely of stars. In 1784, Herschel was the first astronomer to observe what seemed to be holes in the Milky Way: small regions totally deprived of stars. Their origin remained uncertain for over a century, until Barnard published in 1919 the first photographic survey of our Galaxy. His work brought new evidence that these "holes" actually revealed the presence of obscuring material in the foreground of distant stars, as suggested by Spitzer in the 1950s. These regions were later identified as dense gas clouds, often associated with regions of stellar formation. The optical obscuration was attributed to the presence of dust within these clouds. More difficult to identify, diffuse clouds were also detected during the twentieth century by two observations: absorption lines (e.g. Ca^+, CN, CH, CH^+), which revealed the presence of sparse foreground material on stellar sightlines (e.g. Hartmann, 1904; Adams, 1949), and the detection of gradual dimming of distant clusters, which showed the presence of dust on Galactic scales (Trumpler, 1930).

Figure 1.1: The heterogeneous interstellar medium. Picture of the N11 region in the Large Magellan Cloud, as seen by the *Hubble Space Telescope*. Background stars are seen through diffuse material in the foreground. Compact dense regions (dark clouds) induce total obscuration. The light from young stellar objects is scattered by dust and sculpts this large star forming region. Credits: NASA, ESA, J. Lake.

1.1.2 Phases of the ISM

The interstellar medium (ISM) is composed of $\sim 99\%$ gas and $\sim 1\%$ dust in mass. It accounts for $10-15\%$ of the total baryonic mass of the Galactic disk (which is $\sim 6 \times 10^{11}$ solar masses for the Milky Way). Its cold component is concentrated along the spiral arms in the Galactic plane, although its spatial distribution is very inhomogeneous. The interstellar material is divided into several phases with very different physical conditions: temperatures span from ~ 5 K to $\sim 10^6$ K and densities from $\sim 10^6$ cm^{-3} to $\sim 6 \times 10^{-3}$ cm^{-3}. These media can be classified as follows, with decreasing temperature: the hot ionised medium (HIM), the warm ionised medium (WIM), the warm neutral medium (WNM), the cold neutral medium (CNM) and molecular clouds (MC) (Table 1.1). These different phases coexist in the ISM in rough pressure equilibrium, and whereas the ionised medium occupies most of its volume, the neutral medium actually contains about half its mass.

In the lowest density regions, the presence of UV (≥ 13.6 eV) photons both maintain a high ionisation fraction ($x_e = n(\mathrm{e}^-)/n_\mathrm{H} \gtrsim 10^{-3}$) and a high ($\gtrsim 5000$ K) temperature. All hydrogen is ionised (H^+). With increasing density, the ionising flux becomes less intense and the temperature decreases.

In denser regions (> 20 cm^{-3}), there is no more UV photon with enough energy to ionise hydrogen, which is then neutral and atomic. The decrease in the UV heating and efficient cooling processes make the temperature drop and some small molecules can survive. Those regions form the cold neutral ISM, traced through the HI 21cm emission line. The ionisation fraction is $x_e \approx 10^{-4}$, equal to the abundance of carbon which is mostly ionised. The cold neutral medium will be further described in Section 1.2, and Section 1.3 is dedicated to dense molecular clouds.

Table 1.1: Typical physical conditions in the major phases of the ISM. Adapted from Ferrière (2001) .

Component	T [K]	n [cm^{-3}]
Hot ionised medium (HIM)	$\sim 10^6$	~ 0.0065
Warm ionised medium (WIM)	~ 8000	$0.2 - 0.5$
Warm neutral medium (WNM)	$6000 - 10000$	$0.2 - 0.5$
Cold neutral medium (CNM)	$50 - 100$	$20 - 50$
Molecular clouds	$5 - 40$	$10^2 - 10^6$

1.2 Classification of gas clouds

The cold neutral medium is composed of a large number of isolated clouds with various physical conditions. These clouds are commonly referred to as diffuse, translucent and molecular clouds, with increasing density. Yet, definitions of these clouds are not uniform in the literature and Snow and McCall (2006) suggested a new classification in their review on the neutral medium. This new classification relies on chemical models and the expected local atomic and molecular fractions of hydrogen and carbon. Figure 1.2 shows the predicted abundances obtained with the `PDR MEUDON` code of the main reservoirs of carbon and hydrogen with increasing visual extinction (or depth), together with the density and temperature profiles in an isobaric cloud. This Figure also shows the theoretical boundaries of the different kinds of clouds.

With this definition, clouds are called molecular as soon as at least 50% of hydrogen is molecular (H_2). The dominant form of carbon, whether it is $> 90\%$ ionised (C^+), atomic (C) or molecular (CO), defines diffuse, translucent and dense molecular clouds, respectively. It is important to note that these clouds are defined by their local characteristic, as opposed to quantities present all along the line of sight. These clouds are expected to coexist along sight lines and even to be be mixed together.

Regions where far-UV photons dominate the heating or some important aspect of the chemistry, namely through the dissociation of H_2 and CO, are called photodissociation regions (PDR, Hollenbach and Tielens, 1999; Le Petit et al., 2006). In these regions, molecules are photodissociated and form small neutral species or radicals, such as CH or CH_2. PDRs englobe most of the volume of the atomic gas, and extend to places up to $A_V \sim 10$ mag (Hollenbach and Tielens, 1999), where most of the carbon is in the molecular form, CO.

To understand the processes at play, a simple view is that dense molecular clouds are surrounded by some diffuse material which shields them from most of the ionising FUV flux. This confers them an onion-like structure, where the outer layer is a PDR which stops the ionising flux, and where the gas gets colder and denser with depth. Therefore, observations of sight lines towards dense clouds must be interpreted as a mixture of dense and translucent material, whereas it is possible to find sight lines that cross exclusively diffuse material.

The column density of hydrogen $N_{\mathrm{H}} = N(\mathrm{H}) + 2N(\mathrm{H_2})$ (in molecular clouds, $N_{\mathrm{H}} \approx 2N(\mathrm{H_2})$) is a proxy of the total amount of material along the line of sight. One defines the total visual extinction A_V as the difference between the visual magnitude of a star at 540 μm in absence of absorbing material (essentially dust) in the foreground and the actual observed magnitude. The visual extinction is related to the hydrogen column density through $N_{\mathrm{H}} \sim 1.87 \times 10^{21}$ cm^{-2} mag^{-1} $\times A_V$ (Bohlin et al., 1978). The different types of clouds can thus also be described by ranges of observed visual extinction or H column densities (Figure 1.2).

1.3 Dense molecular clouds

In the following, I will refer to dense molecular clouds as *molecular clouds*, and diffuse molecular clouds as *diffuse clouds.* A large fraction of molecular clouds result from the local condensation of material within giant molecular clouds at temperature $30 - 40$ K. With the increase in density, the gas heating is less efficient and the temperature drops due to radiative cooling (Section 1.3.1), maintaining pressure equilbrium. Within molecular clouds, the coldest regions, referred to as dark clouds or dense molecular clouds, are the densest regions of the ISM, with densities typically above 10^3 cm^{-3} and temperatures below 20 K. Most of the interstellar chemistry takes place in these parts, which are where stars form. The largest molecular clouds span from 10 to 100 pc and encompass 10^4 to 6×10^6 solar masses, for a mean density of $\sim 10^2$ cm^{-3}(diffuse

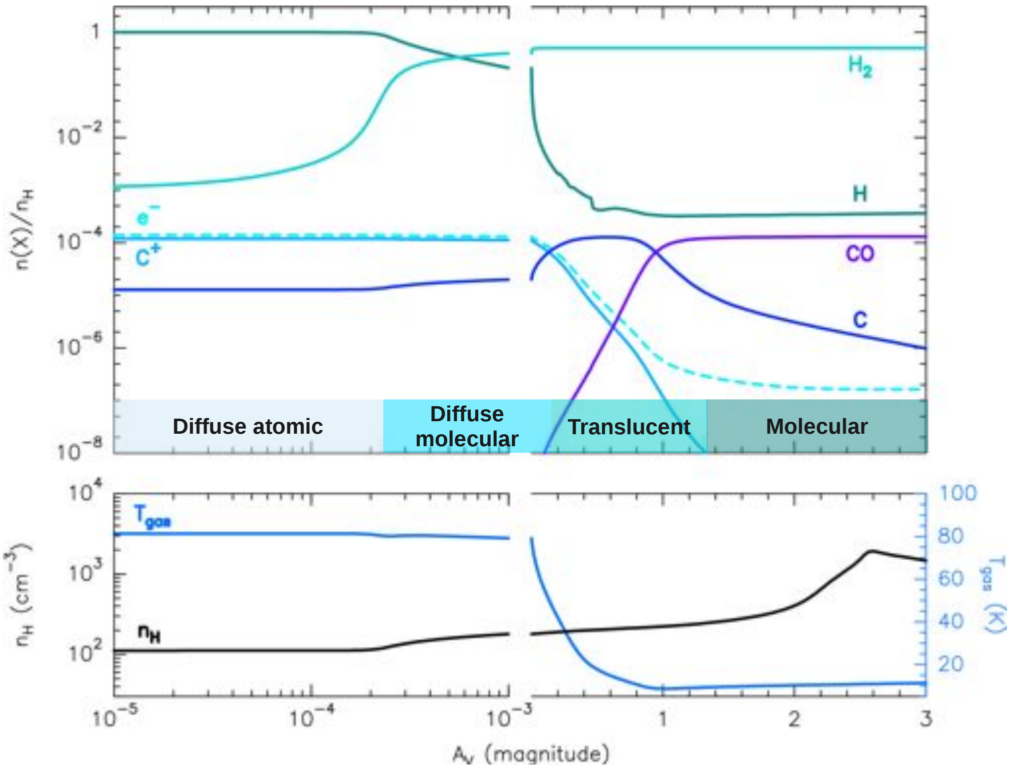

Figure 1.2: **Top:** Classification of clouds w.r.t. the visual extinction, based on the dominant reservoirs of C and H, following Snow and McCall (2006). **Bottom:** Corresponding density and temperature profiles. The visual extinction is computed from $N_{\rm H} \sim 1.87 \times 10^{21}$ cm^{-2} mag^{-1} $\times A_V$ (Bohlin et al., 1978).

material). Within these inhomogeneous clouds, dark clouds are limited to much smaller regions of typically a few pc and hundreds solar masses. About 4000 dense clouds have been identified in the Galaxy.

1.3.1 Thermal balance in molecular clouds

The temperature reached by the gas at equilibrium is the result of competing radiative cooling (through line emission) and heating processes. The processes of thermal equilibrium were detailed by Goldsmith and Langer (1978). Radiative cooling mostly depends on the gas density and the molecular composition, two co-dependent parameters. For instance, the main cooling transitions for the neutral gas from ~ 300 K down to ~ 50 K (this corresponds to PDR) are the fine structure lines of the abundant C^+ and O atoms. Below 50 K, at densities $10^2 - 10^4$ cm^{-3}, cooling from CO lines becomes dominant.

Due to its very high abundance, transitions of the main CO isotopologue ^{12}CO usually get optically thick and cooling becomes less efficient. The contribution of rarer isotopologues like ^{13}CO and C^{18}O become more and more important with increasing density and can contribute up to 70% of the total CO cooling. This is because these transitions can remain optically thin, in other words photons emitted through these transitions can escape the cloud, taking away some energy. Molecular depletion can reduce the gas-phase cooling efficiency, but this effect is limited by the large contribution of optically thick lines to cooling (Goldsmith, 2001).

At $10^3 - 10^4$ cm^{-3} densities, the time scale for radiative cooling ($\sim 10^5$ yr) is about one order of magnitude shorter than the free-fall time scale. In absence of UV photons, this implies the existence of other heating sources to reach equilibrium (Goldsmith and Langer, 1978). Heating is dominated in molecular clouds by CRs at lower ($\lesssim 10^5$ cm^{-3}) densities, and by dust-gas collisions at higher densities (Tielens, 2005, Chapter 3).Other sources are gravitational contraction or ambipolar diffusion.

1.3.2 Formation of molecules

In molecular clouds, the relatively large density favors encounters, yet the temperature is very low and the gas-phase chemistry is governed by kinetics over thermodynamics. Neutral-neutral reactions are especially slow, and the gas-phase chemistry is dominated by ion-neutral reactions.

Ion-neutral reactions are in general exothermal and have no energy activation barriers, therefore they play a crucial role in cold molecular clouds, despite the low ionisation fraction $x_e = n(\mathrm{e}^-)/n_\mathrm{H}$ (see e.g. Herbst, 2005). In those regions shielded from the interstellar UV radiation field, CRs are the only source of ionisation, as they can still penetrate deep inside the cloud, at $A_V > 10$ mag. CRs will ionise H_2 which will rapidly lead to H_3^+ and initiate the formation of many subsequent ions. They will also ionise He and form He^+, which will destroy molecules in the gas. Chapter 3 is dedicated to the description of the CR induced chemistry in molecular clouds.

The nature of molecular clouds enables the accretion of molecules onto grains, where they can undergo further reactions. The freeze-out of CO can for instance reach 50% in cloud interiors, and even 80-90% in prestellar cores (see e.g. Caselli and Ceccarelli, 2012). The freeze-out time scale is $t_{freeze-out} \propto 10^9/n_\mathrm{H}$ yr (Jones and Williams, 1985), which is significantly shorter than the free-fall time scale ($t_{ff} \sim 4 \times 10^7/\sqrt{n_{\mathrm{H}_2}}$) or estimated life time in $> 10^4$ cm^{-3} clouds. Therefore one would expect CO to be totally depleted. Yet, CO is still observed in high density regions, which means there is a desorption process other than thermal evaporation (the dust is cold) or photodesorption (the visual extinction is high), or that there is still some C^+ atoms to form CO. Once again, CRs are believed to be the dominant source of desorption (Leger et al., 1985). They let CO be re-injected in the gas along with other molecules, which formed on the grain surface.

The dense ISM is where molecular complexity builds up. The chemistry is dominated by ion-neutral reactions in the gas phase, enabled by the presence of CRs. It is possible that CRs also have a role in the formation of large ($\gtrsim 6$ atoms) molecules on grain mantles (e.g. Garrod and Herbst, 2006). This rich chemistry will then be included from the initial steps all along stellar and planetary formation.

1.4 ISM-star cycle

Since the early photographs by E. Barnard, molecular clouds are known to exhibit filamentary structures. The recent observations from the *Herschel* satellite show the ubiquity of filaments in molecular clouds (André et al., 2014). Stars are formed within the densest clumps in molecular clouds, called pre-stellar cores, where the density can reach $10^6 - 10^7$ cm^{-3}. Small-scale observations of the mass distribution indicate that filaments are not a consequence of star formation but rather precede it, and protostellar cores inherit this spatial distribution.

An ongoing debate addresses the question of the dynamics of star formation (Bergin and Tafalla, 2007). At first, molecular clouds were thought to be in quasistatic equilibrium in their evolution toward star formation, but this view was recently challenged by observations and numerical simulations which suggest a faster evolution of clouds and star formation. In this view, molecular clouds would result from turbulent flows, evolve and dissipate before reaching equilibrium.

The presence of heavy elements (heavier than H and He) in the gas phase, and the presence of dust tell us that the cloud material results from previous generations of stars, as these heavy elements can only be formed by stellar nucleosynthesis. This reveals a wide process of ISM-star cycle, where stars are born inside molecular clouds and give some of their material back to the ISM. This material can either be delivered by stellar winds during the late phases of star evolution, or it can be expelled during supernova explosions. The next generation of stars will thus incorporate metal-enriched material compared to previous generations. This ISM-star cycle will gradually enrich locally the ISM in heavier elements across the Galaxy, and lead to the existence Galactic gradients of the gas composition.

Chapter 2

Cosmic rays

Contents

Cosmic rays (CR) are very energetic, relativistic, charged particles which pervade the Galaxy. They have a major impact on the physics and chemistry of the interstellar medium, as they are the only ionisation source able to reach the dense interiors of molecular clouds.

As charged particles, CRs are sensitive to magnetic fields and are deflected all along the way from their source to Earth. Therefore, all information about the location of CR sources is lost, and low-energy CRs are prevented from entering the Solar System by the Heliosphere. Besides, most CRs are then neutralized by our own atmosphere before they reach the ground. Yet, one can gather information about CRs from particles that indeed reach Earth's orbit or atmosphere, or from their observational signature outside the Solar System.

In this chapter, I describe the discovery and techniques of observation of CRs, and present their influence in particular on dense clouds. Chapter 3 is dedicated to their influence on the cloud chemistry.

2.1 Discovery

This thesis started in 2012, which marked the 100th anniversary of the discovery of CRs by Victor Hess. He was an Austrian physicist who personally flew atmospheric balloons to carry out precise measurements of the ionising radiation in the atmosphere up to more than 5 km, using electroscopes. He discovered that the level of ionisation increased with altitude above 1 km, which proved there was a flux of ionising particles coming from the sky. The outer space origin of these particles was confirmed in 1925 by R. Millikan who named them *cosmic rays* (this unfortunate name can be confusing and one has to keep in mind that these cosmic *rays* are actually *particles*). Then, C. Anderson, Millikan's former student, discovered new subatomic particles in the incoming CR flux. He indeed confirmed the existence of the positron in 1932, which had been recently predicted by P. Dirac, before he discovered the unexpected muon in 1936. V. Hess and C. Anderson shared the 1936 Nobel Prize in Physics for their respective works on CRs.

2.2 Observations

2.2.1 The solar cosmic-ray spectrum

Figure 2.1 shows the overall CR spectrum in the solar environment, i.e. CRs that actually reach Earth's orbit or atmosphere. It is a collection of results from various experiments that are sensitive to complementary energy ranges. One can divide this overall spectrum into 3 parts that can be fitted by three different power-laws, and which are limited by two characteristic features, the *knee* and the *ankle* (if you wish to identify this spectrum with a leg). These two "body parts" mark a modification in the origin and composition of CRs (Blandford et al., 2014). Low energy particles ($\lesssim 30 \times 10^9$ eV) originate in the Sun, solar wind and planets. At these low energies, the Heliosphere alters the flux and spectrum of CRs as it prevents Galactic CRs from entering the Solar System, with variations in efficiency that follow the Solar activity (in a process called modulation, see e.g. Blasi, 2013). It is generally assumed that supernovae can accelerate CRs up to the knee at $\sim 3 \times 10^{15}$ eV (see section 4.1.3). At energies higher than the knee, the spectrum is dominated by heavy nuclei. The ankle ($\sim 5 \times 10^{18}$ eV) allegedly marks the change from a Galactic origin of CRs at lower energies to an extragalactic origin at higher energies. Spectral breaks up to the knee can be naturally explained by the superposition of energy cut-offs, i.e. limitations from the physical processes involved in the acceleration and propagation of CRs. These processes and the actual sources of CRs are yet not fully understood and are awaiting more observational evidence (e.g. Blasi, 2013).

The flux of CRs reaching Earth decreasese with energy (see Figure 2.1), down to 1 particle/km^2/ century for the highest energies. Whereas at lower energies detectors onboard satellites can easily detect CRs, the low fluxes at highest energies beg for the construction of detectors with very large surfaces, if one is to detect these particles. This naturally led to two families of CR detectors: those which can fit in satellites or ballon experiments and directly detect the incoming particles that didn't interact with the atmosphere, and detectors that look for secondary particles created when CRs enter the atmosphere.

Today, the most common technique for the detection of CRs is based on Cherenkov radiation. When a particle encounters a medium at a speed greater than the speed at which photons can travel through this medium, it will slow down and lose energy by emitting a characteristic blue light. Cherenkov radiation is actually broader than visible light and spread to UV. It is emitted within a cone whose angle gives a direct measure of the initial particle energy. Cherenkov was a Russian physicist who was awarded the Nobel Price in 1960 for his discovery.

2.2.2 Direct measurement

The electroscopes used by Hess which measured the amount of electrons in the atmosphere became obsolete, and several types of detectors have been since invented. In the early 1920's, another technique was already available, when Anderson used cloud chambers to discover the positron. In these chambers, ionising particles leave tracks, each track being characteristic of the type of particle. Other types of chambers were later developed to observe the tracks of incoming particles. For instance, the $1 - 100$ GeV energy range in Figure 2.1 was determined by the LEAP ballon experiment in the 1980's. It aimed at direct particle detection and included a liquid Cherenkov detector (Seo, 1991). Capabilities of particle detectors are constantly improved and used in particle physics experiments, for instance at CERN, or the AMS experiment aboard the International Space Station.

2.2.3 Indirect measurement

The second main family of detectors was designed for higher energy CRs. These detectors will look for the secondary particles at ground level generated by CRs in the atmosphere. When entering the atmosphere, particles of high energies will generate a shower of secondary particles, mostly electrons and positrons, and also muons in a smaller amount. The shower is beamed, depending on the initial particle energy, but since it is initiated at high altitude, it will spread over a large region. The shower is associated with fluorescence, Cherenkov radiation, and radio emission.

For instance, the *Pierre Auger Observatory* was specifically designed to detect the highest-energy CRs above 10^{18} eV, on the far-right side in Figure 2.1. The total detection area is of almost 3000 km^2, spread over Argentina, in order to detect a significant amount of such particles. It was named after Pierre Auger, a French physicist who showed the association of air showers with CR events.

2.2.4 Beyond the Solar System

The CR spectrum observed from Earth is modified by the Solar modulation. The Heliosphere, where the influence of the solar magnetic field predominates, acts indeed like a deflective shield and prevents many particles from entering the Solar System.

The *Voyager* probes were launched in 1977 to visit the planets of the Solar System. They are now on the way out and *Voyager 1* showed evidence that it left the inner part of the Heliosphere on 2012 August 25 and it gave the first glimpse at the extrasolar CR spectrum (Stone et al., 2013). As evidence of its entry into unknown territory, *Voyager 1* measured a drop in the amount of low-energy ions (~ 1 GeV) and an increase in Galactic CRs. The intensity of the CR flux indeed apparently became isotropic, confirming their Galactic origin, since CRs no longer originated in the Sun.

2.2.5 Gamma-ray observations

It is important to keep in mind that CRs are particles and not photons. Dedicated telescopes have been built aiming at the direct or indirect detection of these particles from Earth. Nevertheless, CRs can also induce gamma-ray emission. As an example, a molecular cloud under intense CR irradiation will be a bright source of GeV to TeV gamma rays: in that case, gamma rays are induced by the disintegration of neutral pions following collisions of protons with the dense material (see Chapter 4). Therefore, gamma-ray observatories can be used for indirect observations of Galactic CRs close to supernova remnants. Telescopes such as the space *Fermi*-LAT experiment ($1-100$ GeV) and the ground-based H.E.S.S. Cherenkov array ($0.01-10$ TeV) or MAGIC ($0.05-30$ TeV) are dedicated to the observation of gamma-ray sources and can trace indirect signature of Galactic CRs. Observations from these facilities will be valuable in the source selection process for this work (Section 5.3).

Gamma-ray observations are based on techniques similar to CR detection. Detectors aboard satellites use photon interaction processes, such as Compton scattering or pair production, whereas ground-based telescopes are Cerenkov detectors observing particle showers induced by gamma rays entering the atmosphere. Because of differences in their structure and composition, air showers initiated by gamma rays or CRs can be distinguished.

Gamma-ray telescopes can therefore also directly detect CRs, aside their primary objectives. Their measurements of faint gamma-ray sources are actually disturbed by the intense CR flux on Earth. Therefore, both *Fermi* and H.E.S.S. have been designed to rule out CRs in the detection process of gamma rays. They are disregarding about 10^5-10^6 CR signatures for each detected gamma ray when pointing to a gamma-ray source. Collecting these CR events allowed to derive the spectrum of CR electrons at GeV to TeV energies (Thompson et al., 2012; Aharonian and Collaboration, 2008b).

2.3 Influence of cosmic rays

CRs pervade the Galaxy and play a crucial role in the physical heating and the chemical ionisation of the ISM. They have a major impact on the chemistry of the cloud, as they initiate efficient chemical reactions and the formation of molecular ions. Chapter 3 is dedicated to the description of the CR induced chemistry. CRs also create light elements (Li, Be, B) *via* spallation of heavier nuclei in the ISM. In the following, I focus on CR effects in dense clouds.

The interstellar UV radiation cannot penetrate dense regions with $A_V \gtrsim 2$ mag where CRs become the dominant source of ionisation and control the ionisation degree. The ionisation degree in the molecular gas is a fundamental parameter throughout the star and planet forming process. The abundances of ions indeed regulate the coupling of the gas to the magnetic field in a process called ambipolar diffusion. Collisions of neutrals with ions which remain bound to magnetic field lines slow down the gravitational collapse and decrease the star formation rate. Typical measurements in prestellar cores give ionisation fractions between $x_e = 10^{-8}$ and 10^{-6} (Caselli et al., 1998). The time scale for ambipolar diffusion varies linearly with the ionisation fraction and can get 2 to 200 times larger than free-fall time scales (see Caselli and Ceccarelli, 2012, and references within). In addition, ions sustain turbulence within protoplanetary discs and introduce non-ideal magnetohydrodynamics effects, which influence the accretion rate onto the protostar (Balbus and Hawley, 1998; Lesur et al., 2014).

In the absence of UV radiation, CRs may also be the dominant source of heating in low-density dark clouds, where they counteract the efficient radiative cooling by molecules. Each CR ionisation (mainly with H_2, He or H in molecular clouds) produces electrons with enough energy to produce a secondary ionisation. Slow electrons will then deposit some of their kinetic energy in the gas. They will heat the gas through several effects such as ionisation, electronic or vibrational excitation (followed by collisional de-excitation), and dissociation (Dalgarno et al., 1999). In a recent paper, Glassgold et al. (2012) showed that the dominant contribution to heating in molecular clouds (outside protostellar cores) comes from chemical heating. Chemical heating corresponds to the energy released by chemical reactions following the formation of primary ions induced by CRs: H_2^+, He^+ and H^+. The next contributors are H_2 dissociation and rotational excitation, vibrational excitation is ineffective.

Finally, UV photo-desorption in well-shielded regions is inefficient. It is believed that CRs allow the desorption of molecular material from dust grains into the gas phase (Leger et al., 1985; Hasegawa and Herbst, 1993). This concerns species that were accreted onto the grains due to low temperatures in the dense gas, such as CO, or species that were formed by chemical reactions at the surface of the grains and are otherwise absent from the gas phase. CRs therefore counteract a possible complete freeze-out (Walmsley et al., 2004) of molecular species on the grains and contribute to the release of complex molecules in the gas phase.

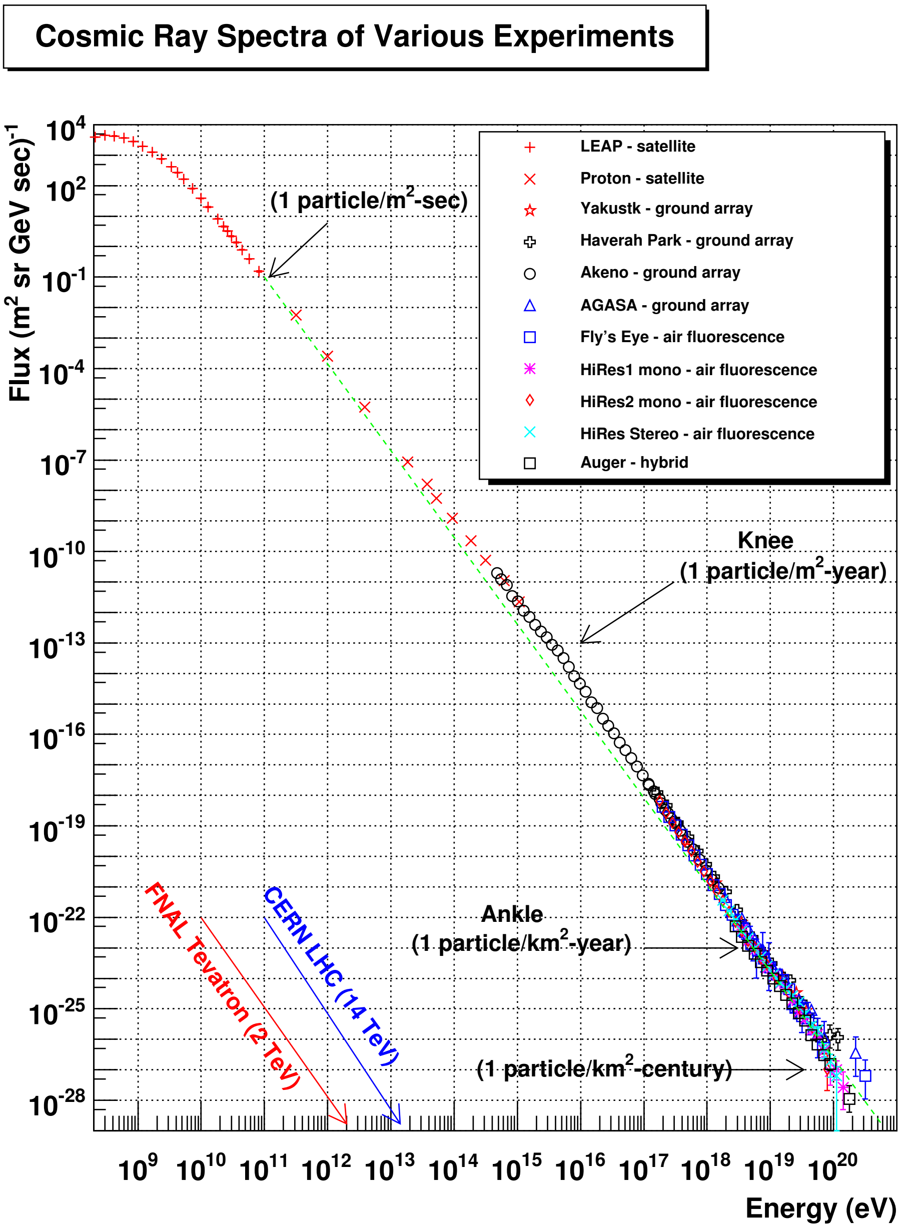

Figure 2.1: CR spectra of various experiments, detected from Earth. Adapted by W.Hanlon (see `http://www.physics.utah.edu/~whanlon/spectrum.html`).

Chapter 3

Cosmic-ray induced chemistry

Contents

In this chapter, I further describe the effects of CRs on the molecular cloud chemistry. Dense regions are shielded from the interstellar UV field and CRs are the dominant source of heat and ionisation. Observing some specific species formed subsequently to the ionisation of H and H_2 can lead to the determination of the ionisation degree in the gas-phase and further information on the low-energy tail of the CR spectrum.

3.1 The cosmic-ray ionisation rate

Molecular clouds (Section 1.2) are dense cold environments efficiently shielded from the interstellar UV radiation field, and where more than 50% of hydrogen is in the molecular form, H_2. In diffuse clouds, carbon is ionised (C^+), as UV photons with < 13.6 eV energies remain, whereas in dense clouds, all carbon in the gas phase is trapped in CO, provided that $C/O< 1$. The low temperatures slow down the kinetics of gas-phase reactions and the chemistry is dominated by fast ion-neutral reactions, despite the low ionisation fraction. By the ionisation of H and H_2, CRs initiate a series of reactions which can lead to the formation of a large variety of more complex molecules, either in the gas-phase or on the surface of grains.

CRs can ionise any species at any depth in the cloud, but H, H_2 and He ions will be the largest source of ionisation due to their high abundances. He^+ will cause the destruction of every molecule it will encounter, whereas H^+ and H_2^+ will be the starting points of basically all formation reactions in the gas phase. The rate at which CRs first ionise these species is called the CR ionisation rate ζ $[\mathrm{s^{-1}}]$. It can be seen as a kinetic rate for the first-order chemical reaction:

$$\mathrm{X + CR \rightarrow X^+ + e^- + CR'}, \tag{3.1}$$

where X is either H, H_2 or He and the CR loses some energy in the reaction. Following Indriolo and McCall (2013), there exists three slightly different definitions of ζ regarding the hydrogen chemistry: 1) the primary ionisation rate (ζ_p), which includes solely direct ionisation of atomic H by the primary CR particle ; 2) the total ionisation rate of atomic H (ζ_{H}), which includes the ionisation by secondary electrons formed by the primary ionisation ; 3) the total ionisation rate of molecular hydrogen (ζ_2 or $\zeta_{\mathrm{H_2}}$), which is specific to H_2 and also includes secondary electrons. These rates are related to one another by factors of the order of a few, which are mainly due to differences in ionisation cross sections and contributions from secondary electrons (Glassgold and Langer, 1974).

In my PhD work, ζ refers to the total ionisation of molecular hydrogen ζ_2, associated with the reaction:

$$\mathrm{H_2 + CR \rightarrow H_2^+ + e^- + CR'}, \tag{3.2}$$

and the formation rate of H_2^+ through this reaction reads:

$$\frac{\mathrm{d}n(\mathrm{H}_2^+)}{\mathrm{d}t} = \zeta n(\mathrm{H}_2). \tag{3.3}$$

The contribution from secondary electrons is disregarded in analytical derivations but is taken into account in the chemical network for the modeling of the gas-phase chemistry (Chapter 8).

The ionisation of H and H_2 induced by CRs will then initiate a series of fast ion-neutral reactions, which will eventually lead to large amounts of molecules or molecular ions that wouldn't be obtained in absence of CRs. These species, characteristic of the presence and amount of CRs, are called tracers of the ionisation. Estimating ζ using these tracers requires to correctly identifying the relevant chemical reactions involved in their formation and destruction, and determining accurate kinetic rates associated with these reactions.

3.2 Diffuse molecular clouds

In diffuse clouds ($A_V \simeq 10^{-3} - 0.3$ mag), both H and H_2 are present in significant amounts (Figure 1.2) and photons still play a major role, e.g. in the formation of C^+ or photodissociation of molecules. In the 1970s, OH and HD were identified as probes of the CR ionisation rate (Black and Dalgarno, 1973, 1977). The formation of OH is initiated by the charge exchange reaction of H^+ with O and involves subsequent reactions with H_2. Similarly, H^+ reacts with atomic D to form D^+, which leads to HD through reaction with H_2. Both OH and HD were therefore thought to be introduced in the gas-phase following the ionisation of H by CRs. They were first used to infer the CR ionisation rate in the Ophiuchus and Perseus clouds, where values spanning from 1.5×10^{-17} s^{-1} to 8×10^{-16} s^{-1} were reported (see Dalgarno, 2006, and references within). The large uncertainties come from the poorly known kinetic rates for the destruction processes. With additional observations in the late 1990s consistent with earlier values, a canonical value of $\zeta_\mathrm{H} = 3 \times 10^{-17}$ s^{-1} was adopted and assumed relatively uniform throughout the Galaxy (see Indriolo and McCall, 2013, and references therein). Since then, the chemistry of these two molecules has been revised, in the sense that HD is now thought to be mainly formed on grains and the abundance of OH is also affected by the photodissociation of H_2O.

More recently, H_3^+ has been proposed as a more reliable probe of the CR ionisation rate (McCall et al., 2003; Dalgarno, 2006; Indriolo et al., 2007). There are no rotational transitions of H_3^+ due to its symmetry, but absorption lines of H_3^+ can be observed in the infrared L-band at 3.7 μm. This method requires strong background sources in this spectral band, such as young OB stellar objects. The chemistry of H_3^+ is very simple and can be described by a set of three reactions, starting with the ionisation of H_2 by CRs (Reaction 3.2). Then, H_3^+ is formed through:

$$\mathrm{H}_2 + \mathrm{H}_2^+ \rightarrow \mathrm{H}_3^+ + \mathrm{H} \tag{3.4}$$

and the destruction of H_3^+ is dominated by electronic dissociative recombination:

$$\begin{aligned} \mathrm{H}_3^+ + \mathrm{e}^- &\rightarrow \mathrm{H}_2 + \mathrm{H} & (3.5)\\ &\rightarrow \mathrm{H} + \mathrm{H} + \mathrm{H}. & (3.6) \end{aligned}$$

Thanks to this very simple chemistry, H_3^+ is expected to be more reliable than the previous probes, OH and HD, since the estimates of ζ rely on a reduced number of kinetic rates and chemical abundances:

$$\zeta = k_e x_e n_\mathrm{H} \frac{N(\mathrm{H}_3^+)}{N(\mathrm{H}_2)} , \tag{3.7}$$

with the ionisation fraction $x_e = n(\mathrm{e}^-)/n_\mathrm{H}$, the total hydrogen density n_H, column densities $N(\mathrm{H}_3^+)$ and $N(\mathrm{H}_2)$, and the kinetic rate for electronic recombination of H_3^+ k_e (Table 3.1). Still, uncertainties remain quite large, mainly due to the large abundance gradients of O, CO and H_2, and the determination of ζ requires careful modeling of these PDR-like regions.

The sample of sight lines where H_3^+ is detected has been rapidly expanded in the past few years (Indriolo et al., 2007, 2010; Indriolo and McCall, 2012). From this survey where H_3^+ is detected toward about half of the lines of sight, ζ was found to be about one order of magnitude higher than previously measured in dense clouds, with quite large variations around a mean value $\zeta = 3.5 \times 10^{-16}$ s^{-1}. The variability is thought to come from local effects and show no large scale correlation. When including data from dense clouds, the CR ionisation rate decreases with increasing total column density N_{H}, which can be explained by propagation effects (Section 3.4).

Finally, OH^+ and H_2O^+ were recently observed in absorption with the *Herschel Space Observatory* to infer the CR ionisation rate in the outer parts of a diffuse cloud (Gerin et al., 2010; Neufeld and Collaboration, 2010; Indriolo et al., 2015). These species are formed during the CR induced formation of OH. The authors found $\zeta \sim 0.6 - 2.4 \times 10^{-16}$ s^{-1}, in good agreement with rates from H_3^+ observations. Simultaneous observations with H_3^+ toward W51 (Indriolo et al., 2012) allowed a tentative calibration to prepare a potential future use of these species as independent tracers, along sight lines where H_3^+ cannot be observed.

3.3 Dense molecular clouds

The formation of H_3^+ occurs as well in dense molecular clouds, where more than 99% of hydrogen is molecular and gaseous carbon is mostly trapped in CO, provided that C/O< 1. The observations of infrared absorption lines are possible (McCall et al., 1999), yet more difficult due to the high column densities, and other tracers are thus to be found. The most usual tracers in dense clouds, first suggested by Guélin et al. (1977), are the molecular ions HCO^+ and DCO^+, which form dominantly through the reaction of CO with H_3^+ and H_2D^+, respectively:

$$\mathrm{H_3^+ + CO \rightarrow HCO^+ + H_2} \ , \tag{3.8}$$

$$\mathrm{H_2D^+ + CO \rightarrow DCO^+ + H_2} \ . \tag{3.9}$$

Enhanced abundances of deuterated molecules are observed in dense clouds (Watson, 1973) and have been explained by chemical fractionation reactions, in particular H_2D^+ is supplied by the isotope exchange reaction:

$$\mathrm{H_3^+ + HD \rightleftharpoons H_2D^+ + H_2} + \Delta E \ , \tag{3.10}$$

where $\Delta E \approx 220$ K, meaning the binding energy of the heavier isotopologue H_2D^+ is slightly larger than that of H_3^+, therefore the reaction proceeds from H_3^+ to H_2D^+ in cold clouds ($e^{-\Delta E/T} \sim 10^{-5}$ at 20 K) .

Assuming reactions (3.8) and (3.9) are the dominant formation routes of DCO^+ and HCO^+, and that both species are dominantly destroyed through electronic recombination, the $R_D = \mathrm{DCO^+/HCO^+}$ abundance ratio relates to H_2D^+/H_3^+ at steady-state:

$$R_D = \frac{x(\mathrm{DCO^+})}{x(\mathrm{HCO^+})} \approx \frac{1}{3}\frac{x(\mathrm{H_2D^+})}{x(\mathrm{H_3^+})} \ , \tag{3.11}$$

where the 1/3 coefficient comes from a statistical argument and $x(X_i)$ is the abundance of species X_i relative to H. Following Guélin et al. (1977), it is also possible to derive an analytic formula for the H_2D^+/H_3^+ ratio if we assume the chemistry of H_2D^+ is governed by reactions (3.9), (3.10), and electronic recombination (Table 3.1):

$$\frac{x(\mathrm{H_2D^+})}{x(\mathrm{H_3^+})} \approx \frac{k_f x(\mathrm{HD})}{k_e x_e + 1/2 \ k_f e^{-220/T} + k_D x(\mathrm{CO})} \ , \tag{3.12}$$

with chemical rates and their values listed in Table 3.1 (the 1/2 factor comes from $x(\mathrm{H_2}) = n(\mathrm{H_2})/n_{\mathrm{H}} = 1/2$ in dense molecular clouds). The HD abundance w.r.t. H is $x(\mathrm{HD}) \sim 1.6 \times 10^{-5}$ (Linsky et al., 1995), i.e. equals the cosmic D/H ratio.

The R_D abundance ratio is observed up to a few 10^{-2} in dense clouds, i.e. about a factor 10^3 higher than $x(\mathrm{HD})$. This implies a low ionisation fraction $x_e < 10^{-6}$. If not, electronic recombination would dominate the destruction processes of H_2D^+ and lead to much lower R_D ratios. In other words, a high ionisation fraction would significantly reduce the abundance of DCO^+ through the destruction of H_2D^+. Also, at higher temperatures ($T \gtrsim 50$ K), the backward reaction of 3.10 drastically reduces the abundances of H_2D^+ and thus DCO^+.

When applicable, the analytical formula (Eq. 3.12) allows the determination of the ionisation fraction x_e, and it was applied to dense clouds measurements (Guélin et al., 1982). To better take into account

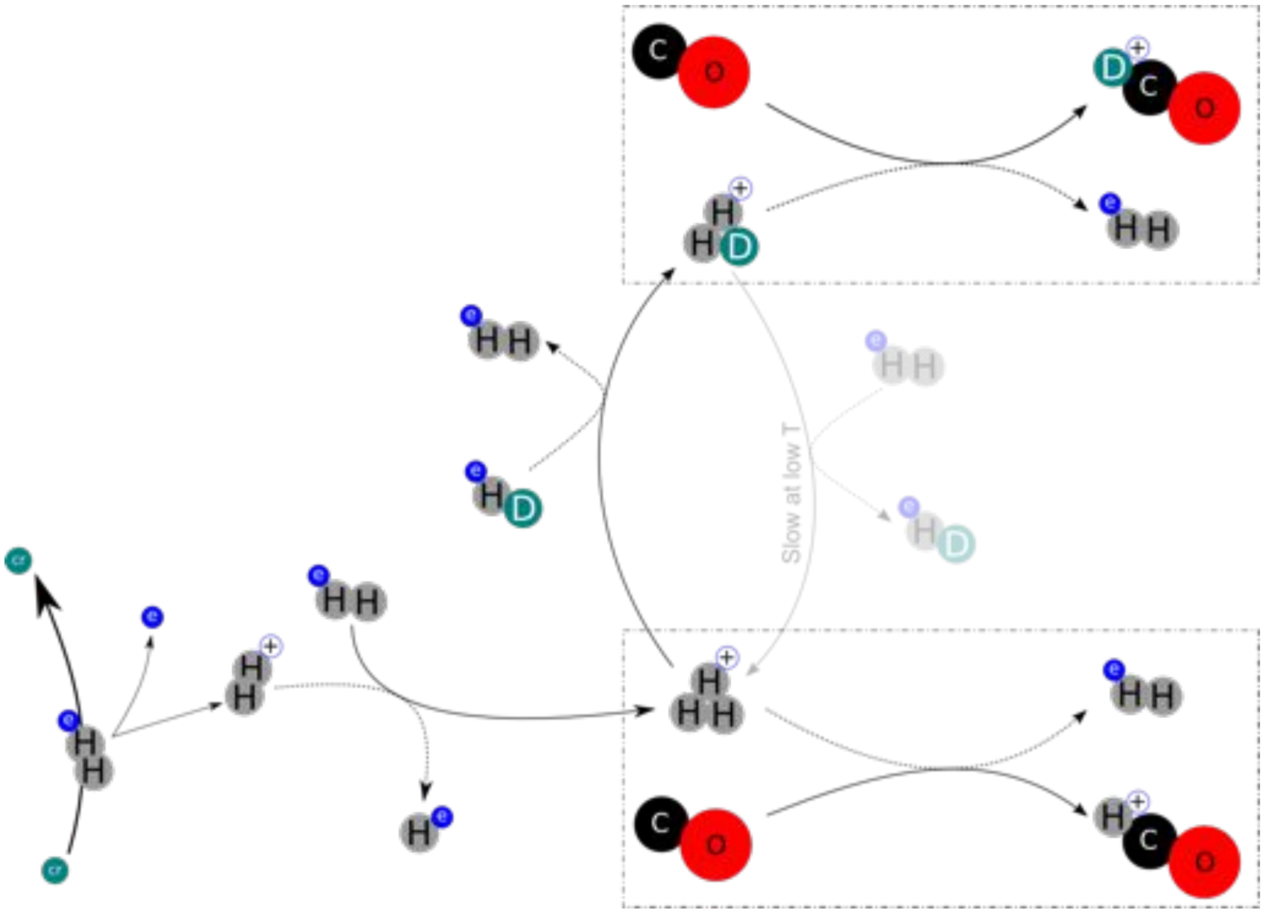

Figure 3.1: Schematic view of the CR (cr) induced formation of HCO^+ and DCO^+ in dense clouds through chemical reactions described in the text. All ions are subject to electronic recombination. In cold dense clouds, large amounts of DCO^+ can be observed when the ionisation fraction is low, so that the destruction of H_2D^+ by e^- is limited.

the various chemical routes that were ignored in the original analytical determination, Caselli et al. (1998) extended, and updated, the chemical network involved in the formation of DCO^+ and H_2D^+. Using chemical models allows to derive the DCO^+/HCO^+ ratio in a given environment and compare it to observations (see Chapter 8). From these models, it will then be possible to derive the CR ionisation rate in dense molecular clouds. In Chapter 9, I will describe the application of this method in a dense cloud near W28, and its limitations (Vaupré et al., 2014).

3.4 Propagation of the cosmic-ray spectrum

Combining the results from different studies in various environments, the CR ionisation rate tends to decrease with increasing column density. Rates in diffuse clouds are about one order of magnitude higher than in dense clouds (Indriolo and McCall, 2013), and values $\leq 10^{-17}$ s^{-1} are reported in dense, pre-stellar cores. Figure 3.3 shows a compilation by Padovani and Galli (2013) of values in various environments. This evolution can be explained by propagation effects of the CR spectrum into the cloud (Padovani et al., 2009; Padovani and Galli, 2013).

CRs experience several energy-loss processes during collisions with H_2, including ionisation. Cross sections for each process depend on the nature of the CR particle (proton or electron) and its kinetic energy. Ionisation cross sections are highest ($\sim 10^{-15}$ cm^{-2}) for low-energy particles (e.g. $1 - 100$ keV). The CR spectrum is however poorly known in this energy range due to Solar modulation. Yet, it can be extrapolated for both

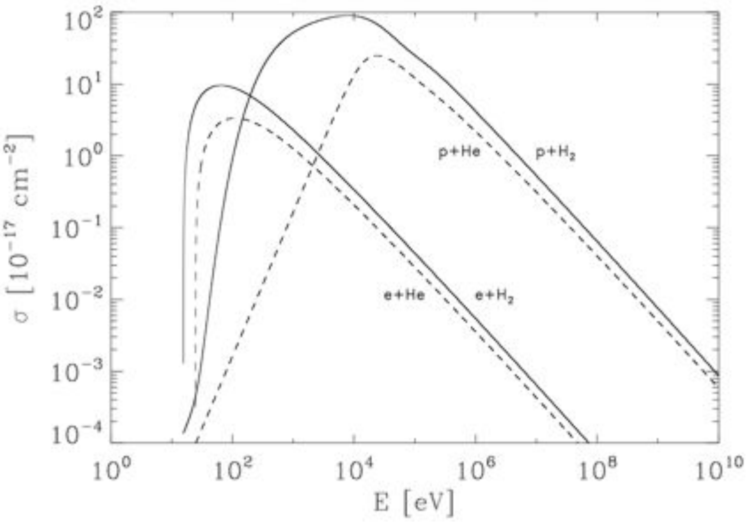

Figure 3.2: Ionisation cross sections for proton and electron impact on H_2(solid lines) and on He (dashed lines). From Padovani and Galli (2013).

protons and electrons up to energies $\lesssim 1$ GeV, assuming power-law distributions. Different models have been proposed which lead to discrepancies at 1 eV by up to 15 orders of magnitude. Improvements are expected from recent observations by *Voyager*.

Padovani and Galli (2013) considered the maximum and minimum extrapolated spectra and their propagation into molecular clouds, taking into account the relevant energy-loss processes and their associated cross sections. They derived the evolution of the CR ionisation rate with the total column density N_{H}, for each spectrum. With increasing N_{H}, low-energy CRs are not simply excluded from the spectrum, as more low-energy particles are constantly produced by the slowing down of CRs of higher energy. In dense cores, this model also shows that most of the ionisation is produced by $10 - 1000$ MeV protons. Observations, including the decrease in ζ of one order of magnitude from diffuse to dense clouds, were best reproduced by spectra that increase at low energy (Padovani and Galli, 2013, Figure 6). A combination of electrons and protons gives better results but still fails over the entire range of column densities $N_{\mathrm{H}} = 10^{21} - 10^{23}$ cm^{-2} (Figure 3.3).

Measurements of ζ vary within two orders of magnitude at all N_{H}, mainly because of uncertainties in the chemistry. This makes it difficult to know how much local variations account for the global variability of ζ. Yet, the decrease in ζ with the column density seems clear, with even measurements of $\zeta \leq 10^{-17}$ s^{-1} in dense cores. These very low values in compact regions could be explained by CR exclusion by magnetic fields, through magnetic focusing and mirroring, which are predicted by theoretical models (e.g Padovani and Galli, 2013).

Table 3.1: Reduced chemical network for the analytical derivation of DCO^+/HCO^+ (Vaupré et al., 2014).

Reaction				Rate constants		
				α	β	γ
No. 1	$CR + H_2$	$\xrightarrow{\zeta}$	$H_2^+ + e^-$	ζ	-	-
No. 2	$H_2^+ + H_2$	$\xrightarrow{k_{H_2^+}}$	$H_3^+ + H$	2.1 (-9)	-	-
No. 3	$H_3^+ + CO$	$\xrightarrow{k_H}$	$HCO^+ + H_2$	1.61 (-9)	-	-
No. 4	$HCO^+ + e^-$	$\xrightarrow{\beta'}$	$CO + H$	2.8 (-7)	-0.69	-
No. 5	$H_3^+ + e^-$	$\xrightarrow{\beta}$	$H + H + H$	4.36 (-8)	-0.52	-
			$H_2 + H$	2.34 (-8)	-0.52	-
No. 6	$H + H$	$\xrightarrow{k'}$	H_2	4.95 (-17)	0.50	-
No. 7	$H_3^+ + HD$	$\xrightarrow{k_f}$	$H_2D^+ + H_2$	1.7 (-9)	-	-
No. 7b	$H_2D^+ + H_2$	$\xrightarrow{k_f^{-1}}$	$H_3^+ + HD$	1.7 (-9)	-	220
No. 8	$H_2D^+ + CO$	$\xrightarrow{k_D}$	$DCO^+ + H_2$	5.37 (-10)	-	-
No. 9	$DCO^+ + e^-$	$\xrightarrow{\beta'}$	$CO + D$	2.8 (-7)	-0.69	-
No. 10	$H_2D^+ + e^-$	$\xrightarrow{k_e}$	$H + H + D$	4.38 (-8)	-0.50	-
			$H_2 + D$	1.20 (-8)	-0.50	-
			$HD + H$	4.20 (-9)	-0.50	-
No. 11	$H + D$	$\xrightarrow{k''}$	HD	7.0 (-17)	0.50	-
No. 12	$H_2D^+ + CO$	$\xrightarrow{k'_D}$	$HCO^+ + HD$	1.1 (-9)	-	-
No. 13	$H_3^+ + D$	$\xrightarrow{k'_f}$	$H_2D^+ + H$	1.0 (-9)	-	-
No. 13b	$H_2D^+ + H$	$\xrightarrow{k'^{-1}_f}$	$H_3^+ + D$	1.0 (-9)	-	632

Note - The reduced network corresponds to the original description by Guélin et al. (1977) and Caselli et al. (1998). Rate constants are described by an Arrhenius equation:

$$k = \alpha \left(\frac{T}{300}\right)^{\beta} \exp\left(-\frac{\gamma}{T}\right) \ ,$$

and we used the notation $a\ (b) = a \times 10^b$. The units of k depend on the order of the reaction: for two-body reactions (reactions 2-13), which are of the second order, these are $cm^3\ s^{-1}$. The rates of reactions 2-6 are contained in the original OSU 2009 network. We appended deuterated reactions 7-13 for which chemical rates are taken from Roberts and Millar (2000).

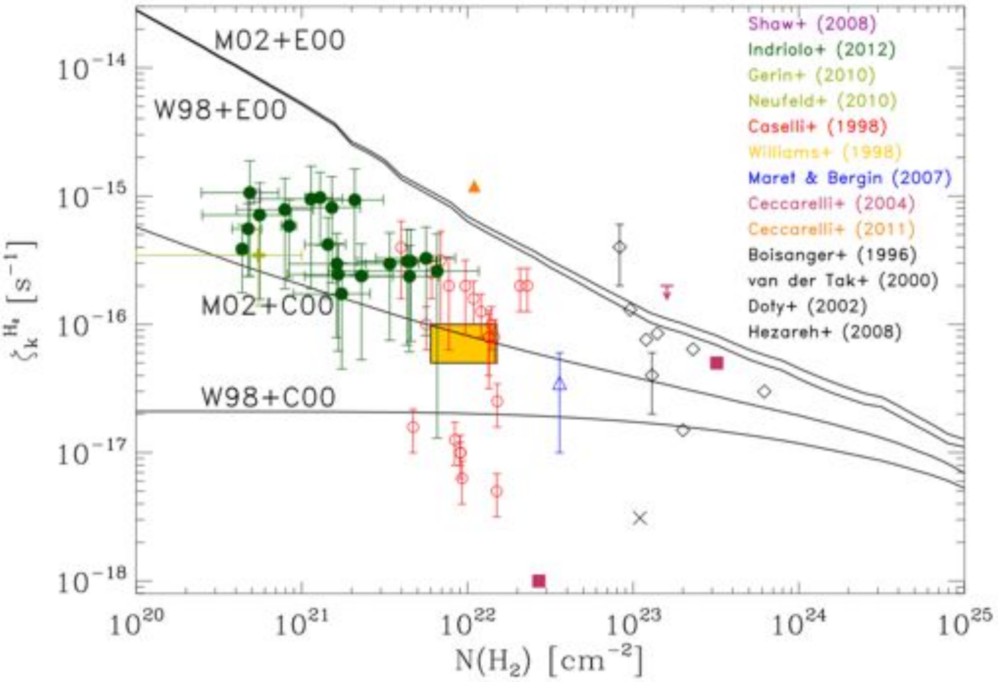

Figure 3.3: Compilation of measured CR ionisation rates of H_2 (ζ), towards various environments, from Padovani and Galli (2013). Measurements in diffuse clouds were carried out with H_3^+ (filled circles, Indriolo and McCall, 2012) or OH^+ and H_2O^+ (green cross, Neufeld and Collaboration, 2010). Measurements in dense cores were derived from the DCO^+/HCO^+ ratio (empty circles, Caselli et al., 1998). The filled triangle shows the enhanced ionisation toward W51C, measured with DCO^+/HCO^+ (Ceccarelli et al., 2011). The solid lines show the theoretical ζ values from extreme extrapolations of the CR spectrum, combining contributions of electrons (E00, C00) and protons (W98, M02). These models can reproduce the overall decrease in ζ with increasing column density, but fail to reproduce the observations over the whole column density range.

Chapter 4

Interaction of supernova remnants with molecular clouds

Contents

Almost 300 supernova remnants have been identified in our Galaxy. When expanding into the interstellar medium with time, they interact with nearby molecular clouds which were probably the progenitors of the exploded stars. The supernova remnants (SNR) can interact with molecular clouds, influencing their dynamical properties. They can also interact through the propagation of CRs accelerated at the SNR shock into the cloud.

In this chapter, I describe SNRs and observations that can confirm the existence of such an interaction with molecular clouds, aside from chemistry. These SNR-MC associations will be ideal targets for the study of enhanced CR induced chemistry in the gas.

4.1 Supernova remnants

4.1.1 Supernovae

Supernovae (SN) are part of the most energetic phenomena in the Universe. A supernova is the result of the explosion of a star which expels the stellar material with an initial velocity of several thousands of km s^{-1}, which will generate shock waves, and with a total initial kinetic energy of about 10^{51} erg. SN in our own Galaxy can sometimes appear brighter than Venus in the sky, and extra-galactical SN can appear brighter than their whole host galaxy. The oldest records of humans witnessing a supernova come from ancient Chinese astronomers in 185, 1006 and 1054, the remains of the latter being known today as the Crab Nebula.

The statistical occurrence of supernovae, based on extragalactic observations, is about 3 per century in our Galaxy. This means our chances to spot such an event in a lifetime are very low, considering one might occur

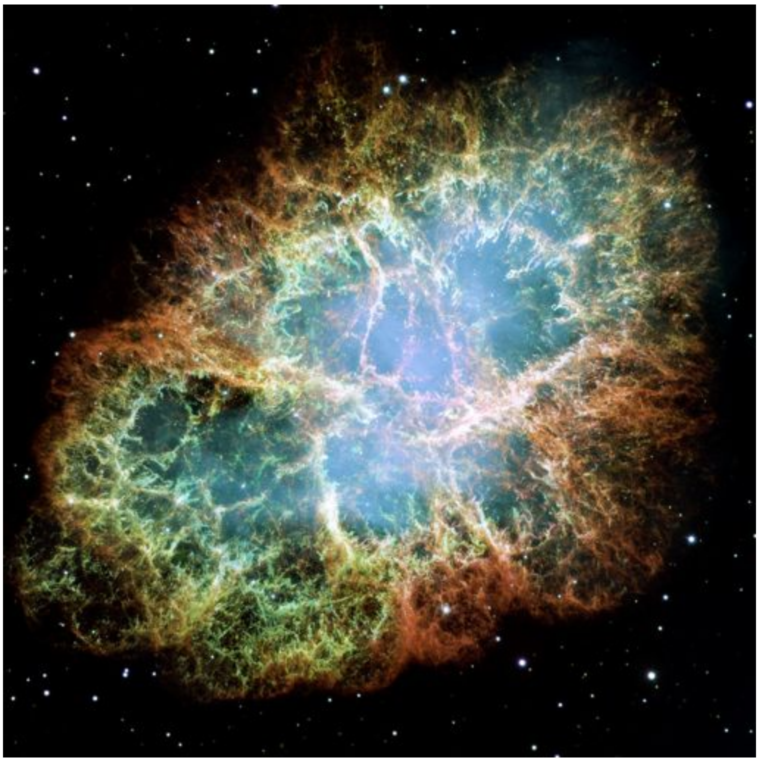

Figure 4.1: The Crab Nebula as seen by the *Hubble Space Telescope*. It is the supernova remnant of the 1054 explosion witnessed by Chinese astronomers. Credits: NASA.

on the other side of the Galaxy without our knowing. Yet, two events visible to the naked eye occurred over one generation during the emergence of modern astronomy, in 1572 (Tycho Brahe) and 1604 (Kepler). These were the latest SN in our Galaxy visible from Earth, although another supernova visible to the naked eye occurred in the nearby Large Magellan Cloud (SN 1987A). Today, thousands supernovae have been detected in other galaxies[1], which helped to better understand this phenomena. SN are typically visible for a few weeks with an intensity close to maximum, before their luminosity declines over a few months.

There are several types of SN, depending on the processes leading to the explosion. Basically, one can divide SN into two great categories further subcategorized.

- First, if the star was born too massive, namely more than 8 solar masses, it will collapse at the end of its life, when the nucleosynthesis inside the star will create iron (Fe). Being unable to form heavier elements, the internal radiation pressure opposing gravity will cease, and the star will collapse. There will remain a central object which can be a neutron star or a stellar black hole, depending on the initial mass.

- Second, a white dwarf, the ultimate stage of the stellar evolution of low-mass stars, can start accreting material from a nearby companion. When its mass increases and reaches a limit known as the Chandrasekhar limit, it will collapse. There can be no remaining central object. This type of supernovæ, known as Type Ia, can be used as standard candles, as they release every time the same amount of total energy. This means they can be used for instance to determine the precise distances of their host galaxy.

One can determine the type of a supernova by observing its spectral features.

---

[1] An updated list of supernovae is available on `http://www.cbat.eps.harvard.edu/lists/Supernovae.html`

4.1.2 Evolution of supernova remnants

Supernova remnants (SNR) illustrate the interaction of stellar material, initially expelled with tremendous kinetic energy, with the surrounding medium. They can still be detected for tens of thousands years across the whole spectrum, from radio to gamma rays, yet radio detection remains the most common identifier of remnants. Radio emission is mainly due to synchrotron emission of electrons. The physical processes at the origin of high energy emission from the remnant will be described in Section 4.2 (for a review, see e.g. Reynolds, 2008). Almost 300 remnants are identified today in our Galaxy. Information about these remnants can be found in online catalogues[2].

Supernova remnants will undergo different phases from the moment of the explosion to their definitive extinction. This overall evolution will last $\lesssim 10^6$ yr. The SNR will experience three phases: the free-expansion phase, the Sedov-Taylor phase and the radiation phase (Chevalier, 1982; Blondin et al., 1998).

- During the free-expansion phase, the expansion is fast and adiabatic to a good approximation. This phase will last until the mass of swept material is about the mass of the ejecta, typically a few hundreds years.
- The Sedov-Taylor phase follows, when the energy has been transferred to the shell and the blast wave keeps sweeping material until it has sufficiently slowed down so that the expansion is no longer adiabatic. This phase typically lasts a few 10^5 yr.
- Finally, the cooling of the remnant is efficient during the radiative phase and the remnant rapidly loses all of its energy.

4.1.3 Supernova remnants as cosmic accelerators

SNRs have long been thought to be the main acceleration sites of Galactic CRs, up to the knee at $\sim 10^{16}$ eV. One of the main arguments is that the total density of Galactic CRs could be accounted for by the conversion of about $10 - 20\%$ of the total kinetic energy of SNRs in the Galaxy.

In the Diffusive Shock Acceleration process (Bell, 1978), charged particles gyrate around magnetic fields lines with a radius depending on their energy, the Larmor radius:

$$R_L \propto \frac{\gamma m c^2}{|q|B} , \tag{4.1}$$

with the charge q, the magnetic field B and relativistic energy $\gamma m c^2$. Particles gyrating close to the front shock can then cross it back and forth, gaining energy every time. The Larmor radii of these particles therefore increase and CRs can diffuse further away from the shock, until they are too far and escape, taking energy away from the system.

The increasing density of high-energy CRs close to the shock modify the structure of the shock itself by locally amplifying the magnetic field ahead of the shock, in the so-called precursor region. The existence of this precursor region and the escape of high-energy CRs would both contribute to make the expanding shells of SNRs efficient CR accelerators, as suggested by numerical models (Vink, 2013).

Radio, X-ray and gamma-ray observations now build up evidence of particle acceleration in SNRs. Studies of the shape of the spectra and of the emission regions reveal direct evidence of the presence of high energy particles, the amplification of magnetic fields (up to $\gtrsim 100$ times the ISM value, e.g. Uchiyama et al., 2007) or the evolution of acceleration processes at different stages of the SNR (Helder et al., 2012), supporting this hypothesis. Although direct evidence that would come from detection of neutrinos created during proton-proton interactions in SNRs (Katz and Waxman, 2008) is still lacking, further evidence will come from the gamma-ray study of SNRs interacting with nearby molecular clouds.

4.2 Physical processes associated with gamma-ray emission

Recent surveys with gamma-ray observatories, such as H.E.S.S. or the *Fermi*-LAT experiment, showed that many bright GeV-TeV sources are coincident with SNRs. This emission can be well explained by a variety

---

[2] See e.g. `http://www.mrao.cam.ac.uk/surveys/snrs/` which collects information on known SNRs and related publications, or `http://www.physics.umanitoba.ca/snr/SNRcat/`, which collects available high energy observations of remnants.

of physical processes that take place at different stages of the SNR evolution (Slane et al., 2014; Yamazaki et al., 2006; Uchiyama and Collaboration, 2011).

4.2.1 Emission from the SNR shell

The emission from the SNR shell is dominated by photons revealing the presence of electrons. There are three types of emission involving leptonic processes in a SNR:

- First, synchrotron emission is a radiative process which occurs when the charged particle trajectory is deflected by magnetic fields. Magnetic fields in SNRs are typically $\gtrsim 10\ \mu$G and can generate photons from radio to X-rays, but cannot produce gamma rays.
- Second, Bremstrahlung occurs when the charged particle trajectory is deflected by the electric field of another charged particle. This process can produce photons up to photons up to MeV-TeV, and reveals the interaction of particles within the plasma of the SNR.
- Third, inverse Compton emission occurs when a relativistic particle transfers some of its energy to a low-energy photon. Here, photons from the cosmic microwave background can be scattered up to TeV energies by the highest-energy electrons.

Some of the GeV-TeV emission can also be explained by proton-proton interactions. When encountering denser material, inelastic collisions of protons can produce neutral π^0 mesons if the incoming particle has an energy higher than the threshold energy 280 MeV:

$$p_{CR} + p_{ISM} \rightarrow p'_{CR} + p'_{ISM} + \pi^0 \ , \tag{4.2}$$

where a CR proton p_{CR} encounters a local, low-energy proton p_{ISM}. Then, these pions π° dominantly decay into two gamma rays of energy $\sim 10\%$ that of the incoming proton (i.e. a 1 TeV photon is induced by a ~ 10 TeV CR particle):

$$\pi^0 \rightarrow 2\gamma \ . \tag{4.3}$$

The dense target material can be the expelled material from the explosion, within the shell of the remnant, or can be found in a nearby molecular cloud, as I describe in more details in the next paragraph. Pion-decay is the dominant hadronic process of gamma-ray emission.

4.2.2 Emission from the cloud

Pion-decay dominates the gamma-ray emission from a cloud close to the SNR, as the cloud contains a large density of target protons. As shown by Figure 4.2, the gamma-ray spectrum from the cloud then mimics the incoming CR spectrum (Ackermann and Collaboration, 2013). This interaction between CR protons from the SNR and a molecular cloud can occur when the expanding shock of the remnant runs into the cloud, or when accelerated protons escape the shell and reach the cloud nearby. In both cases, this usually means that the SNR is old.

- In the first case, the SNR needs enough time to expand and reach the cloud, which is typically at least a few pc from the center of the SNR. If the cloud is crushed by the expanding shock, CR protons are likely to be freshly reaccelerated in-situ because of the increasing compression, leading to localized bright TeV emission.
- In the second scenario, the SNR also needs enough time to accelerate protons to the highest energies, so they escape the shell and diffuse away to the cloud. The energy of the irradiating CR protons is thus very high and TeV emission can be strong. The flux of gamma rays from the irradiated cloud reads:

  $$F_\gamma \propto \frac{M_{MC} F_{CR}}{d^2} \ , \tag{4.4}$$

  where M_{MC} is the mass of the molecular cloud, F_{CR} the initial flux of CRs escaping the SNR and d the distance of the cloud from the SNR. If the cloud is not too far away (no more than a few tens pc), then energy-dependent propagation properties are likely to be negligible.

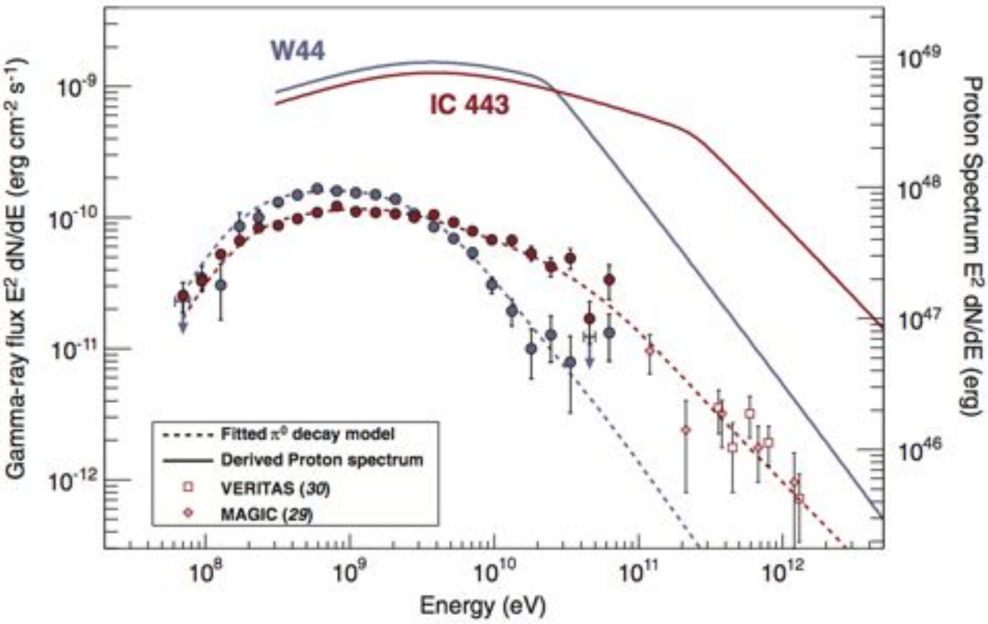

Figure 4.2: Proton and gamma-ray spectra determined for IC 443 and W44 (Ackermann and Collaboration, 2013). The energy of a gamma ray is $\sim 10\%$ that of the incoming CR proton, and the gamma-ray spectrum mimics the CR spectrum.

Nevertheless, if the SNR gets too old, namely older than $\gtrsim 5 \times 10^4$ yr, wave-damping and energy losses become more efficient (Yamazaki et al., 2006), and CRs likely can not be accelerated to high-enough energies to produce TeV gamma-ray emission.

4.2.3 Determination of the operating physical processes from observed gamma-ray spectra

To discriminate between the different processes, especially when no spatial correlation with dense gas can be confirmed (e.g. due to a low spatial resolution of the instruments), one has to model the spectral energy distribution (SED) of the gamma-ray source. The shape of the SED is described in terms of spectral indexes (i.e. the index in the power-laws that best fit the data), spectral breaks (i.e. energies at which spectral indexes change) and hardness (relative contributions of low- and high energies in the SED). The SED can be fitted by overlapping spectral emissions of several physical processes. Therefore, the SED is characteristic of the processes at play and can be used to determine the dominant processes.

Gabici et al. (2009) presented a theoretical study in which they derived the expected broad-band non-thermal emission from a molecular cloud next to a SNR. The predicted emission is dominated by hadrons as the electrons lose their energy too quickly to escape the SNR. Gabici et al. (2009) also studied the evolution of the expected emission with the age of the remnant and its distance to the cloud. As compared to an isolated cloud, two characteristic peaks come out in the SED at high energy gamma rays ($\gtrsim 100$ GeV) and in the X-ray band ($\approx 0.01 - 100$ keV), due repsectively to pion decay and to synchrotron emission of secondary electrons produced in the process. These two peaks are therefore both a clear signature of π^0-decay, and the cloud can become 1000 times brighter at TeV wavelength than an isolated non-interacting cloud. The flux ratio of TeV to X-ray emission is complementary evidence of the hadronic process as it can increase up to a few tens in such cases (see Gabici et al., 2009, Figure 4).

The position and intensity of these peaks move to lower energies with time, as the maximum energy of CRs produced at the SNR decrease and lower energy CRs escape the shell. It varies also with the distance to the cloud, as the actual flux reaching the cloud varies with the distance and the diffusion time to the cloud is energy-dependent. Interestingly, Gabici et al. (2009) also showed that the emission at GeV is dominated by background CRs in most clouds (called passive clouds), except for oldest SNRs ($\gtrsim 3 \times 10^4$ yr) closest to

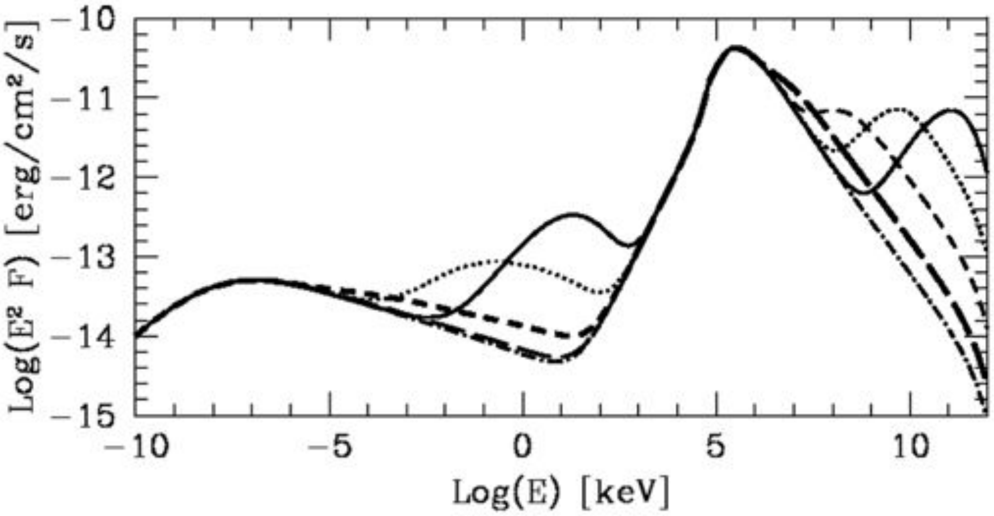

Figure 4.3: Time dependence of the SED from a molecular cloud next to a SNR (Gabici et al., 2009, Figure 4). The solid, dotted, short-dashed and long- dashed lines refer to the emission at increasing times after the explosion. The dot-dashed line represents the spectrum of an isolated passive cloud. The two time-dependent characteristic bumps at TeV and X-ray (keV) energies are due to π°-decay due to CR protons, and synchrotron emission from the secondary electrons induced in the process, respectively.

the adjacent cloud ($\lesssim$ 50 pc). This means that in some cases, the GeV emission can be no different from an interacting cloud and an isolated cloud. Yet, one has to make sure of the spectral compatibility between GeV and TeV emission in the identification process of such SNR-MC associations. To do so, observations of GeV gamma rays by Fermi-LAT are of tremendous importance, as the spectrum from SNRs is very steep in this energy range.

Recent TeV observations led to the determination of the dominant physical processes at play. In several SNR-MC associations (oldest SNRs), the π^0-decay origin of TeV emission seems to prevail (Ackermann and Collaboration, 2013; Giuliani and Collaboration, 2011; Abramowski and Collaboration, 2015b), whereas for some isolated SNRs (youngest SNRs), leptonic processes can still well reproduce the observations (Ellison et al., 2010; Abdo and Collaboration, 2011). For the brightest GeV SNRs observed with *Fermi*-LAT, inverse Compton from electrons is disfavored, thus supporting the π^0-decay scenario (Thompson et al., 2012).

4.2.4 Evolution with time

The contribution of each process varies depending on the age of the remnant:

- During the Sedov phase, the X-ray band is dominated by synchrotron radiation of primary electrons for youngest SNRs ($\lesssim 10^4$ yr). Then, with age, since the energy-loss timescale of electrons is short, the emission becomes dominated by π°-decay.
- During the radiative phase, the maximum energy achieved by electrons is small and the TeV emission is dominated by π^0-decay. The X-ray band is then dominated by synchrotron radiation of secondary electrons, created during the decay of charged pions.

4.2.5 Contamination

Finally, the gamma-ray emission can be contaminated by emission from a nearby pulsar wind nebula (PWN). A PWN is a nebula powered by an outflow of relativistic electrons from a pulsar. It emits gamma rays due to inverse Compton scattering by electrons, and shows an X-ray counterpart due to synchrotron emission. The pulsar can be given a kick at the moment of the explosion and slowly get out of the field of view of a telescope within the lifetime of the SNR. Yet, it can still be close enough to the SNR to contribute to the high energy source (see e.g. Aleksić and Collaboration, 2012, about W51C).

4.3 Evidence of the SNR interaction with molecular clouds

To determine whether a supernova remnant is interacting with a nearby molecular cloud, one has to look for several consistent pieces of evidence. Especially, one has to make sure that the cloud and the remnant are not just spatially coincident by "accident", but they are physically connected. To confirm the existence of an interaction, one can use complementary observations at different wavelength, described in the following paragraphs and illustrated in Figure 4.4.

4.3.1 Evidence from the cloud properties

Systemic velocities

A first obvious requirement is that the SNR and the cloud not only overlap on the sky but have also the same distance from the Sun. Since usually SNRs have distances larger than about 1 kpc, their distance is derived from their systemic velocity. Because of the rotation of the Milky Way, sources at different distances have also different velocities seen from the Sun. Therefore, using models of the Galactic rotation curve (e.g. Kerr, 1962; Gómez, 2006, and references therein), one can assess whether objects on the same line of sight are also at the same Heliocentric distance.

Therefore, one should make sure that the systemic velocities of the SNR and that of the cloud are consistent. However, since the systemic velocity can significantly vary within one cloud (up to a few tens $\mathrm{km\ s^{-1}}$), if the velocity of the SNR falls in the cloud range of velocities, this is evidence of a *possible* interaction. If not, the existence of an interaction cannot be ruled out yet and one needs to look for stronger evidence.

The systemic velocity of the SNR is usually inferred from H I emission (e.g Koo and Heiles, 1991). The velocity of the molecular cloud is usually measured with emission lines, such as CO.

Presence of a shock

Another piece of evidence is provided by the presence of a shock. Since the SNR expels matter at supersonic velocities into the diffuse medium, a shock wave is formed and traces of it might be visible when it encounters the dense gas of the cloud.

The shock induces an important velocity dispersion which increases the line width of emission lines in the cloud. For example in W28, Slysh et al. (1980) report the broadening of H_2CO absorption lines in the cloud, form 3.5 to 10 $\mathrm{km\ s^{-1}}$as one moves toward the SNR.

Besides this line broadening, some molecular species are known to be characteristic of the presence of a shock. This is for instance the case of SiO, which forms rapidly after the passage of a shock releases the silicon incorporated in the grains into the gas phase (Schilke et al., 1997).

Another unambiguous tracer of the shocked material is the presence of OH masers. Masers are compact sources of stimulated emission of the OH transition at 1720 MHz. They show narrow linewidth and their brightness temperature can range from 10^4 to 10^8 K, orders of magnitude higher than expected in the cold gas environment (Claussen et al., 1997). Such masers have been observed extensively at the edges of radio shells of SNRs. The population inversion leading to maser emission can be achieved by either collisional or radiative pumping at low OH densities. These are most effective at H_2 densities of $10^3 - 10^5\ \mathrm{cm^{-3}}$ (Elitzur, 1976), which correspond to typical densities in molecular clouds.

Ionisation enhancement

The observation of an enhanced ionisation in the cloud may be additional evidence of an interaction, *via* the presence of an intense CR flux accelerated in the SNR nearby. This high ionisation can be revealed by unusual abundances of the tracers of the CR ionisation (see Chapter 3), w.r.t. their abundances in standard isolated clouds. Looking for the CR induced ionisation in dense molecular clouds is the main purpose of this thesis and will be presented in the next Chapters.

4.3.2 Evidence from gamma-ray emission

In several cases, the molecular emission from a cloud next to an SNR is spatially coincident with gamma-ray emission at GeV or TeV energies, suggesting gamma-ray production *via* proton-proton collisions. The

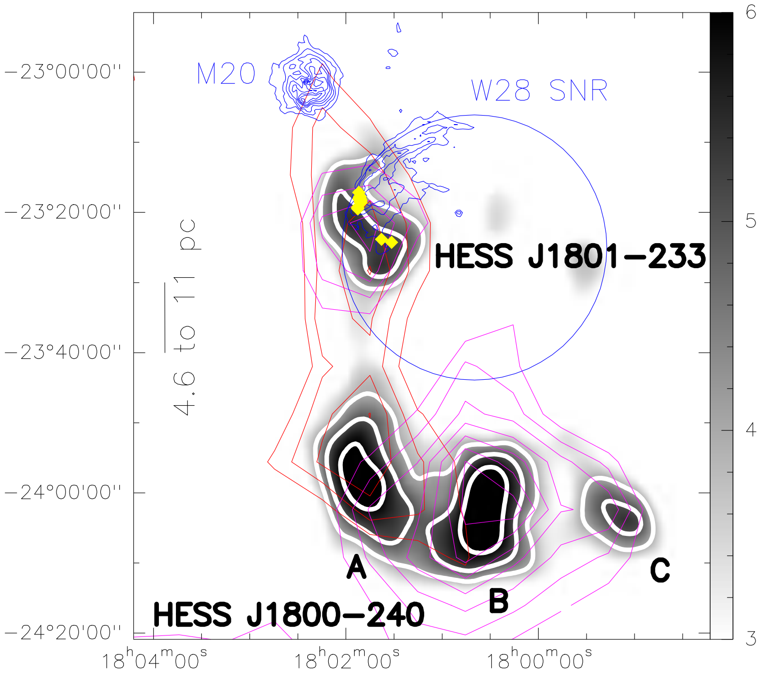

Figure 4.4: Large scale map of the W28 complex: evidence of the interaction (Vaupré et al., 2014). The blue circle gives the approximate radio boundary of the SNR W28 (Brogan et al., 2006). A large molecular cloud next to the remnant is shown by CO(1-0) emission (Dame et al., 2001): red contours show the emission integrated over $15-25$ km s^{-1} and magenta contours trace the emission integrated over $5-15$ km s^{-1} (levels are $40-70$ K km s^{-1} by 5 K km s^{-1}). Extended TeV emission from the cloud is suggestive evidence of the interaction of the SNR with the cloud through proton-proton collisions and pion-decay. TeV emission as seen by HESS is shown by the grayscale (in σ) and thick white contours(levels are $4-6$ σ). Further evidence of the interaction can be found e.g. in the presence of OH masers (Claussen et al., 1997), shown by yellow diamonds, which are a signature of shocked gas.

Fermi-LAT space telescope can detect sources at GeV energies with an angular resolution going down from 3° to 0.04° with increasing energies. The H.E.S.S. Cherenkov telescopes can achieve a resolution of $\sim 0.1°$ and MAGIC $\sim 0.05°$. Typical angular sizes of molecular clouds are $\sim 1°$ at 5 kpc. Thus, in each case, the resolution is much lower than that of radio observations (< 30 arcsec for the IRAM 30m telescope) and it can happen that the SNR is not resolved. In such cases, it remains uncertain whether the gamma-ray emission comes from the SNR or the nearby cloud.

Nevertheless, additional information on the gamma-ray spectrum can help determine the physical process at the origin of the gamma-ray emission, as presented in Section 4.2. An hadronic origin of the gamma emission which implies an interaction with the denser material of the molecular cloud would be conclusive evidence of this interaction.

Chapter 5

Thesis work: targets and methods

Contents

5.1 Open questions addressed by the thesis

During my PhD work, I studied the CR ionisation in dense molecular clouds in the vicinity of supernova remnants. This work addressed the following questions:

1. Do dense molecular clouds next to supernova remnants experience an enhanced ionisation w.r.t. standard clouds? A possible enhancement can be measured by the chemical abundances of tracers of the ionisation, and would give constraints on the low-energy tail of the CR flux.

2. Is there an ionisation gradient away from the shock? Measuring the ionisation in the gas at increasing distances from the shock, it may be possible to observe a variation in the CR ionisation. Such a gradient would bring evidence of the propagation of ionising CRs from the shell. Therefore, it would bring constraints on the propagation properties of low-energy CRs.

3. Can we constrain the CR spectrum at the acceleration site? By observing the effects of CRs close to a SNR, we can constrain their initial spectrum. At high energy, CRs induce gamma-ray emission from dense clouds through pion decay, and the gamma-ray spectrum mimics the CR spectrum. At lower ($<$ 280 MeV) energy though, pion-decay is ineffective, thus the low-energy tail of the initial CR spectrum is poorly constrained. By studying the ionisation in these clouds by low-energy CRs ($\lesssim$ 1 GeV), we could provide unprecedented constrains on the initial CR spectrum at these energies.

4. How to accurately measure the ionisation in dense clouds? There is a two-order of magnitude uncertainty in the determination of ζ from DCO$^+$/HCO$^+$ at low ionisation, and this method only gives lower limits at high ionisation. This suggests to try and identify a new set of tracers of the ionisation, both at low and high ionisation.

5.2 Methods

My thesis work combines radio observations and chemical modeling of dense molecular clouds. I used the IRAM radio telescopes to observe the emission lines of a few chosen species.

- From the observations, I computed the integrated intensities of the targeted emission lines. By comparing observations of ^{13}CO and C^{18}O emission lines with predictions from a radiative transfer code, I

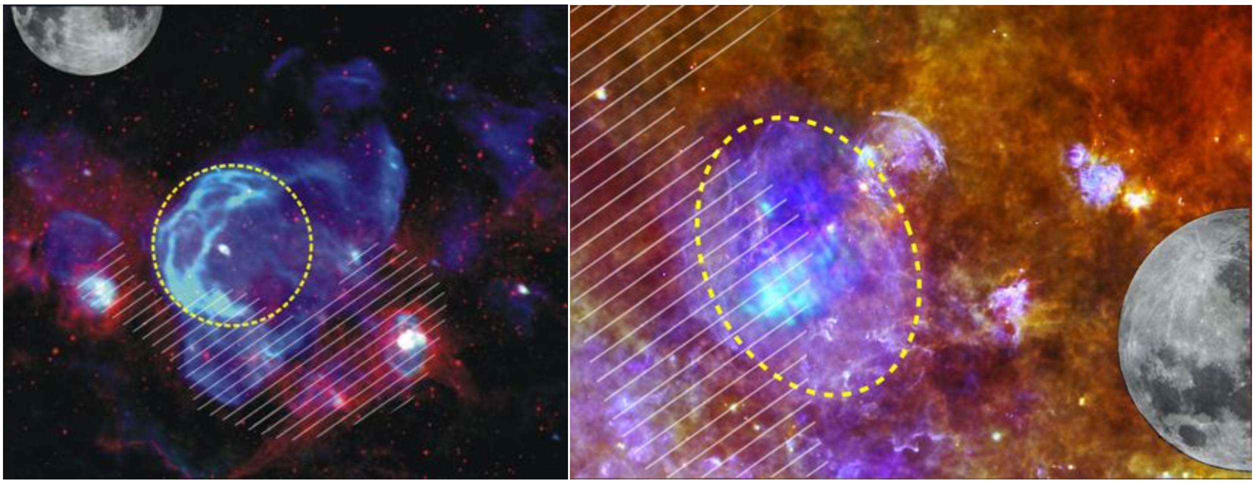

Figure 5.1: The interacting SNR W28 (left) and W44 (right). In each picture, the yellow dashed line shows the approximate limit of the expanding shell of the SNR traced by synchrotron emission ; the gray hatched region shows the approximate *projected* location of the nearby molecular cloud, which is not visible at these wavelength. The Moon is overlaid to give the projected scale on the sky. Many other objects (SNRs, HII regions, ...) are visible in the field of view. **Left:** Adapted from the composite radio/infrared image of the SNR W28 region (Brogan et al., 2006). **Right:** Adapted from the composite X/infrared image of the SNR W44 region. Credits: ESA/PACS/SPIRE/Quang Nguyen Luong & Frederique Motte, HOBYS Key Program consortium (far-infrared); ESA/XMM-Newton (X-rays)

inferred the physical conditions in the gas. Then, I deduced the chemical abundances of other species in the cloud, and abundance ratios, e.g. DCO^+/HCO^+.

- Chemical modeling allowed me to compare the observed abundance ratios to theoretical predictions in a gas cloud matching the observed physical conditions, and constrain the ionisation fraction and CR ionisation rate. I also explored the model to look for the influence of the CR ionisation rate on other species and identify candidate new tracers of the ionisation.

I will describe in more details each step of these methods in Chapters 6 to 8.

5.3 Selection of the studied regions

For the purpose of my study, a sample of confirmed interacting SNRs was selected, starting with W51C, W28 and W44 (see Figures 5.1 and 5.2, and Table 5.1). In each case, several pieces of evidence favour the physical interaction of the SNR with ambient molecular clouds, from radio synchrotron emission to π^0-decay signature at GeV-TeV energies and including evidence of shocked gas. CO maps of the nearby clouds are available from Dame et al. (2001). They are spatially coincident with high-energy sources as seen by H.E.S.S., *Fermi*-LAT or MAGIC. These three SNR-MC associations are therefore good candidates for further investigation of the CR induced chemistry in the gas. Each source will be further described in the corresponding paper included in this thesis (see Chapter 9, 10, 12).

Several unidentified TeV sources are being explored very actively by the H.E.S.S. community, and recent publications are suggesting the next sample of SNR-MC associations where to look for effects of the CRs on the chemistry, for instance W41 (Abramowski and Collaboration, 2015c,a) or G349.7+0.2 (Abramowski and Collaboration, 2015b). At GeV energies, it was also showed that SNR-MC associations constitute the main population of SNRs detected by the *Fermi*-LAT telescope (Thompson et al., 2012, Figure 7). In the next few years, a new sample of targets could also be suggested by these GeV observations.

Table 5.1: Comparison of the age and distance of the SNRs W51C, W44 and W28, and typical physical conditions I measured in the nearby clouds.

		W51C	W44	W28
	Galactic coordinates	(49.3, 0.3)	(34.6, -0.5)	(6.3, 0)
SNR	Age [yr]	$\sim 3 \times 10^4$	$\sim 2 \times 10^4$	$\gtrsim 10^4$
	Heliocentric distance [kpc]	~ 5.5	~ 3	$2 - 4$
	Galactic distance [kpc]	~ 6.9	~ 6.3	$4.5 - 6.5$
Cloud	Density n_{H} [cm^{-3}]	$\sim 10^4$	$10^4 - 10^5$	$10^3 - 10^4$
	Temperature [K]	$21 - 24$	$7 - 17$	$8 - 20$

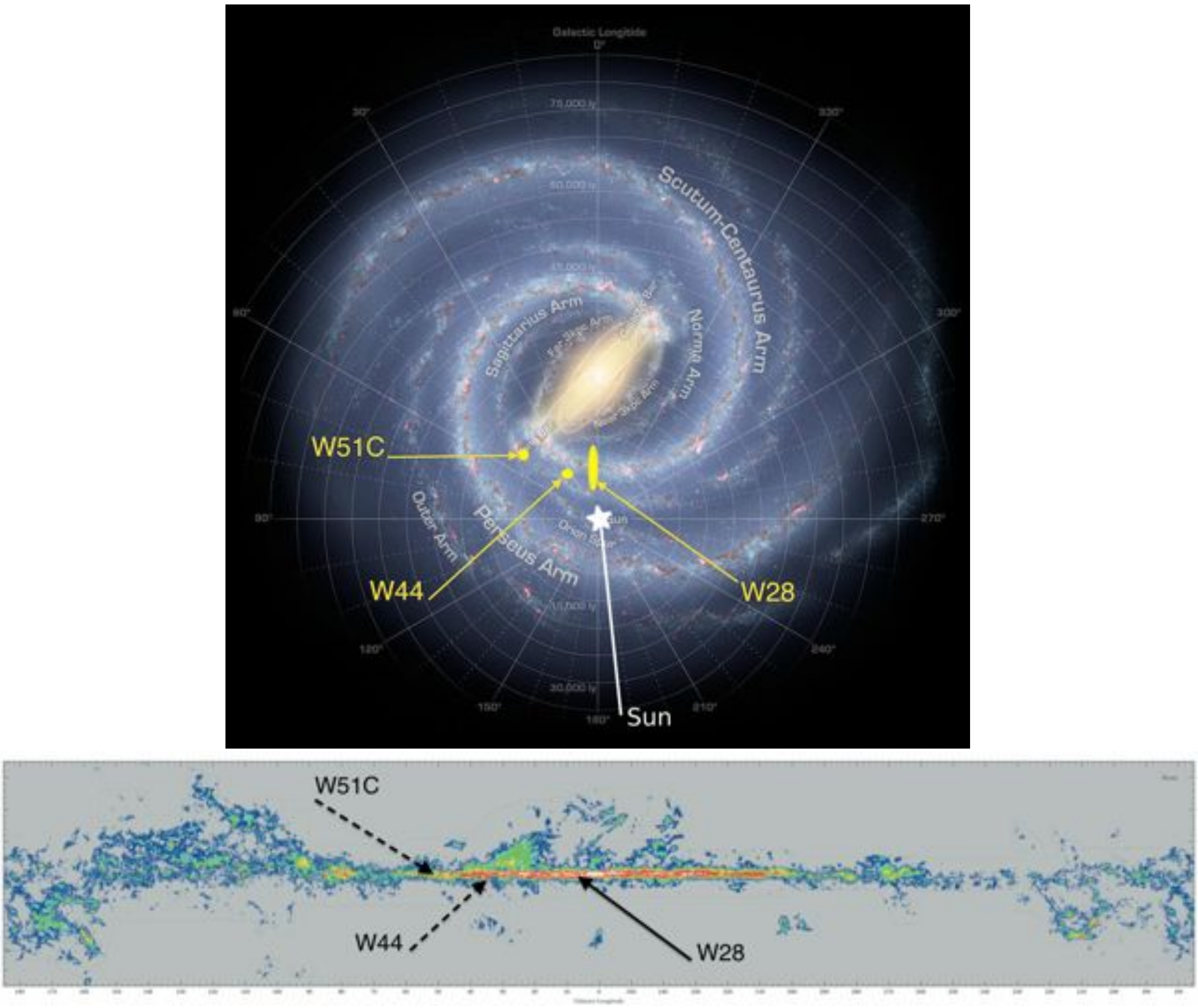

Figure 5.2: **Top:** Model of the Galaxy with approximate positions of W51C, W44 and W28. Credit: NASA/JPL-Caltech. **Bottom:** Dense molecular clouds in the Galactic disk, surveyed using ^{12}CO (Dame et al., 2001). Coordinates are Galactic. The positions of the three SNR-MC associations I studied are overlaid. All three are very close to the disc mid-plane, and W28 is particularly close to the Galactic center, in complex regions where other objects on the line of sight can introduce confusion in the observations (see Chapter 7).

Part II

Methods: Radio observations and chemical modeling

Chapter 6

Observations

Contents

In this chapter, I describe the observational aspect of the thesis. The sources have been presented in section 5.3. Here I introduce the field of radio astronomy, the basics of molecular spectroscopy and the 30m observations.

6.1 Radio astronomy

6.1.1 Beginnings of radio astronomy

After the discovery of the similar nature of light and radio waves, which both are electromagnetic waves, it was predicted in the late 1890s that stars and especially the Sun should be the source of electromagnetic radiation outside the optical domain. Yet, the poor quality of the radio detectors at the time prevented any radio detection from the Sun and the prediction was forgotten for a few decades.

It is then by accident that the first radio source in the Galaxy was detected in 1930 by K. Jansky, an engineer who worked at the Bell Telephone Laboratories. When working on sources of parasites in radio communications, he actually discovered bright emission at 20.5 MHz from Sagittarus A, at the center of our Galaxy. Unfortunately, his company assigned him to another project and Jansky had to give up his project to build a 30m single-dish radio telescope dedicated to the observation of Galactic sources.

A few years later, inspired by these results, G. Reber built his own radio 9m antenna, and published in the early 1940s the very first radio surveys of the Galaxy. He was an amateur astronomer who literally metamorphosed the field of radio astronomy from his backyard. His observations also led in 1950 to the identification of synchrotron emission as the dominant process in Galactic radio sources.

The field of radio astronomy was really gaining interest in the 1960s, when A. Penzias and R. Wilson experimented with a new radio antenna. They were two physicists also working at Bell Labs. They detected a

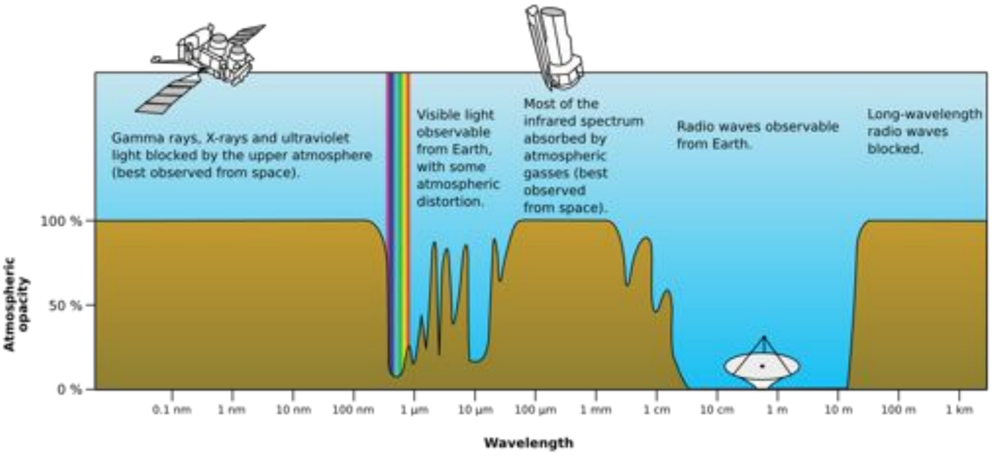

Figure 6.1: Atmospheric electromagnetic opacity. Credits: NASA, public domain.

remaining noise of $\sim$ 3 K at 4.08 GHz after they had cleared the signal from all known sources of interference. They concluded the noise was of extragalactic origin. Their discovery was attributed by the theorists R. Dicke, P. Peebles, P. Roll and D. Wilkinson to the previously predicted cosmic microwave background (CMB) radiation. This constituted a major contribution to the field of cosmology and a test to the Big Bang theory. A. Penzias and R. Wilson were awarded the Nobel Prize in 1978 for their discovery.

6.1.2 The atmospheric transmission in the radio to submillimeter range

Figure 6.1 shows the atmospheric opacity in the electromagnetic spectrum. The atmosphere introduces limitations to ground-based observations due to different physical processes: in general, the shortest wavelength are blocked by the upper atmosphere, the infrared radiation by atmospheric gasses (especially H_2O, O_2 and O_3) and long-wavelength radio waves by reflexions in the ionosphere. For parts of the spectrum where the atmosphere is opaque, one needs to use space telescopes (like the *Herschel Space Observatory* which observes at submillimeter wavelengths) or indirect observations (e.g. Cherenkov telescopes at high energy, see section 2.2).

Here we focus on the atmospheric transmission in the radio to submillimeter range, where the molecules used in the work of this thesis emit through rotational transition lines. Figure 6.2 shows a partially transparent atmosphere at these wavelengths (note that this figure gives the atmospheric transparency, whereas Figure 6.1 gives the opacity). The spectral variations of the atmospheric transmission are due to the presence of water vapor and molecular oxygen (and ozone to a lesser extent).

6.1.3 The IRAM observatories

During my thesis, I used the IRAM telescopes to carry out the observations. IRAM[1] stands for *Institut de Radioastronomie Millimétrique*. The institute is co-funded by Germany, France and Spain. Its main objective is to maintain and develop its two observatories: the single-dish 30m telescope and the PdBI/NOEMA interferometer.

The 30m telescope is located at Pico Veleta in the Spanish Sierra Nevada, at an altitude of 2850m (Figure 6.3). It is a single-dish telescope, equipped with state-of-the-art heterodyne receivers and bolometers. It is well suited for both continuum and line observations. The recent upgrades of the heterodyne receivers EMIR (Carter et al., 2012) allow efficient spectral surveys, up to 16 GHz simultaneously at 195 kHz resolution (i.e. $\sim$0.5 km s^{-1} at 110 GHz), or 4 GHz at 50 kHz resolution ($\sim$0.1 km s^{-1}). These survey capabilities rely on sideband separating mixers (2SB), where both sidebands resulting from the frequency modulation can be extracted independently. This is a great improvement w.r.t. double side band (DSB) mixers, which

---

[1] This acronym also works in German (*Institut für Radioastronomie im Millimeterbereich*) or Spanish (*Instituto de Radioastronomía Milimétrica*), but not in English.

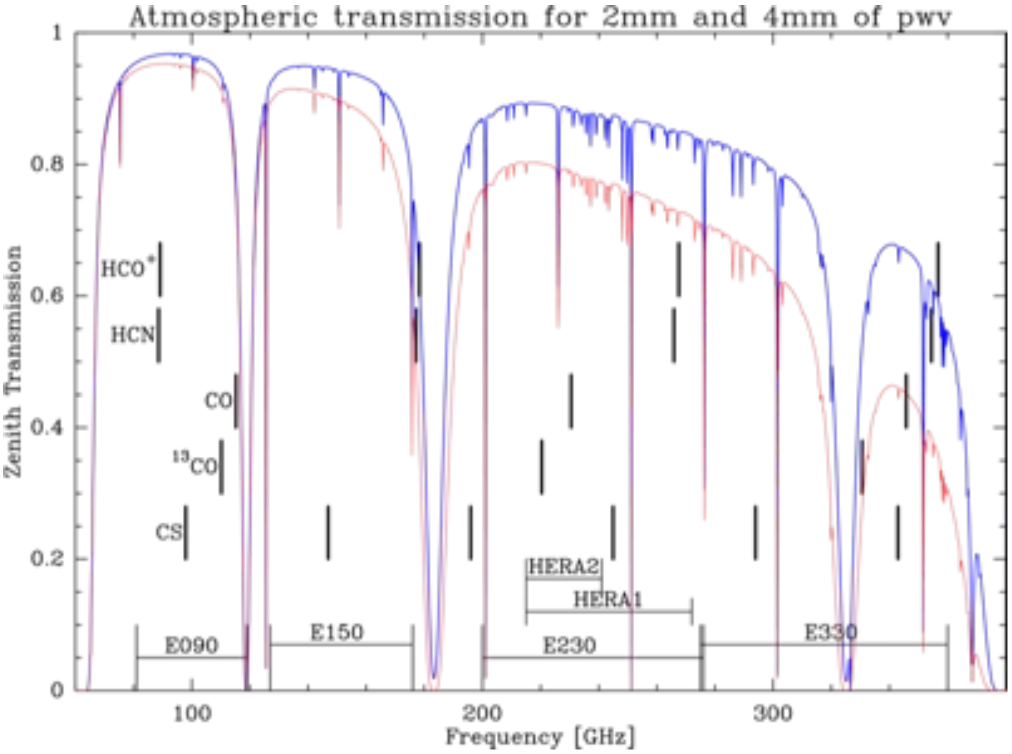

Figure 6.2: Atmospheric transmission at the IRAM 30m telescope. The transparency decreases with bad weather conditions, quantified by the precipitable water vapor (pwv). The available receivers (e.g. E090) and main molecular lines(e.g. CO) are indicated in each window. Figure from the IRAM website.

superimpose both sidebands and can introduce confusion in the line identification process, and single side bands (SSB) which reject one of the sidebands, i.e. half the data.

The Plateau de Bure Interferometer (PdBI) is a six-antenna interferometer in the French Alps, at 2250m. Each antenna is 15m diameter, and the maximum baseline can currently reach ∼800 m, providing a spatial resolution of 0.5 arcsec at 230 GHz. Heterodynes receivers of the PdBI rely on SSB and DSB mixers. The wide band correlator offers a total of 3.6 GHz of bandwidth at 1.95 MHz resolution. A spectral resolution of 40 kHz can be reached with the narrow band correlator.

The PdBI/NOEMA and 30m facilities are highly complementary, as the single-dish allows to recover the short spacings that are missing from interferometric observations alone. Used together, they permit to better probe compact regions at high spatial resolution.

PdBI has transitioned into the NOEMA interferometer, which will eventually be composed of twelve such antennas. The 7th antenna, the first of the second series of antennas, was inaugurated in September 2014.

6.2 Molecular spectroscopy

In the millimeter range, the continuum is dominated by dust emission and non-thermal free-free emission from electrons. Spectral lines reveal the presence of atoms and molecules in the gas, via their spectroscopic transitions. This section provides a very brief description of the physical origin of these lines, and how this can help determining what species might be observed (Spitzer, 1998; Tielens, 2005)

6.2.1 Molecular energy level diagram

The energy level diagram of a molecule is a sketch summarising the levels of the internal energy that a molecule/atom can have. Transitions between two different states are accompanied by emission/absorption of photons with the same energy difference. The energy transitions span from radio to UV, within three very

Figure 6.3: **Left:** The IRAM 30m telescope, near Pico Veleta in Spain. **Right:** The 15m antennas of the NOEMA interferometer, on Plateau de Bure, France. Credits: Solenn Vaupré.

different energy ranges. The highest energy transitions involve electronic levels. As for atoms, electronic transitions occur in the visible/UV range, i.e. at energies of the order of a few eV or $\sim 10^4$ K. At lower energies, in the mid-infrared, vibrational transitions involve changes in the nuclei relative distance, namely vibrations, bending and stretching. The larger the number of atoms in the molecule, the larger the number of possible vibration modes. Energies of these transitions are typically of a few 0.1 eV, or 10^3 K. Finally, the rotational modes of a molecule, within a given electronic and vibrational state, induce low energy transitions of $\sim 10^{-3} - 10^{-2}$ eV or $\sim 10 - 500$ K. These are the transitions, which can be detected with radio telescopes, in the (sub)millimeter range.

6.2.2 Observability of emission lines

At the low temperatures, but large densities, of molecular clouds, only rotational levels are typically populated and we will therefore focus on rotational transitions in the following.

First, dipolar electric transitions require the molecule to possess a permanent dipole μ‘, hence species such as H_2, or H_3^+, which are symmetric, emit only through higher-order interaction transitions, which have intrinsically much weaker probabilities. The strength of a dipolar electric transition is related to the probability of spontaneous decay given by the Einstein coefficient (see Table 6.1):

$$A_{ul} \propto \nu^3 \mu^2 \ . \tag{6.1}$$

Second, the species has to be abundant enough along the line of sight, so that the total emission is strong enough to be detectable. Of course, the limit of detectability depends on the sensitivity of the detector. The most abundant species in cold (< 100 K) molecular cloud are H_2, which is symmetric, and CO, which is not. Besides its dipolar moment, CO is very abundant and has a low critical density (see below), therefore it is easily collisionally excited. That's why CO became the main tracer of dense clouds. The strength of the CO emission allows maps and Galactic surveys (e.g. Dame et al., 2001) to be performed in a reasonable time. Besides well known abundant molecules in the ISM, chemical models can help to determine which species are abundant enough to be detected in a given environment (see Chapter 8).

Finally, when using a ground-based radio telescope, an observer is limited by the atmospheric windows (see section 6.1.2). Consequently, one has to make sure that potential strong emission lines for a given species do not fall into one of the opaque spectral bands of the atmosphere. For instance, due to high amounts of water in the atmosphere, space telescopes are mandatory to observe H_2O in the ISM (except for high-redshift objects, where the Doppler shift of the water lines is large enough to fall into an atmospheric window).

6.2.3 Critical densities

The rotational level populations of a molecule result from the competition between radiative processes and collisional excitation and de-excitation. Radiative processes are characterised by Einstein coefficients, relative to each transition. In molecular clouds, collisions are a major source of excitation and de-excitation. Collisions can be non-reactive and nonelastic, mainly with H_2 because of its high abundance, but also with He. In some instances, collisions with electrons need to be taken into account, too (e.g. HCO^+, Faure, 2011). Finally, it may be necessary to distinguish between collisions with ortho- or para-H_2. In our calculations at low temperatures we have assumed that $o/pH_2 \ll 1$, hence collisions are dominated by pH_2.

Reactive collisions can also play a role in the excitation state of a molecule when the chemical timescales of this molecule are comparable with those of nonreactive nonelastic collisions. The excitation is due to the energy involved in the formation and destruction reactions of the molecules (Godard and Cernicharo, 2013).

Studying a two-level diagram with an upper- (u) and a lower (l) energy levels can help understanding the basics of the processes involved. First, an isolated excited molecule can spontaneously emit a photon to release some energy (spontaneous emission). An incoming photon can also excite or de-excite an energy level of the molecule (absorption or induced emission). The most common source of (de-)excitation is through collisions, mainly with H_2 or He.

The dominant (de-)excitation process depends on the so-called critical density $n_{\rm crit}$:

$$n_{\rm crit} = \frac{A_{ul}}{\gamma_{ul}} \ , \tag{6.2}$$

defined here for an isolated two-level system, with the Einstein coefficient for spontaneous emission A_{ul} and the collisional rate coefficient γ_{ul}. The critical density is characteristic of a species and transition. It depends on the kinetic temperature $T_{\rm kin}$ through γ_{ul}, and from equation 6.1, one gets approximately:

$$n_{\rm crit} \propto \nu^3 \mu^2 T_{\rm kin}^{-1/2} \ . \tag{6.3}$$

The critical density is an important parameter to describe the dominant de-excitation process:

- If $n_{\rm crit} < n_{\rm coll}$ (where $n_{\rm coll}$ is the density of colliders, e.g. H_2, He or e^-), then de-excitation is dominated by collisions rather than photon emission. The level populations are then determined by collisions, and follow Boltzmann's distribution (local thermal equilibrium is achieved). The transition is then *thermalised*. In that case, the measured intensities of these transitions will give the kinetic temperature of the gas, regardless of their abundance. These transitions can be regarded as thermometers.

- On the other hand, if $n_{\rm crit} > n_{\rm coll}$, then photon emission dominates de-excitation. The levels are *sub-thermally* populated and their relative populations can be described by the excitation temperature $T_{\rm ex} < T_{\rm kin}$.

The intensity of a thermalised transition only depends on the gas temperature, whereas sub-thermal transitions can give information on the gas density and the species abundance. In that sense, species with higher critical densities can be used as probes of higher density regions. Table 6.1 gives the critical densities of the transitions observed in this work, under the assumption of an isolated two-level energy diagram.

6.2.4 Optical depth

Finally, the molecular radiation has to make its way to Earth. Since it can go through gas and dust, all the material along the line of sight ultimately contributes to the observed intensities of molecular lines. The signal that reaches Earth from the cloud at a given frequency is described by the radiative transfer equation (e.g Spitzer, 1998). This equation takes into account the emission of background signal (Cosmic Microwave Background, stellar radiation, ...) by the cloud and emission/absorption from the cloud itself. It is then possible that several isolated clouds between the source and the observer come to alter the initial signal. The radiative transfer equation defines the optical depth τ_ν to describe the total amount of absorbing material on the line of sight, which of course depends on the frequency ν.

For large amounts of material along the line of sight, a transition can become optically thick ($\tau_\nu \gg 1$). An optically thick transition means that the signal observed from Earth at this frequency is dominated by the source function of the material, i.e. photons deep inside the cloud, including backgroud emission, cannot escape. In other words, the amount of material along the line of sight is so large that the cloud becomes opaque at this frequency. In this case, the emission also saturates and the observed intensity becomes a direct measurement of the excitation temperature (see section 6.3.3).

Table 6.1: Critical densities and dipole moments computed under the assumption of an isolated two-level energy diagram, for the species and transitions used in this work. Einstein coefficients for spontaneous emission A_{ul} and the electric dipole moments μ are taken from the online Cologne Database for Molecular Spectroscopy (CDMS), `http://www.astro.uni-koeln.de/cdms/`. The collisional rate coefficients γ_{ul} at 20K for collisions with H_2 are taken from the BASECOL database, `http://basecol.obspm.fr/`.

Species	μ [D]	Transition	Frequency [GHz]	A_{ul} [s^{-1}]	γ_{ul} [cm^3.s^{-1}]	n_{crit} [cm^{-3}]
^{13}CO	0.11046	(1 – 0)	110.201	6.3×10^{-8}	3.2×10^{-11}	2.0×10^{3}
CO	0.11011	(1 – 0)	115.271	7.2×10^{-8}	3.2×10^{-11}	2.2×10^{3}
		(2 – 1)	230.538	6.9×10^{-7}	3.1×10^{-11}	2.2×10^{4}
		(3 – 2)	345.795	2.5×10^{-6}	6.4×10^{-11}	3.9×10^{4}
N_2H^+	3.40	(1 – 0)	93.174	3.6×10^{-5}	2.3×10^{-10}	1.6×10^{5}
$H^{13}CO^+$	3.90	(1 – 0)	86.754	3.9×10^{-5}	2.3×10^{-10}	1.7×10^{5}
HCO^+	3.90	(1 – 0)	89.188	4.2×10^{-5}	2.3×10^{-10}	1.8×10^{5}
		(2 – 1)	178.375	4.1×10^{-4}	1.2×10^{-10}	3.4×10^{6}
		(3 – 2)	267.558	1.5×10^{-3}	3.7×10^{-10}	4.1×10^{6}
DCO^+	3.90	(2 – 1)	144.077	2.1×10^{-4}	2.3×10^{-10}	9.1×10^{5}
HCN	2.9852	(1 – 0)	88.632	2.4×10^{-5}	1.9×10^{-11}	1.3×10^{6}
CN	1.45	(1 – 0)	113.500	1.2×10^{-5}	7.2×10^{-12}	1.7×10^{6}

For optically thin transitions ($\tau_\nu \ll 1$), on the contrary, the cloud remains transparent, and given a few approximations, the observed intensity is proportional to the total column density of the considered species. This can be used to infer the column density.

For the intermediate case where $\tau_\nu \sim 1$, if τ_ν and the excitation temperature can be determined, one can estimate the total column density.

For instance in molecular clouds, CO is so abundant that it is usually optically thick. The emission thus saturates and one cannot determine the total amount of CO on the line of sight. Yet, isotopologues of CO, like ^{13}CO or C^{18}O, emit at other frequencies. These species are much less abundant (^{12}CO/^{13}CO ≈ 50 and ^{12}CO/C^{18}O ≈ 500) and their transitions can remain relatively thin ($\tau_\nu \lesssim 1$), which means these transitions would probe the entire cloud. Using isotopologues, one can determine e.g. the column density of ^{13}CO, then deduce the column density of CO, under the assumption of the isotopic ratio ^{13}CO/^{12}CO (see section 7.3.2).

6.3 IRAM 30m observations

6.3.1 Observing runs

Every semester, a call for proposals is published by IRAM. Based on the scientific aims and technical justification, the best projects are then ranked by the Program Committee and scheduled on the telescope.

My PhD work relies on several proposals, listed in Table 6.2, that got accepted in the past few years. Depending on the project, we performed maps of the regions we studied, using the on-the-fly mode, or long integrations on several lines of sight using the position-switching mode. Further technical details on the observation runs can be found in the relevant sections in Part III.

6.3.2 Observed line intensities

In radio astronomy, energies are of the order of $10^{-2} - 10^{-3}$ eV and the Kelvin scale is particularly appropriate to measure line intensities.

Table 6.2: List of observation runs relevant to this thesis

Date of observations	Index	Objects	Telescope	Nb. of hrs	Rank
Dec. 2011, Mar. 2012†	173-11	W51C / W28	30m	22	B
July 2012	W01D	W51C	PdBi	20	A
January 2013†	121-12	W51C	30m	16	A
July 2014†	020-14	W44	30m	41	B
October 2014†	019-14	W28	30m	19	A
May 2015†	024-15	W28	30m	42	A
Total				160	

Note - † marks observations that I carried out myself at the telescope.

Amplitude calibration

The effective brightness temperature of the emission lines that we want to detect is typically $\lesssim 1$ K and very small compared to the various contributions to the antenna output signal. Therefore, a careful amplitude calibration of the telescope needs to be performed in order to detect the molecular emission.

The conversion from Volts to Kelvin, assuming a linear relationship, needs two points, called the cold and hot loads. At the 30m, a three-phases calibration scheme is adopted which allows to further derive atmospheric parameters, through an atmospheric model (ATM), such as the amount of precipitable water and the zenith opacity. In this method, the atmospheric emission is measured typically every 1 to 30 seconds by a dedicated instrument working at 225 GHz, called the Taumeter. The calibration procedure has to be performed every $\sim 10 - 15$ min. This also serves to compensate the receivers gain fluctuations.

System temperature $T_{\rm sys}$

The system temperature $T_{\rm sys}$ is a parameter used to evaluate the overall noise performance of the receiver plus the atmosphere (IRAM report 2009-1, online). It depends on the receiver, the frequency band and the atmospheric transmission at the moment of the observations. It is meant to include all sources of noise and energy losses from the sky down to the backend output. The system temperatures reads:

$$T_{\rm sys} \approx T_{\rm sky} + T_{\rm rec} + T_{\rm spill} \tag{6.4}$$

where $T_{\rm sky} \sim 30$ K (at 3 mm) is the sky temperature, which relates to the opacity of the atmosphere, $T_{\rm rec} \sim 50$ K (at 3 mm) is the receiver temperature and $T_{\rm spill} \sim 20$ K is the spillover temperature, which takes into account signal from beyond the edge of the subreflector and primary. At 3 mm, under good weather conditions, $T_{\rm sys} \sim 80 - 100$ K. It goes up to 250 K at 1.3 mm. The system temperature is directly linked to the noise level in the data (see Section 7.2).

To decrease the atmospheric noise contribution, the source should be observed close to its meridian passage, especially when the source has a low elevation, e.g. W28. This can be predicted prior to observations through the ASTRO package of the GILDAS software. As an example, Figure 6.4 gives the elevation of the sources included in this study as seen from Pico Veleta on the date of my PhD defence.

Observing modes

In general, the antenna output signal (T_A^*, where the *star* means it takes into account correction of the atmospheric opacity) is dominated by the emission of the atmosphere $T_{\rm sky} \gg T_A^*$. To subtract the atmospheric contribution to the output signal, line radio observations are usually done in the so-called ON-OFF mode, where ON is the position on source, and OFF is a reference position. Since I observed extended sources in the crowded Galactic plane (Figure 5.2), I defined reference positions as far out as needed to avoid contamination from other sources. The reference position has to be devoid of signal at the frequency of observation (it can contain signal at other frequencies if it doesn't introduce confusion), but should be as close as possible to reduce the atmospheric noise contribution.

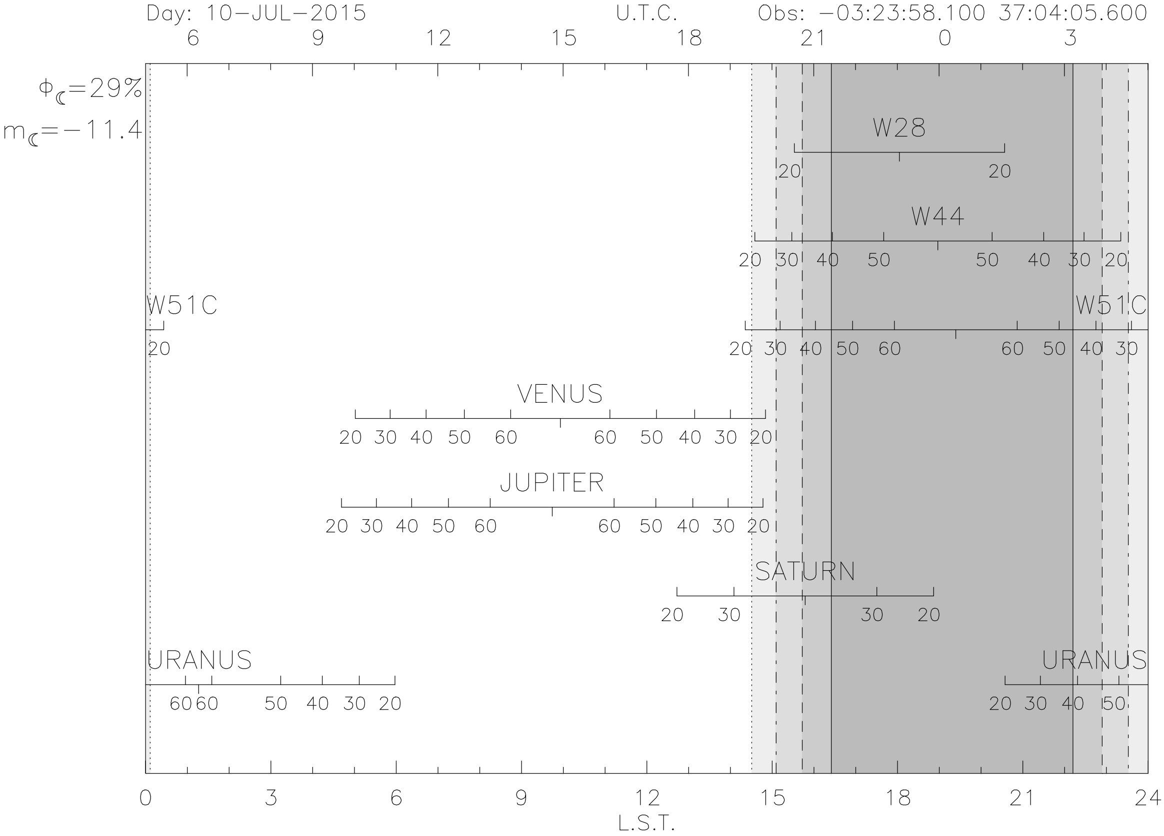

Figure 6.4: Elevation (degrees) of W28, W44 and W51C, observed from Pico Veleta on July 10th, 2015. A few planets are given, which could be used to tune the telescope. This prediction was obtained with the ASTRO package of the GILDAS software. The gray zone indicates night time. Although observations can continue during day time, pointing and focus have to be performed again at sunrise and sunset because of rapid changes in temperature. The upper scale is the Universal Time, bottom is Local Sidereal Time. Symbols on the left are the phase and magnitude of the Moon.

6.3.3 Temperature scales

It is convenient to define a series of temperature scales to describe the excitation state of a species or the observed intensity of a molecular line. These scales relate to physical temperatures only under certain circumstances. Here, I briefly describe some interesting parameters to get a better understanding of the observed intensity.

- First, the specific intensity of the signal reaching the telescope at a given frequency ν, I_ν [W m^{-2} Hz^{-1} sr^{-1}], corresponds to the power flux per solid angle along a sigthline. It satisfies the simplified radiative transfer equation and is a function of the optical depth τ_ν.

  $$I_\nu(\tau_\nu) = I_\nu(0)e^{-\tau_\nu} + S_\nu(1 - e^{-\tau_\nu}) \ , \tag{6.5}$$

  with $I_\nu(0)$ the background emission. The source function S_ν describes the own emissivity of the cloud.

- The *brightness temperature* T_B is the temperature of a black-body that would give the same observed specific intensity, i.e. $I_\nu = B_\nu(T_\mathrm{B})$. It describes the intensity of the source that is collected by the main beam of the antenna.

- The *excitation temperature* T_{ex} describes the excitation state of a given transition. It is the temperature

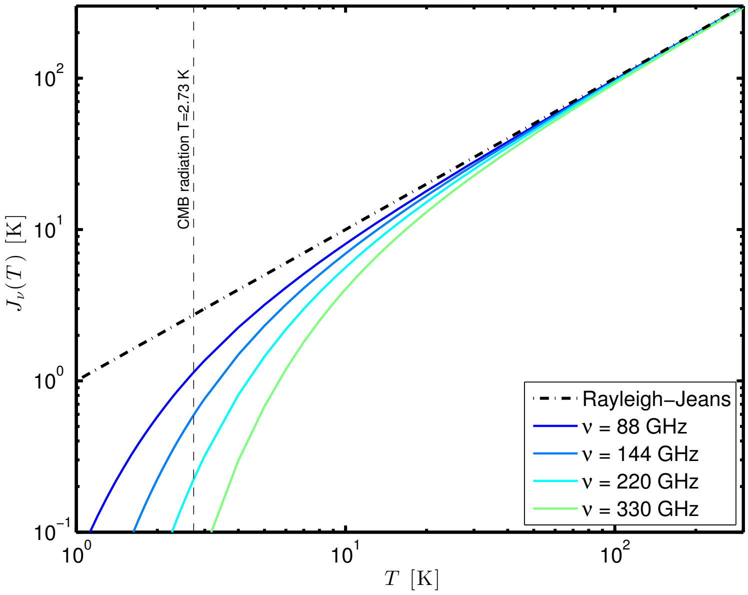

Figure 6.5: Non-validity of the Rayleigh-Jeans approximation, where $J_\nu(T) \approx T$, at low temperatures in the frequency range of the IRAM 30m telescope.

that would satisfy Boltzmann's equation for relative level populations of a transition $u \to l$:

$$\frac{n_u}{n_l} = \frac{g_u}{g_l} \exp\left(-\frac{\Delta E}{kT_{\rm ex}}\right) . \tag{6.6}$$

At local thermal equilibrium, $T_{\rm ex} = T_{\rm kin}$ for all rotational levels.

- In the Rayleigh-Jeans approximation where $h\nu \ll k_B T$, the black-body emissivity is proportional to T. The *effective temperature* $J_\nu(T)$ is defined as follows:

  $$J_\nu(T) = \frac{h\nu/k_B}{e^{h\nu/k_B T} - 1} , \tag{6.7}$$

  and $J_\nu(T) \approx T$ under the Rayleigh-Jeans approximation, which is valid at centimeter wavelength and low temperatures, yet is not valid at the temperature or frequency range of concern in this work (see Figure 6.5).

- The signal measured after amplitude calibration is called the antenna temperature T_A^*. Taking into account the diffraction pattern of the telescope and assuming that the emission mainly fills the main beam of the telescope, it can be converted into the main-beam temperature scale $T_{\rm mb}$:

  $$T_{\rm mb} = \frac{F_{\rm eff}}{B_{\rm eff}} T_A^* , \tag{6.8}$$

  with the forward efficiency $F_{\rm eff}$ and beam efficiency $B_{\rm eff}$ of the antenna.

Finally, the actual signal measured at the telescope in the position switching mode is related to $T_{\rm B}$, $T_{\rm ex}$ and the opacity τ_ν *via* the following relation:

$$T_{\rm mb} = J_\nu(T_B) - J_\nu(T_{\rm cmb}) = (J_\nu(T_{\rm ex}) - J_\nu(T_{\rm cmb})) \times \left(1 - e^{-\tau_\nu}\right) \tag{6.9}$$

where $J_\nu(T_{\rm cmb})$ comes from the CMB radiation at the frequency of observation, assumed to be the only signal in the reference position.

Chapter 7

Derivation of the column densities

Contents

In this chapter, I describe the real work on the data to infer the physical conditions in the gas, and the column densities, from observations.

7.1 Methodology

Figure 7.1 gives a schematic view of the derivation of the column densities from observations. This procedure involves a few steps, which will be described in the following Sections.

1. First, the data reduction of the observations allows to derive the integrated intensities and line width of each observed transition. This is done by performing Gaussian fits on the spectra.
2. The integrated intensities of CO isotopologues ^{13}CO and C^{18}O are then used simultaneously to constrain the physical conditions. This is done by a comparison to theoretical values from a non-LTE LVG analysis (Section 7.3.1), and a χ^2 minimisation. In some cases, the $N_2H^+(1-0)$ hyperfine transitions can be used, too, to better constrain the gas density. The column densities of the species used here are computed in the process.
3. The integrated intensities of other transitions (e.g. $HCO^+(1{-}0)$, $DCO^+(2{-}1)$, ...) are then compared to LVG predictions, taking into account the previously derived physical conditions. From this comparison, we derive the column densities of the corresponding species.

7.2 Data reduction

During my thesis, I used the GILDAS package, developed by IRAM (`http://www.iram.fr/IRAMFR/GILDAS`). In the following, I describe the main steps I used in the data reduction process.

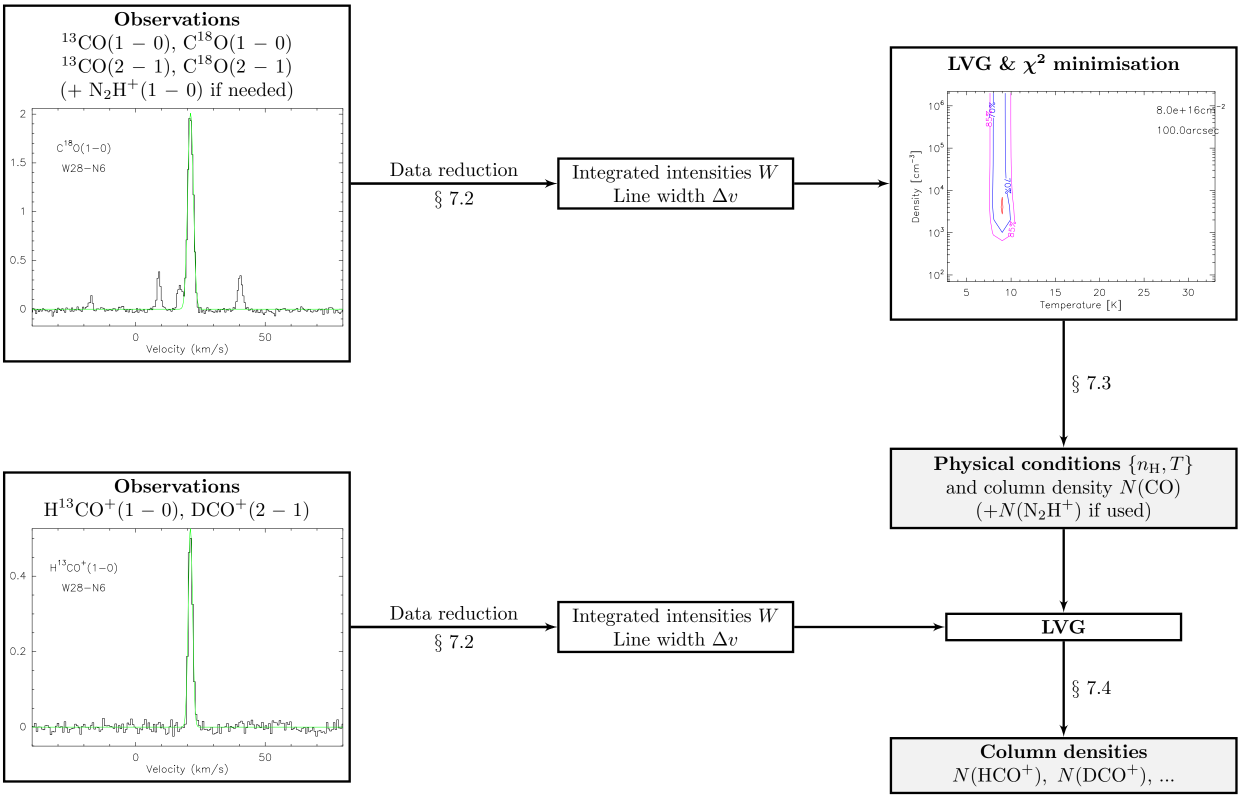

Figure 7.1: Schematic view of the derivation of physical conditions and column densities from observations.

7.2.1 Spectra averaging

Long observations are often needed to detect weak emission lines. The total statistical noise follows the radiometer equation:

$$\sigma = \frac{T_{\text{sys}}}{\eta_{spec}\sqrt{d\nu\ t_{\text{sig}}}} \tag{7.1}$$

with the previously defined system temperature T_{sys} (Section 6.3.2), the frequency resolution $d\nu$, the spectrometer efficiency η_{spec} and the integration time t_{sig} spent on the source (please note that in the position switching observing mode, half of the time is spent off-source).

Individual spectra are automatically calibrated in frequency and amplitude in the telescope pipeline. However, some residual effects have to be corrected to carry out the spectra averaging.

First, for each line of sight, the exact velocity shift of all spectra has to be corrected (all velocities refer to the local standard of rest (LSR)). I determined the center velocity of the source at each line of sight using unambiguous transitions with a single velocity component, usually HCO^+ or $H^{13}CO^+$.

Second, residual bandpass effects (namely differences in weather conditions, exposure times, and/or true continuum, e.g. dust or free-free emission) must be accounted for, which is achieved by subtracting low-order (≤ 3) polynomials to each spectrum.

Now, all these spectra are consistent, i.e. aligned in frequency and amplitude. The noise is measured for each spectrum during the baseline fit and then used to weigh each spectrum during the averaging. The top spectrum in Figure 7.2 shows an example of the resulting averaged spectrum.

Finally, the last step of the data reduction is to convert the antenna temperature T_A^* into main-beam temperature T_{mb} (Equation 6.8). The main-beam efficiency of the antenna varies with the frequency (Ruze's equation), and was measured at several frequencies on the IRAM 30m telescope by the IRAM staff[1]. From these measurements, I interpolated the main beam efficiency at every frequency (Figure 7.3).

---

[1] `http://www.iram-institute.org`

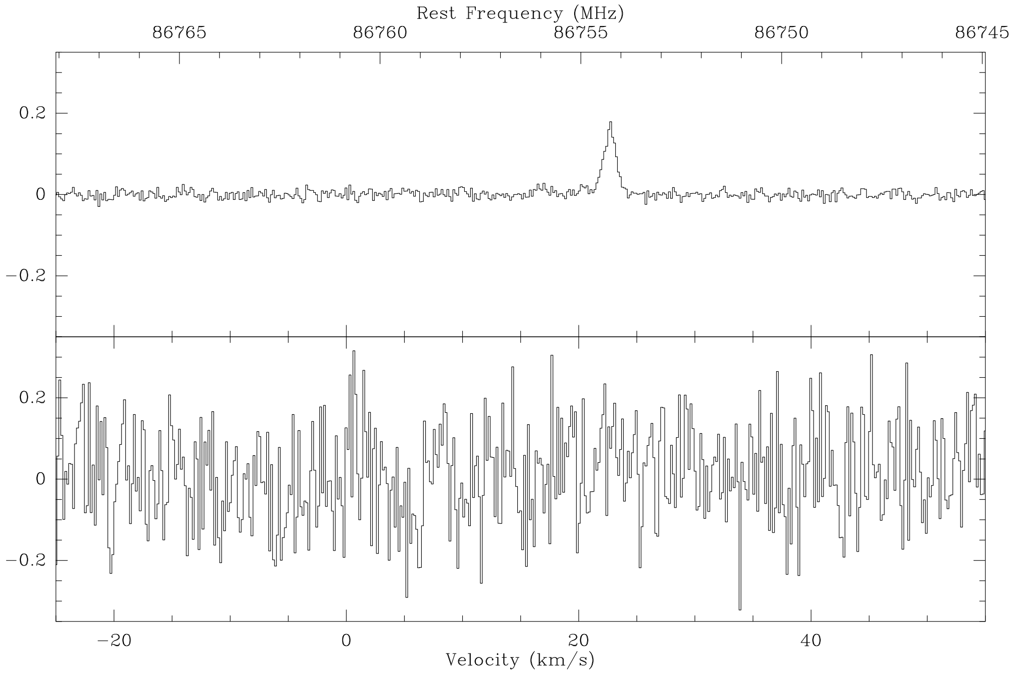

Figure 7.2: Example spectra for the $H^{13}CO^+(1-0)$ transition at 86.7544 GHz, along the data reduction at the position W28-N7, in T_A^* (K). **Bottom:** Individual spectrum, 3.7 min exposure. The noise is $\sigma = 120$ mK and the transition is not detected. The velocity shift was adjusted and the baseline subtracted. **Top:** Average from 108 spectra, total time 6.4 hours. The scale on the y-axis is the same for both spectra. The noise is now $\sigma = 9.6$ mK and the line is perfectly detected at 17σ. The velocity is $v_{LSR} = 22.3$ km s^{-1}, it may be used to help identify weaker lines.

The order of these steps does not really matter, as long as the spectra are consistent when they are averaged, i.e. the same corrections have been applied to all spectra. The only mandatory step prior to averaging is the baseline subtraction.

7.2.2 Integrated intensities

The averaged spectra will now be analysed. From the width and intensity of the molecular lines, we deduce information about the physical conditions in the gas or the abundance of the species.

The line profile

The line width can be the result of several effects. First, the so-called natural line width arises from the uncertainty principle in quantum mechanics. It is always insignificant in astronomical molecular lines. Thermal broadening induces a Doppler profile of the line whose width is proportional to $\sqrt{T/m}$, with m the mass of the molecule. The line width is usually much smaller than those observed in cold clouds. For instance, CO lines at 30 K have ~ 0.2 km s^{-1} width.

In our observations, the molecular emission lines show bandwidth of typically a few km s^{-1}. Such line width are due to the presence of non-thermal motions at the emission site, such as rotation, expansion, collapse or turbulence. Both Gaussian and non-Gaussian profiles may result.

Discrepancies from a Gaussian profile can mainly be due to three effects. First, when optically thick lines saturate, their peak emission remains the same while their width increases. Second, when several lines close in velocity are blended, for example because there are at least two large regions of emission on the line of sight, with a difference in mean velocities smaller than the line width. Third, gas dynamics influences the line profile, e.g. molecular lines can show high-velocity wings in shocked gas and outflows.

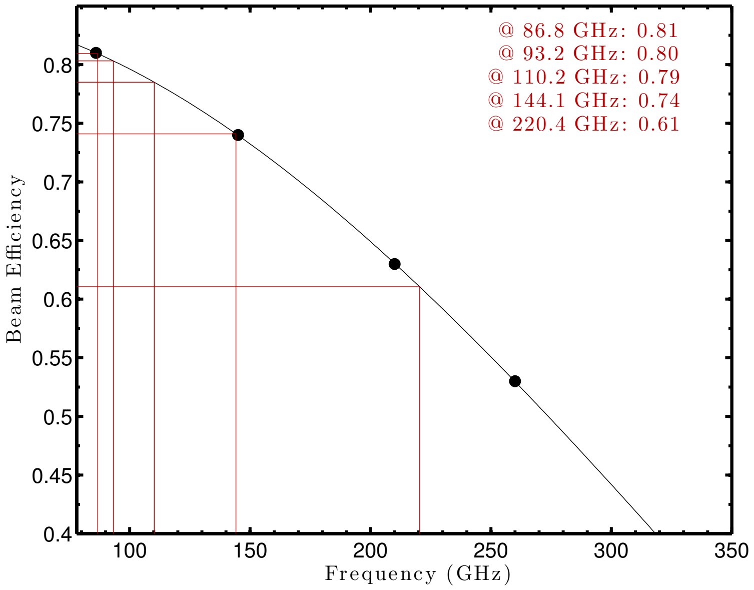

Figure 7.3: Polynomial interpolation of beam efficiencies of the IRAM 30m antenna for at the frequencies of a few transitions observed in this work. Bullets mark values measured by the IRAM staff.

Gaussian fits

I performed Gaussian fits of the observed emission lines (Figure 7.4). Additional care was given to observations where several velocity components were detected on the line of sight. In such cases, the several components can be fitted simultaneously to get better results. The uncertainty on the fits are negligible w.r.t. overall calibration uncertainties, generally estimated at $\sim 10-20\%$ in integrated intensity.

The fit can be difficult when several velocity component are blended. Yet, in most cases in my thesis work, the separation in velocity is sufficient to discriminate between the components. Otherwise, the fit can be improved by assuming some of the parameters based on other similar observations. For instance, the center velocity and line width of $C^{18}O(1-0)$ can help constraining the fit of $^{13}CO(1-0)$.

In case of non-detections, upper limits on the peak intensity are given using the rms noise σ of the spectrum,

$$W < \alpha\sqrt{\mathrm{d}v\ \Delta v} \times \sigma \tag{7.2}$$

where dv is the width of the velocity channels in the spectrum, which is set by the spectral resolution, and Δv is the expected line width. This can be assumed based on other detected lines. α is the number of σ considered for the upper limit. Typical constraints are $T_{\mathrm{peak}} < 3\sigma$ or $W < 5\sigma$.

Hyperfine structure

Some transitions have hyperfine structures (HFS) which can be spectrally resolved by the telescope. It is for instance the case of $N_2H^+(1-0)$, which has 15 hyperfine transitions (e.g Daniel et al., 2006). With a spectral resolution of 50 kHz, three groups of transitions can be resolved. In this case, I performed HFS fits (Figure 7.4).

The procedure constrains the line width and excitation temperature, assumed to be the same for all HFS transitions. It then returns the line width, the center velocity of the main component, the main group opacity τ_0, and $\tau_0 \times [J_\nu(T_{ex}) - J_\nu(T_{bg})]$. From these parameters, I derived the integrated intensity of each component:

$$W_i = [J_\nu(T_{ex}) - J_\nu(T_{bg})] \times \left(1 - e^{-r_i \tau_0}\right) \times \Delta v\ , \tag{7.3}$$

where r_i is the relative intensity of the HFS transition i. In the example of N_2H^+, I derived the total integrated intensities for each of the three groups of HFS components that are resolved.

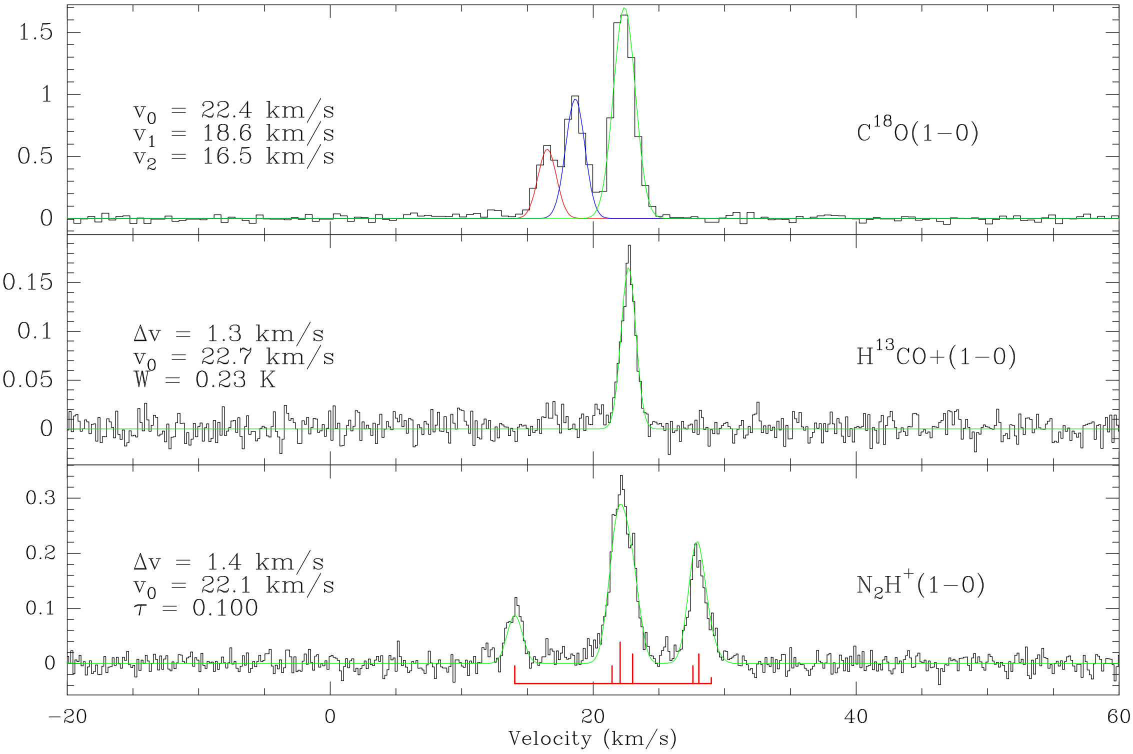

Figure 7.4: Example fits on W28-N7. **Top:** Multiple velocity component Gaussian fits of $C^{18}O(1-0)$. Here, the three lines are emitted in three separate regions along the line of sight, with mean LSR velocities 16.5, 18.6 and 22.4 km s^{-1}. Only the line at 22.4 km s^{-1} is physically related to the two other species below, which interestingly emit only at this velocity. **Middle:** Gaussian fit of the $H^{13}CO^+(1-0)$ transition, W is the integrated intensity of the line, v_0 the center velocity and Δv the line width. **Bottom:** Fit of the hyperfine structure of $N_2H^+(1-0)$. The red peaks show the 15 theoretical HFS components (some overlap). Only three groups of components are resolved with the telescope, at a spectral resolution of 50 kHz. The parameter τ is the group opacity. The 0.1 value of τ means the transition is optically thin and the fit couldn't determine τ, i.e. τ is actually lower than 0.1. For these spectra, the peak intensity of the fit doesn't perfectly match the observed peak intensity. Yet, the residuals stay within the $\sim$ 20% calibration uncertainties.

7.2.3 Line blending and instrumental effects

Nice unique Gaussian line detections are the ideal situation in data processing. Unfortunately, many spectra are much more difficult to process. Some examples are given in Figures 7.5 and 7.6.

A classical problem with sources close to the Galactic center is the presence of several clouds on the line of sight (Figure 7.5). This can lead to just as many velocity components in the spectra, especially for abundant species such as CO. In case of unique component transitions, i.e. if the transition does not show a (hyper-)fine structure, then the several components shouldn't introduce any confusion in the line detection. Multi-line fits might be needed to better discriminate the one component actually from the source (Figure 7.4, top). Yet, it can happen that two velocity components are too close to each other to be treated separately. In that case, the lines are blended, and further effort might be needed to determine the contribution of each component, when possible. Blended lines usually occur for abundant species such as ^{13}CO. To disentangle between two blended components, I assumed the center velocity of the source component, based on single-component observations of other species such as $H^{13}CO^+$. I could also assume the line width, based e.g. on observations of $C^{18}O$ at the same position. The case becomes much more complicated for the processing of hyperfine structures, e.g. $HCN(1-0)$. The three hyperfine components of this transition are separated by a few km s^{-1}. Their relative intensities depend on the total opacity of the transition. The HFS and velocity structure can become degenerate. Therefore, the presence of other velocity components makes it impossible

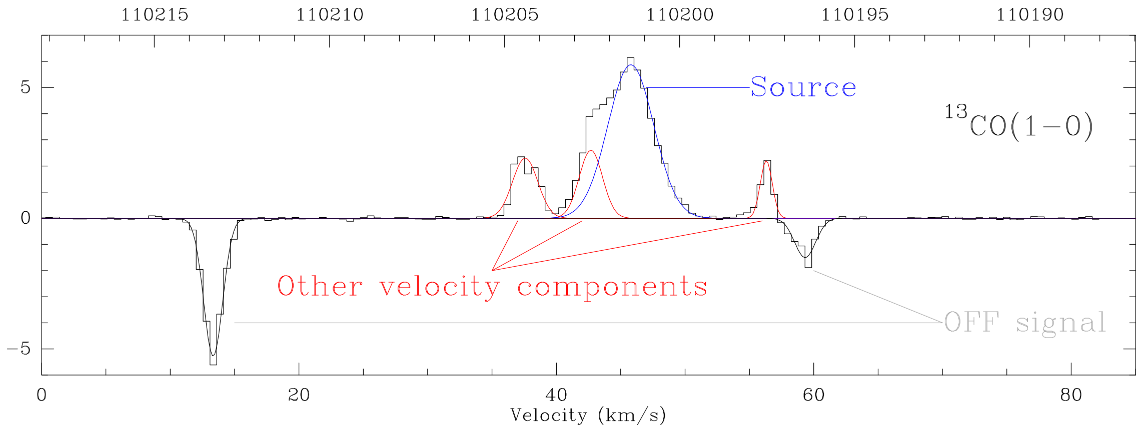

Figure 7.5: *The reality of observations*, for the ^{13}CO$(1-0)$ transition in W44-L3. Gaussian fits are overlaid on the spectrum. I identified several velocity components due to material on the line of sight (red). One of them seems blended with the emission line from the source at 46 km s^{-1} (blue), but still allowed a successful fit. Two absorption lines are due to the presence of signal in the OFF position (gray). Here, the OFF signal is sufficiently shifted from the source to be disregarded.

to determine the relative contribution of each velocity component.

The complexity of the Galactic plane makes it also difficult to find a relevant reference position for the line calibration process. As presented Section 6.3.2, the reference position (called OFF position) should be devoid of signal and close enough to the source to correctly cancel the atmosphere fluctuations. If some signal remains in the OFF position, the resulting spectra will show absorption features (Figure 7.5), which can be disregarded as long as they are clearly shifted from the velocity of the source.

In some cases, the shape of the line is modified by self-absorption. Self-absorption occurs when a colder layer of material is in the foreground of some warmer material. Ideally, the absorption feature is small and centered w.r.t. the emission line. The symmetry can be broken by a small velocity shift, and one has to make sure the absorption does not come from signal in the OFF position.

In position switching, the baselines of the spectra are usually clean and can be fitted by low-order polynomials. Yet, a stair-like structure can be introduced by instabilities in the digital backends (Figure 7.6). Being interested in individual transitions, what I did was to substract the baseline locally around the frequency of each transition.

Spikes can also show up on the spectra, due to the backends (Figure 7.6). They can be easily identified, as very strong and narrow lines regularly spaced in frequency. They appear during the frequency tuning of the receivers. During observations, I looked for the presence of spikes each time I changed the settings, before going any further.

7.3 Derivation of physical conditions

From the integrated intensities and line widths, I determined the physical conditions in the cloud. To do so, I used a radiative transfer code to predict the intensities of the two lowest rotational transitions of CO isotopologues for a grid of different physical conditions, and compared them to observations.

7.3.1 Radiative transfer

The code that I used performs non-local thermal equilibrium (non-LTE) calculations of the rotational level populations under the large velocity gradient (LVG) approximation and is described in Ceccarelli et al. (2003). During my thesis, I benchmarked the code against the LVG code `RADEX`, available online. The advantage of our code is that it is built up to run large grids and to solve the problem of high opacities.

The code computes the non-LTE population of the rotational levels of each species separately, assuming its column density, the H_2 density (i.e. the density of colliders) and the gas temperature. The data needed

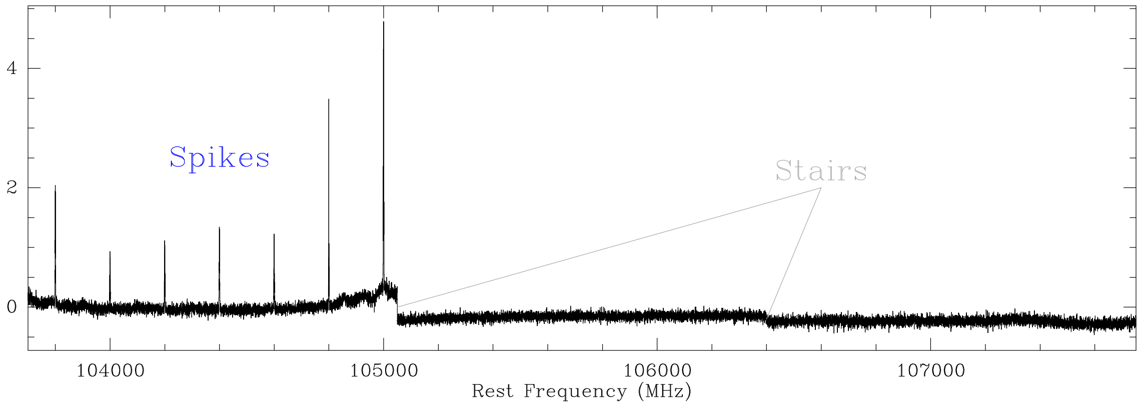

Figure 7.6: Raw spectrum in W44 in the Upper Inner band at 3 mm. Spikes induced by stationary waves in the receiver are easily identified as strong lines distributed regularly in frequency. The discontinuities in the baseline ("stairs") are due to instabilities in the digital backends. One has to make sure no emission line of interest falls too close to any of these unfortunate features.

Table 7.1: References of the collisional coefficients with H_2 used in my PhD work.

Species	Reference
^{13}CO, C^{18}O	Yang et al. (2010)
HCO$^+$, DCO$^+$	Flower (1999)
N$_2$H$^+$	Daniel et al. (2005)
HCN, H^{13}CN	Green and Thaddeus (1974)
HNC	Dumouchel et al. (2010)
CCH	Spielfiedel et al. (2012)

for the calculation are the transition probabilities (Einstein coefficients) and collisional rate coefficients for excitation and de-excitation of all the transitions. References for these collisional coefficients are listed in Table 7.1. They can be found on the BASECOL database[2], or the Leiden Atomic and Molecular Database[3].

Under the LVG approximation, it is assumed that there exists a velocity gradient within the cloud large enough so that the frequency of the emission at one point of the cloud will be shifted by Doppler effect out of the absorption profile of other molecules in the cloud. In this approximation, the radiative transfer can thus be considered locally, as all emitted photons will either be absorbed locally or escape the cloud with an escape probability $\beta \leq 1$ (e.g Elitzur, 1992). This escape probability means that a portion of the emitted photons actually remain trapped in the cloud. It can be seen as a decrease in the spontaneous emission coefficient of the transition $A'_{ul} = \beta A_{ul}$. Therefore, it also decreases the critical density (cf. Equation 6.2):

$$n'_{\rm crit} = \beta n_{\rm crit} = \beta \frac{A_{ul}}{\gamma_{ul}} \ . \tag{7.4}$$

Optically thick transitions are thus more easily thermalised.

The escape probability depends on the assumed geometry of the cloud. In our code, we can consider semi-infinite slabs, expanding or uniform spheres. In my work, I always considered clouds as semi-infinite slabs. The expression of the escape probability in that case follows Scoville and Solomon (1974):

$$\beta = \frac{1 - e^{-3\tau}}{3\tau} \ . \tag{7.5}$$

This expression is replaced in the code by power law approximations at $3\tau < 0.1$ and $3\tau > 50$.

---

[2] `http://basecol.obspm.fr/`

[3] LAMDA, `http://home.strw.leidenuniv.nl/~moldata/`

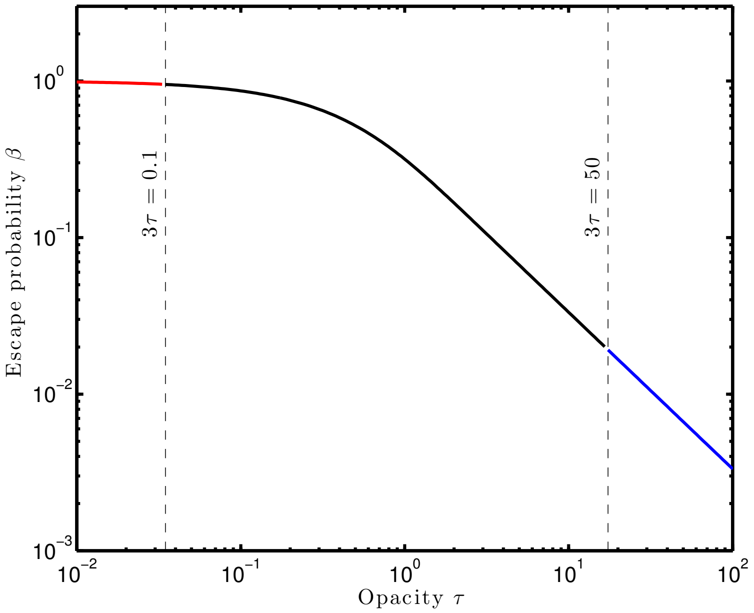

Figure 7.7: Escape probability for a slab geometry (as in our LVG code).

7.3.2 Comparison to observations and χ^2 minimisation

CO observations

The next step is to compare the predicted emission to observations. In general, the results are degenerate. For instance, an increase in gas temperature will populate higher levels. So will an increase in density, which makes collisional excitations more efficient. I didn't use the main isotopologue ^{12}CO, which in molecular clouds is usually optically thick. In that case, the intensity of the transition is equal to the excitation temperature and gives a lower limit on the kinetic temperature (these two are equal if the transition is also thermalized).

To remove the degeneracy, I used several transitions simultaneously of the rare CO isotopologues ^{13}CO and C^{18}O, whose opacity remains lower than ^{12}CO. The two lowest transition for ^{13}CO and C^{18}O fall in the 3 mm and 1.3 mm bands of the IRAM 30m telescope. Used together, these four transitions ^{13}CO$(1-0)$, ^{13}CO$(2-1)$, C^{18}O$(1-0)$ and C^{18}O$(2-1)$ allowed a reasonable constraint on the physical parameters, as shown by the χ^2 minimisation procedure of the LVG package (Figure 7.8).

Reduced χ^2

Taking into account the observed line width Δv and the integrated intensity W within 20% uncertainties, I computed the minimum χ^2 values when comparing to theoretical values. The code considers four free parameters: the gas density $n(\mathrm{H_2})$, the kinetic temperature T, the column density of the considered species and the solid angle of the emitting region Ω. This last parameter is added to consider possible flux dilution, if the source is smaller than the smallest telescope beam. It then calculates a 4-dimension grid of χ^2 values.

The overall minimum χ^2 allows the determination of the best set of parameters. Then, the column density and Ω are set and reduced χ^2 maps can then be created in the density/temperature space. The dependence of the column density on χ^2 is checked to ensure it is well constrained. Otherwise, several density/temperature maps can be considered with different column densities.

The reduced χ^2 is simply computed as follows (Bevington and Robinson, 1992):

$$\chi^2_\delta = \frac{\chi^2}{\delta} \tag{7.6}$$

where δ is the number of degrees of freedom and can be determined as the number of data points minus the number of parameters to be determined by the data points.

For instance, in our case, there are four observation points, i.e. one integrated intensity for each CO transition. There are four free parameters, but two are fixed when exploring χ^2 values in the density/temperature space. Therefore $\delta = 4 - 2 = 2$ and $\chi^2_\delta = \chi^2/2$.

Isotopic ratio

In the determination of the column density of CO, I used isotopologues ^{13}CO and C^{18}O, thus I needed to assume the isotopic ratio ^{13}CO/C^{18}O. This means that I didn't consider the isotopologues as independent species and their simultaneous analysis permits the determination of N(CO). Another way to look at it is that ^{13}CO observations allow the determination of $N(^{13}\mathrm{CO})$ and C^{18}O observations that of $N(\mathrm{C}^{18}\mathrm{O})$. In that case we add a free parameter (a second column density) but add a constraint at the same time: $N(^{13}\mathrm{CO})/N(\mathrm{C}^{18}\mathrm{O})$.

We assume the molecular isotopic ratio to be equal to the atomic isotopic ratios:

$$\frac{^{13}\mathrm{CO}}{\mathrm{C}^{18}\mathrm{O}} = \frac{^{13}\mathrm{C}}{^{12}\mathrm{C}} \times \frac{^{16}\mathrm{O}}{^{18}\mathrm{O}}. \tag{7.7}$$

This approximation stands in absence of chemical fractionation or selective photodissociation (Federman et al., 2003). The local ISM values are $^{12}\mathrm{C}/^{13}\mathrm{C} \approx 75$ and $^{16}\mathrm{O}/^{18}\mathrm{O} \approx 500$ (Wilson and Rood, 1994).

There exists a Galactocentric gradient of isotopic ratios, such as e.g. $^{12}\mathrm{C}/^{13}\mathrm{C}$ which have been measured from millimeter transitions of CN (Milam et al., 2005). This gradient is the result of the gradual depletion of ^{12}C and enrichment of ^{13}C with stellar nucleosynthesis. It reflects the stellar formation history of the Galaxy. One can then deduce from the gradient values in Milam et al. (2005) the isotopic ratio expected in a cloud at a given Galactocentric distance. Yet, there can be a local dispersion of the ratio values up to a factor of 2. Besides, the determination of the Galactocentric distance is affected by the uncertainty on the Heliocentric distance, which can be quite large depending on the method.

In the case of W28, I used several values of the isotopic ratio ^{13}CO/C^{18}O in an attempt to get the best constraints on the physical conditions. This was a way to use the code to also constrain this ratio. The constraints on the physical conditions were significantly improved for all positions in W28 for a ratio $^{13}\mathrm{CO}/\mathrm{C}^{18}\mathrm{O} = 10 \pm 1$, which corresponds to $^{12}\mathrm{C}/^{13}\mathrm{C} \approx 50$ if we keep $^{16}\mathrm{O}/^{18}\mathrm{O} \approx 500$. This $^{12}\mathrm{C}/^{13}\mathrm{C}$ value is consistent with the Galactocentric distance of W28 (Milam et al., 2005).

Improvement using N_2H^+

Adding observations of lines sensitive to other ranges of density may alleviate the degeneracy among physical parameters such as density and temperature. HCO$^+$ or N_2H^+ have higher critical densities (Table 6.1) and could be used to better constrain the density, yet their relative abundance to CO are expected to vary locally. Therefore, one needs to add one free parameter (the relative abundance to CO) as well as one observation (for one transition), which doesn't remove any degeneracy. Yet, the observation of two transitions could.

This is the situation for $N_2H^+(1-0)$, which shows a hyperfine structure. When the transition is neither thin nor thick ($0.1 \lesssim \tau \lesssim 30$), the relative intensities of the HFS components depend on the gas density, and can give additional constraints. In the case of N_2H^+, one observation actually gives three integrated values, one for each resolved group of HFS components. One then gains two degrees of freedom, and it is possible to determine the abundance ratio N_2H^+/CO which gives the best constraint on physical conditions. Yet, this ratio varies locally, from one line of sight to the other. Note that for optically thin transitions of N_2H^+, the relative abundances of the HFS components are set by quantum properties and N_2H^+ actually gives no additional information.

In W44 (Chapter 12), the derived densities from CO isotopologues are very much degenerate, and the simultaneous use of the three hyperfine transitions of $N_2H^+(1-0)$ helped greatly to constrain the density (Figure 7.8). The constraints on temperature are unaffected as they were usually sufficient from CO transitions.

7.3.3 Physical conditions

Physical conditions were determined, with uncertainties, from the χ^2 contours maps in the density/temperature space. From χ^2_δ values, I plotted the confidence intervals at 70 and 85%, corresponding for instance to $\chi^2_\delta = 1$

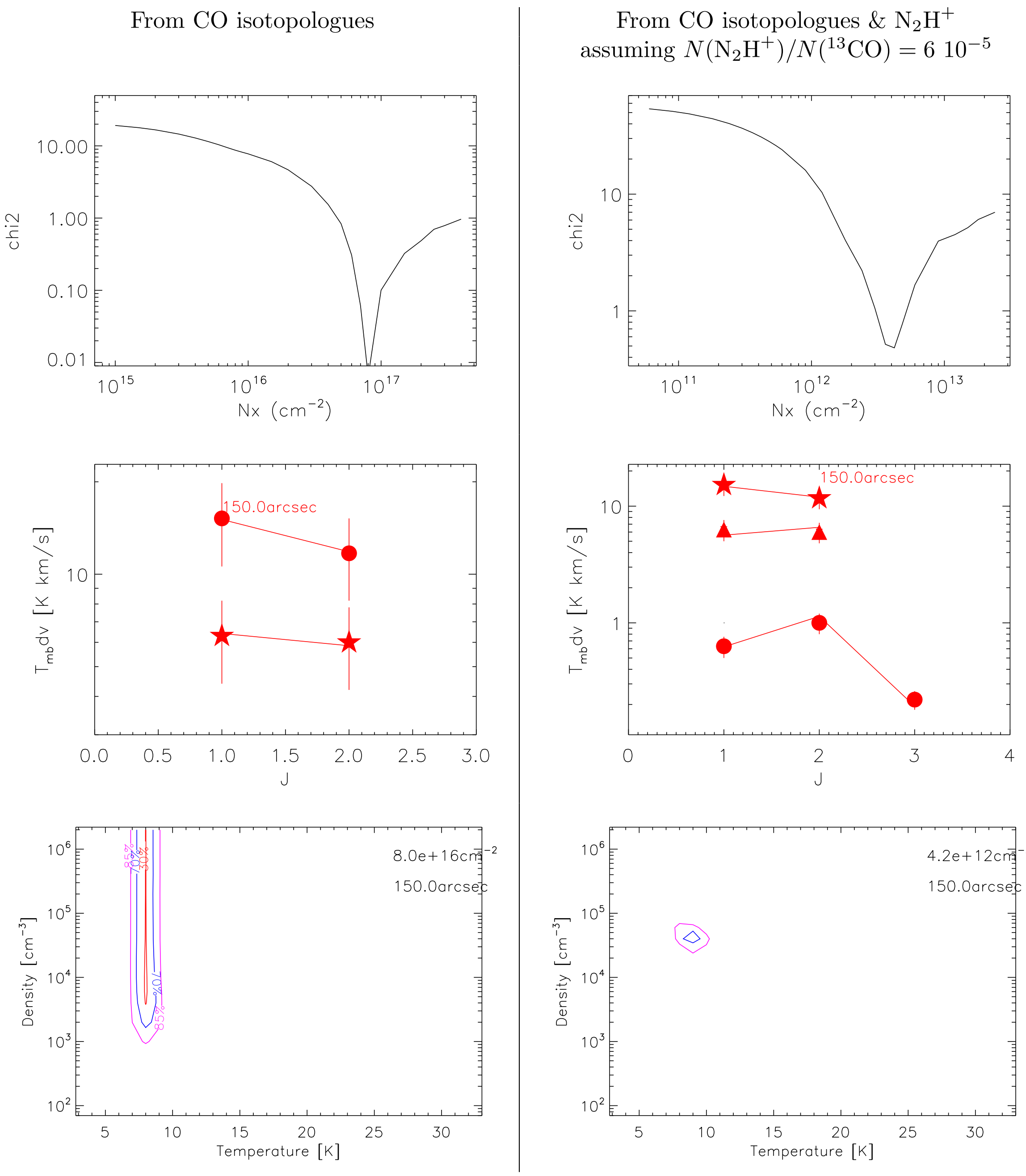

Figure 7.8: Plots for the determination of the physical conditions at position W44-E11 using our LVG code. Plots on the left column were obtained using the four observed CO transitions (see text). Plots on the right column include the additional HFS components of $N_2H^+(1-0)$. A value of $N(N_2H^+)/N(^{13}CO) = 6 \times 10^{-5}$ is assumed and was determined from the best constrains it gave on the density. This ratio gives $N(^{13}CO) = 7\times10^{16}$ cm^{-2}, consistent with the value obtained from CO only. **Top:** Global minimum of χ^2 for each column density of ^{13}CO(left) or N_2H^+(right). All other parameters are free. **Middle:** Comparison of the observed (symbols, with error bars) and expected (line) integrated intensity for each transition (the HFS components of N_2H^+ are noted as independent transitions). **Bottom:** χ^2 maps in the H_2 density/temperature space. Contours are 85% (purple), 70% (blue) and 30% (red) confident intervals (Bevington and Robinson, 1992). The degeneracy removal on the density induced by the use of N_2H^+ is magnificent.

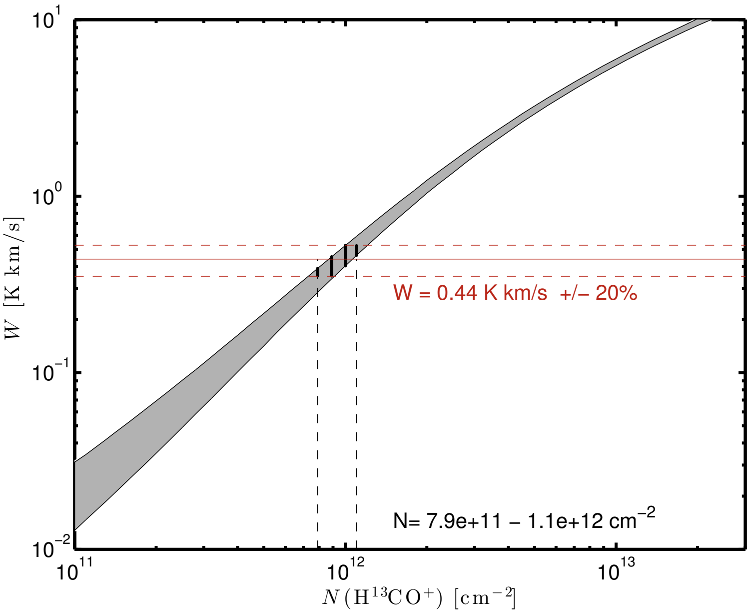

Figure 7.9: Determination of the $H^{13}CO^+$ column density from comparison of observations to predictions, at position W28-N1. The observed integrated intensity W was derived from Gaussian fits of the $H^{13}CO^+(1-0)$ emission line. The gray shade shows theoretical predictions from the LVG code, using the previously derived physical conditions $\{n_{\mathrm{H}_2}, T\}$ at this position and their uncertainties (see text).

and 2, respectively, with $\delta = 1$ (Bevington and Robinson, 1992). Uncertainties on the column densities are defined with the $\chi^2_\delta = 1$ contour.

Table 5.1 gives a comparison of typical physical conditions in clouds next to W51C, W44 and W28. They are consistent with dense molecular clouds, and W44 shows gas densities significantly higher than in the other sources.

Complete tables of the physical conditions derived in each source can be found in the relevant sections in Part III.

7.4 Derivation of column densities

During the determination of physical conditions, the column densities of ^{13}CO and $C^{18}O$ (and N_2H^+ when involved) were previously constrained. Now, from the gas density and temperature, it is possible to derive the column densities of other species, even from a unique transition, e.g. for $HCO^+(1-0)$, assuming that the same density and temperature apply. To do so, I considered the physical conditions and looked for the best agreement of the observed integrated intensities to the theoretical predictions. Uncertainties on n_{H_2} and T from χ^2 maps were taken into account, as were 20% uncertainties on observed integrated intensities. Figure 7.9 gives an example of the determination of $H^{13}CO^+$ column density at position W28-N1.

As we are more interested in abundance ratios than individual abundances (see Chapter 8), I constrained simultaneously the column densities for different species, in order not to propagate the uncertainties to the abundance ratios. In other words, the same $\{n(\mathrm{H}_2), T\}$ values were used for both species in the process, when computing any abundance ratio.

Complete tables of the column densities and abundance ratios derived in each source can be found in the relevant sections in Part III. They will then be compared to chemical predictions, see Chapter 8.

Chapter 8

Chemical modeling

Contents

In this chapter, I introduce the chemical code I adopted and its configuration, which I used to compare theoretical predictions to observations.

8.1 Chemical models

The fast discoveries of more than 180 molecules thanks to the advances in radio astronomy led to the development of several chemical models starting from the 1970s. The idea is to reproduce numerically the observed chemical abundances in the ISM to better understand the chemical processes at play, and also to predict the existence of other species in the ISM. Today, a large number of chemical models have been developed with different degrees of complexity. Most of these models are developed to match specific needs, for instance different regions (dense ISM, prestellar cores, photo-dissociation regions, planetary atmospheres, ...), and include different levels of complexity (gas phase, gas-grain or grain surface chemistry, 1D or 3D, time-dependence,...). In some models, the chemistry is coupled to additional effects (dynamical evolution, thermal balance, CR propagation...). A short list of models dedicated to gas-phase and gas-grain chemistry in the ISM is available at `http://kida.obs.u-bordeaux1.fr/models/`.

The chemical computation relies on a list of chemical reactions and their associated kinetic rates called a *chemical network*. Some extended chemical networks are public (OSU, KIDA, ...). In some specific parts of my work, I also used reduced networks, to better understand the role of some specific reactions.

Chemical codes solve a system of non-linear differential equations:

$$\frac{\mathrm{d}n_i}{\mathrm{d}t} = \sum_j \sum_k k_{j,k} n_j n_k - n_i \sum_i k_{i,l} n_l \tag{8.1}$$

where n_i is the abundance of the species i considered. The first term includes all the formation routes of the species i from other species of abundances n_j and n_k, associated with the chemical reaction rates $k_{j,k}$'. The second term includes all the destruction routes of i, from reactions with species l, with rate $k_{i,l}$. In this example, the differential equations assume second order kinetic reactions, which are the dominant types of gas-phase reactions in the ISM, due to the very low density of the gas, as compared to atmospheric conditions. The form of the kinetic equation can be different when including other types of reactions, e.g. first-order reactions such as CR ionisation reactions. In steady-state codes, the time derivative on the left-hand side equals to zero.

8.2 The `astrochem` code

8.2.1 Presentation

During my thesis work, I used the code `astrochem`[1], developed by T.Bergin and S.Maret (see e.g. Maret et al., 2013) that computes the time-dependent chemical abundances in a gas cell with fixed density and temperature. The gas cell is described by the total H density $n_{\rm H}$, the kinetic temperature T, the visual extinction A_V and the dust temperature T_d. In addition, the interstellar radiation field χ and CR ionisation rate ζ can be provided as parameters.

The code includes 25 different types of reactions, including gas-phase reactions (e.g. neutral-neutral, ion-neutral, dissociation recombination ...), as well as basic grain chemistry (e.g. H_2 formation on grains, freeze-out, photo-desorption) and CR induced reactions (ionisation, desorption, ...).

The code builds a system of kinetic rate equations from the chemical network file and solves it using the Jacobian matrix. The solution takes typically a few seconds for several thousands chemical reactions. The computation is done at a given temperature, i.e. chemical abundances do not influence the thermal balance. I didn't consider a cloud structure in the computation, and always assumed a high ($A_V = 20$ mag) visual extinction, therefore no UV ionisation needed to be computed. Finally, I carefully benchmarked the results I got from `astrochem` with the `PDR Meudon` code.

The regions I studied in the thesis are the dense interior parts of molecular clouds. There, the gas is efficiently shielded from the UV or X-ray interstellar field and the ionisation is therefore likely dominated by CRs (see Section 3). The `astrochem` code is, thus, very well suited for these UV-shielded regions.

8.2.2 Chemical network

To model the chemistry in our sample of molecular clouds close to SNRs, I used an extended version of the OSU 2009 chemical network available online[2]. This network takes into account 468 species involved in 6046 reactions. To account for the DCO^+ chemistry, I added 11 more reactions involving D, HD, H_2D^+ and DCO^+, labeled 7-13 in Table 3.1. Chemical rates for these reactions are taken from Roberts and Millar (2000).

In this study, I considered only gas-phase reactions, thus grains were not involved (in particular the dust temperature has no effect). Specifically, the time-dependence of chemical processes such as depletion and CR desorption is not computed. To account for CO depletion at steady-state, I directly changed the initial C or CO gas-phase abundance. The only gas-grain reaction considered here is the formation of H_2 and HD on grains (see also Section 13.2.3).

The default initial abundances that I adopted are listed in Table 8.1. Initial abundances of C, O and N abundances are taken from Graedel et al. (1982). Metals follow the low-metal abundances from Wakelam et al. (2006). The He abundance was updated following Asplund et al. (2009).

Table 8.2 lists the typical ranges of physical parameters used with `astrochem` in this study.

8.2.3 The CR ionisation rate ζ

In `astrochem`, ζ is a parameter given in the input file, together with the initial abundances. The code uses ζ to scale all chemical reaction rates k of the reactions associated with CR ionisation within the network. The rates read:

$$k = \alpha\zeta \tag{8.2}$$

where α is taken from the chemical network file for each reaction. These rates include both direct and indirect ionisation induced by incoming CRs. In other words, they are meant to take into account both

---

[1] `http://smaret.github.io/astrochem/`. I used the version `0.5` of the code during my PhD.

[2] `http://faculty.virginia.edu/ericherb/research.html`

Table 8.1: Default elemental abundances relative to H used in our modeling with `astrochem`

Element	Abundance	Reference
He	0.09	[A09]
D	1.60×10^{-5}	[L95]
N	2.14×10^{-5}	[G82]
O	1.76×10^{-4}	[G82]
C^+	7.30×10^{-5}	[G82]
S^+	8×10^{-8}	[G82]
Si^+	8×10^{-8}	[G82]
Fe^+	3×10^{-9}	[G82]
Na^+	2×10^{-9}	[G82]
Mg^+	7×10^{-9}	[G82]

Note - Abundances are taken from [A09] Asplund et al. (2009), [L95] Linsky et al. (1995) and [G82] Graedel et al. (1982)

Table 8.2: Range of initial physical parameters used in the `astrochem` code.

Parameter	Range
A_V [mag]	20
$n_{\rm H}$ [cm^{-3}]	$10^3 - 10^4$
T_{kin} [K]	$5 - 80$
T_d [K]	20
ζ [s^{-1}]	$10^{-18} - 10^{-14}$
t_f [yr]	$10^6 - 10^9$

Note - The chemical abundances actually depend on the ratio $\zeta/n_{\rm H}$ (see text). The input parameters are the visual extinction A_V, the total H density $n_{\rm H}$, the kinetic and dust temperatures T_{kin} and T_d, the CR ionisation rate ζ and the final time of the computation t_f.

direct ionisation by CR encounters with H_2 (or H, He...) and the ionisation of other species by secondary UV photons emitted during electronic recombinations of H_2^+ (or H^+, He^+, ...). For instance in the OSU network, $\alpha = 0.93$, 0.50 and 0.46 for H_2, He and H ionisation, respectively. For the CR dissociation of CH, $\alpha = 730$.

In this study, I performed grids of models with increasing values of ζ, for a given set of physical parameters, in order to compare the predicted abundances to observations (see Section 8.4).

8.3 Steady-state abundances

`astrochem` computes the time evolution of chemical abundances. It means that it is possible to follow the abundance of every species with time. Figure 8.1 shows the time evolution of a few species involved in the formation of DCO^+, starting from atomic abundances (Table 8.1). Steady-state is reached after typically 10^7 yr. The time scale is dominated by the formation of H_2 on grains in $\sim 5 \times 10^5$ yr.

In most cases, we were interested in the steady-state abundances of the cloud, when the chemical abundances do not evolve with time anymore. It means that the chemical equilibrium in the cloud is reached and this is of course a questionable assumption. Yet, doing so, the results are not dependent on the details of the time evolution, especially the definition of the initial time and the associated initial abundances. Besides, at a given time, there could be discrepancies between different models due to different computational techniques. At steady-state though, the results should not be model dependent, assuming the physical and chemical parameters are the same.

The steady-state assumption can be questioned especially because the typical time to reach equilibrium exceeds the free-fall time of the cloud $t_f = 4.3 \times 10^7 \{n_{\rm H}\}^{-1/2}$ yr (Spitzer, 1998). Yet, the time scale for ambipolar diffusion which slows down gravitational collapse (see Section 2.3) is actually consistent with a cloud life time of 10^7 yr (see Bergin and Tafalla, 2007, Figure 8).

For objects known to be young, though, it may be inevitable to consider some time dependence. In our

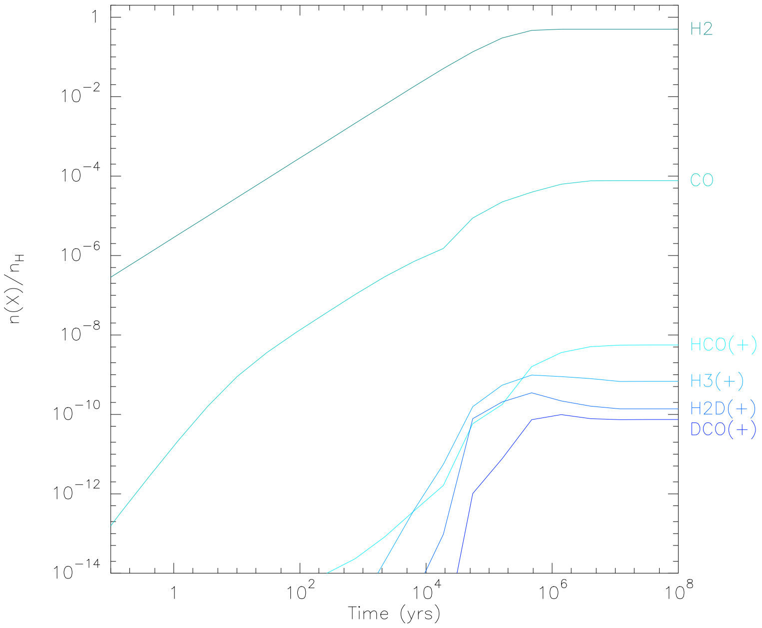

Figure 8.1: Time-dependent evolution of a few species involved in the formation of DCO^+, determined with `astrochem`. The initial abundances used are listed in Table 8.1 and are in the atomic form. Steady-state is reached after $\sim 10^7$ yr and the time scale is dominated by the formation of H_2 on grains. Here, the ionisation of the cloud is *standard*: $\zeta = 1.3 \ \times 10^{-17} \ \mathrm{s}^{-1}$. The physical conditions in the gas are $n_{\mathrm{H}} = 10^4 \ \mathrm{cm}^{-3}$, $T_{kin} = 10$ K and $A_V = 20$ mag.

study, the existence of an increased CR ionisation rate in clouds close to SNRs implies that the cloud would have been irradiated for a time shorter than the age of the remnant. Therefore, it is relevant to consider a possible time dependence of the observed chemical abundances. But what should be the initial abundances? What I did was to consider an initial molecular cloud that had reached steady-state before the supernova occurred, irradiated by a standard ionisation rate $\zeta = 1.3 \ \times 10^{-17} \ \mathrm{s}^{-1}$. Then, I considered an instantaneous increase in ζ and followed the evolution of the chemical abundances until a new equilibrium was reached. This study could give some more constraints, as will be discussed in further details in Chapter 12.

8.4 Comparison to observations

8.4.1 Abundance ratios

As described in the previous sections, the code computes the chemical abundances $x(X) = n(X)/n_{\mathrm{H}}$ of a species X, given a source model (density, temperature, ...), initial abundances and a chemical network. Local variations of the amount of material on the line of sight influence the observed intensity and the determination of $N(\mathrm{H})$ is always uncertain. Therefore, I didn't considered species abundances, but abundance ratios, e.g. $R_D = N(\mathrm{DCO}^+)/N(\mathrm{HCO}^+) = n(\mathrm{DCO}^+)/n(\mathrm{HCO}^+) = x(\mathrm{HCO}^+)/x(\mathrm{HCO}^+)$, where N is the column density, n the density and x the abundance of the species (assuming a constant-density cloud).

The CR ionisation rate ζ is an input parameter and I performed grids of models for a given set of physical parameters, varying ζ. Thus, I can follow the steady-state abundance of any species with ζ. Some species are highly sensitive to ζ and are called *tracers of the ionisation*. This can sometimes be easily interpreted with the formation routes of these species which involve e.g. CR induced H_3^+ (see Section 3). The observation of these species give constraints on ζ when compared to predictions (see Chapter 9). From chemical models, one can also look for other species strongly dependent on the ionisation state in the cloud (see Chapter 11).

The ionisation state is controlled by ζ/n_{H}, therefore I considered only one density $n_{\mathrm{H}} = 10^4 \ \mathrm{cm}^{-3}$ (model predictions at other densities confirmed that they only depend on ζ/n_{H}). I then run models for every temperature to match the physical conditions for each observation. Figure 8.2, published in Vaupré et al.

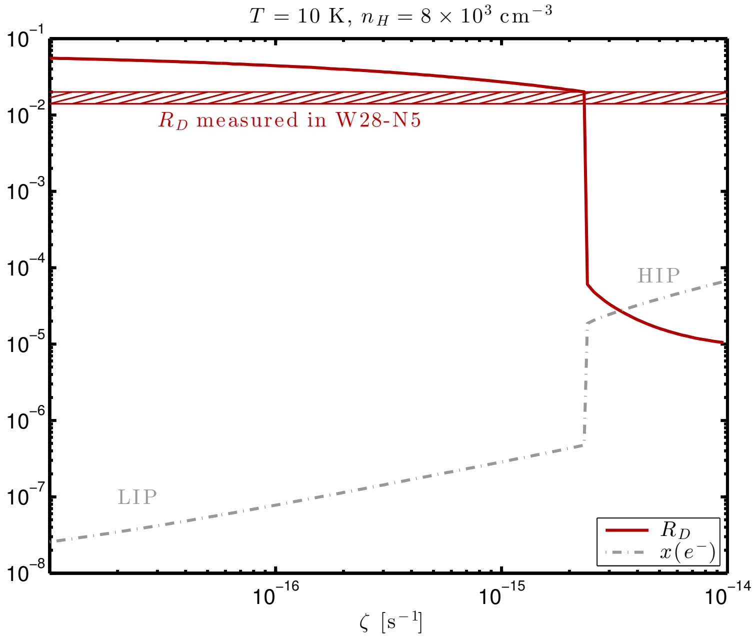

Figure 8.2: Comparison of the expected steady-state chemical abundance ratio $R_D = N(\mathrm{DCO}^+)/N(\mathrm{HCO}^+)$ from `astrochem` (red solid line) to observations in W28-N5 (dashed area). The physical conditions are set to correspond to this particular position: $n_\mathrm{H} = 8 \times 10^3$ cm^{-3} and $T = 10$ K. A sharp transition from a low-ionisation phase (LIP) to a high-ionisation phase (HIP) is visible at $\zeta \sim 2 \times 10^{15}$ s^{-1} and is characterised by a steep rise in the electron abundance (dot-dashed line). This comparison allows to constrain the ionisation fraction x_e and the CR ionisation rate ζ (Vaupré et al., 2014).

(2014), gives an example of such a comparison in W28, for the determination of ζ.

In W44, I also modeled the influence of elemental abundances on the expected abundance ratio, to better match the observations.

These results will be further described in the relevant sections in Part III.

8.4.2 Chemical instability

A remarkable feature of the evolution of the abundance ratio $\mathrm{HCO}^+/\mathrm{DCO}^+$ in Figure 8.2 is the dramatic change at $\zeta \sim 2 \times 10^{-15}$ s^{-1}. This figure corresponds to the particular case of W28-N5 and takes into account the physical conditions derived at this temperature (Vaupré et al., 2014). This jump corresponds to the transition from the so-called low ionisation phase (LIP) to the high ionisation phase (HIP) (Pineau des Forêts et al., 1992; Le Bourlot et al., 1993), which are two stable phases characterised by a low and high abundance of electrons, respectively (Figure 8.2). The existence of the jump is due to the sensitivity of interstellar chemical networks to ionisation. The role of reaction cycles between key elements such as S^+, O_2 and H_3^+ was shown by Boger and Sternberg (2006). Wakelam et al. (2006) showed that the ratio of the CR ionisation rates of He and H_2 can be an independent control parameter of the chemical instability, besides the standard control parameter ζ/n_H.

In our calculations, the value of ζ at which the jump occurs depends only slightly on the temperature (see Vaupré et al., 2014, Figure 5). More details, including a study of the hysteresis curves around the jump are given in Chapter 9.

Part III

Results

Chapter 9

Enhanced ionisation in W28 and CR properties

Contents

In this chapter, I present the high ionisation in a molecular cloud close to the SNR W28, determined from the DCO$^+$/HCO$^+$ method. These results were published in 2014 in an A&A paper, which is included below.

9.1 Introduction

W28 is an old ($\gtrsim 10^4$ yr) SNR known to be in interaction with a nearby molecular cloud, based e.g. on molecular observations (Wootten, 1981; Nicholas et al., 2012) and spatially coincident TeV emission (Aharonian and Collaboration, 2008a). In the northern part of the cloud, which is closest to the shell of the remnant with a projected distance of a few pc, there is further evidence that the shock of the SNR is reaching the cloud, with observations of OH masers (Claussen et al., 1997). The southern part of the cloud is much further away from the shock front ($\gtrsim 10$ pc). TeV emission is observed by H.E.S.S. in both the northern and southern parts, probably because of the presence of a flux of accelerated protons over the whole cloud. This SNR-molecular cloud (SNR-MC) association is therefore an ideal target to search for CR induced chemistry in the dense gas.

9.2 Summary of the article and main results

We obtained observations with the IRAM 30m telescope during winter 2011-2012. As described in detail in Part II, we used the method based on the measured DCO$^+$/HCO$^+$ ratio to derive the ionisation fraction $x_e = n(\mathrm{e}^-)/n_\mathrm{H}$ in the gas, and consequently, the CR ionisation rate ζ.

Since the derived ionisation fraction from the DCO$^+$/HCO$^+$ ratio depends on the gas density and temperature, in order to apply it the latter have also to be measured. For this purpose, we observed the CO rare isotopologues, ^{13}CO and C^{18}O, lowest two transitions.

Before summarising the obtained results, here I explain in more detail how the DCO$^+$/HCO$^+$ ratio method was used to reach these results.

The CR ionisation rate ζ is a free parameter of the chemical modeling. Given a set of physical conditions, consistent with observations, I computed grids of chemical abundances predicted with `astrochem` in the cloud (see Chapter 8), including e$^-$, DCO$^+$ and HCO$^+$, to plot the evolution of x_e with $R_D = $ DCO$^+$/HCO$^+$.

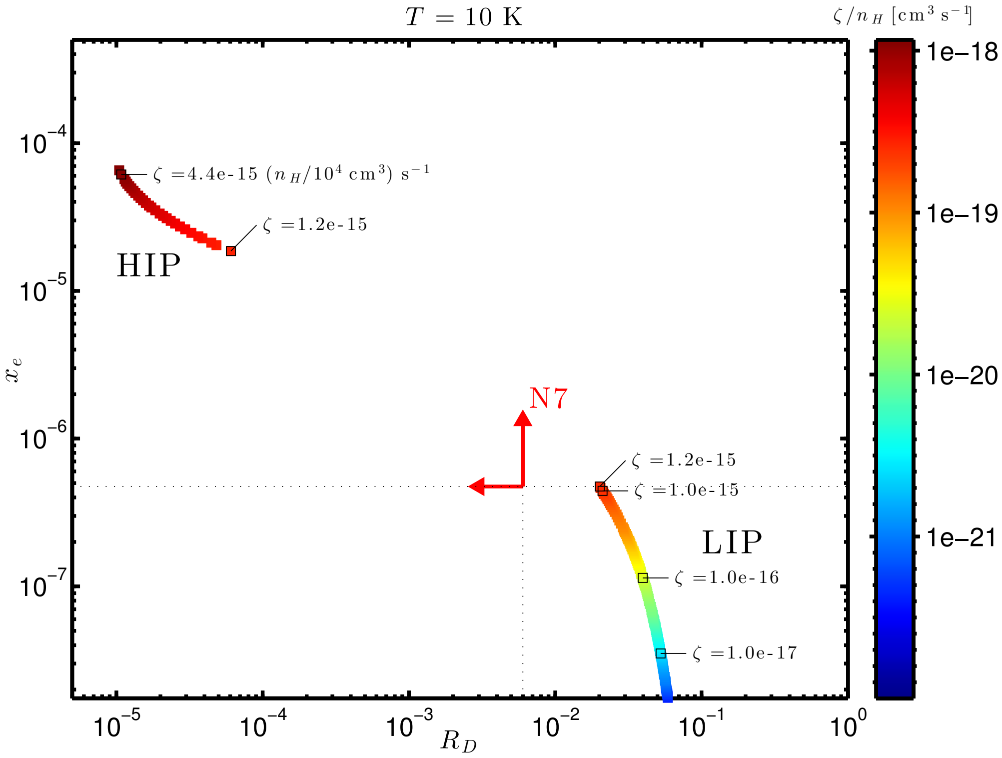

Figure 9.1: Example of the determination of the CR ionisation rate in W28-N7. The theoretical values shown in the colored curves are derived with the chemical model at the physical conditions of this position: $T = 10$ K and $n_{\rm H} = 4 \times 10^3$ cm^{-3}, derived from LVG analysis. For these conditions, the jump from LIP to HIP occurs at $\zeta = 1.2 \times 10^{-15}$ s^{-1} (or $\zeta/n_{\rm H} = 3 \times 10^{-19}$ cm^3 s^{-1}). The red point shows the measured upper limit on R_D, which translates into a lower limit on x_e and ζ.

Figure 9.1 shows a simple example toward one particular position in W28. The LVG analysis supplied the physical conditions in W28-N7 from CO observations, and I found a temperature $T = 10$ K and a density $n_{\rm H} = 4 \times 10^3$ cm^{-3}, which I used in the computation with `astrochem`. The evolution with $\zeta/n_{\rm H}$ is given by the color scale. For a better understanding, I point out the predicted values corresponding to a few CR ionisation rates for the gas density of W28-N7. If we consider the observed upper limit on the abundance ratio $R_D < 0.007$, it falls in the gap between the low-ionisation phase (LIP) and the high-ionisation phase (HIP), i.e. R_D is significantly smaller than possible values in the LIP ($R_D > 0.02$ at 10 K) and significantly larger than values in the HIP ($R_D < 6 \times 10^{-5}$ at 10 K). In this example, the flip occurs at $\zeta = 1.2 \times 10^{-15}$ s^{-1}, and we conclude that this is therefore the lower limit on ζ at this position. Besides, the ionisation fraction x_e increases with ζ, and this gives also a lower limit $x_e \gtrsim 5 \times 10^{-7}$. The possible R_D values in the HIP are too low to be detected, so we cannot further constrain the CR ionisation rate.

Towards the positions located close to the SNR, we find much larger ($>$ 100 times) CR ionisation rates than those in standard galactic clouds. Conversely, towards one position situated at a larger distance from the edge of the SNR, we derive a standard CR ionisation rate. Overall, these observations support the hypothesis that the gamma rays observed in the region are probably due to pion decay from proton interaction with the cloud material. AGILE observations (Giuliani et al., 2010) show that GeV photons are only detected in the Northern cloud, which constitutes evidence that GeV protons remain bound to the SNR shell and did not reach the Southern cloud. This has important consequences on the CR diffusion properties: if we consider that ∼1 GeV protons didn't have time to reach the Southern cloud at a *projected* distance of 10 pc (position W28-SE1) within the age of the remnant $\sim 10^4$ yr, then we get the following constraint on the diffusion coefficient of ∼10 GeV protons:

$$D_{(10\ \mathrm{GeV})} \gtrsim 3 \times 10^{27} \left(\frac{R}{10\ \mathrm{pc}}\right)^{2} \left(\frac{t}{10^{4}\ \mathrm{yr}}\right)^{-1} \mathrm{cm}^{2}/\mathrm{s}\ . \tag{9.1}$$

In addition, we find that the ionisation of the gas is likely due to $0.1 - 1$ GeV CRs, and there is an overlap in energy between CRs responsible for ionisation and those responsible for γ emission. Finally, these observations are also in agreement with the global picture of CR diffusion, in which the low-energy tail of the CR population diffuses later and, consequently, at a given time covers smaller distances than the high-energy counterpart.

A&A 568, A50 (2014)
DOI: 10.1051/0004-6361/201424036

Astronomy & Astrophysics

Cosmic ray induced ionisation of a molecular cloud shocked by the W28 supernova remnant

S. Vaupré[1], P. Hily-Blant[1], C. Ceccarelli[1], G. Dubus[1], S. Gabici[2], and T. Montmerle[3]

[1] Univ. Grenoble Alpes/CNRS, IPAG, 38000 Grenoble, France
e-mail: `solenn.vaupre@obs.ujf-grenoble.fr`
[2] APC, AstroParticule et Cosmologie, Université Paris Diderot, CNRS, CEA, Observatoire de Paris, Sorbonne Paris, 75205 Paris, France
[3] Institut d'Astrophysique de Paris, 98bis Bd Arago, 75014 Paris, France

Received 19 April 2014 / Accepted 5 June 2014

ABSTRACT

Cosmic rays are an essential ingredient in the evolution of the interstellar medium, as they dominate the ionisation of the dense molecular gas, where stars and planets form. However, since they are efficiently scattered by the galactic magnetic fields, many questions remain open, such as where exactly they are accelerated, what is their original energy spectrum, and how they propagate into molecular clouds. In this work we present new observations and discuss in detail a method that allows us to measure the cosmic ray ionisation rate towards the molecular clouds close to the W28 supernova remnant. To perform these measurements, we use CO, HCO^+, and DCO^+ millimetre line observations and compare them with the predictions of radiative transfer and chemical models away from thermodynamical equilibrium. The CO observations allow us to constrain the density, temperature, and column density towards each observed position, while the DCO^+/HCO^+ abundance ratios provide us with constraints on the electron fraction and, consequently, on the cosmic ray ionisation rate. Towards positions located close to the supernova remnant, we find cosmic ray ionisation rates much larger ($\gtrsim$100) than those in standard galactic clouds. Conversely, towards one position situated at a larger distance, we derive a standard cosmic ray ionisation rate. Overall, these observations support the hypothesis that the γ rays observed in the region have a hadronic origin. In addition, based on CR diffusion estimates, we find that the ionisation of the gas is likely due to 0.1–1 GeV cosmic rays. Finally, these observations are also in agreement with the global picture of cosmic ray diffusion, in which the low-energy tail of the cosmic ray population diffuses at smaller distances than the high-energy counterpart.

Key words. ISM: clouds – cosmic rays – ISM: supernova remnants – ISM: individual objects: W28

1. Introduction

Cosmic rays (CRs) are energetic charged particles that reach the Earth as an isotropic flux. They pervade the Galaxy and play a crucial role in the evolution of the interstellar medium, because they dominate the ionisation of molecular clouds where the gas is shielded from the UV radiation field. The ionisation degree in the molecular gas is a fundamental parameter throughout the star and planet forming process. First, ions couple the gas to the magnetic field and, therefore, they regulate the gravitational collapse of the cloud. In addition, ions sustain turbulence within protoplanetary discs and introduce non-ideal magnetohydrodynamics effects, which influence the accretion rate onto the protostar (Balbus & Hawley 1998; Lesur et al. 2014). Finally, the CR induced ions initiate efficient chemical reactions in the cold molecular clouds, which eventually lead to the formation of complex molecules, which enrich the gas even up to the first stages of planet formation.

However, in order to fully understand the influence of CRs on the above processes across the Galaxy, it is necessary to know where CRs are accelerated and how they propagate through the gas. Unfortunately, since CRs are scattered by magnetic fields all along their path through the Galaxy, the production sites of CRs cannot be observed directly, and the diffusion of CRs also makes the evolution of the energy spectrum during their propagation difficult to determine observationally.

However, we can detect indirect signatures of the interaction of hadronic CRs (essentially protons) with matter. Protons above a kinetic energy threshold of ≈280 MeV produce π^0 pions when they collide with particles in the molecular cloud. Each pion then decays into two γ-ray photons ($\pi^0 \rightarrow 2\gamma$), each with a typical energy that thoseis ~10% that of the colliding proton. Bright γ-ray sources thus indicate regions with a large density of protons with energies above 0.28 GeV. In these regions, the observed γ-ray photon spectrum can, in addition, be used to derive the spectrum of the parental CR particles, before the scattering and propagation within the Galaxy (Ackermann et al. 2013).

Supernova remnants (SNR) are thought to be the sources of CRs. In this scenario, protons are accelerated in the expanding shell of the SNR, following the diffusive shock acceleration process (Bell 1978). Supporting this scenario, there is now clear evidence that SNR are spatially associated with GeV to TeV sources (Aharonian 2013). Moreover, several SNR are close to the molecular cloud that gave birth to the SN precursor. These molecular clouds now act as reservoirs of target material for the freshly accelerated protons, thus enhancing the production rate of γ rays. Although it is compatible with γ-ray observations, the hadronic scenario is challenged by the leptonic scenario involving electron CRs. In this alternative scenario, the γ-ray emission can be explained mainly by inverse Compton scattering of the cosmic microwave background (e.g. Morlino et al. 2009; Abdo et al. 2011). Yet, this scenario cannot explain the spatial correlation of TeV emission with molecular clouds. Moreover, recent observations of the IC443 and W44 SNR with the *Fermi*-LAT telescope (Ackermann et al. 2013) specifically

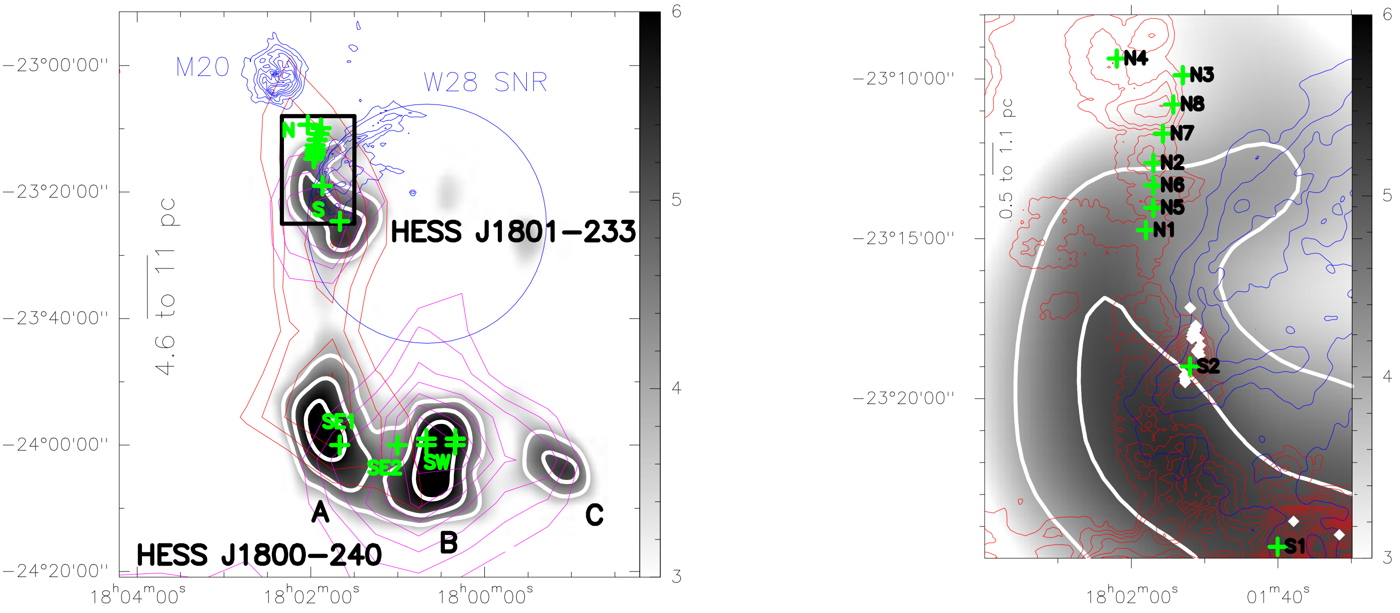

Fig. 1. *Left*: the W28 complex on large scales. Grayscale (in σ) and thick contours show TeV emission as seen by HESS (levels are 4−6σ). Red contours show the CO(1−0) emission (Dame et al. 2001) integrated over 15−25 km s^{-1} and magenta contours trace the emission integrated over 5−15 km s^{-1} (levels are 40−70 K km s^{-1} by 5 K km s^{-1}). Crosses show the positions observed with the IRAM 30m telescope and discussed in this paper. The blue contours show the 20 cm free-free emission in the M20 region (Yusef-Zadeh et al. 2000). The blue circle gives the approximate radio boundary of the SNR W28 (Brogan et al. 2006). *Right*: the northern cloud in the W28 complex (zoom on the black box). The red contours show the CO(3−2) emission in K km s^{-1}, integrated over 15−25 km s^{-1} (levels are 15−130 K km s^{-1} by 5 K km s^{-1}) (Lefloch et al. 2008). Diamonds show the locations of OH masers in the region (Claussen et al. 1997).

support a hadronic origin of γ rays, consistent with the so-called *SNR paradigm* for the origin of primary CR (see e.g. Hillas 2005, for a review).

Cosmic ray protons with kinetic energy below the ≈280 MeV threshold of π^0 production cannot be traced by the emission of γ-rays. Nevertheless, recent calculations suggest that the ionisation of UV-shielded gas is mostly due to keV-GeV protons (Padovani et al. 2009). Accordingly, low-energy CR protons can be traced indirectly by measuring the ionisation fraction of the dense gas. It has thus been proposed that an enhanced electron abundance in molecular clouds located in the vicinity of SNR could be the smoking gun for the presence of freshly accelerated CRs, with energies $\lesssim$1 GeV.

This idea was put forward by Ceccarelli et al. (2011, hereafter CC2011), who measured the ionisation fraction $x_e = n(e^-)/n_H$ in the W51C molecular cloud, located in the vicinity of the W51 SNR. The detection of TeV emission by both HESS and MAGIC telescopes close to the molecular cloud is evidence of a physical interaction with the SNR. This supports the idea of the pion-decay production of γ rays with W51C acting as a γ-ray emitter. In CC2011, an enhanced ionisation fraction was reported towards one position, W51C-E, which required a CR ionisation rate two orders of magnitude larger than the typical value of 1×10^{-17} s^{-1} in molecular clouds. This observational evidence strongly supports the hadronic scenario of γ-ray production, at least for W51.

Complementary studies of the CR ionisation rate in several diffuse clouds close to SNR have been carried out using different techniques, such as H_3^+ absorption (McCall et al. 2003). These studies also show an enhancement of a factor of 10−100 of the CR ionisation rate (Indriolo et al. 2010; Indriolo & McCall 2012) with respect to the canonical value. However, the interpretation is not straightforward, as Padovani et al. (2009) showed that the penetration into the cloud of high energy CRs results into an enhanced CR ionisation rate in low density molecular clouds even in absence of an increased CR flux.

The combined observations of two extreme energy ranges, namely TeV and millimetre, seems a powerful method to characterise an enhanced concentration of proton CRs. It also gives additional evidence supporting a physical interaction of the SNR shock with molecular clouds. From a theoretical point of view, it is expected that the most energetic CR protons diffuse at larger distances ahead of the SNR shock front, whilst the low-energy tail of the distribution remains closer. As a consequence, one expects that any ionisation enhancement by low energy CRs should be localised accordingly. In CC2011, however, only one location could be used to derive the ionisation fraction, and no constraint could be given regarding the spatial distribution of the ionisation and therefore the diffusion properties of CRs.

The aim of this paper is to present measurements of the ionisation fraction within the molecular clouds in the vicinity of the W28 SNR. The paper is organized as follows. In Sect. 2, the W28 association is presented, with particular emphasis on the physical link between the SNR and the molecular clouds. In Sect. 3, the millimetre observations are described. The derivation of the physical conditions is presented in Sect. 4. The derivation of the ionisation fraction and the CR ionisation rates are described in Sects. 5 and 6, where we stress the strengths and limitations of the method. The results are discussed in Sect. 7.

2. The W28 association

The W28 SNR has an age greater than 10^4 yr, and is likely in the Sedov or radiative phase (Westerhout 1958; Lozinskaya 1974). Its distance is estimated between 1.6 kpc and 4 kpc, based on kinematic determinations and Hα observations (Goudis 1976; Lozinskaya 1981). The LSR velocity, based on Hα and [NII] observations, is estimated to be 18 ± 5 km s^{-1} (Lozinskaya 1974).

Table 1. Molecular transitions observed with the IRAM 30 m telescope.

Species	Line	Frequency [GHz]	$F_{\rm eff}$	$B_{\rm eff}$	*HPBW* [arcsec]	$T_{\rm sys}$ [K]	$\sigma_{\rm rms}$ [mK]
$H^{13}CO^+$	(1–0)	86.754	0.95	0.81	29	100–130	6–12
$C^{18}O$	(1–0)	109.782	0.95	0.79	22	140–200	20–50
^{13}CO	(1–0)	110.201	0.95	0.79	22	140–200	20–50
$C^{17}O$	(1–0)	112.359	0.95	0.79	22	140–200	20–50
DCO^+	(2–1)	144.077	0.92	0.74	16	100–200	8–20
$C^{18}O$	(2–1)	219.560	0.94	0.61	11	160–220	20–80
^{13}CO	(2–1)	220.399	0.94	0.61	11	160–220	20–80
$C^{17}O$	(2–1)	224.714	0.94	0.61	11	160–220	20–80

Notes. $T_{\rm sys}$ indicates the range of system temperatures during the observing run, and the corresponding sensitivity fluctuations. The adopted values of the telescope parameters follow from the IRAM observatory recommendations: $F_{\rm eff}$ and $B_{\rm eff}$ are the forward and main-beam efficiencies of the telescope, respectively; HPBW is the half-power beam width.

In the remainder of the text, all velocities will refer to the local standard of rest (LSR) and projected distances will be given for distances of both 1.6 and 4 kpc. The boundary diameter of the SNR is 42 arcmin, corresponding to a linear radius of 9.6 to 24 pc (Fig. 1).

The large-scale region towards W28 contains a variety of objects such as HII regions (e.g. M8, M20, W28A2), molecular clouds, SNR, and new SNR candidates (Brogan et al. 2006). Molecular gas, as seen in CO(1−0) (Wootten 1981; Dame et al. 2001), coincides spatially with the W28 SNR, suggesting a physical association, and supporting a view in which the W28 SNR is interacting with its parental molecular cloud. Probably related is the fact that ongoing massive star formation has been observed in these molecular clouds, consistent with the triggered star formation scenario (Elmegreen 1998). The molecular gas located towards the north-east of the SNR boundary was mapped at high spatial resolution, in the CO(3−2) rotational line, by Lefloch et al. (2008) revealing a fragmented filamentary structure elongated north-south (Fig. 1).

In γ rays, the high spatial resolution H.E.S.S. imaging array of Cherenkov telescopes has revealed the presence of extended TeV emission (Aharonian et al. 2008), which splits into two components, separated by 14−34 pc: HESS J1801-233, in the north, and HESS J1800-240 in the south. The latter further splits into three well-separated components (Fig. 1). In projection, the entire TeV emission coincides with the molecular gas seen in CO(1−0) which also appears to bridge the northern and southern TeV components. The molecular gas coinciding with the northern TeV component J1801-233 shows velocities predominantly from 15 km s^{-1} to 25 km s^{-1}, as does the southern J1801-240 A component observed in CS(1−0) by Nicholas et al. (2012). However, the southern components J1801-240 B and C coincide with molecular emission characterised by somewhat lower velocities, from 5 km s^{-1} to 15 km s^{-1}.

Whether the TeV emission is physically associated with the molecular clouds is of utmost importance, for the question of pion-decay production. However, there are several indications, based on kinematic information, that this may well be the case.

First, when inspected in velocity space, the CO(1−0) emission covers the entire range from 5 to 25 km s^{-1} continuously (Fukui et al. 2012a). This indicates that the molecular emission, traced either by CS or CO, is physically linked over the entire region, and not only in projection.

Second, OH masers have been reported towards the northern component (Claussen et al. 1997; Hewitt et al. 2008), with velocities ranging from 7.1 km s^{-1} to 15.2 km s^{-1}. Such OH masers are thought to trace the interaction of the SNR shock with the molecular gas, an interpretation which is consistent with the velocity range of the CO(1−0) emission.

Finally, velocity differences observed between the northern and southern clouds are compatible with the differences up to ~6 km s^{-1} observed in the M20 map of CO(3−2), encompassing the northern TeV component (Lefloch et al. 2008), indicating that velocity shifts of several km s^{-1} are found which could be due to an interaction with the SNR.

Taken all together, these data strongly suggest a 3D picture in which the SNR is interacting with surrounding molecular clouds covering a wide and continuous velocity range, typically from 5 km s^{-1} to 25 km s^{-1}, and characterised by large variations along the line of sight.

It is therefore most likely that the W28 association displays the interaction of the SNR with molecular clouds, and thus is an excellent target in which to study the ionisation by CRs.

3. Observations and data reduction

Observations were carried out over 40 h in December, 2011, and March, 2012, with the IRAM 30 m telescope. We used the EMIR bands with the Fast Fourier Transform Spectrometer as a backend in the position-switching mode, using OFF positions about 1000″ to the east. Amplitude calibration was done typically every 15 min, and pointing and focus were checked every 1 and 3 h, respectively, ensuring ≈2″ pointing accuracy. All spectra were reduced using the CLASS package of the GILDAS[1] software (Pety 2005). Residual bandpass effects were subtracted using low-order (≤3) polynomials. The weather was good and $T_{\rm sys}$ values were lower than 220 K. The observed molecular transitions used in the present work are listed in Table 1, along with the associated system temperature and sensitivity ranges $T_{\rm sys}$ and $\sigma_{\rm rms}$ obtained during the successive runs of observations. All spectra are presented on the main-beam temperature scale, $T_{\rm mb} = (F_{\rm eff}/B_{\rm eff})T^*_{\rm ant}$, with $F_{\rm eff}$ and $B_{\rm eff}$ the forward and main-beam efficiencies of the telescope, respectively.

We observed towards 16 positions, of which 10 are located in the northern cloud and 6 in the southern cloud. The coordinates of these positions are listed in Table 2. The two lowest rotational transitions of ^{13}CO and $C^{18}O$ are used to derive the physical conditions in the cloud, while $H^{13}CO^+$(1−0) and DCO^+(2−1) are used to derive the cosmic ray ionisation rate.

---

[1] http://www.iram.fr/IRAMFR/GILDAS/

Table 2. J2000 coordinates of the 16 observed positions.

Source	α_{2000} (hms)	δ_{2000} (° ′ ″)
J1801-N1	18 01 58.0	−23 14 44
J1801-N2†	18 01 57.0	−23 12 38
J1801-N3†	18 01 53.0	−23 09 53
J1801-N4†	18 02 02.0	−23 09 22
J1801-N5	18 01 57.0	−23 14 02
J1801-N6	18 01 57.0	−23 13 20
J1801-N7	18 01 55.7	−23 11 43
J1801-N8	18 01 54.3	−23 10 48
J1801-S1	18 01 40.0	−23 24 38
J1801-S2	18 01 52.0	−23 19 00
J1801-SE1	18 01 40.0	−24 00 00
J1801-SE2	18 01 00.0	−24 00 00
J1801-SW1	18 00 40.0	−24 00 00
J1801-SW2	18 00 20.0	−24 00 00
J1801-SW3	18 00 40.0	−23 59 00
J1801-SW4	18 00 20.0	−23 59 00

Notes. † N2, N3, and N4 correspond to TC5, TC7, and TC6, respectively, as referred to in Lefloch et al. (2008). N2 also coincides with a high-mass protostar.

4. Results

4.1. Observed spectra

The resulting spectra towards all positions are shown in Fig. 2. The ^{13}CO and C^{18}O spectra show multiple velocity components, most likely associated with several clouds along the line of sight. In some instances, negative features are apparent, which are due to emission from the reference position at different velocities. Isotopologues ^{13}CO and C^{18}O are detected towards 12 of the 16 positions, and the spectra show clearly two main components. The velocity of the dominant component varies between the northern ($\lesssim$21 km s^{-1}) and southern ($\gtrsim$7 km s^{-1}) cloud, as presented in Sect. 2. At most positions, the rarer C^{17}O isotopologue is also detected, although the hyperfine structure of the (1−0) transition is not always well resolved. The H^{13}CO$^+$(1−0) and DCO$^+$(2−1) emission lines have only one velocity component, at 21 km s^{-1}. The C^{18}O(1−0) and (2−1) lines show a clear distinction between the northern positions, where the line emission is the strongest, and southern positions. The compound H^{13}CO$^+$ is detected towards all northern positions but N8. However, DCO$^+$ is detected only towards three positions, N2, N5, and N6. Southern positions display much weaker emission and SE1 is detected in both H^{13}CO$^+$ and DCO$^+$.

The analysis was essentially driven by the H^{13}CO$^+$ and DCO$^+$ lines which are the main focus of the present work. The velocity of the dominant CO transition always corresponds to the velocity of the H^{13}CO$^+$ line when detected. When more velocity components are detected in CO, we limited the Gaussian fits to the first two dominant components. Upper limits are given at the 1σ level for $T_{\rm peak}$, and for the integrated intensity W by assuming Δv = 3 km s^{-1}. The results from the Gaussian fits are summarised in Table 3 (CO isotopologues) and Table 4 (H^{13}CO$^+$, DCO$^+$).

In the following, we describe the two-step analysis of the measured line intensities. First, the physical conditions are derived according to the ^{13}CO and C^{18}O lines. Second, the HCO$^+$/DCO$^+$ abundance ratio is compared with model predictions computed using the derived physical conditions.

4.2. Determination of physical conditions

The physical conditions prevailing at the various locations were determined based on the ^{13}CO (1−0) and (2−1) lines and the C^{18}O (1−0) and (2−1) lines. To accomplish this, we performed non-local thermal equilibrium (non-LTE) calculations of the rotational level populations under the large velocity gradient (LVG) approximation (Ceccarelli et al. 2003). The H$_2$ density, gas kinetic temperature $T_{\rm kin}$, and total column density of each species covered a large parameter space. For each set of input parameters, the expected line intensities and integrated intensities were computed adopting the linewidth Δv derived from the Gaussian fits (Table 3), and taking into account beam dilution effects by varying the size of the emitting regions. A simple χ^2 minimization was then used to constrain the physical conditions that best reproduce the observed intensities. The LVG analysis was performed towards positions where all four lines were detected. We considered collisions of ^{13}CO and C^{18}O with both para and ortho H$_2$, assuming an ortho-to-para ratio in Boltzmann equilibrium. Hence, in the temperature range considered here, H$_2$ is mainly in its para configuration. We used the collisional cross sections from Yang et al. (2010).

In this process, the relative abundances of C^{18}O to ^{13}CO need to be known, and we have assumed that the molecular isotopic ratios are equal to the elemental isotopic ratios, namely that

$$\frac{[\mathrm{C^{18}O}]}{[\mathrm{^{13}CO}]} = \frac{[\mathrm{C^{18}O}]}{[\mathrm{^{12}C^{16}O}]} \times \frac{[\mathrm{^{12}C^{16}O}]}{[\mathrm{^{13}CO}]} \approx \left(\frac{^{18}\mathrm{O}}{^{16}\mathrm{O}}\right) \times \left(\frac{^{12}\mathrm{C}}{^{13}\mathrm{C}}\right). \quad (1)$$

It is known that isotopic ratios may vary with the position within the Milky Way, resulting from the gradual depletion of ^{12}C and enrichment of ^{13}C with the cycling of gas through stars (e.g. Wilson & Rood 1994; Frerking et al. 1982). In addition, local variations are also possible, resulting from the competition of chemical fractionation and selective photodissociation (van Dishoeck & Black 1988; Federman et al. 2003). The dependence of the ^{12}C/^{13}C isotopic ratio on galactocentric distance was studied by Milam et al. (2005). Applying their results to W28, which is 4–6 kpc from the Galactic center, one gets ^{12}C/^{13}C = 50 ± 7. In practice, in our non-LTE analysis, we varied the ^{13}C/^{12}C ratio. The best χ^2 values were obtained using an isotopic ratio of 50, consistent with the above expectation, which we therefore adopted in what follows. Regarding the ^{16}O/^{18}O isotopic ratio, we adopted the value of 500 representative of the solar neighborhood.

The results of the LVG analysis are summarised in Table 5. At each position, the size of the emitting regions was found to be larger than the beam size. Position N2, which is considered a protostar in Lefloch et al. (2008), shows a peculiar behaviour with a visual extinction at least 5 times higher than for the other positions. Overall, the density and kinetic temperature we derived are typical of dense molecular clouds with visual extinctions larger than 10 mag. We also note that the H$_2$ densities we derived in the northern cloud are consistent with values published by Lefloch et al. (2008).

4.3. The DCO$^+$/HCO$^+$ abundance ratio

The species DCO$^+$ was detected towards four positions, for which it was possible to derive values of the DCO$^+$/HCO$^+$ abundance ratio. For all other positions where H^{13}CO$^+$ was detected, upper limits at the 1σ level on the abundance ratio we derived. We determined the column densities of H^{13}CO$^+$ and DCO$^+$ from the same non-LTE LVG calculation, using the collisional cross sections from Flower (1999) and the physical conditions derived

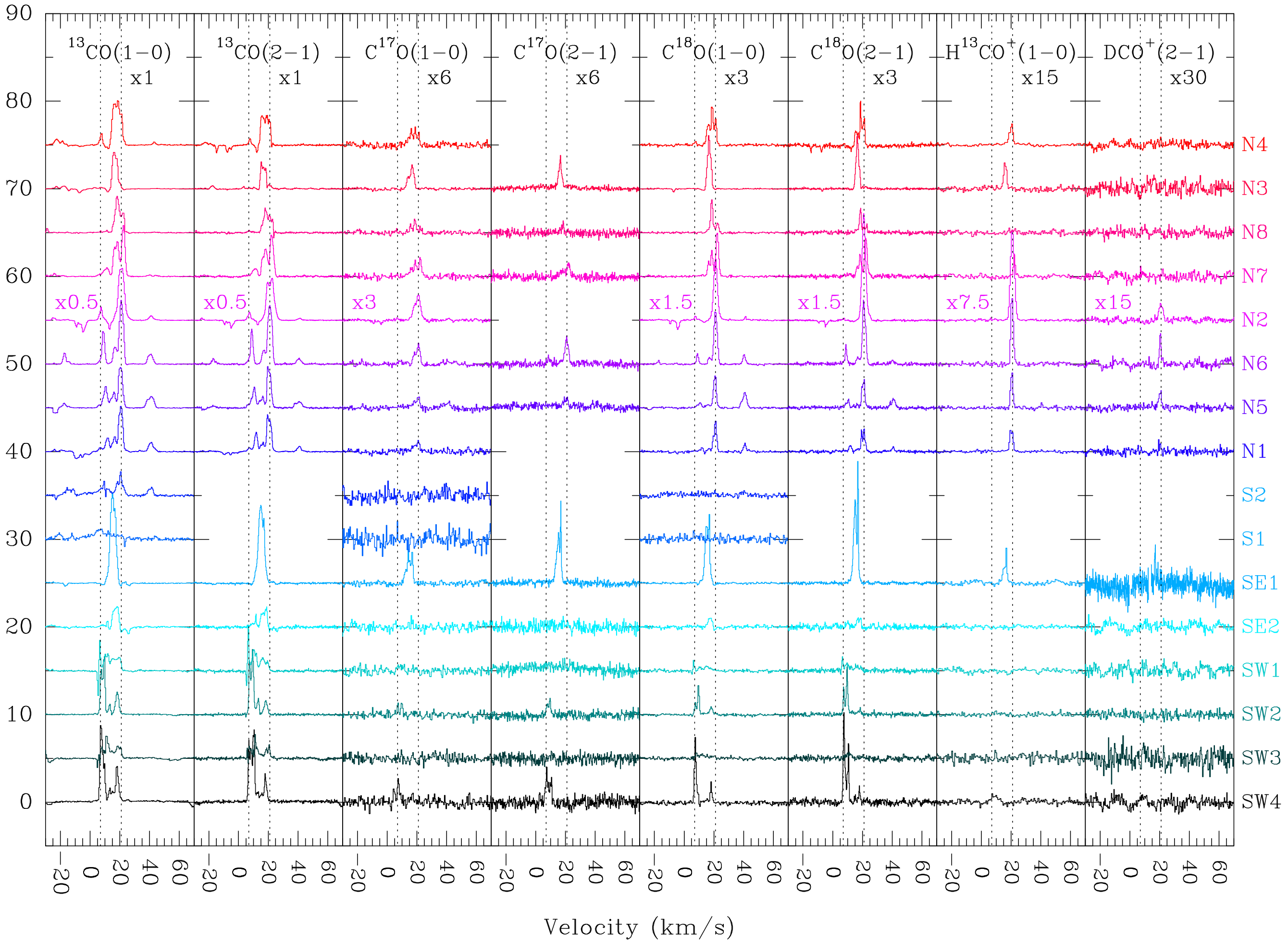

Fig. 2. Observations of millimetre emission lines towards all positions. The intensities are in units of main-beam temperature (K). For readibility, a multiplicative factor was applied to the spectra and is given under each transition line label. This factor was decreased for position N2 (protostar) where the signal is very strong. Vertical dashed lines indicate the two extreme velocity components of the complex at 7 and 21 km s^{-1}.

from the CO observations (Table 5). We derived the observed DCO$^+$/HCO$^+$ abundance ratio for each set of physical conditions (n_{H_2}, T), assuming $^{12}C/^{13}C = 50$ (see Sect. 4.2). The uncertainty in the abundance ratio is dominated by the uncertainties in the physical conditions. Results are listed in Table 5 and will be used in the next section to constrain the CR ionisation rate.

5. Methods to measure the CR ionisation rate ζ

5.1. Analytical method

In their seminal paper, Guélin et al. (1977, hereafter G77) suggested that the abundance ratio of DCO$^+$ to HCO$^+$, which we denote R_D = DCO$^+$/HCO$^+$, can be used to measure the ionisation fraction in molecular clouds, $x_e = n(e^-)/n_H$. Subsequently, Caselli et al. (1998, hereafter C98) proposed using the R_H = HCO$^+$/CO abundance ratio in combination with R_D to derive both x_e and ζ in dark clouds. The basic idea is that DCO$^+$ and HCO$^+$ are chemically linked, and depend on a reduced number of chemical reactions where the CR ionisation rate plays a crucial role, through the ionisation of H$_2$ into H_2^+ (Herbst & Klemperer 1973), leading to the formation of the pivotal H_3^+ ion. The fast ion-neutral reaction of H_3^+ with HD produces the deuterated ion H$_2$D$^+$ which then initiates the formation of several deuterated species, including DCO$^+$. In a similar fashion, HCO$^+$ is formed by the reaction of H_3^+ with CO. This forms the basis of the method of C98 which uses CO, DCO$^+$, and HCO$^+$ to derive x_e and ζ. The full set of reactions used in the C98 analysis is given in Table A.1 with updated reaction rates.

The steady-state abundance ratios R_H = HCO$^+$/CO and R_D = DCO$^+$/HCO$^+$ can be analytically derived from this network, provided that HCO$^+$ and DCO$^+$ are predominantly formed and destroyed by reactions 1–4 and 7–9, respectively. One then finds that

$$R_H = \frac{[\mathrm{HCO}^+]}{[\mathrm{CO}]} = \frac{k_H}{\beta'}\frac{x(\mathrm{H}_3^+)}{x_e} \approx \frac{k_H}{(2\beta x_e + \delta)\beta'}\frac{\zeta/n_H}{x_e}, \qquad (2)$$

and

$$R_D = \frac{[\mathrm{DCO}^+]}{[\mathrm{HCO}^+]} \approx \frac{1}{3}\frac{x(\mathrm{H_2D}^+)}{x(\mathrm{H}_3^+)} \approx \frac{1}{3}\frac{k_f x(\mathrm{HD})}{k_e x_e + \delta + k_f^{-1}/2}, \qquad (3)$$

where $n(X)$ is the number density of species X and $x(X) = n(X)/n_H$ its fractional abundance. In the following, we will assume that the gas is fully molecular such that $n_H = 2n(H_2)$. The coefficients β, β', and k are the reaction rates listed in Table A.1. Finally, $\delta \sim \delta_{H_3^+} \sim \delta_{H_2D^+}$ is the total destruction rate of H_3^+ or H$_2$D$^+$ by neutrals. Provided that R_H, R_D, n_H, and the kinetic temperature are known, x_e and ζ can then be derived

Table 3. Results from the Gaussian fits of the emission lines of ^{13}CO and C^{18}O towards the 12 positions where they are detected.

Pos.	^{13}CO(1–0)				^{13}CO(2–1)				C^{18}O(1–0)				C^{18}O(2–1)			
	v_0	W	$T_{\rm peak}$	Δv	v_0	W	$T_{\rm peak}$	Δv	v_0	W	$T_{\rm peak}$	Δv	v_0	W	$T_{\rm peak}$	Δv
First dominant velocity component																
N1	20.7	17.4	5.3	3.1	20.5	15.1	4.1	3.5	20.9	2.7	1.0	2.4	21.1	1.5	0.8	1.9
N5	20.6	15.7	5.0	3.0	20.5	15.0	4.7	3.0	20.8	2.8	1.3	2.1	20.7	2.6	1.0	2.4
N6	21.2	23.9	7.4	3.0	21.1	24.2	7.0	3.3	21.2	5.5	2.0	2.5	21.1	6.2	2.3	2.5
N2	21.1	59.6	12.6	4.5	21.5	57.4	9.6	5.6	21.1	14.7	4.5	3.0	21.0	25.0	7.9	3.0
N7	22.5	15.3	5.8	2.5	22.4	13.9	4.8	2.7	22.3	3.6	1.7	1.9	22.3	3.4	1.5	2.1
N8	18.4	15.4	4.0	3.6	18.2	9.7	2.5	3.6	18.6	2.4	1.3	1.7	18.6	1.3	0.9	1.4
N3	16.8	17.3	4.4	3.7	16.6	11.6	2.8	3.9	16.8	5.3	1.9	2.6	16.7	4.6	1.9	2.3
N4	18.9	15.2	4.9	2.9	19.0	11.3	3.3	3.2	18.9	2.2	1.5	1.4	18.8	1.4	1.6	0.8
SE1	15.0	34.3	9.9	3.3	15.1	39.7	8.7	4.3	15.3	6.7	2.1	3.0	15.0	7.5	3.0	2.4
SE2	16.3	5.8	2.0	2.7	16.3	5.6	1.6	3.2	16.9	0.8	0.3	2.5	16.9	0.6	0.3	1.9
SW2	9.6	10.5	7.0	1.4	9.5	13.2	7.4	1.7	9.7	1.3	1.1	1.1	9.7	2.2	1.8	1.2
SW4	8.9	14.7	4.7	3.0	7.8	18.6	6.4	2.7	7.5	3.4	2.4	1.4	7.6	4.6	3.1	1.4
Second dominant velocity component																
N1	11.7	5.6	1.5	3.6	11.8	5.7	2.2	2.5	11.9	0.3	0.2	1.8	11.9	0.5	0.2	2.1
N5	10.4	8.0	2.3	3.3	10.4	7.3	2.1	3.3	10.4	0.6	0.2	3.2	10.1	0.8	0.3	3.0
N6	9.0	8.3	3.7	2.1	9.0	8.1	3.9	2.0	9.0	0.6	0.4	1.5	9.0	1.0	0.7	1.4
N7	18.6	10.0	3.9	2.4	18.3	9.1	3.2	2.7	18.7	1.8	1.0	1.8	18.6	1.6	0.8	1.9
N8	22.3	4.5	2.2	1.9	21.3	3.0	1.6	1.8	22.3	0.9	0.3	2.3	22.1	0.8	0.2	3.3
N4	16.0	12.4	4.5	2.6	15.8	8.3	3.4	2.3	16.3	2.3	0.8	2.6	16.1	1.5	0.5	2.5
SE1	17.3	10.4	4.6	2.1	17.2	1.9	2.6	0.7	17.0	1.6	1.9	0.8	17.0	3.0	4.3	0.7
SE2	18.6	4.3	2.2	1.9	18.8	3.0	1.9	1.5	18.5	0.3	0.2	1.5	18.8	0.4	0.3	1.1
SW2	7.6	9.1	5.3	1.6	7.5	8.0	6.2	1.2	7.6	0.6	0.4	1.3	7.5	1.0	1.0	0.9
SW4	7.3	11.8	6.9	1.6	10.4	12.7	7.9	1.5	–	–	–	–	10.5	2.5	1.9	1.2

Notes. The fit parameters are: the centre line velocity v_0 (in km s^{-1}, in the local standard of rest), the integrated intensity W (in K km s^{-1}), the peak temperature $T_{\rm peak}$ (in K), and the full width at half maximum Δv (in km s^{-1}). In case of non-detections, upper limits are given at the 1σ level. Uncertainties are dominated by calibration (~20%). Integrated intensities and peak temperatures are given on the main-beam temperature scale.

Table 4. Results from the Gaussian fits of the emission lines of H^{13}CO$^+$ and DCO$^+$ towards the nine positions where H^{13}CO$^+$ is detected.

Pos.	H^{13}CO$^+$(1–0)				DCO$^+$(2–1)			
	v_0	W	$T_{\rm peak}$	Δv	v_0	W	$T_{\rm peak}$	Δv
N1	20.3	0.44	0.17	2.5	–	<0.01	<0.01	3.0
N5	20.6	0.53	0.27	1.8	20.4	0.15	0.06	2.3
N6	20.8	1.11	0.53	2.0	20.5	0.16	0.12	1.2
N2	21.0	4.39	1.38	3.0	21.0	0.41	0.12	3.1
N7	22.3	0.23	0.16	1.3	–	<0.01	<0.01	3.0
N3	16.2	0.49	0.20	2.3	–	<0.02	<0.02	3.0
N4	20.2	0.47	0.14	3.0	–	<0.01	<0.01	3.0
SE1	17.0	0.15	0.23	0.6	17.0	0.13	0.16	0.76
SW4	9.3	0.25	0.05	5.2	–	<0.02	<0.02	3.0

Notes. The fit parameters are the same as Table 3. In case of non-detections, upper limits are given at the 1σ level. Uncertainties are dominated by calibration (~20%). Integrated intensities and peak temperatures are given on the main-beam temperature scale.

as

$$x_{\rm e} = \left(\frac{k_{\rm f}\, x({\rm HD})}{3R_{\rm D}} - \delta - \frac{k_{\rm f}}{2}{\rm e}^{-\Delta E/T} \right) \frac{1}{k_e}, \tag{4}$$

$$\zeta / n_{\rm H} = \frac{\beta'}{k_{\rm H}} \left(2\beta x_{\rm e} + \delta\right) R_{\rm H} x_{\rm e}, \tag{5}$$

where $\Delta E = 220$ K, such that at sufficiently low temperatures the last term in brackets in Eq. (4) becomes negligible. Equation (4) demonstrates that $x_{\rm e}$ only depends on the abundance ratio $R_{\rm D}$ and the gas kinetic temperature, as originally proposed by G77.

Figure 3 shows $x_{\rm e}$ as a function of $R_{\rm D}$, as predicted from Eq. (4), assuming a kinetic temperature of 20 K (blue dashed line). We note two regimes in the dependence of $x_{\rm e}$ on $R_{\rm D}$. For low $R_{\rm D}$ values ($\lesssim 10^{-2}$), $x_{\rm e}$ is proportional to $1/R_{\rm D}$ with a factor that depends on the chemical reaction rates and the HD abundance. For higher $R_{\rm D}$ values, $x_{\rm e}$ drops sharply. In this regime, $x_{\rm e}$ varies by more than two orders of magnitude when $R_{\rm D}$ is changed by only a factor of two. The slope becomes steeper with increasing temperature, due to the predominance of the reverse reaction of the formation of H$_2$D$^+$ (Table A.1). This indicates that accurate values of $x_{\rm e}$ in dark clouds through this method require extremely accurate values of $R_{\rm D}$. It also suggests that in regions with higher ionisation, where $x_{\rm e}$ is proportional to $1/R_{\rm D}$, DCO$^+$ will be difficult to detect.

5.2. Numerical models

To assess the validity of the analytical approach of G77 and C98, we have solved the OSU 2009[2] chemical network for the abundances of DCO$^+$, HCO$^+$, and e$^-$, using the `astrochem`[3] code. The time evolution of the gas-phase abundances was followed until a steady state was reached, after typically 10 Myr. The underlying hypothesis is that the cloud was already molecular when it was irradiated by the CRs emitted at the SN explosion. The chemical changes caused by the sudden CR irradiation are dominated by ion-neutral reactions, whose timescale is only ~10^2 yr, much shorter than the W28 SNR age (~10^4 yr; see Introduction). Details of the models are given in Appendix A. In

---

[2] http://www.physics.ohio-state.edu/~eric/research.html

[3] http://smaret.github.io/astrochem/

Table 5. Physical conditions and cosmic ray ionisation rates.

Pos.	Δv [km s^{-1}]	n_{H_2} [10^3 cm^{-3}]	T_{kin} [K]	$N(C^{18}O)$ [10^{15} cm^{-2}]	A_V [mag]	$N(H^{13}CO^+)$ [10^{12} cm^{-2}]	$N(DCO^+)$ [10^{12} cm^{-2}]	$R_D = \frac{[DCO^+]}{[HCO^+]}$	ζ [10^{-17} s^{-1}]
N1	3.5	0.6 {0.2–1}	15 ± 5	4 {2–6}	21 {11–32}	0.8–1.3	<0.22	<0.005	>13
N5	3.0	4 {2–5}	10 ± 2	3 {2–8}	16 {11–32}	1.1–1.4	0.89–1.30	0.014–0.020	130–330
N6	3.0	4 {2–6}	13 ± 3	6 {4–20}	32 {21–105}	1.8–2.5	0.79–1.30	0.008–0.012	130–400
N2†	5.0	> 2	16 ± 2	20 {15–30}	105 {79–158}	5.6–8.9	1.10–2.00	0.003–0.006	–
N7	2.5	2 {2–5}	10 ± 2	4 {3–10}	21 {16–53}	0.6–0.9	<0.25	<0.007	>130
N8	3.5	1 {0.6–2}	8 ± 1	3 {2–4}	16 {11–21}	<0.2	<0.35	–	–
N3	3.5	6 {4–10}	8 ± 1	6 {5–7}	32 {26–37}	1.0–1.4	<0.35	<0.006	>260
N4	3.0	2 {0.6–4}	12 ± 3	2 {2–3}	11 {5–16}	1.0–1.4	<0.35	<0.006	>40
SE1	4.0	2 {1–5}	19 ± 5	6 {5–20}	32 {26–105}	0.4–0.56	0.79–1.0	0.032–0.05	0.2–20
SE2	3.0	4 {2–10}	8 ± 2	0.9 {0.4–20}	5 {2–105}	<0.2	<0.28	–	–
SW2	1.5	2 {1–4}	20 ± 4	4 {3–10}	21 {16–53}	<0.1	<0.22	–	–
SW4†	1.5	6 {4–10}	16 ± 2	1.5 {1–3}	5 {5–16}	0.5–0.8	<0.25	<0.009	–

Notes. n_{H_2} is the molecular hydrogen density (cm^{-3}), T_{kin} the gas kinetic temperature, $N(C^{18}O)$ the total column density of $C^{18}O$. A_V is the visual extinction assuming $[C^{18}O] = A_V \times 1.9\ 10^{14}$ cm^{-2} (Frerking et al. 1982; Bolatto et al. 2013). We assumed isotopic ratio values $^{18}O/^{16}O = 500$ and $^{13}C/^{12}C = 50$ (see text). Values in brackets indicate the range of values satisfying $\chi^2_\nu < 1$. Uncertainties on n_{H_2} and T_{kin} are at the 70% confidence level, and are propagated in the abundance ratios and upper limits. Lower limits of ζ were deduced from chemical modelling (see Sect. 6). $^{(\dagger)}$ N2 and SW4 are probably ionised by a source other than CRs (see text).

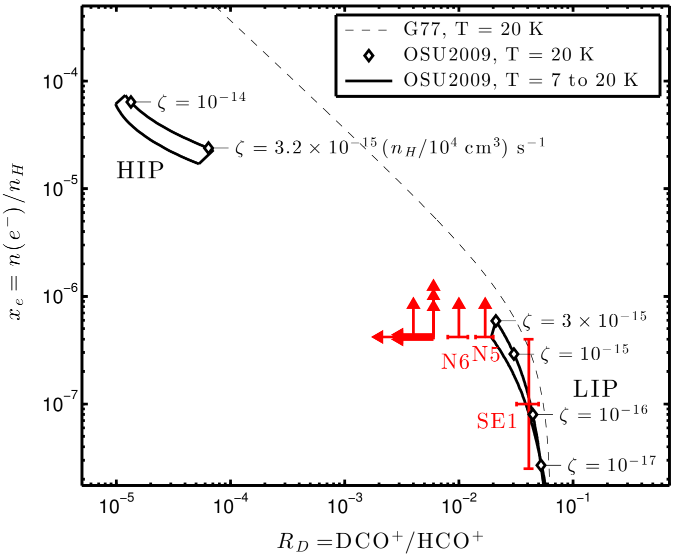

Fig. 3. $x_e = n(e^-)/n_H$ as a function of R_D. Values from the analytical method (G77) in Sect. 5.1 are given at $T = 20$ K (dashed line). Results from our calculation (see Sect. 5.2) for temperatures between 7 K and 20 K are contained within the solid lines. ζ values are given for $n_H = 10^4$ cm^{-3}, although the model only depends on the ζ/n_H ratio (see text). R_D values or upper limits as derived from observations are indicated by the red symbols; see Sect. 6.1.

one calculation, the gas is shielded by 20 mag of visual extinction, such that UV photons can safely be ignored.

As anticipated from Eq. (2), we found that the abundances mostly depend on the ζ/n_H ratio, rather than on ζ and n_H separately. This behaviour is similar to photon-dominated regions in which a good parameter is the ratio of the UV radiation field to the total density. For each temperature from 7 K to 20 K, a series of calculations with ζ/n_H increasing from 10^{-22} cm^3 s^{-1} to 10^{-18} cm^3 s^{-1} were performed, and the steady-state values of x_e and R_D were recorded.

In these calculations, we assumed a standard CO abundance of $\sim 7.3 \times 10^{-5}$ in the cloud. Indeed, since the density of the studied clouds is relatively low (Table 5), we do not expect CO depletion to play an important role here. However, in general, one has to take into account this uncertainty. In addition, our calculations do not consider separately the H2 ortho-to-para ratio, which is known to affect the DCO^+/HCO^+ abundance ratio when it is larger than about 0.1 (e.g. Pagani et al. 2011). Our choice here is based on the published observations that indicate that the H2 ortho-to-para ratio is smaller than about 0.01 in molecular clouds (e.g Troscompt et al. 2009; Dislaire et al. 2012).

5.3. A new view of the DCO^+/HCO^+ method

The results of the numerical models are shown in Fig. 3. As expected, the ionisation fraction x_e increases with ζ/n_H, with R_D decreasing in the process. There is good overall agreement between the analytical and numerical predictions for $R_D \gtrsim 2 \times 10^{-2}$. In this high-$R_D$ regime, the small differences between analytical and numerical values are due to the abundances of HD and CO not being constant as originally assumed by G77 and C98. Instead, as ζ/n_H and x_e increase, atomic deuterium becomes more abundant. Similarly, the CO abundance decreases because of the dissociating action of CRs. When R_D decreases and reaches $\approx 2 \times 10^{-2}$, the abundances predicted by the numerical model change dramatically to a regime characterised by large values of x_e and low values of R_D. This jump corresponds to the well-known transition from the so-called low ionisation phase (LIP) to the high ionisation phase (HIP) (Pineau des Forêts et al. 1992; Le Bourlot et al. 1993), and is due to the sensitivity of interstellar chemical networks to ionisation. The LIP is associated with R_D larger than 10^{-2}, whilst the HIP is characterised by $R_D \lesssim 10^{-4}$. In our calculations, the LIP-HIP transition occurs at $\zeta/n_H \sim 3 \times 10^{-19}$ cm^3 s^{-1}, and we note that this value depends only slightly on the temperature, although it is known to depend on other parameters such as the gas-phase abundance of metals (Wakelam et al. 2006a). A detailed analysis of the LIP-HIP transition is, however, not the aim of this study. Here, it is rather the existence of this instability which is of interest since it produces a sharp difference between the analytical and the numerical predictions from the ionisation point of view. Application to a practical case shows that what changes is not the jump itself but (slightly) the ζ at which it occurs (see e.g. Ceccarelli et al. 2011). In the former, the variations of x_e and R_D are continuous and, as already mentioned, predict $x_e \sim 1/R_D$ in the low-R_D regime. This scaling is, however, not observed in the numerical models, and is replaced by a discontinuous variation of both x_e and R_D. The present calculations show that the LIP is characterised by $R_D = 10^{-2} - 10^{-1}$, $x_e \lesssim 5 \times 10^{-7}$, and the HIP is characterised by $R_D \approx$ few 10^{-5} and $x_e \approx$ few 10^{-5}.

As shown in Fig. 4, the low values of R_D in the HIP are due to a very low abundance of DCO$^+$, whilst the abundance of HCO$^+$ decreases by a smaller amount. This has important consequences when using the DCO$^+$/HCO$^+$ method to derive the ionisation fraction and CR ionisation rate. First, it must be recognised that this method may provide a value of x_e only for LIP-dominated gas conditions. In other words, where DCO$^+$ is detected, the line of sight is dominated by low-x_e gas. For lines of sight dominated by HIP gas, the abundance of DCO$^+$ is expected to be well below detectable thresholds, such that only upper limits on R_D can be derived. Yet, an upper limit on R_D still provides essential information, since it is associated with a lower limit on x_e, which in turn corresponds to a lower limit of ζ/n_H. On the contrary, for LIP-dominated lines of sight, the value of x_e and ζ/n_H may be derived directly from R_D, although x_e is extremely sensitive to uncertainties on R_D in this regime.

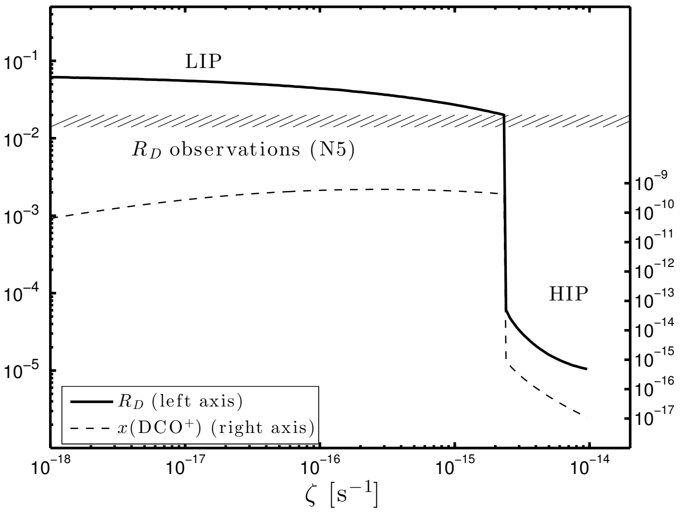

Fig. 4. R_D = DCO$^+$/HCO$^+$ (thick line, left axis) and x(DCO$^+$) = n(DCO$^+$)/n_H (dashed line, right axis) as a function of ζ, for T = 10 K and n_H = 8 10^3 cm^{-3}, i.e. the physical conditions characterising position N5. The HIP and LIP are marked. The hatched area shows the range of observed R_D at that position.

6. The CR ionisation rate in W28

6.1. Constant density and temperature cloud analysis

A new view of the DCO$^+$/HCO$^+$ method thus emerges, which stresses its strengths and limitations. The method allows the determination of the ionisation fraction x_e and the ζ/n_H ratio for gas in the LIP, and provides lower limits of x_e and ζ/n_H for gas in the HIP. In the following, we apply this method to the sample of observed points, using the constraints on the gas temperature and density, and the R_D value in each point (Table 5). We emphasise that the model calculations summarised in Fig. 3 assumed constant density and gas temperature. In the next section, we will discuss how the DCO$^+$/HCO$^+$ method can be used to constrain x_e and ζ/n_H, taking into account the thermal structure of the cloud.

Of the 16 lines of sight initially observed in CO, 12 were also detected in H^{13}CO$^+$, of which 4 led to R_D determinations and 5 to upper limits (Table 5). The four points with measured R_D are N5, N6, SE1, and N2. In the following analysis, we exclude N2 as it coincides with a protostar, which means that a more accurate analysis taking into account the structure of the protostar and the inner ionisation is necessary. The values obtained towards N5, N6, and SE1 are shown in Fig. 3.

The SE1 point lies on the LIP branch, enabling a determination of the ionisation fraction $x_e = (0.15{-}4) \times 10^{-7}$ and of the CR ionisation rate $\zeta = (0.2{-}20) \times 10^{-17}$ s^{-1}. On the contrary, the values of R_D towards N5 and N6 lie in the gap between the LIP and HIP branches, even when considering a kinetic temperature as high as 20 K, a temperature which is larger than the values derived for these positions. In these cases, adopting $n_H = 2n(H_2) \gtrsim 4 \times 10^3$ cm^{-3} (Table 5), Fig. 3 provides the following lower limits: $x_e \gtrsim 4 \times 10^{-7}$ and $\zeta \gtrsim 1.3 \times 10^{-15}$ s^{-1} for both points. We note that the detection of DCO$^+$ indicates that the line of sight includes a non-negligible amount of LIP, which can serve to further constrain the value of ζ/n_H. This can be seen in Fig. 4, which shows R_D and DCO$^+$ as a function of ζ, for a density and temperature appropriate to position N5 (Table 5). The measured R_D intersects the model predictions at the edge of the LIP/HIP jump, at $\zeta \approx 2.5 \times 10^{-15}$ s^{-1}. More importantly, the figure shows that the gas is neither entirely in the LIP nor HIP state as expected from the detection of DCO$^+$. A similar plot has also been obtained for N6, leading to the same conclusion.

Finally, the non-detection of DCO$^+$ in the other lines of sight leads to upper limits on R_D that are well outside the LIP branch. At these positions, the gas is very likely to be almost entirely in the HIP state, which means that $\zeta/n_H \gtrsim 3 \times 10^{-19}$ cm^3 s^{-1}. An exception is the point SW4, where an extremely energetic outflow has been detected (Harvey & Forveille 1988), and where the HCO$^+$ is therefore likely contaminated by the outflowing material.

6.2. Constant density cloud analysis

As discussed in the previous section, the points N5 and N6 are likely composed of a mixture of gas in the LIP and HIP state. This is similar to the situation observed in W51C-E (CC2011). In that case, ζ was estimated with a model that takes into account the thermal and chemical structure of a constant density cloud, where a fraction (the deepest) is in the LIP and the rest in the HIP (Fig. 2 in CC2011). Here, we do a similar analysis, using basic arguments instead of a sophisticated model, and we show that it leads to similar results, namely the determination of ζ to within a factor of 2. The advantage of this analysis is that it shows in a straightforward way the uncertainty due to the model parameters.

The crucial point is understanding what causes the gas to flip from the HIP to the LIP state going deeper into the cloud. Since the column density is too low to appreciably reduce ζ across the cloud, the only macroscopic quantity that changes is the gas temperature. Specifically, the temperature increases by a few K (in the UV-shielded region) going deeper into the cloud because the CO line opacity increases and, consequently, the line cooling becomes less efficient. The effect is larger for larger ζ as the heating, dominated by the CR ionisation, is less compensated by the line cooling.

It is instructive to see how the R_D ratio changes as a function of the gas temperature for different ζ. This is shown

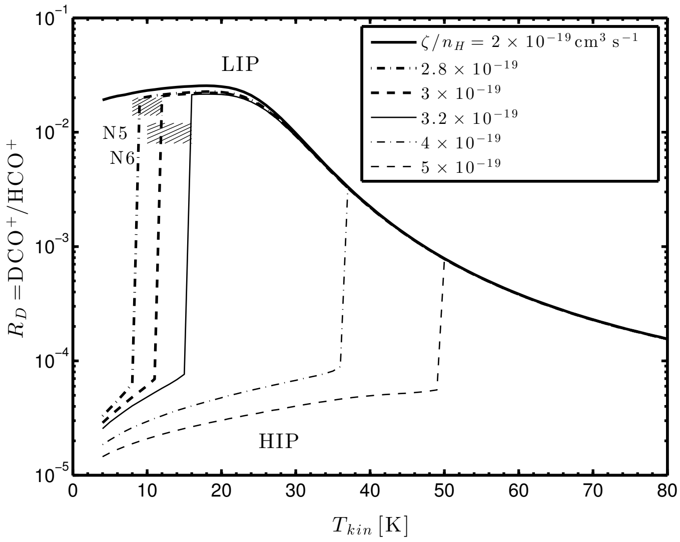

Fig. 5. R_D as a function of the gas temperature T_{kin} for different values of ζ/n_H: from 2 to 5 $\times10^{-19}$ s^{-1}, as marked. Note that for $\zeta/n_H \le 2\times10^{-19}$ cm^3 s^{-1} (thick solid line), the cloud is always in the LIP, regardless of the temperature. For $\zeta/n_H > 5\times10^{-19}$ cm^3 s^{-1} (thin dashed curve), the cloud is always in the HIP for temperatures ≤50 K. Hatched areas show observations of N5 and N6. We assume A_V = 20 mag.

in Fig. 5, for a range of temperatures (5–80 K) and ζ/n_H (2–5 $\times10^{-19}$ cm^3 s^{-1}, appropriate to the N5 and N6 points). In these calculations, we consider a cell of gas of constant density, shielded by 20 mag of visual extinctions as before, such that the ionisation is driven by the CRs. The figure shows important features:

i) for $\zeta/n_H \lesssim 2\times10^{-19}$ cm^3 s^{-1}, the cloud is always in the LIP, regardless of the temperature;
ii) for $\zeta/n_H \gtrsim 5\times10^{-19}$ cm^3 s^{-1}, the cloud is always in the HIP for temperatures lower than 50 K;
iii) for intermediate values of ζ/n_H, the gas flips from HIP to LIP with increasing temperature, and the larger ζ is, the larger the temperature where the flip occurs.

These calculations show that there is a range of ionisation rates in which the gas is extremely sensitive to temperature variations. A tiny increase in temperature is sufficient to make the gas flip from the HIP to the LIP. In particular, for position N5, there is such a combination of values of R_D, T_{kin}, and ζ/n_H (see Fig. 5) that places it precisely in a region where the transition from HIP to LIP can be triggered by an increase in T_{kin} as small as a few K. A similar argument applies to N6. In addition, in regions exposed to an enhanced CR ionisation rate, the outer part characterised by large ionisation fractions will be extended farther into the cloud, thus decreasing the relative amount of LIP with respect to the HIP.

Based on the derived kinetic temperatures and values of R_D (Table 5) and using Fig. 5, we can further constrain the value of ζ/n_H. Towards N5, the temperature was found to be 10 ± 2 K, while R_D = 0.014–0.020. When inserted into Fig. 5, these delineate a region that is compatible with a narrow range of $\zeta/n_H = (2.8\text{–}3.0)\times10^{-19}$ cm^3 s^{-1}. For the N6 line of sight, we find similar values, $(2.9\text{–}3.2)\times10^{-19}$ cm^3 s^{-1}. The densities derived from the analysis and their uncertainties then lead to cosmic ray ionisation rates of $(1.3\text{–}3.3)\times10^{-15}$ s^{-1} and $(1.3\text{–}4.0)\times10^{-15}$ s^{-1} for N5 and N6 respectively. Results are summarised in Table 5 and are included in Figs. 6 and 7.

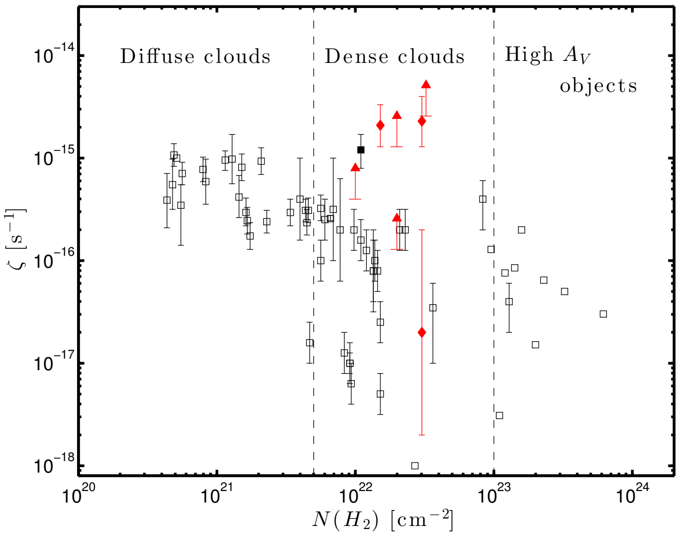

Fig. 6. Compilation of measured ζ in different objects (open squares), as reported by Padovani & Galli (2013). The black filled square denotes W51 (Ceccarelli et al. 2011). Red points and lower limits report the values derived in this work. The dashed lines show the range of column densities $(0.5-10)\times10^{22}$ cm^{-2}, typical of dense molecular clouds, corresponding to visual extinctions of 5 and 100 mag, respectively. On the left lie the diffuse clouds and on the right highly obscured environments such as infrared dark clouds or protoplanetary discs.

7. Discussion

Table 5 lists the observed positions and the corresponding CR ionisation rates derived using the method described in the previous section. With the exception of the SE1 point, in all other points ζ is at least 10 to 260 times larger than the standard value $(1\times10^{-17}$ s$^{-1})$ in Galactic clouds. This is shown in Fig. 6, where we present a compilation of the ζ measured in various objects (from Padovani & Galli 2013), plus our measurements. In the range of column densities $(0.5-10)\times10^{22}$ cm^{-2}, typical of dense molecular clouds, the points in which we derived ζ are those with the highest values, together with the CC2011 point (filled square). The first conclusion of this work is, therefore, that clouds next to SNR are indeed irradiated by an enhanced flux of CRs of relatively low energy (see below for a more quantitative statement on the CR particle energies).

The dependence of ζ on the projected distance from the SNR radio boundary (assuming a W28 distance of 2 kpc) is shown in Fig. 7. Remarkably, the point farthest (~10 pc) from the SNR edge is the one with the lowest ζ. Actually, it is the only point where the gas is predominantly in the LIP state. All other points, at distances ≲3 pc, have at least a fraction of the gas in the HIP, namely they have a larger x_e and ζ. Of course, this analysis does not take into account the 3D structure of the SNR complex. Yet, this can still provide us with constraints on the propagation properties of CRs, as will be discussed in the following.

Valuable additional information is provided by observations in the γ-ray domain. Both the northern and southern clouds coincide with sources of TeV emission, as seen by HESS. This means that the clouds are illuminated by very high energy (≳10 TeV) CRs, which already escaped the SNR expanding shell and travelled the ≳10 pc (or more, if projection effects play a role) to the southern cloud. Conversely, the low CR ionisation rate measured in SE1 tells us that the ionising lower energy CRs remain confined closer to the SNR. In the same vein, GeV emission has been detected towards the northern region but only towards a

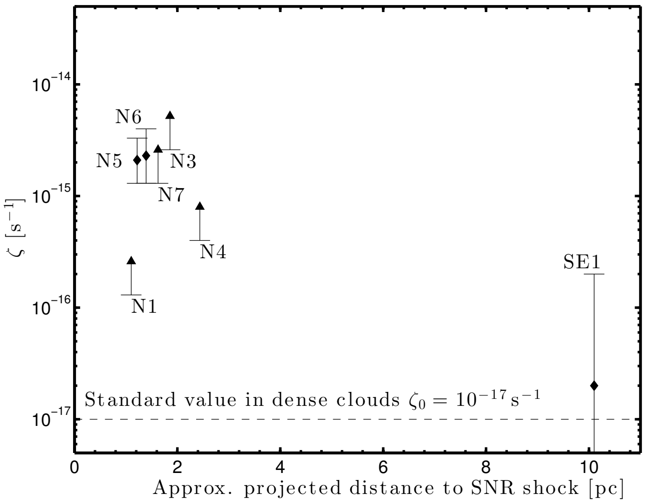

Fig. 7. CR ionisation rate ζ as a function of the approximate projected distance from the SNR radio boundary (blue circle in Fig. 1), assuming a W28 distance of 2 pkc. We note that the ζ error bars are dominated by the uncertainties on the H_2 densities (see text).

part of the southern one. This difference between the GeV and TeV γ-ray morphology has been interpreted as a projection effect: the portion of the southern region that exhibits a lack of GeV emission is probably located at a distance from the shock significantly larger than the projected one, >10 pc, and thus can be reached by $\gtrsim$TeV CRs but not by $\gtrsim$GeV ones (Gabici et al. 2010; Li & Chen 2010; Nava & Gabici 2013). Remarkably, the SE1 point is located in the region where the lack of GeV emission is observed.

The picture that emerges is that of a stratified structure with CRs of larger and larger energies occupying larger and larger volumes ahead of the shock. Within this framework, it is possible to estimate the CR diffusion coefficient in the region. This can be done by recalling that in a given time t, CRs diffuse over a distance $R \sim \sqrt{D \times t}$, where D is the energy dependent diffusion coefficient. For the situation under examination, one gets

$$D_{(\approx 10\ \mathrm{GeV})} \gtrsim 3 \times 10^{27} \left(\frac{R}{10\ \mathrm{pc}}\right)^2 \left(\frac{t}{10^4\ \mathrm{yr}}\right)^{-1} \mathrm{cm^2/s}, \quad (6)$$

where $D_{(\approx 10\ \mathrm{GeV})}$ is the diffusion coefficient of $\approx$10 GeV CRs, which are those responsible for the $\approx$GeV γ-ray emission, and t is the time elapsed since the escape of CRs from the SNR. The value obtained in Eq. (6) is in substantial agreement with more accurate studies (see e.g. Nava & Gabici 2013).

The diffusion coefficient obtained in Eq. (6) can then be rescaled to lower energies, according to $D \propto p^s \beta$, where p is the particle momentum, $\beta = v/c$ its velocity in units of the speed of light, and s depends on the spectrum of the ambient magnetic turbulence. The typical value of s in the interstellar medium is poorly constrained to be in the range 0.3 to 0.7 (Castellina & Donato 2011). In the following, we adopt $s = 0.5$. To estimate the diffusion length of low energy CRs, one has to keep in mind that, while CRs with energies above $\approx$GeV are virtually free from energy losses (the energy loss time for proton–proton interactions in a density $n_H \approx 10^3\ \mathrm{cm^{-3}}$ is comparable to the age of the SNR), lower energy CRs suffer severe ionisation losses over a short timescale (Berezinskii et al. 1990):

$$\tau_{\mathrm{ion}} \approx 14 \left(\frac{n_H}{10^3\ \mathrm{cm^{-3}}}\right)^{-1} \left(\frac{E}{\mathrm{MeV}}\right)^{3/2} \mathrm{yr}. \quad (7)$$

This approximate expression is sufficiently accurate in the range of energies spanning 1−100 MeV. The diffusion length of low energy CRs can then be estimated by equating the diffusion time $\tau_d \sim R_d^2/D$ to the energy loss time τ_{ion}, which gives $R_d \approx 0.02$, 0.3, and 3 pc for CRs of energy 1, 10, and 100 MeV, respectively. This implies that only CRs with energies $\gtrsim$100 MeV can escape the shock and spread over a distance of 3 pc or more, and thus these are the CRs that play a major role in ionising the gas. Whether the ionisation of the gas is due directly to these CRs or to the products of their interaction with the gas (namely slowed down lower energy CRs) remains an open question. It is remarkable that the particle energies of ionising CRs ($\approx$0.1−1 GeV) also make them capable of producing sub–GeV γ rays, given that the kinetic energy threshold for π^0 production is $\approx$280 MeV.

Of course, the order of magnitude estimates discussed in this section cannot substitute in any way more sophisticated calculations, yet they clearly indicate an intriguing possible link between low and high energy observations of SNR environments. In fact, in the scenario described above, the very same CRs are responsible for both ionisation of the gas and production of low energy γ rays. If confirmed, such a link would constitute robust evidence for the presence of accelerated protons in the environment of the SNR W28, a thing that would bring further support to the idea that SNR are the sources of Galactic CRs. Additional theoretical investigations are needed in order to examine and possibly rule out alternative scenarios which may include other contributions to the ionisation rate (e.g. CR electrons, X-ray photons) or different means of propagation (e.g. straight-line or advective propagation of low energy CRs).

8. Conclusion

In this work, we presented new observations to measure the CR ionisation rate in molecular clouds close to supernova remnants (SNR). In doing so, the DCO^+/HCO^+ method was also revisited. The major results may be summarised as follows.

1) We observed the two lowest rotational transitions of ^{13}CO and $C^{18}O$ towards 16 positions in the northern and southern clouds close to the SNR W28. The four lines were detected in emission towards 12 of these positions, where we could, therefore, derive the physical conditions using a non-LTE LVG analysis. With the exception of one position (N2) coinciding with a protostar in the region, we derived H_2 densities and temperatures typical of molecular clouds, namely $n_{H_2} = (0.2–10) \times 10^3\ \mathrm{cm^{-3}}$ and $T = 6–24$ K. We searched for $H^{13}CO^+$ and DCO^+ line emission in the above 12 positions, and detected it in 9 and 4, respectively. From these data, we could derive the $R_D = DCO^+/HCO^+$ in 4 positions, one of which coincides with the protostar, and give upper limits for the remaining 5 positions.
2) We reinvestigated the DCO^+/HCO^+ method used to derive the ionisation fraction $x_e = n(e^-)/n_H$ and the relevant CR ionisation rate ζ causing it. To this aim, we compared the steady-state abundances of HCO^+, DCO^+, and e^- as predicted by the analytical model of G77, to numerical calculations, assuming constant density and gas temperature. The numerical model leads to two well separated regimes of ionisation, also known as the low- and high-ionisation phases (LIP and HIP; Pineau des Forêts et al. 1992). In the context of this work, these two phases lead to two separated regimes in terms of ζ and R_D values:
   i) for $\zeta/n_H \lesssim 3 \times 10^{-19}\ \mathrm{cm^3\ s^{-1}}$, the gas is in the LIP, where $R_D \gtrsim 2 \times 10^{-2}$ and $x_e \lesssim 6 \times 10^{-7}$. In this regime, the dependence of x_e on R_D is very steep leading to large uncertainties on x_e;

   ii) for $\zeta/n_{\rm H} \gtrsim 3{\times}10^{-19}$ cm^3 s^{-1}, the gas is in the HIP, where $R_{\rm D} \lesssim 10^{-4}$ and $x_{\rm e} \gtrsim 2 \times 10^{-5}$. In this regime, DCO$^+$ is not detectable and the numerical prediction for $x_{\rm e}$ differs significantly from the analytical one.

   Therefore, the DCO$^+$/HCO$^+$ abundance ratio can provide a measure of $x_{\rm e}$ and ζ in the LIP, and only lower limits if the gas is in the HIP.

3) We found only one position, SE1, in the LIP, where $R_{\rm D} = 0.032{-}0.05$, $x_{\rm e} = (0.3{-}4) \times 10^{-7}$ and $\zeta = (0.2{-}20) \times 10^{-17}$ s^{-1}. Two positions, N5 and N6, lie in the gap between the LIP and HIP, namely the gas is neither entirely in the LIP nor in the HIP, although it certainly contains a fraction of gas in the LIP, where DCO$^+$ is detectable (and detected). The jump from the HIP to the LIP when penetrating farther into the cloud is associated with an increase in the temperature, and we showed that model calculations at several temperatures further constrain the value of ζ. The uncertainty in ζ towards these positions is dominated by the uncertainty in the H$_2$ density and the derived values are ζ = (1.3–3.3) and (1.3–4.0) $\times 10^{-15}$ s^{-1} for N5 and N6, respectively. Towards the remaining 5 positions with upper limits on $R_{\rm D}$, the derived ζ values are at least 10 to 260 times higher than the standard value of 1×10^{-17} s^{-1}.
4) The points of the northern cloud have the largest CR ionisation rates measured so far in the Galaxy. The point towards the southern cloud is, on the contrary, consistent with the average galactic CR ionisation rate of molecular clouds not interacting with a SNR. Since the northern and southern clouds have projected distances from the SNR shock of $\leq$3 and $\sim$10 pc, respectively, this can be explained by the fact that the low energy ionising CRs have not reached the southern cloud yet. On the other hand, the observations show that both the northern and southern clouds coincide with TeV emission sources, suggesting that high $\gtrsim$10 TeV CRs have reached both. This is also consistent with γ-ray emission sources inciding with the northern cloud but only partially with the southern cloud, indicating that the former is irradiated by $\approx$0.1–1 GeV CRs, while only the nearest portion of the southern cloud is so affected.
5) The emerging picture is that of energy-dependent diffusion properties of hadronic CRs. The high-energy CRs responsible for TeV γ-ray emission through π^0-decay can diffuse far ahead of the SNR shock, while the low-energy CRs (0.1–1 GeV), responsible for both the low γ-ray emission and the ionisation of the gas, remain closer to the SNR shock. The present work thus gives first observational evidence to the theoretical predictions that hadrons of energy 0.1–1 GeV contribute most to the ionisation in dense gas (Padovani et al. 2009).

Acknowledgements. We warmly thank Marco Padovani for providing us with his compilation and for useful discussions. This work has been financially supported by the Programme National Hautes Énergies (PNHE). Based on observations carried out with the IRAM 30 m telescope. IRAM is supported by INSU/CNRS (France), MPG (Germany) and IGN (Spain). S. Gabici acknowledges the financial support of the UnivEarthS Labex Program at Sorbonne Paris Cité (ANR-10-LABX-0023 and ANR-11-IDEX-0005-02).

Appendix A: Chemical models

We solved the OSU 2009[4] chemical network using the `astrochem`[5] code.

Table A.1. Reduced chemical network for the analytical derivation of DCO$^+$/HCO$^+$.

	Reaction			Reaction rate [cm^3 s^{-1}]
No. 1	CR + H$_2$	$\xrightarrow{\zeta}$	H$_2^+$ + e$^-$	ζ [s^{-1}]
No. 2	H$_2^+$+ H$_2$	$\xrightarrow{k_{\rm H_2^+}}$	H$_3^+$ + H	$k_{\rm H_2^+}$ = 2.1 10^{-9}
No. 3	H$_3^+$ + CO	$\xrightarrow{k_{\rm H}}$	HCO$^+$ + H$_2$	$k_{\rm H}$ = 1.61 10^{-9}
No. 4	HCO$^+$ + e$^-$	$\xrightarrow{\beta'}$	CO + H	$\beta' = 2.8\ 10^{-7}\left(\frac{T}{300}\right)^{-0.69}$
No. 5	H$_3^+$ + e$^-$	$\xrightarrow{\beta}$	H + H + H	$\beta = 4.36\ 10^{-8}\left(\frac{T}{300}\right)^{-0.52}$
			H$_2$+ H	$+2.34\ 10^{-8}\left(\frac{T}{300}\right)^{-0.52}$
No. 6	H + H	$\xrightarrow{k'}$	H$_2$	$k' = 4.95\ 10^{-17}\left(\frac{T}{300}\right)^{0.50}$
No. 7	H$_3^+$ + HD	$\underset{k_{\rm f}^{-1}}{\overset{k_{\rm f}}{\rightleftharpoons}}$	H$_2$D$^+$ + H$_2$	$k_{\rm f}$ = 1.7 10^{-9}
				$k_{\rm f}^{-1} = k_{\rm f}\ {\rm e}^{-220/T}$
No. 8	H$_2$D$^+$ + CO	$\xrightarrow{k_{\rm D}}$	DCO$^+$ + H$_2$	$k_{\rm D}$ = 5.37 10^{-10}
No. 9	DCO$^+$ + e$^-$	$\xrightarrow{\beta'}$	CO + D	$\beta' = 2.8\ 10^{-7}\left(\frac{T}{300}\right)^{-0.69}$
No. 10	H$_2$D$^+$ + e$^-$	$\xrightarrow{k_{\rm e}}$	H + H + D	$k_{\rm e} = 4.38\ 10^{-8}\left(\frac{T}{300}\right)^{-0.50}$
			H$_2$ + D	$+1.20\ 10^{-8}\left(\frac{T}{300}\right)^{-0.50}$
			HD + H	$+4.20\ 10^{-9}\left(\frac{T}{300}\right)^{-0.50}$
No. 11	H + D	$\xrightarrow{k''}$	HD	$k'' = \sqrt{2}k'$
No. 12	H$_2$D$^+$ + CO	$\xrightarrow{k'_{\rm D}}$	HCO$^+$ + H$_2$	$k'_{\rm D}$ = 1.1 10^{-9}
No. 13	H$_3^+$ + D	$\underset{k_{\rm f}'^{-1}}{\overset{k'_{\rm f}}{\rightleftharpoons}}$	H$_2$D$^+$ + H	$k'_{\rm f}$ = 1.0 10^{-9}
				$k_{\rm f}'^{-1} = k'_{\rm f}\ {\rm e}^{-632/T}$
No. 14	CO$^+$ + HD	$\xrightarrow{k_{\rm CO^+}}$	DCO$^+$ + H	$k_{\rm CO^+}$ = 7.5 10^{-10}

Notes. The reduced network corresponds to the original description by Guélin et al. (1977) and Caselli et al. (1998). The rates of reactions 1–6 are contained in the original OSU 2009 network. We appended deuterated reactions 7–14 for which chemical rates are taken from Roberts & Millar (2000). Reaction 14 is only dominant in the HIP and is not involved in the analytical determination of DCO$^+$/HCO$^+$.

Table A.2. Range of initial physical parameters used in the `astrochem` code.

Parameter	Range
A_V	20 mag
$n_{\rm H}$	10^3 to 10^4 cm^{-3}
$T_{\rm kin}$	5 to 80 K
$T_{\rm d}$	20 K
ζ	10^{-18} to 10^{-14} s^{-1}

`astrochem` is a numerical code that computes the time-dependent chemical abundances in a cell of gas shielded by a given visual extinction A_V and with given physical parameters: the total H density $n_{\rm H}$, the gas kinetic temperature $T_{\rm kin}$, and the dust temperature $T_{\rm d}$. It also takes as an input the initial chemical abundances and the CR ionisation rate. We followed the abundance until a steady state was reached, for a grid of models covering a large range of physical conditions ($n_{\rm H}, T_{\rm kin}$) and CR ionisation rates ζ, at a given A_V = 20 mag, far inside the cloud, where the gas is shielded from the UV radiation field and the ionisation is dominated by CRs. The results only depend on the $\zeta/n_{\rm H}$ ratio (see Sect. 5.2). The role of the dust in `astrochem` is limited to the absorption and desorption processes, namely no grain surface chemistry is considered. As discussed in Sect. 5.2, neither process is relevant to the present discussion. Initial conditions were taken from the low-metal abundances as in Graedel et al. (1982) and Wakelam et al. (2006b) using an updated He/H

---

[4] http://www.physics.ohio-state.edu/~eric/research.html

[5] http://smaret.github.io/astrochem/

relative abundance of 0.09 (Asplund et al. 2009). In Table A.2, we list the range of physical parameters used in this study.

The OSU network contains 6046 reactions involving 468 species. We appended 12 reactions labeled 7−14 in Table A.1 involving the deuterated species: D, HD, H_2D^+, and DCO^+. Chemical rates are taken from Roberts & Millar (2000).

References

Abdo, A. A., Ackermann, M., Ajello, M., et al. 2010, ApJ, 718, 348
Abdo, A. A., Ackermann, M., Ajello, M., et al. 2011, ApJ, 734, 28
Ackermann, M., Ajello, M., Allafort, A., et al. 2013, Science, 339, 807
Aharonian, F. A. 2013, Astropart. Phys., 43, 71
Aharonian, F., Akhperjanian, A. G., Bazer-Bachi, A. R., et al. 2008, A&A, 481, 401
Arikawa, Y., Tatematsu, K., Sekimoto, Y., & Takahashi, T. 1999, PASJ, 51, L7
Asplund, M., Grevesse, N., Sauval, A. J., & Scott, P. 2009, ARA&A, 47, 481
Balbus, S. A., & Hawley, J. F. 1998, Rev. Mod. Phys., 70, 1
Bell, A. R. 1978, MNRAS, 182, 147
Berezinskii, V. S., Bulanov, S. V., Dogiel, V. A., & Ptuskin, V. S. 1990, Cosmic ray astrophysics (Amsterdam: North Holland)
Boger, G. I., & Sternberg, A. 2006, ApJ, 645, 314
Bolatto, A. D., Wolfire, M., & Leroy, A. K. 2013, ARA&A, 51, 207
Brogan, C. L., Gelfand, J. D., Gaensler, B. M., Kassim, N. E., & Lazio, T. J. W. 2006, ApJ, 639, L25
Caselli, P., Walmsley, C. M., Terzieva, R., & Herbst, E. 1998, ApJ, 499, 234
Castellina, A., & Donato, F. 2011, Planets, Stars and Stella Systems (Springer-Verlag) [arXiv:1110.2981]
Ceccarelli, C., Maret, S., Tielens, A. G. G. M., Castets, A., & Caux, E. 2003, A&A, 410, 587
Ceccarelli, C., Hily-Blant, P., Montmerle, T., et al. 2011, ApJ, 740, L4
Claussen, M. J., Frail, D. A., Goss, W. M., & Gaume, R. A. 1997, ApJ, 489, 143
Dame, T. M., Hartmann, D., & Thaddeus, P. 2001, ApJ, 547, 792
Dislaire, V., Hily-Blant, P., Faure, A., et al. 2012, A&A, 537, A20
Elmegreen, B. G. 1998, ASP Conf. Ser., 148, 150
Federman, S. R., Lambert, D. L., Sheffer, Y., et al. 2003, ApJ, 591, 986
Ferrière, K. M. 2001, Rev. Mod. Phys., 73, 1031
Flower, D. R. 1999, MNRAS, 305, 651
Frail, D. A., Goss, W. M., & Slysh, V. I. 1994, ApJ, 424, L111
Frerking, M. A., Langer, W. D., & Wilson, R. W. 1982, ApJ, 262, 590
Fukui, Y., Sano, H., Sato, J., et al. 2012a, ARA&A, 746, 82
Fukui, Y., Sano, H., Sato, J., et al. 2012b, ApJ, 746, 82
Gabici, S., Casanova, S., Aharonian, F. A., & Rowell, G. 2010, in SF2A-2010: Proc. of the Annual meeting of the French Society of Astronomy and Astrophysics, eds. S. Boissier, M. Heydari-Malayeri, R. Samadi, & D. Valls-Gabaud, 313
Giuliani, A., Tavani, M., Bulgarelli, A., et al. 2010, A&A, 516, L11
Goudis, C. 1976, Ap&SS, 45, 133
Graedel, T. E., Langer, W. D., & Frerking, M. A. 1982, ApJS, 48, 321
Guélin, M., Langer, W. D., Snell, R. L., & Wootten, H. A. 1977, ApJ, 217, L165
Harvey, P. M., & Forveille, T. 1988, A&A, 197, L19
Herbst, E., & Klemperer, W. 1973, ApJ, 185, 505
Hewitt, J. W., Yusef-Zadeh, F., & Wardle, M. 2008, ARA&A, 683, 189
Hillas, A. M. 2005, J. Phys. G Nucl. Phys., 31, 95
Ilovaisky, S. A., & Lequeux, J. 1972, A&A, 18, 169
Indriolo, N., & McCall, B. J. 2012, ApJ, 745, 91
Indriolo, N., Blake, G. A., Goto, M., et al. 2010, ApJ, 724, 1357
Kaspi, V. M., Lyne, A. G., Manchester, R. N., et al. 1993, ApJ, 409, L57
Le Bourlot, J., Pineau des Forêts, G., Roueff, E., & Schilke, P. 1993, ApJ, 416, L87
Le Bourlot, J., Pineau des Forêts, G., & Roueff, E. 1995a, A&A, 297, 251
Le Bourlot, J., Pineau des Forêts, G., Roueff, E., & Flower, D. R. 1995b, A&A, 302, 870
Lee, H. H., Roueff, E., Pineau des Forêts, G., et al. 1998, A&A, 334, 1047
Lefloch, B., Cernicharo, J., & Pardo, J. R. 2008, A&A, 489, 157
Lesur, G., Kunz, M. W., & Fromang, S. 2014, A&A, 566, A56
Li, H., & Chen, Y. 2010, MNRAS, 409, L35
Linsky, J. L., & Wood, B. 1995, in Am. Astron. Soc. Meet. Abstr., 27, 1347
Lozinskaya, T. A. 1974, Sov. Astron., 17, 603
Lozinskaya, T. A. 1981, Sov. Astron. Lett., 7, 17
McCall, B. J., Huneycutt, A. J., Saykally, R. J., et al. 2003, Nature, 422, 500
Milam, S. N., Savage, C., Brewster, M. A., Ziurys, L. M., & Wyckoff, S. 2005, ApJ, 634, 1126
Milne, D. K., & Wilson, T. L. 1971, A&A, 10, 220
Morlino, G., Amato, E., & Blasi, P. 2009, MNRAS, 392, 240
Nava, L., & Gabici, S. 2013, MNRAS, 429, 1643
Nicholas, B. P., Rowell, G., Burton, M. G., et al. 2012, ARA&A, 419, 251
Padovani, M., & Galli, D. 2013, Astrophys. Space Sci. Proc., 34, 61
Padovani, M., Galli, D., & Glassgold, A. E. 2009, A&A, 501, 619
Padovani, M., Hennebelle, P., & Galli, D. 2013, in SF2A-2013: Proc. of the Annual meeting of the French Society of Astronomy and Astrophysics. eds. L. Cambresy, F. Martins, E. Nuss, & A. Palacios, 409
Pagani, L., Roueff, E., & Lesaffre, P. 2011, ApJ, L35
Pety, J. 2005, SF2A-2005: Semaine de l'Astrophysique Francaise (EDP Sciences), Conf. Ser., 721
Pineau des Forêts, G., Roueff, E., & Flower, D. R. 1992, MNRAS, 258, 45
Reynolds, S. P. 2008, ARA&A, 46, 89
Rho, J., & Borkowski, K. J. 2002, ApJ, 575, 201
Roberts, H., & Millar, T. J. 2000, A&A, 361, 388
Taquet, V., Ceccarelli, C., & Kahane, C. 2012, ApJ, 748, L3
Troscompt, N., Faure, A., Maret, S., et al. 2009, A&A, 506, 1243
van Dishoeck, E. F., & Black, J. H. 1988, ApJ, 334, 771
Velázquez, P. F., Dubner, G. M., Goss, W. M., & Green, A. J. 2002, AJ, 124, 2145
Wakelam, V., Herbst, E., & Selsis, F. 2006a, A&A, 451, 551
Wakelam, V., Herbst, E., Selsis, F., & Massacrier, G. 2006b, A&A, 459, 813
Westerhout, G. 1958, Bull. Astron. Inst., 14, 215
Wilson, T. L., & Rood, R. 1994, ARA&A, 32, 191
Wootten, A. 1981, ApJ, 245, 105
Yang, B., Stancil, P. C., Balakrishnan, N., & Forrey, R. C. 2010, ApJ, 718, 1062
Yusef-Zadeh, F., Shure, M., Wardle, M., & Kassim, N. 2000, ApJ, 540, 842

9.3 Further considerations

9.3.1 Discussion of the DCO$^+$/HCO$^+$ method

To better understand the CR induced chemistry of DCO$^+$, I revisited the analytical determination of the ionisation fraction, and compared its predictions to a complete chemical modeling.

Based on a reduced network (see Table A.1 in the paper), one can derive an analytic expression relating x_e to R_D (see Equation (3) in the paper):

$$R_D = \frac{[\mathrm{DCO^+}]}{[\mathrm{HCO^+}]} \approx \frac{1}{3}\frac{x(\mathrm{H_2D^+})}{x(\mathrm{H_3^+})} \approx \frac{1}{3}\frac{k_f x(\mathrm{HD})}{k_e x_e + \delta + 1/2\ k_f e^{-220/T}}\ , \tag{9.2}$$

which can be re-written as follows:

$$x_e = \left(\frac{k_f x(\mathrm{HD})}{3R_D} - \delta - \frac{k_f}{2}\mathrm{e}^{-\Delta E/T}\right)\frac{1}{k_e}\ , \tag{9.3}$$

where k_f and k_e are kinetic rates (see Table 3.1) and $x(\mathrm{HD})$ the chemical abundance of HD. The coefficient δ is the total destruction rate of H_2D^+ by neutrals, which can be approximated to $\delta \approx k_D x(\mathrm{CO})$ if we assume the destruction is dominated by reaction with CO. Dependence on the temperature is introduced through kinetic rates, with a crucial contribution of the exponential term due to the endothermic reaction $H_2D^+ + H_2 \rightarrow H_3^+ + HD$, especially at $T \gtrsim 30$ K.

The predicted x_e values as a function of R_D, from the above analytical method, are shown in Figure 9.2, at different temperatures. Overlaid are the steady-state predictions from chemical modeling with our extended version of the OSU chemical network (see Section 5.2 in the paper). We notice a few discrepancies between the two sets of predictions.

First, while there is reasonable agreement at low values of ζ/n_{H}, a small discrepancy is visible: it is due to the invalid assumption of a constant HD abundance in the analytical method (Figure 9.4). The abundance of HD is indeed reduced by the series of reactions:

$$\mathrm{HD} + \mathrm{H_3^+} \rightleftharpoons \mathrm{H_2D^+} + \mathrm{H_2} \tag{9.4}$$

$$\mathrm{H_2D^+} + \mathrm{CO} \rightarrow \mathrm{DCO^+} + \mathrm{H_2} \tag{9.5}$$

$$\mathrm{H_2D^+} + \mathrm{e^-} \rightarrow \mathrm{H} + \mathrm{H} + \mathrm{D} \tag{9.6}$$

$$\mathrm{DCO^+} + \mathrm{e^-} \rightarrow \mathrm{D} + \mathrm{CO}\ , \tag{9.7}$$

where electronic dissociation gets more and more efficient with larger x_e (i.e. larger ζ) and traps deuterium into atomic form (Figure 9.4). Besides, the steep drop of x_e at large R_D values is caused by the canceling of the term in brackets in Equation 9.3, which occurs when the H_2D^+ destruction by the reactions with CO (reaction 9.5) or H_2 (backward reaction 9.4) become comparable to electronic recombination (reaction 9.6). When electronic recombination is negligible, R_D doesn't depend on x_e anymore. This happens in the range of CR ionisation rates typical of dense molecular clouds, which makes the DCO$^+$/HCO$^+$ method relatively uncertain to measure low CR ionisation rates. For instance, a 50% uncertainty in the observed ratio indeed leads to two orders of magnitude uncertainties on x_e and ζ.

Second, the jump from LIP to HIP is a consequence of the instability of the complete chemical network, which cannot be reproduced by the reduced network in the analytical solution. The jump occurs at relatively high R_D values, before the curves enter the power-law regime, where electronic recombination dominates the destruction of H_2D^+.

Finally, in the HIP, the very large difference between the two sets of predictions is caused by the drop in the CO abundance (Figure 9.3). In the HIP, CO is efficiently destroyed by He$^+$ and carbon is dominantly in the atomic form C or C$^+$. This range of R_D corresponds to DCO$^+$ abundances too low to be detected.

For all these reasons, the analytical determination of x_e from R_D has a very limited range of applicability in dense molecular clouds, at low ionisation with high uncertainties. Using a complete chemical network, the DCO$^+$/HCO$^+$ abundance ratio can still provide a measurement of x_e and ζ with a large uncertainty in the LIP, and only lower limits if the gas is in the HIP. This stimulates the quest for a set of new tracers, that would give a more accurate measurement of the CR ionisation rate in the LIP and/or in the HIP. This will be discussed in Chapter 11.

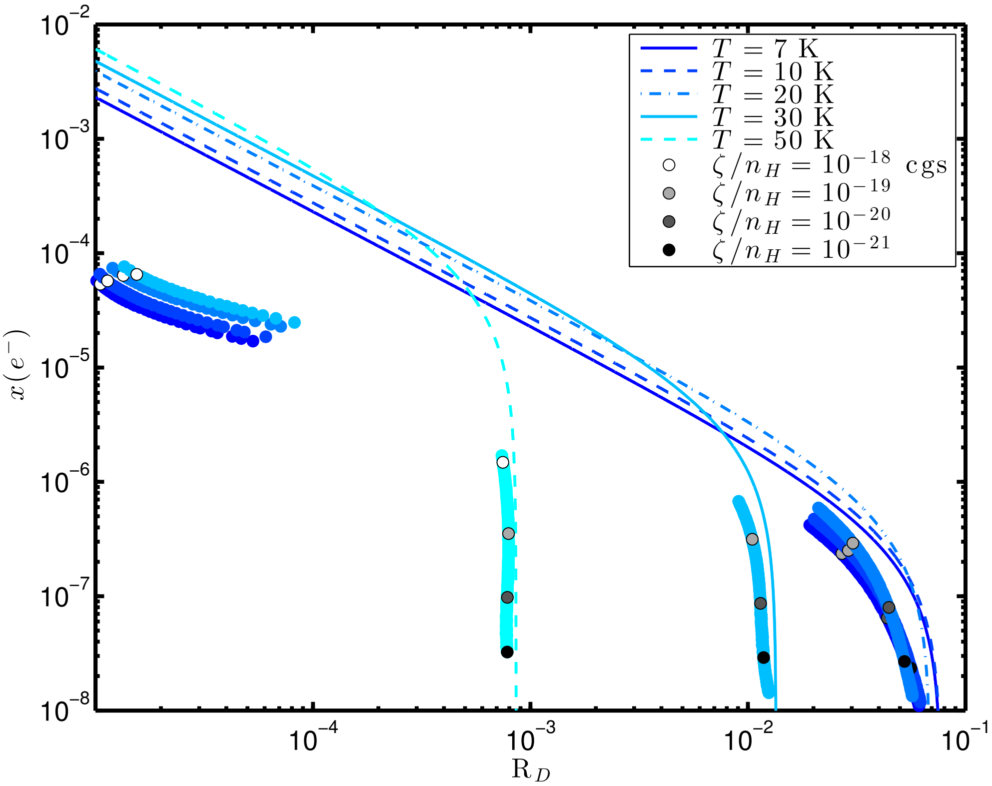

Figure 9.2: Ionisation fraction x_e as a function of the R_D=DCO$^+$/HCO$^+$ abundance ratio. Lines show analytical determinations at different temperatures. Bullets show values from modeling, which were obtained by varying $\zeta/n_{\rm H}$ from 10^{-22} to 10^{-18} cm^3 s^{-1} (i.e. ζ from 10^{-22} to 10^{-18} s^{-1} at $n_{\rm H} = 10^4$ cm^{-3}). Values of R_D decrease with increasing $\zeta/n_{\rm H}$ and gray bullets mark round values of $\zeta/n_{\rm H}$.

9.3.2 More details on the HIP/LIP transition

In our model, the actual position of the HIP/LIP transition depends little on the assumed elemental abundances and gas temperature. Specifically, considering variations in the gas-phase abundance of metals up to a factor 100 and uncertainties (±5 K) in the temperature, the HIP/LIP jump occurs within a factor of 5 in terms of $\zeta/n_{\rm H}$ (see Figure 5 in the paper).

To ensure the robustness of our results, it is also important to consider a possible hysteresis in the HIP/LIP transition (Le Bourlot et al., 1993, 1995a). An hysteresis would reveal a range of parameters where both the LIP and HIP can coexist. The numerical prediction in this range would end on either branch, depending on the initial conditions of the computation. Therefore, it could alter our conclusions when observations fall in the hysteresis region. To test this, I modified the computation technique of the grid by first computing the steady-state abundances in the molecular cloud, starting from atomic species and a standard CR ionisation rate $\zeta = 10^{-17}$ s^{-1} at $n_{\rm H} = 10^4$ cm^{-3} (the exact same results are obtained at other densities, as the results only depend on $\zeta/n_{\rm H}$). I then increased ζ, using the last steady-state abundances as initial conditions for the new model, to reach a new equilibrium. I therefore computed an iterative grid of chemical abundances, with increasing ζ, whereas in Vaupré et al. (2014), all models were computed using the same initial atomic abundances (Table 8.1). I performed the same iterative process with decreasing ζ, starting from a molecular state in the HIP $\zeta = 10^{-14}$ s^{-1}. Figure 9.5 shows indeed the existence of two distinct paths, from LIP to HIP and HIP to LIP. This hysteresis spans over values of $\zeta/n_{\rm H}$ within a factor 5, **i.e. consistent with uncertainties previously derived in Vaupré et al. (2014)**. The effect of the hysteresis is to extend the LIP branch at slightly higher ζ. Yet, if it increases the error bar of ζ towards higher ζ, it doesn't affect the general conclusion that the ionisation is much enhanced. The value of ζ at which the jump occurs that I previously determined in the paper seems to be a minimum, in presence of an hysteresis.

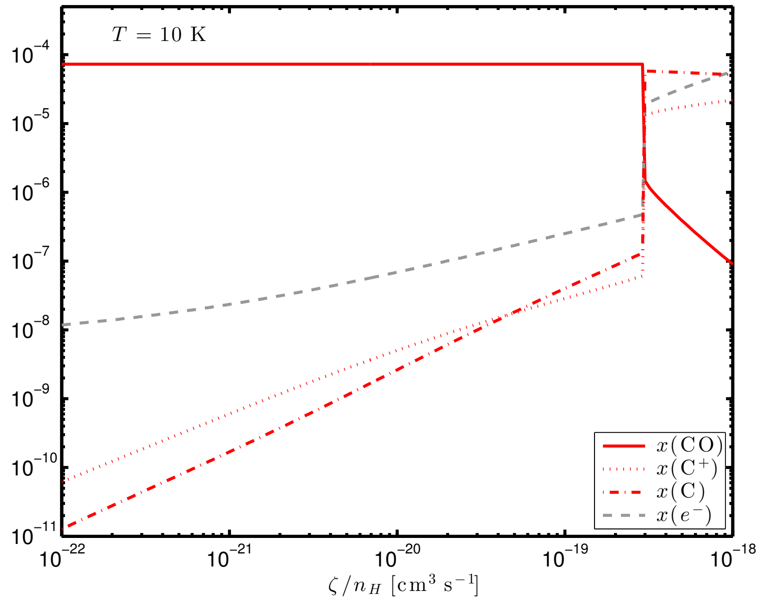

Figure 9.3: Steady-state abundances of the dominant reservoirs of carbon as a function of $\zeta/n_{\rm H}$ (the calculation was done at $n_{\rm H} = 10^4$ cm^{-3}, but only depends on $\zeta/n_{\rm H}$). The abundance of CO is constant in the LIP, in agreement with the assumption in the analytical method. On the contrary, CO is largely destroyed by He$^+$ in the HIP, and carbon is then mainly in the atomic form C and C$^+$.

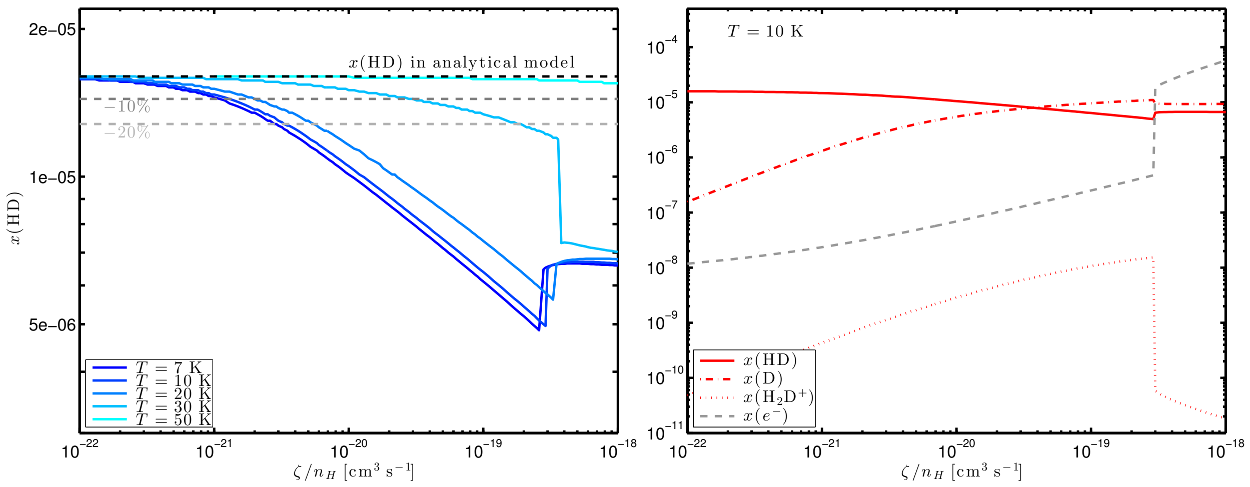

Figure 9.4: **Left:** HD abundance as a function of $\zeta/n_{\rm H}$ at different temperatures, from chemical modeling. The analytical model assumes a cosmic abundance $x({\rm HD}) = {\rm D/H} = 1.6 \times 10^{-5}$. The discrepancy between the predicted values and a constant HD abundance is larger at low temperature and is significant even for low values of ζ. Namely, for a typical density $n_{\rm H} = 10^4$ cm^{-3}, the abundance of HD is reduced by $\sim 10\%$ at $\zeta = 10^{-17}$ s^{-1}, compared to the deuterium elemental abundance. This reduced abundance of HD explains the discrepancy between x_e values from chemical modeling and analytical determination in Figure 9.2 at low ζ. **Right:** The abundance of HD decreases with ζ as the main reservoir of deuterium becomes atomic D.

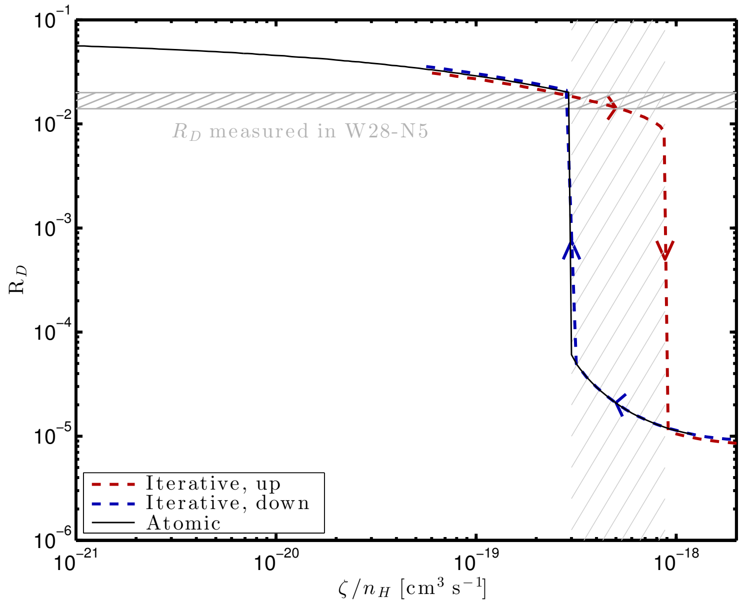

Figure 9.5: Hysteresis of the LIP/HIP transition, for a gas cell at 10 K. The black curve shows the computations using the same initial atomic abundances at each ζ/n_{H}, as we did in Vaupré et al. (2014). The red and blue dashed lines show the iterative processes (see text), with increasing and decreasing ζ/n_{H}, respectively. The vertical hatched area shows the bistable domain. Overall, the existence of an hysteresis does not affect the validity of our results.

Chapter 10

Probing the passage of the W51C supernova remnant shock through a molecular cloud

Contents

10.1 Introduction

The first observational evidence of the enhanced ionisation of a dense molecular cloud in the vicinity of a SNR was given by Ceccarelli et al. (2011). In their paper, the authors used the DCO^+/HCO^+ ratio and derived a CR ionisation rate 100 times higher than the average Galactic value, 10^{-17} s^{-1}, in the direction of W51C-E. The physical conditions in that region were derived from CO observations and gave a gas density $\sim 10^4$ cm^{-3} and a kinetic temperature $\sim$ 20 K. The line of sight at which this enhanced ionisation was observed was relatively close to a protostar, and it was important to further study the region to make sure that no compact DCO^+ emission from the protostar could contaminate the observations within the beam of the IRAM 30m telescope. Follow-up observations were obtained at the 30m telescope to map a $10' \times 2'$ region around W51C-E, and PdBI observations were obtained to search for compact emission within 100" of W51C-E.

Our first result is that no compact emission of DCO^+ was found, which confirms that the W51C-E region studied by Ceccarelli et al. (2011) is filled up with gas ionised by an enhanced flux of CRs.

We also report the unexpected detection of compact $SiO(2-1)$ emission. The detection of SiO in the dense gas is characteristic of the presence of a shock and is often associated with molecular outflows (e.g Schilke et al., 1997; Codella et al., 1999; Arce et al., 2008; Gusdorf et al., 2008). The passage of a shock induces a rapid heating and compression of the region and leads to molecular dissociation, endothermic reactions, ice sublimation, and dust grain disruption. Consequently, silicon present in grain cores or mantles is released into the gas-phase (a process also referred to as *sputtering*) and subsequently endures oxidation to form SiO. This results in enhanced SiO abundances up to a factor $\sim 10^6$ with respect to abundances in quiescent clouds. We investigated the possibility that the SiO emission was associated with an outflow of the nearby protostar. The study of the velocity channel maps of the SiO emission shows that the emission is not driven by the protostar, in agreement with previous studies that showed the absence of an outflow (Cyganowski et al., 2011). Our second result is then that the SiO emission probably traces a low-velocity shock caused by the passage of the primary SNR shock through a dense clump.

These results were published in Dumas et al. (2014).

10.2 IRAM 30m observations

Using the IRAM 30m telescope, I performed $10' \times 2'$ maps around W51C-E, whose contours follow approximatively the main axis of the cloud as seen in CO (see Dumas et al., 2014, Figure 1). The observations cover the following ranges of frequencies: $81 - 89$ GHz, $97 - 105$ GHz, $215 - 223$ GHz and $230 - 238$ GHz. In particular, they include $HCO^+(1-0)$ and $^{13}CO(2-1)$.

Then, using the $H^{13}CO^+$ intensity map (Figure 10.1), I defined a series of new sight lines where to look for $DCO^+(2-1)$ emission and a possible intensity gradient (Table 10.1). The integration on DCO^+ takes some time to achieve a low noise, so I could perform in parallel a spectral survey at 3 mm, covering the whole frequency range from 85 to 114 GHz at these positions.

I computed the integrated intensities from Gaussian fits (Table 10.2). Further analysis has yet to be achieved, to derive the physical conditions and column densities.

The 30m observations were also needed in the analysis of the PdBi data to recover the missing short spacings. The analysis was performed by G. Dumas, and I provided 30m data of $H^{13}CO^+(1-0)$ and $SiO(2-1)$.

10.3 Dumas et al. 2014

The Astrophysical Journal Letters, 786:L24 (5pp), 2014 May 10
doi:10.1088/2041-8205/786/2/L24

LOCALIZED SiO EMISSION TRIGGERED BY THE PASSAGE OF THE W51C SUPERNOVA REMNANT SHOCK

G. Dumas[1], S. Vaupré[2], C. Ceccarelli[2], P. Hily-Blant[2], G. Dubus[2], T. Montmerle[3], and S. Gabici[4]
[1] Institut de Radioastronomie Millimétrique, 300 Rue de la Piscine, F-38406 Saint Martin d'Hères, France
[2] UJF-Grenoble 1/CNRS-INSU, Institut de Planétologie et d” Astrophysique de Grenoble (IPAG) UMR 5274, F-38041 Grenoble, France
[3] UPMC-CNRS, UMR 7095, Institute d'Astrophysique de Paris, 98 bis boulevard Arago, F-75014 Paris, France
[4] APC, AstroParticule et Cosmologie, Université Paris Diderot, CNRS, CEA, Observatoire de Paris, Sorbonne Paris, F-75205 Paris, France

Received 2014 March 4; accepted 2014 March 28; published 2014 April 24

ABSTRACT

The region toward W51C is a convincing example of interaction between a supernova remnant (SNR) and a surrounding molecular cloud. Large electron abundances have been reported toward the position W51C-E located in this interaction region, and it was proposed that the enhanced ionization fraction was due to cosmic ray particles freshly accelerated by the SNR shock. We present Plateau de Bure Interferometer observations of the $H^{13}CO^+$(1–0) and DCO^+(2–1) emission lines centered at position W51C-E. These observations confirm the previous scenario of cosmic-ray-induced ionization at this location. In addition, SiO(2–1) emission has been successfully mapped in the close vicinity of W51C-E, with a spatial resolution of 7″. The morphology and kinematics of the SiO emission are analyzed and strongly suggest that this emission is produced by the passage of the SNR primary shock. Put in conjunction with the enhanced ionization fraction in this region, we give a consistent picture in which the W51C-E position is located downstream of the shock, where a large reservoir of freshly accelerated particles is available.

Key words: cosmic rays – ISM: individual objects (W51C) – ISM: molecules

1. INTRODUCTION

Cosmic rays (CRs) permeate our Galaxy, playing a major role in setting the prevalent physical conditions, notably because they are responsible for the ionization of the dense part of the molecular clouds where stars form. Galactic CRs are thought to originate mostly from the shock of supernovae remnants (SNRs) where they can be accelerated up to PeV energies. Their presence can be inferred from the effects of their interaction with their environment. High-energy CRs ($\gtrsim$1 GeV) can be tracked down because, when they hit a large mass of gas, they cause bright gamma-ray emission due to inelastic proton–proton interactions (Kelner et al. 2006). On the other hand, low-energy ($\lesssim$1 GeV) CRs can be probed by the enhancement of the ionization that they cause in nearby molecular gas (Padovani et al. 2009). In fact, ionization is the only way to probe the low-energy end of the CR spectrum. Hence, SNRs interacting with molecular clouds are particularly promising sites for studying both the properties of freshly accelerated CRs (e.g., density, spectrum) and their feedback on their environment (diffusion, ionization). In this context, the presence of both an enhanced ionization degree and gamma-ray emission associated with dense molecular clouds close to SNRs can provide additional evidence of CR acceleration from sub-GeV (ionization) to multi-TeV (very high energy gamma-rays) energies.

The first dense molecular cloud, where the association of enhanced ionization and gamma-ray emission has been detected, is associated with the SNR W51C (Ceccarelli et al. 2011, hereinafter CHMD2011). W51C is ~5° away from the galactic plane, at a distance of ~5.5 kpc (Cyganowski et al. 2011). It extends about 30′ and its age is $\sim 3 \times 10^4$ yr (Koo et al. 1995). Figure 1 presents the environment of W51C. The thermal X-ray emission (Figure 1, left panel), tracing the SNR primary shock, extends northwest beyond the molecular cloud, hinting that the SNR is situated behind the W51B cloud complex (Koo et al. 1995). A bright and extended GeV–TeV gamma-ray source has been detected toward W51C by Feinstein et al. (2009), Abdo et al. (2009), and Aleksić et al. (2012) who concluded that the origin of such emission is the interaction between the SNR and the nearby molecular cloud (Figure 1, right panel). OH masers, high velocity H I and molecular emission are coincidently observed in the overlapping region of the W51C and the W51B complexes, which suggests that they are associated with the SNR shock (Koo et al. 1995; Green et al. 1997; Brogan et al. 2000), though that is still under debate (Tian & Leahy 2013).

CHMD2011 sampled several lines of sight toward this interaction region using the IRAM 30 m single-dish telescope. They found that the CR ionization rate is about 100 times larger than in standard galactic molecular clouds in the direction of the position of W51C-E $\alpha_{J2000.0} = 19^h23^m08\overset{s}{.}0$; $\delta_{J2000.0} = 14°20'00\overset{''}{.}0$, situated northwest of the SNR, at the edge of the gamma-ray emission detected by *Fermi*/LAT and *MAGIC* as shown in Figure 1 (right panel) and about 2′ north of the H II region, G49.2-0.3. The CR ionization rate was derived by measuring the abundance ratio DCO^+/HCO^+, following the method described in Guélin et al. (1977; see CHMD2011 for further details on the method used). The observations were sensitive to the ionization of the gas in the 28″ beam, corresponding to a linear distance of ~1 pc.

Promptly after the publication of this measurement, NIR observations of the region revealed the presence of a protostar at the edge of the beam of the DCO^+ and HCO^+ observations (Cyganowski et al. 2011), which could alter the interpretation of the results of the CHMD2011 work. In practice, CHMD2011 assumed that all the detected DCO^+ and HCO^+ emissions come from ionization of the dense gas by the CR. However, UV flux from a star formation region and potential outflows could also ionize the surrounding molecular gas. Therefore, if CHMD2011 single-dish observations were contaminated by emission toward the protostar, the beam-averaged measured ionization rate may not be related to the CR. Therefore, we carried out high spatial resolution observations of the same region with the Plateau de Bure Interferometer (PdBI) in order to verify whether the spatial distribution of DCO^+ and HCO^+ emission, used to derive the high CR ionization rate, is linked to the protostar.

In this Letter, we describe the results of these observations which provide additional evidence for an overdensity of freshly accelerated low-energy CRs in W51C-E. In addition, we discuss

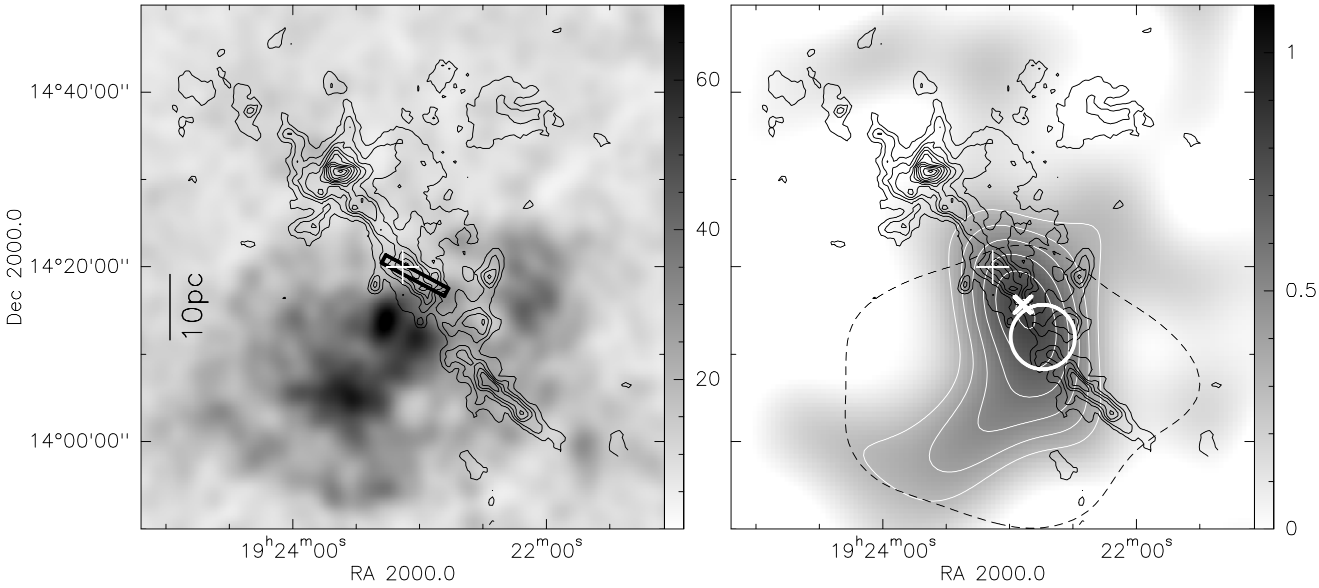

Figure 1. High-energy environment of W51C. In both panels, the large white cross locates the phase center of our PdBI observations at the position of W51C-E, and the ^{13}CO(2–1) integrated intensity between 60 and 75 km s^{-1} is shown as black contours (from 5 to 60 K km s^{-1} in steps of 5 K km s^{-1}; Jackson et al. 2006). Left: the *ROSAT* X-ray map of SNR W51C (in counts s^{-1}; Koo et al. 1995) is shown in gray scale. The black rectangle delineates the field of view of our IRAM 30 m observations. Right: *MAGIC* gamma-ray emission map from 300 Gev to 1 TeV (in relative flux; Aleksić et al. 2012), shown in gray scale. The white plain contours give the *MAGIC* relative flux from 0.3 to 0.8 in steps of 0.1 and the dashed contour marks the 260 counts deg^{-2} measured by the *Fermi*/LAT in the 2–10 GeV energy range. The white cross corresponds to the position of the OH maser emission (Koo et al. 1995; Green et al. 1997) and the white circle shows the region of shocked atomic and molecular gas (Koo & Moon 1997a, 1997b).

the shocked regions probed by the SiO(2–1) emission detected by these PdBI observations.

2. OBSERVATIONS AND DATA REDUCTION

W51C-E was observed with the PdBI between 2012 June and July in the *D* configuration with five antennae, providing baselines between 15 m and 111 m. We used the 2 mm receivers tuned at 144.077 GHz and the 3 mm receivers tuned at 86.754 GHz to map the emission lines DCO$^+$(2–1) and H^{13}CO$^+$(1–0), respectively. A total bandwidth of about 230 MHz with a spectral resolution of 0.156 MHz was used for both setups. At 3 mm, the setup covers the SiO(2–1) line at 86.847 GHz. In parallel, the wideband correlator, WideX, offers a total of 3.6 GHz of bandwidth at 1.95 MHz resolution. The phase center of the observations was at $\alpha_{J2000.0} = 19^{h}23^{m}08\overset{s}{.}0$; $\delta_{J2000.0} = 14^{\circ}20'00\overset{''}{.}0$. MWC349 was used as the flux calibrator and the quasar J1923+210 was used as the phase calibrator and was observed every 23 minutes. At 3 mm (respectively, 2 mm), the primary beam is 58$''$ (respectively, 32$''$) with a conversion factor of 22 Jy K^{-1} (respectively, 29 Jy K^{-1}).

The data reduction was done with the standard IRAM GILDAS[5] software packages CLIC and MAPPING (Guilloteau & Lucas 2000). Each day of observations was calibrated separately and single data sets were created at 2 mm and 3 mm for both the narrow band correlator and WideX. Pure continuum and continuum-subtracted data cubes were then created and deconvolved separately using natural weighting, leading to a beam size of $3\overset{''}{.}8 \times 3\overset{''}{.}4$ at 2 mm and $7\overset{''}{.}4 \times 4\overset{''}{.}4$ at 3 mm. In the case of the WideX data, all detected emission lines were cleaned independently. The final natural-weighted data cubes have a rms of 4.8 mJy beam^{-1} in a channel width of 1.3 km s^{-1} (0.625 MHz) at 2 mm and 1.1 km s^{-1} (0.3125 MHz) at 3 mm.

In addition, we obtained a $10' \times 2'$ map of the SiO(2–1) line with the IRAM 30 m telescope. The observations were carried out in 2013 January. We simultaneously used the EMIR bands, E090 and E230, and tuned the Fast Fourier transform spectrometer backends on H^{13}CO$^+$(1–0) and ^{13}CO(2–1) transitions, respectively. The mapping of the region was conducted in the on-the-fly mode over ∼4 hr, reaching an rms of 90 mK in 0.67 km s^{-1} channel width at 3 mm and 275 mK in 0.27 km s^{-1} channel width at 1 mm. The weather was good and the $T_{\rm sys}$ values were typically lower than 150 K at 3 mm and 350 K at 1 mm.

We used a reference position about δR.A. = 300$''$, δdecl. = $-400''$ away from the mapped area. The amplitude calibration was typically done every 15 minutes, and pointing and focus were checked every 1 and 3 hr, respectively, ensuring $\approx 2''$ pointing accuracy. All spectra were reduced using the CLASS package (Pety 2005) of the IRAM GILDAS software. Residual bandpass effects were subtracted using low-order ($\leqslant 3$) polynomials. Table 1 lists the setups used and the emission lines mapped with these single-dish and interferometric observations.

3. RESULTS

3.1. DCO$^+$ and H^{13}CO$^+$

We find no compact DCO$^+$ or H^{13}CO+ source within the beam covered by previous IRAM 30 m observations of W51C-E by CHMD2011. Therefore, no emission associated with the nearby protostar is contaminating the measurements by CHMD2011. This result supports the conclusions by these authors that the entire region traced by the 30 m beam has an enhanced CR ionization flux.

3.2. SiO(2–1)

Figure 2 (left panel) shows the IRAM 30 m map of the SiO emission. Strong emission is detected only around the position

---

[5] http://www.iram.fr/IRAMFR/GILDAS

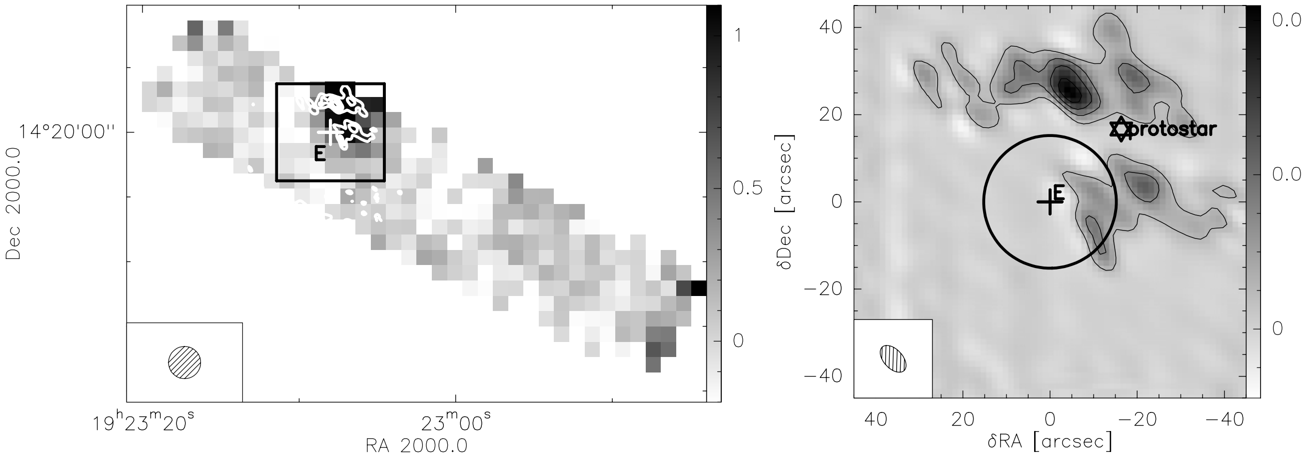

Figure 2. Left: SiO(2–1) map from the IRAM 30 m telescope (K km s^{-1}, in antenna temperature scale, T_A^*). The rms is 60 mK km s^{-1}) overlaid with the SiO(2–1) emission observed with the PdBI (white contours from 0.005 to 0.05 in steps of 0.01 Jy beam^{-1} km s^{-1}). The white cross indicates the W51C-E position and the black square represents the size of the right panel. The left bottom panel shows the 30 m half power beam of 28″. Right: PdBI SiO(2–1) integrated emission (in Jy beam^{-1} km s^{-1}, rms = 4.8 mJy beam^{-1}). The contours are from 0.005 to 0.05 in steps of 0.01 Jy beam^{-1} km s^{-1}. The black circle represents the primary beam of the IRAM 30 m telescope at 3 mm (28″), centered on the W51C-E position (cross). The black star marks the position of the protostar observed in the IR and centimeter wavelengths (Cyganowski et al. 2011). The CLEAN beam of 7.″4 × 4.″4 is shown in the bottom left corner.

Table 1
Observational Parameters of the PdBI and IRAM 30 m Observations

PdBI observations	2 mm	3 mm
Central frequency	144.077 GHz	86.754 GHz
Beam size	3.″8 × 3.″4	7.″4 × 4.″4
Velocity resolution	1.3 km s^{-1}	1.1 km s^{-1}
rms (mJy beam^{-1})	3.1	4.8
Emission lines	DCO$^+$(2–1)	H^{13}CO$^+$(1–0); SiO(2–1)
Primary beam	32″	58″
Conversion factor (Jy K^{-1})	29	22
30 m observations	1 mm	3 mm
Central frequency	220.399 GHz	86.754 GHz
Beam size	11″	28″
Velocity resolution	0.27 km s^{-1}	0.67 km s^{-1}
rms (mK)	275	90
Emission lines	^{13}CO(2–1)	H^{13}CO$^+$(1–0); SiO(2–1)

of the W51C-E source. The PdB SiO integrated map around that position is shown in the right panel of Figure 2. The SiO emission is concentrated in two regions, north and south of the protostar, respectively. The north region is split into three clumps, aligned in the west–east direction over a length of about 1.2 pc (∼45″). The southern SiO structure is weaker and splits into two emitting regions with about a 45° angle and an elongation of about 0.5 pc (∼20″). These SiO clumps are barely resolved, with an average size of about 0.3 pc (10″), and have a velocity dispersion between 5 and 7 km s^{-1}. Figure 3 present the channel maps of the SiO emission, at a 1.08 km s^{-1} velocity resolution. The first thing to note is that no velocity gradient, nor structure apparently associated with the protostar, is evident in these maps. The emission is only present from −6.5 to +6.5 km^{-1} around the systemic velocity (67 km s^{-1}, CHMD2011) with almost constant intensity in both north and south structures.

4. DISCUSSION

The first important result of this work is that the position observed by CHMD2011 does not have any compact region of DCO$^+$ emission, which supports the idea that the whole region encompassed by the IRAM 30 m beam is permeated by gas with a CR ionization rate that is about 100 times larger than the standard one. In other words, the protostar in the field has no impact on the determination of the ionization of the region.

The second, unexpected result is the presence of SiO emission concentrated in that region. As shown from the large-scale map (Figure 2, left panel), SiO is only associated with W51C-E, which adds support to the conclusions by CHMD2011 that it is a peculiar region. The obvious questions are: why is SiO present, what does it trace, and does it have anything to do with the enhanced CR ionization rate in the region? Under typical dark cloud conditions, silicon is almost tied up in interstellar grains, and its abundance in the gas phase is typically $N(\mathrm{SiO})/N(\mathrm{H_2}) \sim 10^{-11}$ or less (see Lucas & Liszt 2000, and references therein), because Si is trapped in the refractory interstellar grains and/or mantles that envelop them. However, in shocked regions, the grains can be shattered and the mantles sputtered (Flower et al. 1996; Schilke et al. 1997; Gusdorf et al. 2008), so that SiO, the major Si-bearing reservoir in molecular gas, becomes orders of magnitude more abundant, up to $\sim 10^{-6}$. In fact, SiO is commonly used to trace molecular shocks (Bachiller 1996). Our observations do not allow us to give an estimate of the abundance nor of the physical conditions of the gas emitting the SiO(2–1) transition. However, it is likely that the two observed structures have an enhanced SiO abundance with respect to the rest of the whole region (over the 10′ × 2′ length of the IRAM 30 m map). Even though we cannot quantify the strength of the shock, there is no doubt that two shocked regions are present, probed by the SiO emission. The next question is: what is the origin of this shock? One would first think that it is powered by the protostar outflow. To check this possibility, we show the SiO emission channel maps in Figure 3. The spatial shift between the red and blue shifted emission parts, which is a signpost of protostellar outflow (e.g., Gueth & Guilloteau 1999) is not seen. Therefore, we conclude that the observed SiO emission is not associated with an outflow driven by this star. This is in agreement with previous studies detecting no outflow associated with the protostar (de Buizer & Vacca 2010; Cyganowski et al. 2011).

Then the second, more plausible, explanation is that the detected shock is connected, in one way or another, to the SNR primary shock that may have created the large flux of CR

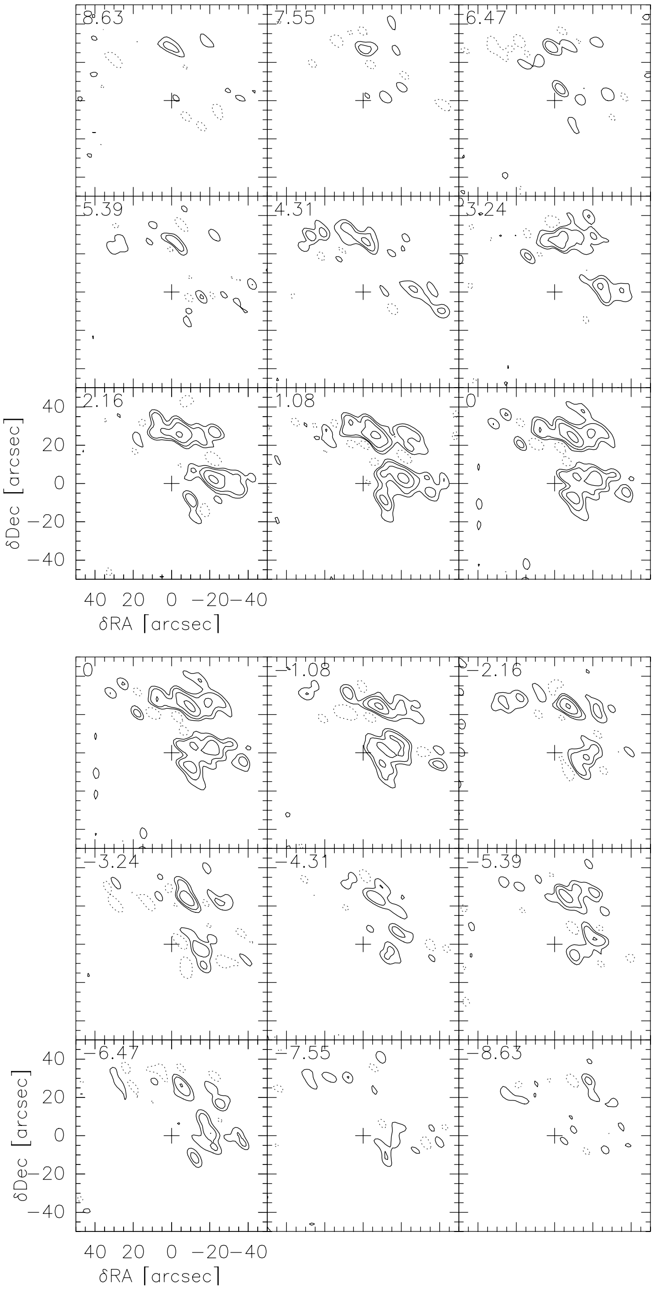

Figure 3. Channel maps of the naturally weighting SiO(2–1) emission toward W51C-E. The channels are 1.08 km s^{-1} wide between $\sim\sim-8.63$ and $\sim+8.63$ km s^{-1} around the LSR velocity ($v_{\mathrm{lsr}} = 67$ km s^{-1}). Contours are plotted at -3σ, 3σ, 6σ, 12σ, and 24σ with $1\sigma = 4.8$ mJy beam^{-1}. The CLEAN beam of $7''.4 \times 4''.4$ is shown in the bottom left corner and the cross marks the phase center of the observations.

probed by the enhanced ionization in W51C-E. Figure 1 shows the high-energy environment of the SNR. In particular, the W51C-E position (black cross in the right panel of Figure 1) lies at the edge of the gamma-ray emission detected by *Fermi*/LAT and *MAGIC*. This leads us to conclude that the W51C-E position, where enhanced ionization has been detected, is situated in the vicinity of the SNR shock. In general, SNR shocks are believed to be the main accelerators of Galactic CRs. Their velocities exceed 10, 000 km s^{-1} in the initial phase of the evolution of SNRs, and gradually decrease as the SNRs age (Vink 2012). Koo et al. (1995) derived a forward shock velocity of $\approx$500 km s^{-1} and a dynamical age of $\approx 3 \times 10^4$ yr from the thermal X-ray emission. Even at this late stage, shocks are believed to be strong enough to accelerate CRs up to GeV energies and possibly more (Ptuskin & Zirakashvili 2003). Theory predicts that if molecular clumps of dense gas obstruct the passage of the primary shock, its propagation stalls, while a complex system of shocks develops in and around the clump (e.g., Jones & Kang 1993; Inoue et al. 2012). The localized SiO emission that we detect in W51C-E could thus arise from a cloud overrun by the SNR. Assuming a primary shock speed of $v_a \approx 500\,\mathrm{km\,s^{-1}}$, a cloud overdensity with respect to the ambient density $n_c/n_a \lesssim 40$ would give a typical transmitted shock speed in the clump of $v_c \approx v_a(n_a/n_c)^{1/2} \gtrsim 25\,\mathrm{km\,s^{-1}}$, enabling grain sputtering (Gusdorf et al. 2008). If correct, this interpretation implies that W51C-E is located downstream of the shock, where a large reservoir of ionizing CRs is available. This is further supported by the general picture that the primary shock, as traced by the thermal X-ray emission, extends northwest beyond the W51B complex (Figure 1). Only a part of the SNR is interacting with the north east portion of the W51B complex, as evinced from the presence of shocked atomic and molecular material coincident with the centroid of the gamma-ray emission, about 20 pc (10′) southwest from our observations (Koo & Moon 1997a, 1997b; Brogan et al. 2013). In principle, the shock traced by SiO emission might also be responsible for the enhanced CR ionization rate of W51C-E. Reflected shocks are expected to be significantly weaker than the primary shock, hence less efficient in accelerating CRs unless the primary shock is CR dominated (Jones & Kang 1993). Though this possibility cannot be ruled out here, it seems less natural as the low-energy CR would also have to escape the clump rapidly to fill in the $\approx$1 pc region where we detect an overionization. A possible way to test this explanation is by observing a gradient of CR ionization rate in positions close to W51C-E: if the SiO shock is responsible for the CR acceleration, then the larger the distance from the SiO shocks, the lower the ionization.

5. CONCLUSIONS

We have presented PdBI observations of the position W51C-E in the interacting region of the SNR W51C with the nearby molecular cloud. Our first result is that we confirm that this region, studied by CHMD2011, is filled up with gas ionized by an enhanced flux of CRs. We also report the presence of two structures probed by SiO(2–1) emission, approximately elongated in the east–west direction, and we propose that these structures are tracing a low-velocity shock caused by the passage of the primary SNR shock through a dense clump. We conclude that the W51C-E region is downstream of the SNR forward shock, exactly where the CRs accelerated at the forward shock would accumulate and cause the enhanced ionization measured there. Although less probable, it is possible that the shock traced by the SiO emission is responsible for the acceleration of low ($\leqslant$1 GeV) CRs, which would contribute to the ionization of the dense gas in this region.

This work has been supported by the French "Programme National Hautes Energies." S.G. acknowledges the financial support of the UnivEarthS Labex program at Sorbonne Paris Cit (ANR-10-LABX-0023 and ANR-11-IDEX-0005-02). We thank the staff at the IRAM 30 m telescope and on the Plateau de Bure, and we also thank the referee for his/her helpful comments.

REFERENCES

Abdo, A. A., Ackermann, M., Ajello, M., et al. 2009, ApJL, 706, L1
Aleksić, J., Alvarez, E. A., Antonelli, L. A., et al. 2012, A&A, 541, 13
Bachiller, R. 1996, ARA&A, 35, 111
Brogan, C., Frail, D. A., Goss, W. M., & Troland, T. H. 2000, ApJ, 537, 875
Brogan, C., Goss, W. M., Hunter, T. R., et al. 2013, ApJ, 771, 91
Ceccarelli, C., Hily-Blant, P., Montemerle, T., et al. 2011, ApJL, 740, L4 (CHMD2011)
Cyganowski, C. J., Brogan, C. L., Hunter, T. R., & Churchwell, E. 2011, ApJ, 743, 56
de Buizer, J. M., & Vacca, W. D. 2010, AJ, 140, 196
Feinstein, F., Fiasson, A., Gallant, Y., et al. 2009, in AIP Conf. Proc. 1112, Science with the New Generation of High Energy Gamma-Ray Experiments, ed. D. Bastieri & R. Rando (Melville, NY: AIP), 54
Flower, D. R., Pineau des Forets, G., Field, D., & May, P. W. 1996, MNRAS, 280, 447
Green, A. J., Frail, D. A., Goss, W. M., & Otrupcek, R. 1997, AJ, 114, 2058
Guélin, M., Langer, W. D., Snell, R. L., & Wootten, H. A. 1977, ApJL, 217, L165
Gueth, F., & Guilloteau, S. 1999, A&A, 343, 571
Guilloteau, S., & Lucas, R. 2000, in ASP Conf. Ser. 217, Imaging at Radio through Submillimeter Wavelengths, ed. J. G. Mangum & S. J. E. Radford (San Francisco, CA: ASP), 299
Gusdorf, A., Pineau des Forets, G., Cabrit, S., & Flower, D. R. 2008, A&A, 490, 695
Inoue, T., Yamazaki, R., Inutsuka, S.-I., & Fikui, Y. 2012, ApJ, 744, 71
Jackson, J. M., Rathborne, J. M., Shah, R. Y., et al. 2006, ApJS, 163, 145
Jones, T. W., & Kang, H. 1993, ApJ, 402, 560
Kelner, S. R., Aharonian, F. A., & Bugayov, V. V. 2006, PhRvD, 74, 034018
Koo, B.-C., Kim, K.-T., & Seward, F. D. 1995, ApJ, 447, 211
Koo, B.-C., & Moon, D.-S. 1997a, ApJ, 475, 194
Koo, B.-C., & Moon, D.-S. 1997b, ApJ, 485, 263
Lucas, R., & Liszt, H. S. 2000, A&A, 355, 327
Padovani, M., Galli, D., & Glassgold, A. E. 2009, A&A, 501, 619
Pety, J. 2005, in SF2A-2005: Semaine de l'Astrophysique Française, ed. F. Casoli et al. (Les Ulis: EDP), 721
Ptuskin, V. S., & Zirakashvili, V. N. 2003, A&A, 403, 1
Schilke, P., Walmsley, C. M., Pineau de Forets, G., & Flower, D. R. 1997, A&A, 321, 293
Tian, W. W., & Leahy, D. A. 2013, ApJL, 769, L17
Vink, J. 2012, A&ARv, 20, 49

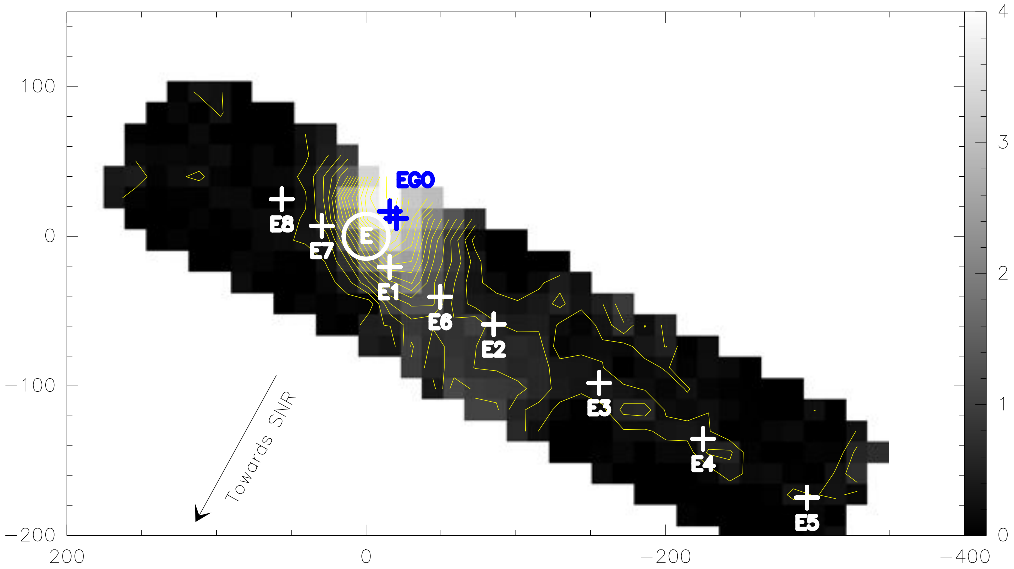

Figure 10.1: Map of the $H^{13}CO^+(1-0)$ emission (grayscale and yellow contours, levels are $0.25-4$ K km s^{-1} by 0.25 K km s^{-1}) around W51C-E (white circle, the size of the circle corresponds to the half-power beam width of the IRAM 30m telescope at the frequency of the $H^{13}CO^+(1-0)$ transition). The blue crosses show candidate protostars (Cyganowski et al., 2011). New positions are shown by white crosses (Table 10.1).

Table 10.1: Offsets w.r.t. reference position of the 8 new positions.

Source	λ ["]	β ["]
J1923-E8	56.3	24.8
J1923-E7	29.6	7.0
J1923-E	0	0
J1923-E1	-15.8	-20.5
J1923-E6	-49.5	-40.5
J1923-E2	-85.3	-58.8
J1923-E3	-155.7	-98.0
J1923-E4	-225.2	-135.4
J1923-E5	-294.7	-174.6

Note - The reference position is W51C-E at $(\alpha_{2000},\ \delta_{2000}) = (19:23:08.0,\ 14:20:00.0)$.

Table 10.2: Integrated intensities W [K. km s^{-1}], peak temperatures T_p [K] and linewidth Δv (km s^{-1}) from Gaussian fits. The center velocity v_0 [km s^{-1}] is given for $^{13}CO(1-0)$.

Pos.	v_0	$^{13}CO(1-0)$			$^{13}CO(2-1)$			$C^{18}O(1-0)$			$C^{18}O(2-1)$			$H^{13}CO^+(1-0)$			$DCO^+(2-1)$		
		W	T_p	Δv	W	T_p	Δv	W	T_p	Δv	W	T_p	Δv	W	T_p	Δv	W	T_p	Δv
E8	67.6	22.2	6.2	3.4	39.8	10.6	3.5	4.3	0.8	5.0	6.9	1.3	4.9	0.16	0.05	3.2	<0.01	<0.01	3.0
E7	67.6	43.6	10.3	4.0	32.6	10.5	2.9	10.1	2.0	4.8	15.9	3.4	4.4	1.04	0.24	4.1	0.12	0.04	2.7
E1	67.6	62.4	8.5	6.9	94.9	15.0	5.9	11.8	2.5	4.4	24.6	5.9	3.9	3.10	0.85	3.4	0.82	0.26	2.9
E6	67.6	52.9	7.9	6.3	76.3	12.9	5.6	7.8	1.4	5.2	14.7	3.0	4.6	1.79	0.41	4.1	0.26	0.06	3.9
E2	67.2	59.9	10.2	5.5	80.8	15.0	5.1	7.2	2.4	2.8	12.3	4.0	2.9	1.03	0.20	4.7	0.17	0.08	2.1
E3	66.4	22.8	4.4	4.9	37.5	7.3	4.8	1.4	0.4	3.8	2.1	0.6	3.3	<0.02	<0.01	3.0	<0.01	<0.01	3.0
E4	65.4	49.3	9.7	4.8	85.3	14.3	5.6	4.3	1.0	3.9	9.5	2.1	4.3	0.45	0.12	3.5	<0.01	<0.01	3.0
E5	60.3	8.5	2.1	3.7	23.1	3.8	5.7	0.5	0.2	2.7	<0.1	<0.1	3.0	<0.03	<0.02	3.0	<0.01	<0.01	3.0

Chapter 11

New tracers of the ionisation

Contents

11.1 Introduction

The DCO^+/HCO^+ method that was adopted in the previous work has some limitations, that have been discussed in Chapter 9: (1) there is a relatively large uncertainty in the determination of x_e and ζ in the LIP, and (2) the method only gives lower limits on ζ in the HIP. Therefore, I aimed at identifying a new set of species that would address these two limitations. Based on chemical modeling, the N_2H^+/DCO^+ and HCN/CN abundance ratios seem to be promising candidates (see below).

In March 2014, I submitted a proposal for 30m observations in the SNR W28 region, toward sight lines where I had previously determined physical conditions and the ionisation fraction (Vaupré et al., 2014). I chose two extreme sight lines: W28-N7, which is typical of a highly ionised gas position with a lower limit $\zeta > 130 \times 10^{-17}$ s^{-1}, and W28-SE1, which is representative of “standard” ionisation with $\zeta \sim 10^{-17}$ s^{-1}. Investigating further the chemical composition of these very different regions would allow to confirm or reject whether N_2H^+, HCN and CN are good tracers of the ionisation.

In the following, I describe the chemical predictions prior to observations which allowed me to suggest a few candidates. I then present the IRAM 30m observations and results for these species.

11.2 Model predictions

I run several grids of models to predict the abundance of different species as a function of the CR ionisation rate ζ. The idea was to find observable tracers of the HIP. In the HIP, the enhanced abundance of electrons and ions (e.g. He^+) favor the destruction of molecules. I looked especially for small molecules that would still be present in sufficient amounts in the HIP to be detected. In addition, I focused on species observable in the frequency range of the IRAM 30m.

From the models, a few species seemed appropriate. In Fig. 11.3, I show that the N_2H^+/HCO^+ abundance ratio should give a better determination of x_e in the LIP than DCO^+/HCO^+, as its variation is larger. Yet, the method can be limited by the uncertainty in the N_2 abundance in the ISM (Maret et al., 2006) as the N_2H^+/HCO^+ ratio roughly linearly depends on it. In addition, the N_2H^+ abundance is affected by the gaseous CO, whose abundance depends on the dust temperature (at $T_{dust} \lesssim 22$ K, CO freezes-out onto the grain mantles) and density (which determines the gas-dust coupling)

As seen in Figure 11.1, the HCN/CN ratio shows a similar dependence on N (Hily-Blant et al., 2010). However, as shown in Fig. 11.3, the dependence of N_2H^+/HCO^+ and HCN/CN on x_e are reversed. From

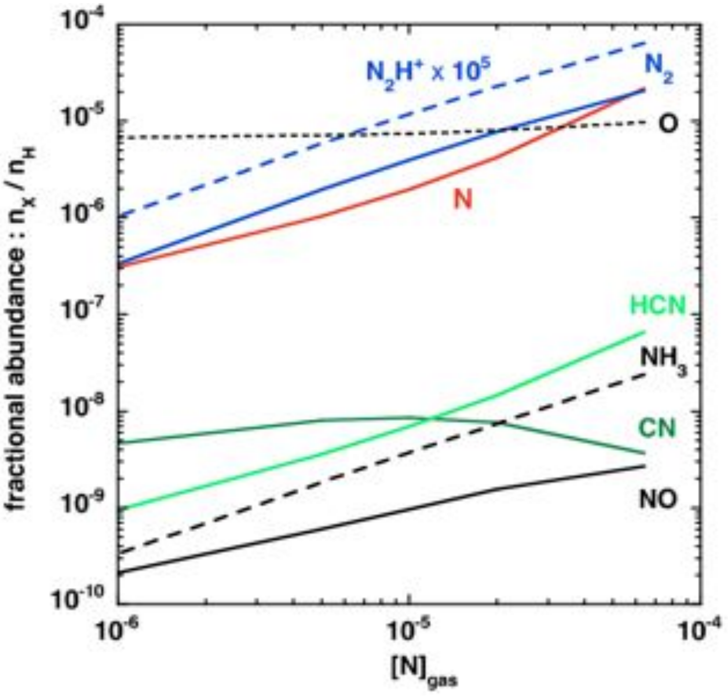

Figure 11.1: Steady-state fractional abundances of nitrogen-containing species for a density $n_{\rm H} = 10^4$ cm^{-3}, a kinetic temperature $T = 10$ K, and CR ionisation rate $\zeta = 10^{-17}$ s^{-1}. From Hily-Blant et al. (2010).

the combined use of these two ratios, we should be able to constrain the value of x_e and, hence, of ζ. As suggested by Boger and Sternberg (2005), a high ratio may be a good proxy for dense gas in the HIP. This is illustrated in Fig. 11.2 where the HCN/CN ratio decreases from ∼10 in the LIP to ∼0.01 in the HIP. Noteworthy, this ratio varies by a factor 10 across the LIP and thus provides an accurate method to measure x_e in the LIP. As in the case of N_2H^+, the situation might, in practice, be a bit more complicated, as HCN and CN are abundant in the skin (PDR) of the cloud.

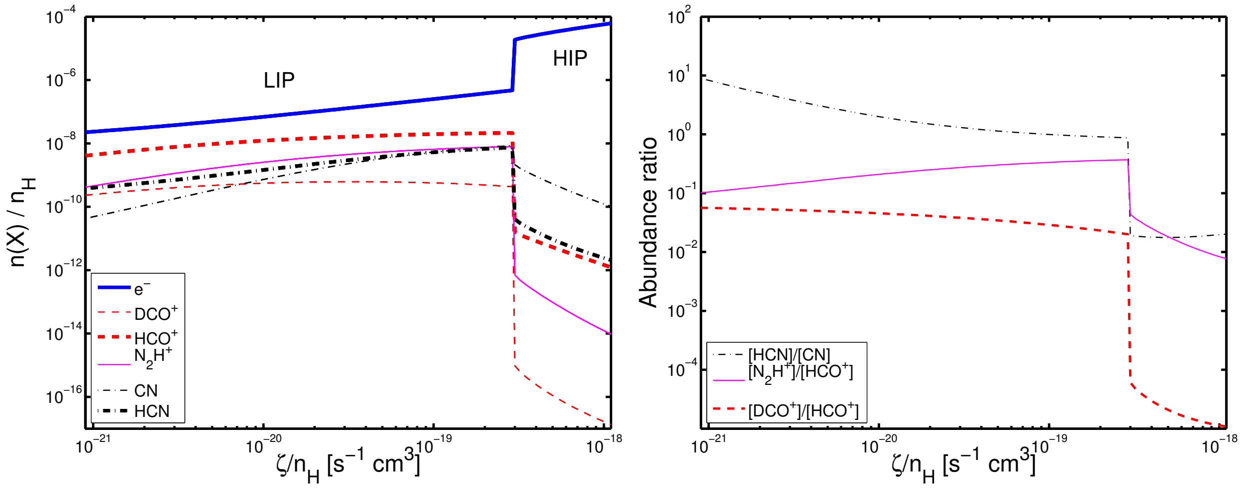

Figure 11.2: **Left:**Chemical abundance of species candidate as new tracers as a function of $\zeta/n_{\rm H}$, at $T = 10$ K. Whereas the abundance of DCO$^+$ drops very low (x(DCO$^+$ $\sim 10^{-16}$), other species are are still present in the HIP with higher abundances ($x \gtrsim 10^{-14} - 10^{-16}$). **Right:** Abundance ratios between species of left panel. Used together, they could allow a better constrain of x_e and ζ.

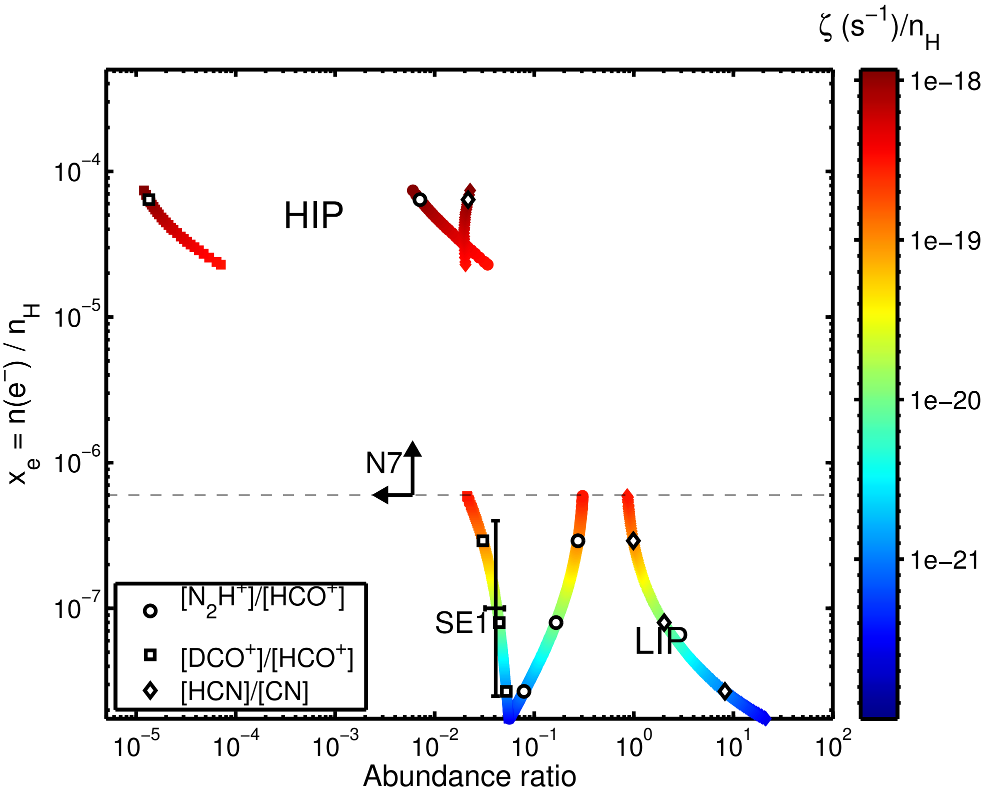

Figure 11.3: The ionization fraction x_e as a function of the different abundance ratios suggested here. Previous observations of DCO^+/HCO^+ at N7 and SE1 (Vaupré et al., 2014) are reported here. Predictions for N_2H^+/HCO^+ and HCN/CN suggest they may be good tracers of the HIP and may allow a more precise measurement of ζ in the LIP.

11.3 Observations and results

The observations of various lines from species that might be used to constrain ζ were carried out between September and October 2014. Specifically, we observed: $N_2H^+(1-0)$, $CCH(1-0)$, $H^{13}CN(1-0)$, $HNC(1-0)$, $HCN(1-0)$ and $CN(1-0)$. The list of the transitions is reported in Table 11.1. During these observations, I obtained high-resolution observations, with a very low noise ($\sigma \approx 7mK$). I used the same procedure for observations and data analysis as before, deriving integrated intensities with GILDAS and column densities with non-LTE LVG calculations.

The hyperfine structure of HCN was not resolved and blended velocity components didn't allow the derivation of integrated intensities. Instead, I used the isotopologue $H^{13}CN$, for which only the dominant HFS component was detected (but not at all positions). The hyperfine structures of CCH, CN and N_2H^+ were resolved and the different HFS components could be used independently in the LVG calculations. Constrained HFS fits were performed in CLASS. In Table 11.2, I report the center velocity and linewidth of the dominant HFS component, together with the integrated intensities of each HFS component, corresponding to frequencies defined in Table 11.1.

Finally, using physical conditions previously derived in W28 from CO (Vaupré et al., 2014), I derived column densities for all species, which are listed in Table 11.3. Ratios are plotted in Figure 11.4. The column density of HCN have been derived from $H^{13}CN$, assuming the isotopic ratio $^{12}C/^{13}C \approx 50$.

Table 11.1: Transitions observed to identify new tracers of ζ. Frequencies of the hyperfine structure components are marked as ν_i.

	$H^{13}CN(1-0)$	$HCN(1-0)$	$CCH(1-0)$	$HNC(1-0)$	$N_2H^+(1-0)$	$CN(1-0)$
ν_1	86.3400	88.6316	87.2841	90.6636	93.1716	113.4881
ν_2	-	-	87.3168	-	93.1735	113.4909
ν_3	-	-	87.3285	-	93.1763	113.4996
ν_4	-	-	87.4019	-	-	113.5089
ν_5	-	-	87.4071	-	-	113.5204
ν_6	-	-	87.4464	-	-	-

11.4 Discussion

Figure 11.4 shows no clear evidence of a correlation between the plotted abundance ratios and the previously determined ionisation at each position. All $N_2H^+/H^{13}CO^+$ are for instance consistent within error bars, regardless of the ionisation. As a comparison, the DCO^+/HCO^+ ratio is significantly higher in W28-SE1, where the ionisation is standard, than in several positions where only upper limits were derived, revealing high CR ionisation rates.

The derivation of the column density of CN in W28-SE1 is complicated by blended velocity components. Additional care should be given to this transition to derive reliable values. I didn't have time to go further with this study, and focused in the following on the N_2H^+/HCO^+ ratio and how it could be used together with DCO^+/HCO^+ to better constrain on the CR ionisation rate (see Chapter 12).

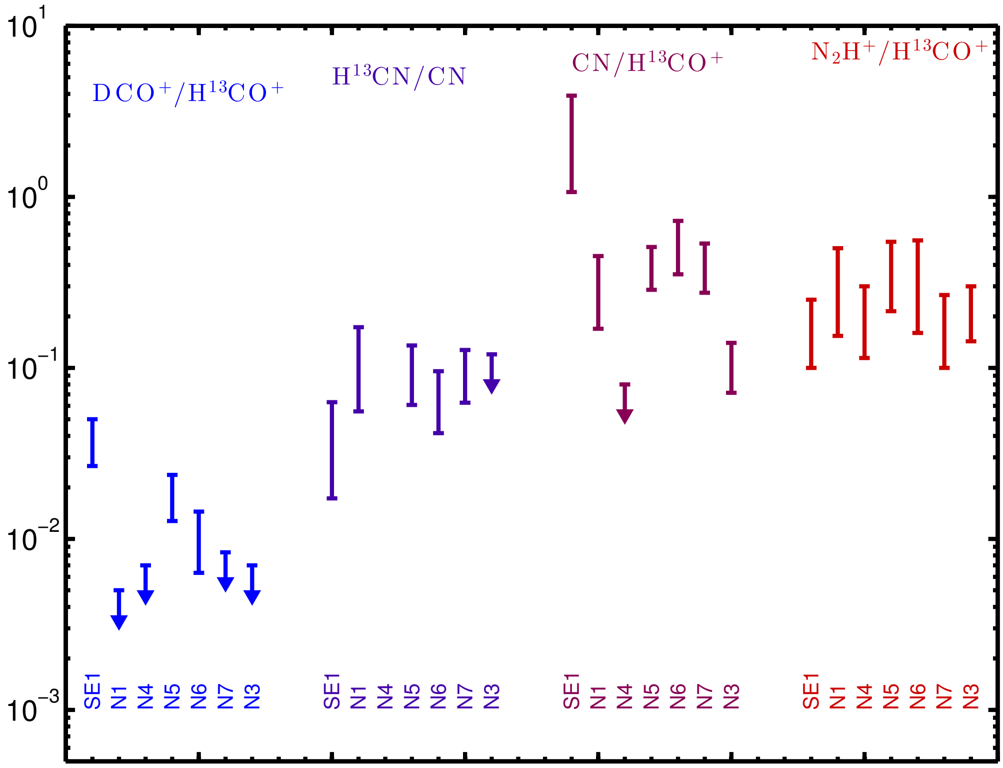

Figure 11.4: Abundance ratios or upper limits for the candidate tracers of the ionisation.
Notes: W28-SE1 is the position where we found a standard CR ionisation rate ; positions are sorted by increasing ζ, based on Vaupré et al. (2014) ; the derivation of the column density of CN in W28-SE1 is complicated by blended velocity components, and the value given here has to be considered tentative ; error bars derive from uncertainties on the column densities.

Table 11.2: Integrated intensities W [K km s^{-1}] from Gaussian fits or HFS fits when applicable, using CLASS. In each case, the central velocity v_0 [km s^{-1}] and linewidth Δv [km s^{-1}] of the main component are given. The HFS component W_i refer to frequencies ν_i defined in Table 11.1.

Pos.	CCH(1-0)								N$_2$H$^+$(1-0)					H^{13}CN(1-0)†			HNC(1-0)			CN(1-0)						
	v_0	Δv	W_1	W_2	W_3	W_4	W_5	W_6	v_0	Δv	W_1	W_2	W_3	v_0	Δv	W_1	v_0	Δv	W_1	v_0	Δv	W_1	W_2	W_3	W_4	W_5
N1	20.4	2.8	0.06	0.46	0.26	0.26	0.11	0.06	20.2	2.2	1.23	2.03	0.41	19.9	2.3	0.09	20.2	2.5	3.03	19.8	1.9	0.27	0.48	0.17	0.40	0.16
N5	20.5	2.3	0.04	0.40	0.20	0.20	0.08	0.04	20.4	2.0	2.05	3.41	0.68	19.7	2.2	0.15	20.2	2.2	5.18	20.1	2.1	0.59	1.08	0.27	0.58	0.14
N6	20.7	1.8	0.08	0.60	0.35	0.35	0.16	0.08	20.5	2.1	4.24	6.86	1.44	19.8	2.0	0.30	20.6	2.7	8.13	20.6	2.2	1.26	2.33	0.55	1.19	0.24
N2	21.1	2.8	0.61	4.2	2.5	2.5	1.1	0.61	21.0	3.0	9.32	15.30	3.13	20.3	4.2	4.54	21.2	5.0	16.1	19.7	2.3	2.43	4.16	1.23	1.84	0.26
N7	22.2	1.8	0.03	0.29	0.15	0.15	0.06	0.03	22.1	1.4	0.39	0.65	0.13	21.6	1.3	0.05	22.5	2.0	1.89	22.6	2.2	0.29	0.73	0.16	0.31	0.06
N8	18.8	4.6	<0.02	0.41	0.21	0.21	<0.02	<0.02	-	-	<0.03	<0.03	<0.03	-	-	<0.012	19.5	5.8	0.93	-	-	< 0.05	< 0.05	< 0.05	< 0.05	< 0.05
N3	16.2	2.5	0.04	0.37	0.19	0.19	0.08	0.04	16.1	2.5	1.15	1.92	0.39	-	-	<0.012	15.3	2.2	1.33	15.3	1.7	0.14	0.31	0.06	0.20	0.02
N4	19.6	3.8	0.07	0.55	0.31	0.31	0.13	0.07	20.4	1.8	0.71	1.18	0.24	-	-	<0.011	20.3	3.2	0.86	-	-	< 0.07	< 0.07	< 0.07	< 0.07	< 0.07
SE1	17.3	1.8	0.57	4.6	2.6	2.6	1.1	0.57	16.9	0.6	0.23	0.34	0.08	14.2	2.4	0.11	16.2	4.8	2.84	15.1	4.0	0.92	2.11	0.69	0.88	0.13
SE2	8.8	3.8	0.05	0.51	0.26	0.26	0.10	0.05	-	-	-	-	-	-	-	<0.011	9.0	2.9	0.24	-	-	< 0.10	< 0.10	< 0.10	< 0.10	< 0.10
SW2	9.8	1.3	0.04	0.22	0.16	0.16	0.08	0.05	-	-	-	-	-	-	-	<0.012	9.8	1.6	0.54	9.7	1.7	0.21	0.95	0.21	0.34	0.08
SW4	10.0	2.4	0.10	0.97	0.49	0.49	0.20	0.10	-	-	-	-	-	-	-	<0.015	10.2	2.1	1.44	10.2	2.0	0.59	2.28	0.64	0.71	0.09

Note - †Only the main HFS component of the H^{13}CN$(1-0)$ transition is reported here, when detected. The HCN$(1-0)$ transition shows blended velocity components and is not reported.

Table 11.3: Column densities derived from LVG calculations, using physical conditions previously determined from CO (Vaupré et al., 2014). Column densities of H^{13}CO$^+$ and DCO$^+$ are also taken from previous work.

Pos.	N(N$_2$H$^+$) [10^{13} cm^{-2}]	N(CCH) [10^{14} cm^{-2}]	N(CN) [10^{13} cm^{-2}]	N(H^{13}CN) [10^{12} cm^{-2}]	N(H^{13}CO$^+$) [10^{12} cm^{-2}]	N(DCO$^+$) [10^{12} cm^{-2}]
N1	$1.0-2.0$	$0.3-2.8$	$1.1-1.8$	$1.0-1.9$	$0.8-1.3$	<0.22
N5	$1.5-3.0$	$0.2-2.5$	$2.0-2.8$	$1.7-2.7$	$1.1-1.4$	$0.89-1.30$
N6	$2.0-5.0$	$0.5-3.2$	$4.4-6.5$	$2.7-4.2$	$1.8-2.5$	$0.79-1.30$
N2	$3.5-10$	$2.8-10$	$9.0-14$	$19-48$	$5.6-8.9$	$1.10-2.00$
N7	$0.4-0.8$	$0.3-2.2$	$1.1-1.6$	$1.0-1.4$	$0.6-0.9$	<0.25
N8	< 0.5	$0.3-2.8$	< 0.4	<0.7	<0.2	<0.35
N3	$1.0-1.5$	$0.3-2.2$	$0.5-0.7$	<0.6	$1.0-1.4$	<0.35
N4	$0.8-1.5$	$0.4-3.5$	< 0.4	<0.6	$1.0-1.4$	<0.35
SE1	$0.3-0.5$	$3.2-10$	$4.0-6.5$†	$1.4-2.1$	$0.4-0.56$	$0.79-1.0$
SE2	-	$0.4-2.8$	< 0.5	<0.6	<0.2	<0.28
SW2	-	$0.2-2.5$	$1.4-2.2$	<0.6	<0.1	<0.22
SW4	-	$0.7-2.8$	$3.6-5.5$	<0.6	<0.25	<0.25

Note - Error bars of CCH$(1-0)$ are very large, due to inconsistent determinations of column densities from the different HFS components.

† In W28-SE1, CN$(1-0)$ shows two blended velocity components, at 15 and 17 km s^{-1}, that make it difficult to measure the integrated intensity at this position. Tentative values are reported for the component at 15 km s^{-1}, whereas intensities of other species (HCO$^+$, DCO$^+$, ...) are given for the component at 17 km s^{-1}. Additional care would be needed to try to discriminate between the two components for CN$(1-0)$.

Chapter 12

The W44 SNR-cloud association

Contents

12.1 Introduction

W44 represents the third source where we carried out a study of the ionisation of molecular clouds close to a SNR. As in the two previous regions, W51 and W28, we used the R_D=DCO$^+$/HCO$^+$ abundance ratio to constrain the CR ionisation rate ζ. However, the analysis of the W28 region showed the limit of this method (see Chapter 9). So we started the study of other tracers of ζ (Chapter 11). In the present work, we focus on the R_N=N$_2$H$^+$/HCO$^+$ abundance ratio. We describe here briefly why this ratio is potentially a good ζ tracer. In a following section, we will show specific chemical predictions that will allow us to use it in practice.

Similarly to HCO$^+$, N$_2$H$^+$ is formed by the reaction of H$_3^+$ with N$_2$:

$$\mathrm{H_3^+ + N_2 \rightarrow N_2H^+ + H_2}\ , \tag{12.1}$$

and similarly to HCO$^+$, in standard ionisation conditions, N$_2$H$^+$ is mainly destroyed by reactions with CO and electronic recombination:

$$\mathrm{N_2H^+ + CO \rightarrow HCO^+ + N_2} \tag{12.2}$$

$$\mathrm{N_2H^+ + e^- \rightarrow H\ + N_2}. \tag{12.3}$$

Interestingly, the destruction of N_2H^+ by CO forms HCO^+, as does the destruction by CO of HCO^+ itself:

$$HCO^+ + CO \rightarrow HCO^+ + CO \tag{12.4}$$

$$HCO^+ + e^- \rightarrow H + CO \; . \tag{12.5}$$

This implies that, for low electron abundances, the destruction of N_2H^+ is dominated by the reaction with CO, which forms HCO^+: therefore, in this regime, the $R_N = N_2H^+/HCO^+$ abundance ratio will be much lower than the N_2/CO abundance ratio. On the contrary, when electron recombination is the main destruction route of N_2H^+ (and HCO^+), R_N will approach the N_2/CO abundance ratio (see also Ceccarelli et al. 2014 and Morales et al. 2014). In summary, the R_N ratio is predicted to be very sensitive to the CR ionisation rate, as CR form H_3^+ and, consequently, N_2H^+ and HCO^+, and also govern the electron fraction. In addition, the R_N ratio will also be sensitive to the N_2/CO abundance ratio, especially in case of large CR ionisation rates. Last, the R_N ratio is not as sensitive to the gas temperature as the R_D ratio, where this dependence is exponential, which makes it useless in warm gas. On the contrary, the R_N ratio can still be used also in those cases, which, by the way, may indeed be the regions with the largest CR ionisation rate.

In the following, we will quantify these predictions and compare the observations obtained towards W44 with a numerical chemical model.

12.2 W44: Source background and strategy of observations

W44 (Westerhout, 1958) is a very well studied mixed-morphology SNR, with a radio shell extending over $\sim 30'$ (Rho and Petre, 1998) and concentrated X-ray emission. W44 is believed to be in a radiative phase, with an age of $\sim 2 \times 10^4$ yr, consistent with the age of the associated pulsar (Wolszczan et al., 1991). A Heliocentric distance of ~ 3 kpc was determined by HI 21cm absorption measurements (Radhakrishnan et al., 1972), and the angular size of the SNR radio shell at this distance corresponds to a linear size ~ 26 pc.

Figure 12.1 shows the W44 region, with a nearby molecular cloud traced by $^{12}CO(1-0)$ (Dame et al., 2001). Large evidence exists of the gas interaction with the SNR, based on both line broadening (Wootten, 1977) and the presence of OH masers (Claussen et al., 1997) which mark the presence of shocked gas. Recently, characteristic spectral features of π^0-decay were found in the extended GeV emission observed by AGILE and *Fermi*-LAT. This provides us with observational constraints to the low-energy tail of the gamma-ray emission (Giuliani and Collaboration, 2011; Ackermann and Collaboration, 2013). These features brought strong evidence of the presence of CR protons irradiating the dense gas. The AGILE (0.4–3 GeV) and *Fermi*-LAT (2–10 GeV) maps show spatially structured gamma-ray emission well correlated with the 1.4 GHz radio continuum. However, the gamma-ray emission at the upper energy end shows a strong emission from the North-East which is not seen in the AGILE data (e.g Yoshiike et al., 2013). These authors also studied the region and concluded that the low-energy target particles involved in the π^0-decay process of gamma-ray production are dominated by molecular hydrogen.

In this context, the neutral gas in the vicinity of SNR W44 is an ideal target to look for enhanced ionisation, which would prove that gamma rays are generated by hadronic processes, namely nuclei rather than electrons. Specifically, there are three peaks of gamma-ray intensity, one of them at the southeast of the remnant, which also coincides with a maximum of CO emission. We focused our study towards this region (Figure 12.1, black box). At this scope, we adopted the same strategy than that adopted to study the ionisation in the W28 association, namely mapping the HCO^+ and CO line emission. Then, in regions of high HCO^+ emission and roughly probing the cloud across the SNR shock direction, we obtained more sensitive observations of CO isotopologues, DCO^+, N_2H^+, and HCO^+, in order to put constraints on the physical conditions and on the ionisation fraction.

12.3 Observations and results

12.3.1 Observations

Observations were carried out in July 2014, with the IRAM 30m telescope. We used the EMIR bands with the Fast Fourier Transform Spectrometer as a backend with 200 kHz spectral resolution for the mapping,

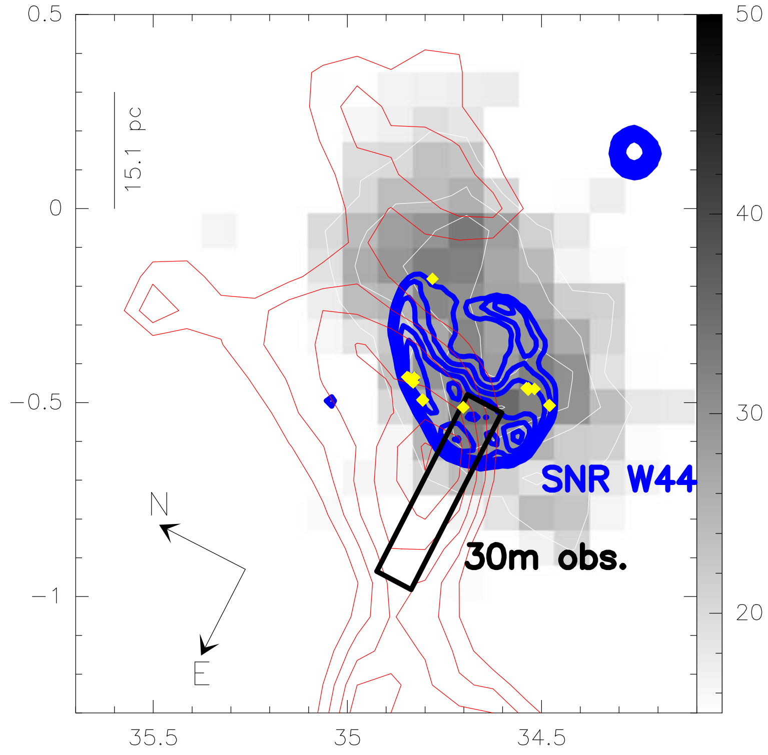

Figure 12.1: The W44 complex. The grayscale (in counts/pixel) and white contours (levels are 20 − 50 counts/pixel by 5 counts/pixel) show the 2 − 100 GeV gamma-ray count map by *Fermi*-LAT (Uchiyama et al., 2012). Red contours (levels are 30 – 70 K km s^{-1} by 5 K km s^{-1}) show ^{12}CO emission (Dame et al., 2001) integrated over 40 – 50 km s^{-1}. Blue contours (levels are 0.3 – 2 K by 50 mK) show 10 GHz free-free emission (Handa et al., 1987) and trace the SNR shell. Yellow diamonds show the locations of OH masers in the region (Claussen et al., 1997). Finally, the black box shows the limits of our IRAM 30m observations. The main axis of the box is perpendicular to the SNR shock and overlays the densest region of the cloud.

Table 12.1: Summary of the W44 IRAM-30m observations.

Species	Line	Frequency [GHz]	$F_{\rm eff}$	$B_{\rm eff}$	HPBW [arcsec]	$T_{\rm sys}$ [K]	σ_{rms} [mK]
$H^{13}CO^+$	(1-0)	86.754	0.95	0.81	29	120 – 230	18 – 80
N_2H^+	(1-0)	93.172	0.95	0.80	26	100 – 150	23 – 55
N_2H^+	(1-0)	93.174	0.95	0.80	26	100 – 150	23 – 55
N_2H^+	(1-0)	93.176	0.95	0.80	26	100 – 150	23 – 55
$C^{18}O$	(1-0)	109.782	0.95	0.79	22	140 – 290	30 – 80
^{13}CO	(1-0)	110.201	0.95	0.79	22	140 – 290	25 – 90
DCO^+	(2-1)	144.077	0.92	0.74	16	120 – 380	24 – 140
$C^{18}O$	(2-1)	219.560	0.94	0.61	11	390 – 1300	150 – 500
^{13}CO	(2-1)	220.399	0.94	0.61	11	390 – 1300	140 – 500

Note - $T_{\rm sys}$ indicates the range of system temperatures during the observing run, and the corresponding sensitivities. The adopted values of the telescope parameters follow from the IRAM observatory recommendations: $F_{\rm eff}$ and $B_{\rm eff}$ are the forward and main-beam efficiencies of the telescope, respectively; HPBW is the half-power beam width.

providing us with nearly 16 GHz instantaneous bandwidth. For pointing observations, we used 50 kHz spectral resolution. The observations consisted in a 10′ × 30′ mapping of the area and on pointed long integrations towards 27 positions distributed over the mapped area. All the observations were performed in the position-switching mode, using OFF positions 1600" to the West. Amplitude calibration was done typically every 15 minutes, and pointing and focus were checked every 1 and 3 hours, respectively, ensuring

Table 12.2: Offsets (in ") from the J2000=(18:57:24.50, 01:17:45.4) reference position of the 27 lines of sight.

Position	dx	dy	Position	dx	dy	Position	dx	dy
W44-E1	-339	43	W44-G5	-300	-60	W44-G14	-380	60
W44-E3	-260	-59	W44-G6	-260	140	W44-G15	-380	20
W44-E2	-283	9	W44-G7	-420	20	W44-L1	-220	-20
W44-E4	-240	131	W44-G8	-420	100	W44-L2	-140	-20
W44-E11	239	-92	W44-G9	-340	100	W44-L3	-60	-20
W44-G1	-260	20	W44-G10	-420	-60	W44-L4	20	-20
W44-G2	-260	100	W44-G11	-340	-60	W44-L5	100	-20
W44-G3	-260	-20	W44-G12	-180	100	W44-L6	180	-20
W44-G4	-260	60	W44-G13	-420	60	W44-L7	260	-20

$\approx$2" pointing accuracy. All spectra were reduced using the CLASS package of the GILDAS[1] software. Residual bandpass effects were subtracted using low-order (≤ 3) polynomials. The weather was good and $T_{\rm sys}$ values were typically lower than 300 K at 3 mm. Thanks to the large instantaneous bandwidth available, several species could be observed simultaneously. The observations and observed molecular transitions are summarised in Table 12.1, along with the associated system temperature and sensitivity ranges $T_{\rm sys}$, and $\sigma_{\rm rms}$ obtained during the successive runs of observations. In the following, all spectra are presented in main-beam temperature scale, $T_{\rm mb} = (F_{\rm eff}/B_{\rm eff})T^{*}_{\rm ant}$, with $F_{\rm eff}$ and $B_{\rm eff}$ the forward and main-beam efficiencies of the telescope, respectively. The coordinates of the 27 positions we explored are listed in Table 12.2. Observations at 1.3 mm of ^{13}CO$(2-1)$ and C^{18}O$(2-1)$ transitions were obtained towards 16 of these 27 positions.

12.3.2 Spatial distribution of the molecular emission

The area covered with the IRAM-30m is delineated in Figure 12.1, and was obtained simultaneously in ^{13}CO$(1-0)$, C^{18}O$(1-0)$, HCO$^+(1-0)$, and N$_2$H$^+(1-0)$. The maps in C^{18}O, HCO$^+$, and N$_2$H$^+$ are shown in Figure 12.1, with the SNR located towards the right. Globally, the morphology is similar for the three tracers, with the line emission being brighter behind the shock front, traced by the 10 GHz continuum emission, and decreasing moving upstream. When inspected into more details, the N$_2$H$^+$ line emission appears spatially shifted from the C^{18}O, whilst it correlates well with that of HCO$^+$. The DCO$^+$ line emission measured towards the 27 positions also appears correlated with that of the N$_2$H$^+$ and HCO$^+$ lines, although no trend with the distance from the shock front is evident. Indeed, the distribution of the DCO$^+$ detections does not show any trend with the distance from the SNR shock, as DCO$^+$ detections and non-detections alternate without a particular apparent order (Figure 12.1). On the contrary, there seems to be a correlation between the local maxima of N$_2$H$^+$ emission and DCO$^+$ detections.

12.3.3 Line properties

The spectra towards the 27 positions are presented in Fig. 12.3. The CO lines show several velocity components, as in the case of W28, reflecting the presence of several clouds/components on the line of sight. In contrast, higher density tracers, such as N$_2$H$^+$, show a single velocity component in all instances. Results from Gaussian fits of CO isotopologues, HCO$^+$, DCO$^+$ and N$_2$H$^+$ are given in Tables 12.3 and 12.4. In the following, the two lowest rotational transitions of ^{13}CO and C^{18}O are used together with the hyperfine structure transitions N$_2$H$^+(1-0)$, when detected, to derive the physical conditions in the cloud.

---

[1] `http://www.iram.fr/IRAMFR/GILDAS/`

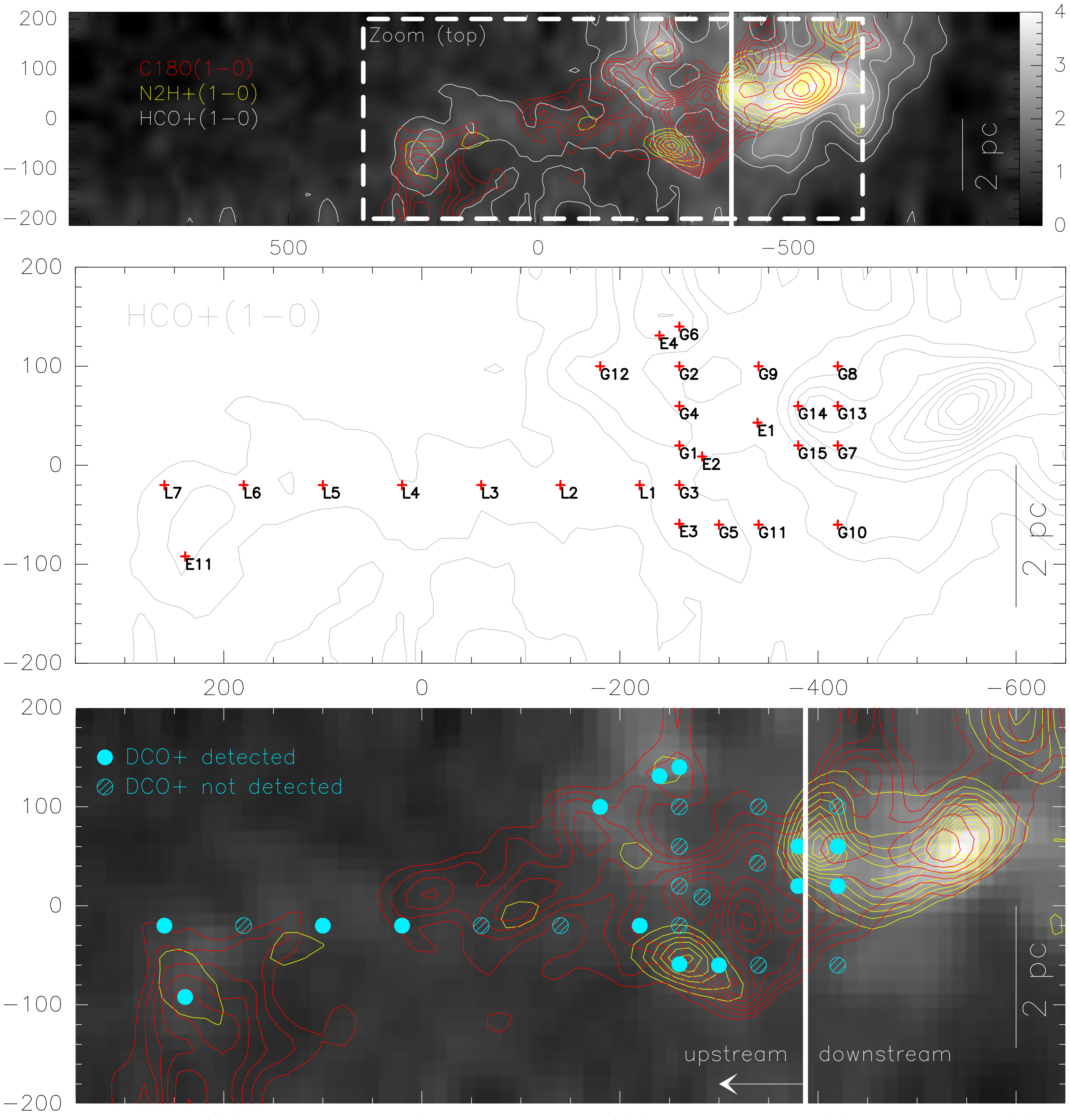

Figure 12.2: Maps of the molecular emission towards W44 (offsets in arcsec). The grayscale (in K km s^{-1}) and gray contours (levels are $1-6$ K km s^{-1} by 0.5 K km s^{-1}) show $HCO^+(1-0)$ observations. Overlaid are $N_2H^+(1-0)$ contours (yellow, levels are $1-6$ K km s^{-1} by 0.5 K km s^{-1}) and $C^{18}O(1-0)$ contours (red, levels are $3-6$ K km s^{-1} by 0.5 K km s^{-1}). The approximate position of the SNR shock from 10 GHz emission is shown by the thick white line **Middle:** Location of the 27 positions observed with high signal-to-noise ratio. **Bottom:** Zoom on the white box (top panel). Observed positions are marked by filled or hatched circles, whether DCO^+ was detected or not, respectively. The size of the circles corresponds to the half-power beam width of the IRAM 30m telescope at the frequency of the $DCO^+(2-1)$ transition.

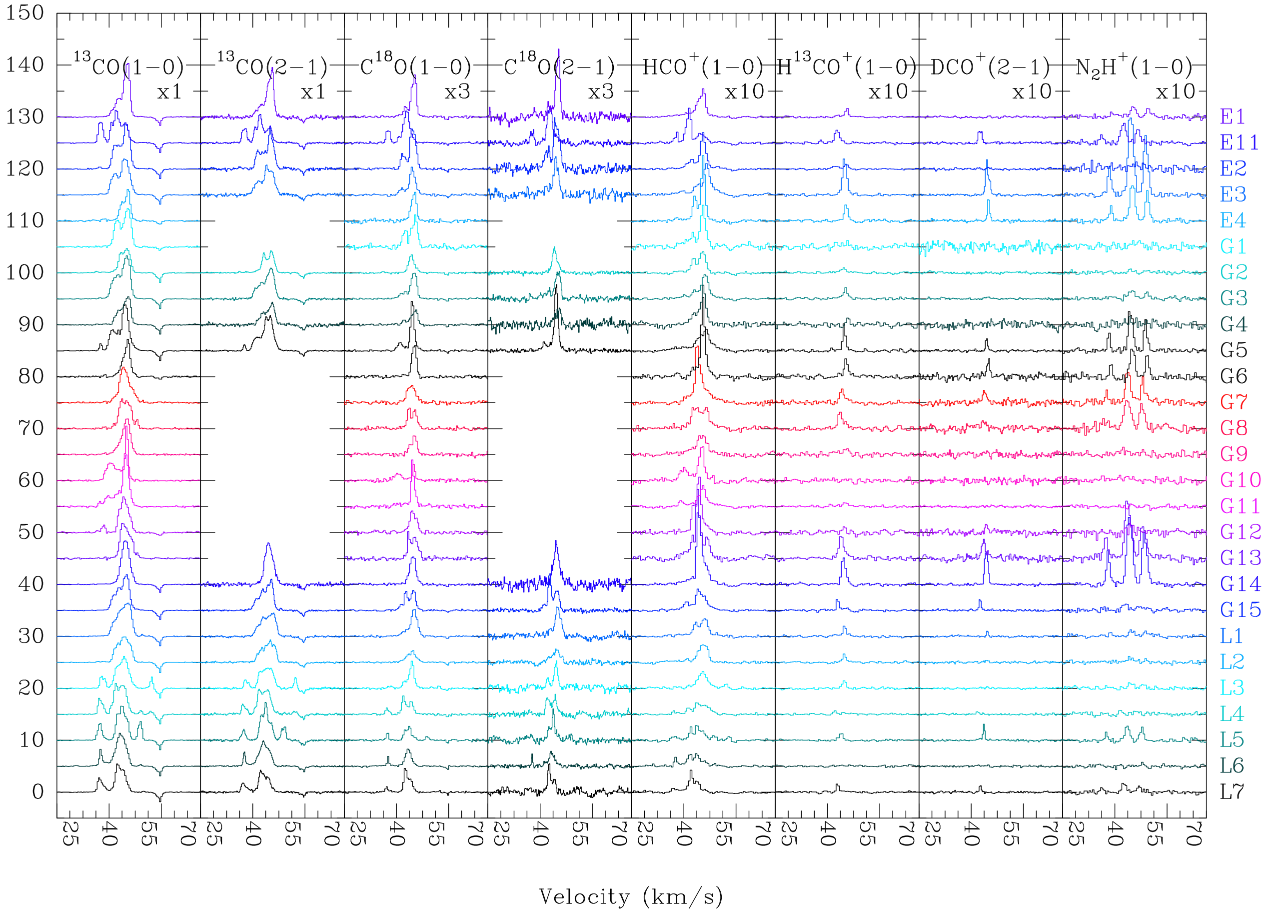

Figure 12.3: Spectra towards the 27 positions in the main-beam temperature scale. Some spectra are scaled to fit in a single scale.

Table 12.3: Results from the Gaussian fits of the emission lines of ^{13}CO and C^{18}O.

Pos.	^{13}CO(1 – 0)				^{13}CO(2 – 1)				C^{18}O(1 – 0)				C^{18}O(2 – 1)			
	v_0	W	$T_{\rm peak}$	Δv	v_0	W	$T_{\rm peak}$	Δv	v_0	W	$T_{\rm peak}$	Δv	v_0	W	$T_{\rm peak}$	Δv
E1	47.0	22.4	9.5	2.2	47.1	19.3	7.9	2.3	46.8	5.8	2.7	2.1	46.9	6.9	4.0	1.6
E2	47.0	22.2	7.5	2.8	46.9	20.7	7.1	2.7	46.4	7.2	2.6	2.6	42.6	2.8	1.2	2.2
E3	46.2	28.4	7.1	3.8	46.2	25.1	5.3	4.5	46.1	4.5	1.7	2.5	46.2	4.4	2.1	2.0
E4	47.4	11.5	5.9	1.8	-	-	-	-	46.7	4.4	1.8	2.3	-	-	-	-
E11	42.8	15.2	6.1	2.3	42.8	11.7	5.4	2.0	43.9	6.3	1.9	3.1	43.8	6.0	2.2	2.5
G1	47.2	23.9	7.6	3.0	-	-	-	-	47.0	5.1	1.8	2.6	-	-	-	-
G3	46.9	25.2	8.0	3.0	47.1	16.3	5.4	2.8	46.8	4.3	1.7	2.4	46.7	4.6	1.7	2.5
G4	47.4	12.2	4.7	2.4	47.6	8.8	3.6	2.3	46.9	2.9	0.9	3.1	46.8	2.7	0.8	3.0
G5	46.2	29.1	8.8	3.1	46.1	29.4	6.8	4.1	46.1	5.4	3.2	1.6	46.2	7.3	4.2	1.6
G6	47.2	22.3	7.2	3.0	-	-	-	-	46.8	4.4	2.1	2.0	-	-	-	-
G7	46.0	33.3	6.4	4.9	-	-	-	-	45.7	4.5	1.1	3.8	-	-	-	-
G8	44.9	15.6	5.2	2.8	-	-	-	-	44.7	1.9	1.4	1.3	-	-	-	-
G9	46.6	27.5	6.6	3.9	-	-	-	-	47.1	2.4	1.3	1.8	-	-	-	-
G10	46.7	15.5	10.2	1.4	-	-	-	-	46.7	1.1	1.0	1.1	-	-	-	-
G11	46.4	31.1	9.2	3.2	-	-	-	-	46.2	4.5	2.8	1.5	-	-	-	-
G12	46.4	20.7	5.2	3.7	-	-	-	-	46.4	4.5	1.3	3.2	-	-	-	-
G13	45.0	8.4	3.9	2.0	-	-	-	-	44.6	1.2	1.5	0.7	-	-	-	-
G14	46.3	33.8	8.5	3.7	46.2	31.3	7.9	3.7	46.3	5.2	1.8	2.7	46.3	7.2	2.3	2.9
G15	43.7	7.9	3.7	2.0	44.0	7.1	3.8	1.8	43.7	1.9	1.2	1.4	43.7	3.2	2.5	1.2
L1	47.7	12.1	4.2	2.7	48.0	8.6	3.2	2.5	46.9	4.8	1.7	2.7	46.9	5.0	1.8	2.6
L2	46.1	25.2	5.0	4.7	47.2	14.6	3.8	3.6	46.4	1.7	0.5	3.3	46.4	2.6	0.8	3.3
L3	45.8	26.3	5.9	4.2	46.4	16.6	4.1	3.8	46.0	3.3	1.6	1.9	46.1	3.0	1.7	1.7
L4	42.5	12.0	4.8	2.3	42.4	8.6	3.9	2.1	42.8	2.0	1.1	1.7	43.0	2.1	1.1	1.8
L5	45.0	9.6	5.9	1.5	45.0	9.2	6.7	1.3	45.0	1.2	0.9	1.3	45.1	1.9	2.0	0.9
L6	44.6	30.5	6.2	4.6	44.5	22.6	4.4	4.8	44.5	3.2	1.1	2.8	44.5	2.6	0.8	3.0
L7	43.1	9.6	4.4	2.0	43.1	7.2	3.4	2.0	43.4	1.9	1.4	1.2	43.5	2.5	1.8	1.3

Note - v_0, centre line LSR velocity (km s^{-1}), the integrated intensity W (K km s^{-1}) and the peak temperature $T_{\rm peak}$ (in K) in main-beam scale, and the FWHM Δv (in km s^{-1}). In case of non-detections, upper limits are given at the 1 σ level. Uncertainties are dominated by calibration ($\sim$ 20 %).

12.4 Analysis

12.4.1 Physical conditions and column densities

The physical conditions are derived from χ^2 minimisation of the observed integrated intensities of CO isotopologues as compared to LVG predictions, in a similar fashion as for W28 (Section 7.3.2). This could be done for the 16 positions for which ^{13}CO(2 – 1) and C^{18}O(2 – 1) lines were observed, out of the 27 lines of sight. The kinetic temperature is well constrained, ranging from 7 to 17 K. This temperature range is slightly narrower than towards W28, and somewhat lower. The CO column density is also in general well constrained. In contrast to W28, the H_2 density remains degenerate in several cases. Towards 9 out of the 16 positions, the N_2H^+(1 – 0) hyperfine structure was also observed and compared with the relevant LVG predictions. The combined minimization of the CO and N_2H^+ lines alleviates, or even breaks, the degeneracy on the H_2 density. This leads to derived densities of typically $\sim 10^5$ cm^{-3}, larger than the clouds next to W28 by about an order of magnitude. Note that, in order to use N_2H^+, the N_2H^+/CO abundance ratio was treated as a free parameter, for each position independently. In practice, the χ^2 minimisation procedure was repeated for different values of the N_2H^+/CO abundance ratio for each point. The set of N_2H^+/CO abundance ratio, N_2H^+ and CO column densities, H_2 density and temperature with the lowest χ^2 (in each position) was finally adopted (see Figure 7.8).

The column densities of H^{13}CO$^+$ and DCO$^+$ are derived from the LVG predictions, adopting the physical conditions derived from the CO and N_2H^+ analysis, described above. Even for positions where N_2H^+ is not detected, and where the gas density is poorly constrained (positions G4, G15, L2, L3, L4, L6), the N(HCO$^+$) and N(DCO$^+$) column densities are constrained within a factor ~10. The results of the χ^2 minimisation analysis are summarised in Table 12.5.

Table 12.4: Results from the Gaussian fits of the emission lines of $H^{13}CO^+$, DCO^+ and N_2H^+.

Pos.	$H^{13}CO^+(1-0)$				$DCO^+(2-1)$				$N_2H^+(1-0)$				
	v_0	W	T_{peak}	Δv	v_0	W	T_{peak}	Δv	v_0	W_1	W_2	W_3	Δv
E1	47.5	0.23	0.21	1.0	-	<0.01	<0.02	3.0	46.9	0.36	0.56	0.13	1.5
E2	47.2	0.17	0.09	1.8	-	<0.01	<0.03	3.0	-	<0.01	<0.07	<0.04	-
E3	46.6	1.44	0.74	1.8	46.0	0.68	0.75	0.9	46.0	2.48	4.03	0.84	1.7
E4	47.2	0.53	0.35	1.4	46.7	0.44	0.53	0.8	46.6	1.05	1.69	0.35	1.3
E11	43.7	0.57	0.26	2.0	43.5	0.41	0.25	1.6	43.1	0.63	1.00	0.22	1.7
G1	47.6	0.13	0.17	0.7	-	<0.08	<0.14	3.0	-	<0.01	<0.06	<0.04	-
G3	47.0	0.41	0.25	3.0	-	<0.01	<0.03	3.0	46.3	0.29	0.49	0.10	2.5
G4	48.0	0.14	0.25	0.5	-	<0.06	<0.10	3.0	-	<0.01	<0.07	<0.04	-
G5	46.4	0.69	0.61	1.1	46.0	0.23	0.28	0.8	45.9	1.02	1.62	0.35	1.0
G6	47.2	0.58	0.37	1.5	46.7	0.45	0.32	1.3	46.6	0.78	1.20	0.27	1.1
G7	45.6	0.54	0.27	1.9	45.2	0.43	0.22	1.8	44.9	0.87	1.43	0.29	1.5
G8	44.9	0.68	0.33	1.9	-	<0.05	<0.08	3.0	44.6	1.19	1.90	0.40	2.3
G9	-	<0.04	<0.06	3.0	-	<0.05	<0.09	3.0	-	<0.01	<0.06	<0.04	-
G10	-	<0.04	<0.06	3.0	-	<0.05	<0.08	3.0	-	<0.01	<0.06	<0.03	-
G11	46.9	0.21	0.07	2.8	-	<0.01	<0.03	3.0	-	<0.01	<0.04	<0.02	-
G12	46.4	0.18	0.13	1.4	45.9	0.21	0.17	1.2	-	<0.01	<0.07	<0.04	-
G13	45.4	1.04	0.44	2.2	44.8	0.69	0.34	1.9	44.9	2.03	3.33	0.68	2.3
G14	46.2	1.07	0.56	1.8	45.9	1.09	0.68	1.5	45.5	2.58	3.91	0.90	1.6
G15	43.9	0.28	0.31	0.9	43.4	0.20	0.26	0.7	43.9	0.24	0.40	<0.02	2.5
L1	46.6	0.29	0.26	1.0	46.2	0.10	0.13	0.7	46.2	0.22	0.29	0.08	1.0
L2	46.5	0.20	0.23	0.8	-	<0.01	<0.02	3.0	-	<0.01	<0.04	<0.02	-
L3	46.4	0.27	0.16	1.6	-	<0.02	<0.03	3.0	45.6	0.16	0.26	<0.02	2.1
L4	42.8	0.09	0.09	1.0	42.4	0.07	0.06	1.1	-	<0.01	<0.03	<0.02	-
L5	45.3	0.18	0.22	0.8	44.9	0.26	0.37	0.7	44.6	0.40	0.63	0.14	1.2
L6	-	<0.02	<0.03	3.0	-	<0.01	<0.03	3.0	-	<0.01	<0.03	<0.02	-
L7	43.9	0.22	0.21	1.0	43.5	0.12	0.17	0.7	43.4	0.23	0.38	0.08	1.3

Note - The fit parameters are the same as Table 12.3. In case of non-detections, upper limits are given at the 1 σ level. Uncertainties are dominated by calibration ($\sim$ 20 %). Integrated intensities and peak temperatures are given on the main-beam temperature scale

12.4.2 The $R_D = DCO^+/HCO^+$ and $R_N = N_2H^+/HCO^+$ abundance ratios

The R_D and R_N abundance ratios were derived by constraining the physical conditions simultaneously for both species in each ratio (see §12.4.1), in order not to unduly propagate the uncertainty. The resulting values are reported in Table 12.5. Figure 12.4 shows the derived R_D versus R_N values for the various points in W44. For comparison, the same figure also shows the observations towards W28, when available (see Table 12.6). First thing to notice, there is not a clear correlation between R_D and R_N although, in principle, they both should be sensitive to the CR ionisation rate (see Introduction). This implies that the latter is not the dominant factor governing one or both ratios. Very likely, the C/N ratio plays a major, even though unexpected, role (see following section).

In order now to fully understand the R_D and R_N behavior, we will compare the observations with a numerical chemical model in the next section.

12.5 Chemical modeling

12.5.1 Influence on R_D and R_N ratios of ζ, T_{gas} and the $^{12}C/^{13}C$ isotopic ratio

As in our previous work on W28, we used the `astrochem` chemical model to interprete the observations. We first run a grid of several models, varying the CR ionisation rate $\zeta/n_H = 10^{-21} - 10^{-18}$ cm^3 s^{-1}, and the gas temperature $T = 7 - 20$ K, which is the range of temperatures derived (§12.4.1). The predictions are shown in Figure 12.4, together with the observed values. The two regions LIP and HIP are easily identifiable in the Figure. As presented previously (Vaupré et al., 2014), the abundance ratios depend on ζ/n_H, and the jump from LIP to HIP occurs at $\zeta/n_H \sim 3 \times 10^{-19}$ cm^3 s^{-1}. In W44, the gas density is typically $n_H = 10^5$ cm^{-3},

Table 12.5: Physical conditions in W44.

Pos.	Δv [km s^{-1}]	n_{H_2} [10^3 cm^{-3}]	T_{kin} [K]	$N(\mathrm{C^{18}O})$ [10^{15} cm^{-2}]	A_V [mag]	$N(\mathrm{H^{13}CO^+})$ [10^{12} cm^{-2}]	$N(\mathrm{DCO^+})$ [10^{12} cm^{-2}]	$N(\mathrm{N_2H^+})$ [10^{12} cm^{-2}]	$R_D = \frac{[\mathrm{DCO^+}]}{[\mathrm{HCO^+}]}$	$R_N = \frac{[\mathrm{N_2H^+}]}{[\mathrm{HCO^+}]}$
E1*	2.0	1e4 - 1e5	11 - 16	3 - 10	16 - 52	0.2 - 0.7	<0.1	1.5 - 3	<0.0044	0.080 - 0.20
E3*	4.0	2e4 - 2e5	8 - 13	2 - 8	10 - 42	0.9 - 2.8	0.5 - 2.5	8 - 16	0.0056 - 0.028	0.080 - 0.21
E11*	2.5	2e4 - 2e5	8 - 11	2.5-20	13 - 105	0.4 - 1.4	0.3 - 1.8	2 - 6	0.010 - 0.041	0.056 - 0.14
G3*	3.0	1e4 - 2e4	8 - 12	1.5-8.5	9 - 44	0.6 - 1.1	<0.2	1 - 2.5	<0.0040	0.046 - 0.11
G4	2.5	6e3 - 2e6	7 - 9	2 - 10	10 - 50	0.1 - 0.6	<0.8	< 2.0	<0.035	<0.08
G5*	3.5	2e4 - 2e5	10 - 17	4 - 7	21 - 38	0.4 - 1.4	0.1 - 1.1	4 - 5	0.0037 - 0.023	0.073 - 0.20
G14*	3.5	5e4 - 2e5	11 - 17	4 - 6	21 - 32	0.6 - 1.6	0.6 - 2.2	8 - 12	0.012 - 0.049	0.094 - 0.25
G15	2.0	2e4 - 2e6	7 - 9	2 - 8	10 - 40	0.2 - 0.9	0.7 - 1.3	< 5.0	0.020 - 0.046	<0.21
L1*	2.5	5e4 - 1e5	7 - 9	2.5-10	13 - 52	0.3 - 0.6	0.1 - 0.5	1 - 2	0.0070 - 0.026	0.032 - 0.086
L2	4.0	2e3 - 2e6	7 - 15	1 - 4	5 - 20	0.1 - 0.9	<0.4	< 1.5	<0.010	<0.048
L3	4.0	2e3 - 2e6	8 - 15	2 - 20	10 - 100	0.2 - 1.1	<0.5	< 1.5	<0.013	<0.038
L4	2.0	6e3 - 2e6	8 - 10	1 - 10	5 - 50	0.1 - 0.5	0.3 - 0.8	< 1.0	0.022 - 0.056	<0.071
L5*	1.5	1e4 - 3e5	8 - 14	0.5-4.5	3 - 23	0.1 - 0.6	0.1 - 1.6	1 - 3	0.016 - 0.088	0.11 - 0.29
L6	4.5	2e3 - 2e3	15 - 17	2 - 10	10 - 50	0.1 - 0.2	<0.3	< 1.0	<0.039	<0.15
L7*	2.0	1e4 - 4e5	7 - 9	1 - 4	5 - 21	0.2 - 0.8	0.1 - 1.1	1 - 2	0.0080 - 0.040	0.050 - 0.13

Note - n_{H_2} is the molecular hydrogen density (cm^{-3}), T_{kin} the gas kinetic temperature, $N(\mathrm{C^{18}O})$ the total column density of $\mathrm{C^{18}O}$. A_V is the visual extinction assuming $[\mathrm{C^{18}O}] = A_V \times 1.9\ 10^{14}\ \mathrm{cm^{-2}}$ (Frerking et al., 1982; Bolatto et al., 2013). We assumed isotopic ratio values $^{16}\mathrm{O}/^{18}\mathrm{O} = 500$ and $^{12}\mathrm{C}/^{13}\mathrm{C} = 50$. Values in brackets indicate the range of values satisfying $\chi^2_\nu < 1$. Uncertainties on n_{H_2} and T_{kin} are at the 70% confidence level, and are propagated in the abundance ratios and upper limits. Stars (*) indicate positions at which $\mathrm{N_2H^+}$ observations could be used together with CO to constrain physical conditions.

and the jump occurs at a very high value $\zeta \sim 3 \times 10^{-14}\ \mathrm{s^{-1}}$. In other words, due to the higher density, the gas remains in the LIP over a large range of ζ values, up to ten times higher than in W28.

When $\mathrm{DCO^+}$ is detected, the observed values of R_D are consistent with the LIP branch within the error bars, or they lie at the edge of the jump to the HIP. On the contrary, the non-detections correspond to upper limits on R_D significantly lower than the values predicted in the LIP, which seems to indicate a large CR ionisation rate. Yet, this picture is not consistent with the observations of $\mathrm{N_2H^+}$. Indeed, all observations of R_N lie within a range of values consistent with the LIP branch, even when $\mathrm{DCO^+}$ is not detected. In fact, $\mathrm{N_2H^+}$ observations alone do not seem able to provide any constrain on ζ.

As noticed already in the previous section, the lack of correlation between R_D and R_N points to ζ not being indeed the governing factor in determining their values. Before exploring the elemental N/C gaseous abundance ratio, it is worth studying whether and how the isotopic ratio $^{12}\mathrm{C}/^{13}\mathrm{C}$ assumed to derive R_D and R_N impacts the determination of $N(\mathrm{HCO^+})$ from observations of the isotopologue $\mathrm{H^{13}CO^+}$. In this study, we adopted the isotopic ratio $^{12}\mathrm{C}/^{13}\mathrm{C} = 50$, following the results by Milam et al. (2005) for the Galactocentric distance of W44. The same authors show that there can locally be up to a factor 2 discrepancy in this ratio. The error in the isotopic ratio transfers straightforwardly to the observed R_D values, assuming:

$$\mathrm{HCO^+} = \mathrm{H^{13}CO^+} \times \frac{^{12}\mathrm{C}}{^{13}\mathrm{C}}\ . \tag{12.6}$$

Therefore, the isotopic ratio can introduce an additional 50% uncertainty in R_D, which would shift the points towards the curves. We emphasise that the $^{12}\mathrm{C}/^{13}\mathrm{C}$ ratio cannot vary across the region so that it would only cause a shift of all the measured values with respect to the curves with the predictions. We conclude that it is not a dominant element to reconcile the observations with the model predictions of Figure 12.4.

12.5.2 Constraints on the C and N volatile budgets

The main parameters that influence significantly the predicted values of R_D and R_N, so that they could better match the observations, are the initial abundances of C and N in the gas-phase that we assumed in to obtain the model predictions.

The total abundance of a given element in the molecular cloud is distributed into the solid refractory material inside grain cores, and the volatiles. Volatiles are in the gas-phase and can be incorporated in ices, on the grain surface. They can react back and forth from the gas-phase to the ice. In the model used in this work, though, gas-grain reactions were not included. Therefore, we initially assumed that the total amount

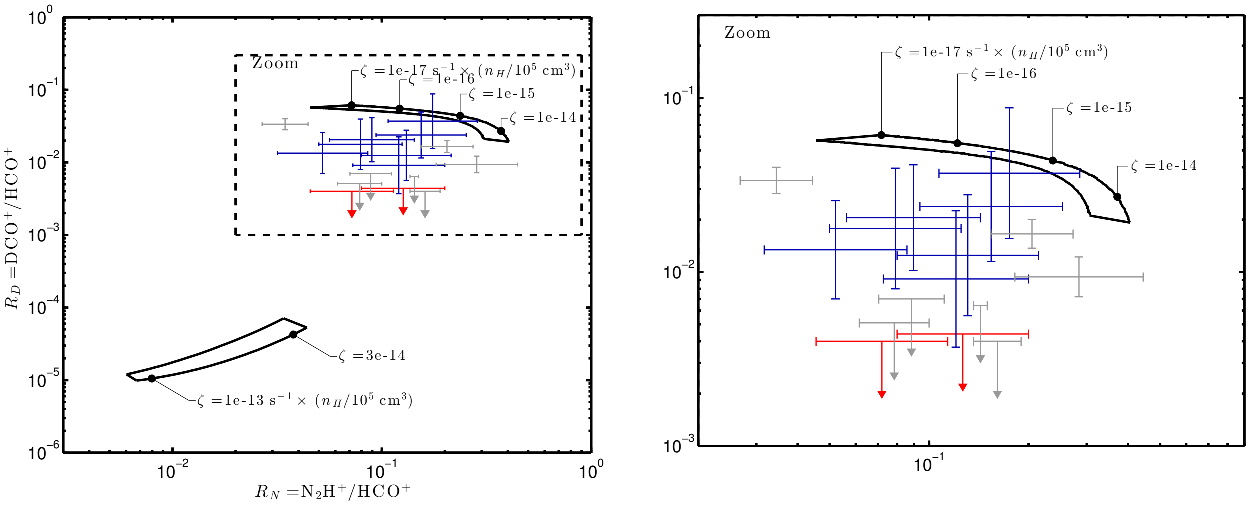

Figure 12.4: The abundance ratio R_D w.r.t. R_N. Blue points and red upper limits show observations in W44. For comparisons, gray points show observations in W28 when available (Table 12.6). The solid lines contain predictions from chemical modeling, which were obtained by increasing $\zeta/n_{\rm H}$ for temperatures between 7 and 20 K. For clarity, ζ values are indicated at $T = 7$ K for a typical density $n_{\rm H} = 10^5$ cm^{-3} in W44, although the model only depends on the $\zeta/n_{\rm H}$ ratio. **Left:** Chemical predictions up to $\zeta/n_{\rm H} = 10^{-18}$ cm^3 s^{-1}. The HIP/LIP transition occurs $\zeta/n_{\rm H} \sim 3 \times 10^{-19}$ cm^3 s^{-1}. **Right:** Zoom on the observations.

Table 12.6: The R_N ratio in W28 when available. The R_D ratio is taken from Vaupré et al. (2014), where physical conditions can also be found for each position.

Pos.	$R_D = \frac{[\rm DCO^+]}{[\rm HCO^+]}$	$R_N = \frac{[\rm N_2H^+]}{[\rm HCO^+]}$
W28-N1	<0.0040	0.14 – 0.19
W28-N3	<0.0064	0.14 – 0.15
W28-N4	<0.0051	0.061 – 0.10
W28-N5	0.014 – 0.020	0.15 – 0.27
W28-N6	0.0072 – 0.012	0.18 – 0.44
W28-N7	<0.0070	0.070 – 0.11
W28-SE1	0.028 – 0.040	0.027 – 0.044

of each element initially in the gas-phase remains in the gas-phase. Specifically, the initial abundances of N and C are respectively (Table 8.1):

$$[{\rm N}]_0 = 2.1 \times 10^{-5} \tag{12.7}$$

$$[{\rm C}]_0 = 7.3 \times 10^{-5} \ , \tag{12.8}$$

and the initial C/N ratio is therefore:

$$\left[\frac{\rm N}{\rm C}\right]_0 = 0.29 \ . \tag{12.9}$$

To study the influence of C and N in the gas-phase on the predicted values of R_D and R_N, we computed a new grid of models in which we varied the abundance of C and the N/C ratio. Specifically, we considered gaseous C abundances from 2.4×10^{-5} to 1.5×10^{-4} (i.e. the C/O ratio remains lower than 1), and gaseous N/C ratios from 3×10^{-2} to 1, for each value of C, namely we assumed that N and C deplete by the same amount. Figure 12.5 shows the results for this new grid of models.

Note that a model is here a set of predicted values obtained by assuming C and N/C, and varying ζ. This means that one model is represented by one solid line in the Figure. Starting from the standard abundances of C and N (solid blue line), the models shift horizontally or vertically with the values of N/C and C, respectively. When decreasing the gas-phase abundance of C, namely increasing the depletion of C, the models shift toward higher values of R_D and do not better reproduce the observations. The observations are better reproduced by increasing C. Similarly, models seem to better match the observations by decreasing N/C.

A simple interpretation is that in the LIP, all carbon is trapped into CO, therefore $x(\mathrm{CO}) = [\mathrm{C}]_0$. Now, CO is involved the destruction of $\mathrm{H_2D^+}$ and, therefore, impacts R_D. Considering the analytical formula for the determination of R_D, which is a reasonable approximation in the LIP (Equation 9.2), R_D decreases as $x(\mathrm{CO})$ increases. In other words, the depletion of CO favors large $\mathrm{DCO^+}$ abundances.

About R_N, in cold gas and steady state the majority of N is trapped into $\mathrm{N_2}$, which then leads to $\mathrm{N_2H^+}$ through Reaction 12.1. Assuming that both $\mathrm{HCO^+}$ and $\mathrm{N_2H^+}$ are formed by $\mathrm{H_3^+}$ and that their destruction is dominated by electronic recombination, then at steady-state:

$$R_N = \frac{x(\mathrm{N_2H^+})}{x(\mathrm{HCO^+})} \propto \frac{x(\mathrm{N_2})}{x(\mathrm{CO})} \propto \frac{[\mathrm{N}]}{[\mathrm{C}]} \ , \tag{12.10}$$

Thus, R_N increases with N/C, as indeed observed in Figure 12.5.

To get a quantitative estimate of the values of {C, N/C} that best reproduce the observations, we computed the χ^2 parameter, defined as follows:

$$\chi^2 = \sum \frac{[\mathrm{dist}(\mathrm{obs}_i,\ \mathrm{model})]^2}{\sigma_i^2} \ , \tag{12.11}$$

where the observation i is defined as the couple of values $\{R_D,\ R_N\}$, and we computed the distance between the observations and one individual model, i.e. a curve with a given set of parameters {C, N/C}. The error σ_i is the quadratic sum of the errors on the observations of R_D and R_N:

$$\sigma_i^2 = \sigma_{R_D}^2 + \sigma_{R_N}^2 \tag{12.12}$$

Figure 12.6 shows the reduced χ^2 values in the {C, N/C} and $\{\mathrm{N/C},\ \zeta/n_\mathrm{H}\}_{[\mathrm{C}]=1.2\times10^{-4}}$ parameter spaces. The "standard" elemental abundances that we used in previous work are marked by red dashed lines. From these maps, we conclude that:

1. The C elemental abundance is $[C] \gtrsim 5\times10^{-5}$, consistent with or higher than the standard value. This suggests that CO is not depleted in the W44 molecular clouds.

2. The gaseous N/C elemental ratio is $0.07 \lesssim \mathrm{N/C} \lesssim 0.2$, lower than previously assumed. This suggests that nitrogen is either depleted on the grain mantles, although CO is not, or that the major reservoir of gaseous nitrogen is N and not $\mathrm{N_2}$. Both hypotheses need to be further explored, in particular to see which one is in best agreement with observations. Note that there is approximately no Galactocentric gradient of the N/C ratio (Carigi et al., 2005).

3. The average CR ionisation rate is large, $4\times10^{-20} \lesssim \zeta/n_\mathrm{H} \lesssim 4\times10^{-19}\ \mathrm{cm^3\ s^{-1}}$ where we considered the typical density $n_\mathrm{H} \sim 10^5\ \mathrm{cm^{-3}}$ in the W44 molecular clouds. This confirms that these clouds are exposed to a large flux of CR, likely freshly accelerated.

4. At high ζ, the N/C ratio that best fits the observations tends toward the observed R_N ratio: $\mathrm{N/C} \rightarrow \mathrm{N_2H^+/HCO^+}$. This is due to the predominance of the electronic recombination in the destruction processes of $\mathrm{HCO^+}$ and $\mathrm{N_2H^+}$ at high ζ.

12.5.3 Time dependence of the LIP/HIP transition

Figure 12.7 shows the time-dependent evolution towards steady-state, starting from a "standard" molecular cloud at steady-state with $n_\mathrm{H} = 10^4\ \mathrm{cm^{-3}}$, $T = 10$ K and $\zeta = 1.0\times10^{-17}\ \mathrm{s^{-1}}$, for different carbon elemental abundances. Under these physical conditions, the LIP/HIP transition occurs at $\zeta_0 \gtrsim 3\times10^{-15}\ \mathrm{s^{-1}}$.

The CR ionisation rate ζ is given a new value at $t = 0$.

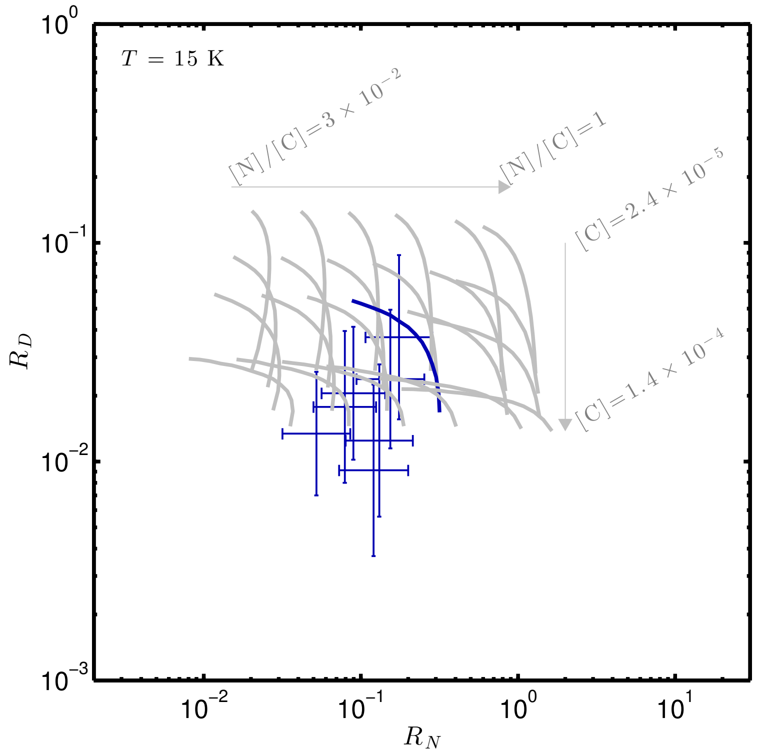

Figure 12.5: Evolution of the model predictions (solid lines) with the initial gas-phase abundances of C and N. In a first approximation, R_D values depend only on C and R_N on the N/C ratio. The solid blue line shows the model with standard initial abundances (Eq. 12.7 and 12.8). Blue points show W44 observations as in Figure 12.4.

- If $\zeta < \zeta_0$, then the gas remains in the LIP, and steady-state is reached in ~ 100 yr.
- If $\zeta > \zeta_0$, then the gas will reach steady-state in the HIP. The time needed for the transition to occur depends on the carbon elemental abundance and is $\gtrsim 10^4$ yr.

The transition to the HIP, if it occurs, requires a large time $\gtrsim 10^4$ yr. Given the age of the SNR $\sim 2 \times 10^4$ yr, it implies that the gas, even if irradiated by a large CR ionisation rate might not have reached equilibrium yet.

On the other end, if we do observed gas in the HIP, it implies that it had enough time for the transition to occur, and this gives a constrain on the carbon elemental abundance. The time at which the transition occurs indeed decreases with C. To be consistent with the age of the remnant, Figure 12.7 shows that the elemental abundance should be [C]$\gtrsim 8 \times 10^{-5}$. This gives an independent constrain on C, consistent with the χ^2 minimisation in Section 12.5.2, which favors a high carbon elemental abundance and disfavors CO depletion.

12.6 Conclusions

The preliminary conclusions of this work are:

- The clouds close to the W44 SNR are in average ten times denser than those in W28 or W51. Whether this is because of the different age of the SNRs is to be confirmed.
- Based on the analysis of the R_D ratio, which has been previously used with success to constrain the CR ionisation rate ζ, there is not a clear trend of increasing ζ with decreasing distance from the SNR shock front. Whether this is because the 2D is misleading is unclear at this stage. It is possible that

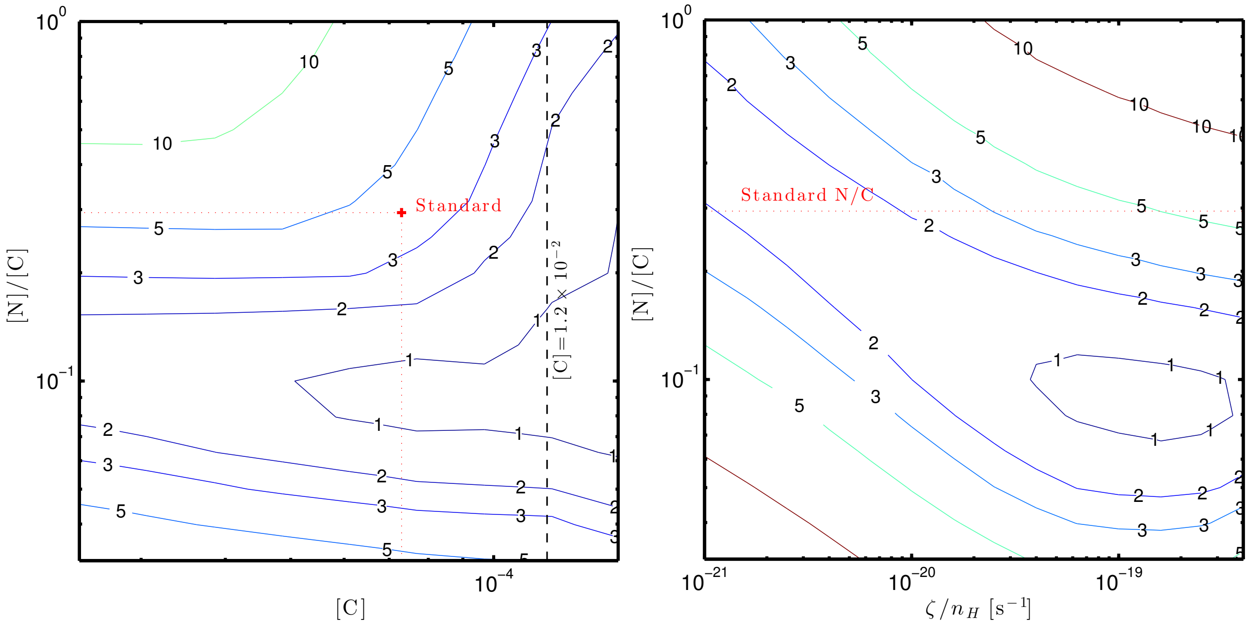

Figure 12.6: **Left:** Map of χ^2_ν in the {C, N/C} parameter space. χ^2_ν is computed through Equation 12.11 with the number of degrees of freedom $\nu = 4$ (ζ is a free parameter). **Right:** Computation in the {N/C, $\zeta/n_{\rm H}$} parameter space, with [C] $= 1.2 \times 10^{-4}$. The number of degrees of freedom is $\nu = 3$.

the low energy CRs are "emitted" in local shocks, which are not uniformly distributed in the region. The case of W51-E, reported in Chapter 10, might therefore be a rather common situation in W44. Obviously, this is at this stage speculative.

- The simultaneous use of the R_D and R_N ratios greatly helps to constrain not only the average ζ in the region but also the content of gaseous carbon and nitrogen.
- The average ζ is very high, confirming the presence of a large flux of freshly accelerated CR in the W44 molecular clouds.
- All carbon not locked into the grain refractory component is in the gas phase, namely there is not evidence of CO depletion in the W44 clouds, despite their relatively large density. This may be explained if the clouds density has increased because of the impact of the SNR shock. In practice, CO has not had time to freeze-out onto the grain mantles. Once again, more observations are necessary to confirm this hypothesis.
- Molecular nitrogen seems to have a lower abundance than expected. This may be due to its freeze-out onto the grain mantles or to the fact that a large fraction of nitrogen is not in the molecular form. The depletion onto the grain mantles seems unlikely as CO, which has a very similar binding energy, does not show signs of depletion. It is possible then that nitrogen is in the atomic form. More observations are necessary to understand better this point.

The new set of observations and modeling presented in this Chapter clarifies a number of issues, but also shows that much is still to be understood.

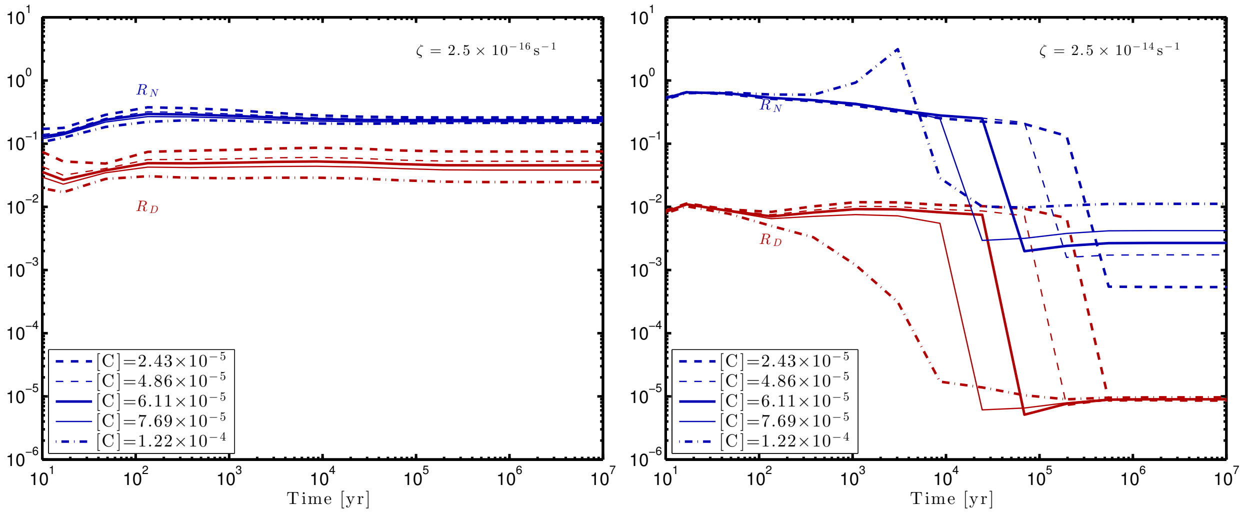

Figure 12.7: Time dependent R_N and R_D abundance ratios, for different C elemental abundances. In this calculation, I assumed N/C=0.25, a kinetic temperature $T = 10$ K, a density $n_{\mathrm{H}} = 10^4$ cm^{-3} and a CR ionisation rate $\zeta = 2.5 \times 10^{-16}$ s^{-1} (left) and $\zeta = 2.5 \times 10^{-14}$ s^{-1} (right). For a low ζ, reaching steady-state takes ~ 100 yr. For a ζ value high enough for the LIP/HIP transition to occur, the time to achieve steady-state is $\gtrsim 10^4$ yr, and depends on the carbon elemental abundance.

Chapter 13

Summary of the results and limits of the method

Contents

13.1 Summary of the results

I studied the ionisation in the molecular clouds close to three SNRs: W28, W51C and W44. In each case, there is definitive evidence of an interaction of the SNR with the nearby cloud, based on observational evidence of the presence of shocked gas (broaden emission lines, OH masers, ...), and gamma-ray emission from the cloud, probably due to CR protons encountering the dense medium. The three objects show similar morphologies. The molecular gas extends from 0 to ~20 pc (projected distance) from the SNR shock, and the SNR shell are $\sim 20 - 30$ pc wide. All three SNRs are a few 10^4 yr.

The physical conditions determined from ^{13}CO and C^{18}O two lowest rotational transitions give densities and temperatures characteristic of molecular clouds. In W28 and W51C, $n_{\rm H} \sim 10^3 - 10^4$ cm^{-3} and $T \sim 7 - 25$ K. The molecular cloud close to W44 seems to be denser, with densities $> 10^5\,$cm^{-3}, as determined from N_2H^+ observations.

The CR ionisation rate has been determined successfully in W28 and W51C, which both show an enhanced ionisation, with values of ζ at least 100 times higher than in isolated (or "standard") molecular clouds. These high values were determined using the DCO$^+$/HCO$^+$ ratio. The highest ionisation rates were determined along sight lines with DCO$^+$ non-detections. The upper limits on DCO$^+$ were sufficient to constrain ζ and assure that the gas lies outside the LIP branch, giving only access to lower limits on ζ. In W44 however, the determination of ζ is less straightforward. Observations of N_2H^+/HCO$^+$ together with DCO$^+$/HCO$^+$ gave constraints which seem inconsistent at first, as the evolution of the N_2H^+ abundance seems unrelated to DCO$^+$ detections or non-detections. Nevertheless, these observations better match theoretical predictions for high values of ζ, and indicate an enhanced CR ionisation in the gas.

The DCO$^+$/HCO$^+$ abundance ratio does not give access to a precise measurement of the CR ionisation rate in high ionisation regions. Therefore, I investigated the possibility of using other complementary tracers to derive ζ in the HIP. I determined from chemical modeling a list of species candidates to look for and obtained observations at the IRAM 30m toward W28. From this study, I showed that N_2H^+ and CN may bring crucial constraints on ζ. More observations are needed, both in the W28 region and towards other sources, to confirm or infirm these preliminary results and define the regime of applicability of these additional tracers, in terms of physical conditions and ionisation state.

Finally, this study gives access to precious information on the physics of low-energy CRs, unaccessible to other means of observation and complementary to high-energy observations. In the W28 region, there is a differential CR ionisation from the Northern cloud to the Southern cloud. Besides, TeV CR protons indeed reached the Southern cloud, whereas GeV protons remain closer to the shell of the remnant, having a smaller gyration radius. These observations give constraints on the propagation properties of low-energy CRs. In the W51C region, high spatial resolution observations showed compact SiO emission as the signature of the passage of the SNR shock, giving a coherent picture of a region filled with ionising CRs downstream the shock.

13.2 Limitations of the method

In order to put constraints on the physical parameters and processes at work in the molecular gas in the vicinity of SNR, one would ideally need a complete model describing, in a time-dependent and self-consistent fashion, the interplay between dynamical and chemical processes together with a broad range of microsopic processes describing the interaction between matter and photons. This is a serious challenge and trade-offs must be adopted, to allow either a detailed description of the microphysics (e.g. the Meudon PDR code) or of the flow dynamics (e.g. 3D MHD simulations, Hennebelle, 2013). In addition, observational constraints are derived from the emission lines of selected molecules. This is the context of radiative transfer which is here essentially an inversion problem which may result in degenerate solutions.

13.2.1 Radiative transfert

The simplest approach of radiative transfer is the LTE approximation with constant and homogeneous physical conditions. LTE assumes that the level populations (here, rotational) can be described by a single parameter, the kinetic temperature. Relaxing this assumption leads to so-called non-LTE models, to which the method we have applied belongs.

Our radiative transfer calculations have been performed under the *escape probability* approximation which gives any photon a probability β to escape the cloud. This allows to decompose a cloud into radiatively decoupled cells, for any photon emitted from a cell are either absorbed locally or escape from it and, hence, from the entire cloud. The escape probability depends on the opacity τ of the transition line, with $\beta \sim 1$ for optically thin transitions, and $\beta \sim 1/\tau$ for optically thick ones. The exact expression of β depends on the geometry of the cloud, but is usually of the form

$$\beta = \frac{1 - e^{-a_1 \tau}}{a_2 \tau}$$

with a_1 and a_2 factors of order unity (see e.g. de Jong et al., 1980). For optically thin transitions, the escape probability assumption thus resumes to an assumption on the physical conditions, namely density and temperature. For non–optically-thin transitions, we have applied the so-called *Large Velocity Gradient* (LVG) assumption, which was introduced in Section 7.3.1. This approximation allows to carry out the calculation of photon emission locally by decoupling cells in velocity (hence frequency) space.

During my PhD work, I focused on the emission of several CO isotopologues, which remain relatively thin whereas ^{12}CO transitions are usually thick. The validity of this local approach must be tested at higher opacities.

To test the validity of the LVG approximation, let us consider a cubic cloud of side $L \sim 20$ pc, which is typically the observed dimension of clouds in the W28 region. The observed line width of the CO$(1-0)$ transition is typically $\Delta v_{\rm tot} \sim 3$ km s^{-1}. This corresponds to a mean velocity gradient:

$$\nabla v = \frac{\Delta v}{\Delta x} \sim \frac{\Delta v_{\rm tot}}{L} = 0.15\,\text{km s}^{-1}\ \text{pc}^{-1}\ , \qquad (13.1)$$

with a variation in the mean velocity Δv on a length Δx. The thermal width of CO lines is $\Delta v_{\rm th} \sim 0.05\sqrt{\frac{T}{10}}$ km s^{-1}. Therefore, at 10 K the LVG approximation stands if one considers decoupled regions of size:

$$\Delta x > \frac{\Delta v_{\rm th}}{\nabla v} \sim 0.3 \text{ pc} < 20 \text{ pc} , \tag{13.2}$$

which for a density $n_{\rm H} = 10^4 \text{ cm}^{-3}$ corresponds to a column density $N_{\rm H} \sim 9 \times 10^{21} \text{ cm}^{-2}$ or $A_V \sim 9$ mag. In this example, the cloud can be divided into ~ 70 decoupled regions, where the escape probability applies.

Another approach to carry out the radiative transfer calculations is for instance the Monte Carlo method. For instance, `RATRAN` (Hogerheijde and van der Tak, 2000) is a code based on this method, where the total emission of a gas cell is derived taking into account a random set of photons which contribute to the radiation field. In this case, there is no assumption on the velocity gradient in the cloud, but we need to assume the structure of the entire cloud.

13.2.2 Cloud modeling

The next step in deriving constraints on the physical and chemical state of the gas consisted in the comparison of the derived abundances with predictions from chemical models. Our chemical model describes the time-dependent evolution of the chemical state of a cell of gas of constant density and temperature, located deep enough within the cloud (typically at an Av of ~ 10 mag or more) such the only UV photons are secondary photons. However, the structure may play a role at two different stages of the computation: during the interpretation of observations and the chemical modeling.

As stressed above, the observed emission lines are interpreted based on the assumption that they emanate from radiatively independent cells of constant density and temperatures. One way of deciphering the spatial variations of the density and temperature is to perform multi-line analysis combining several tracers, covering a broad range of excitation conditions. In particular, each transition can be described in terms of a critical density, as presented in Section 6.2.3. Different transitions are therefore sensible to regions of different gas densities. Complementary observations can thus lead to a determination of the density structure of the cloud. In our case, the critical densities involved are $\sim 10^3 \text{ cm}^{-3}$ for ^{13}CO$(1-0)$ to $\sim 10^5 \text{ cm}^{-3}$ for $N_2H^+(1-0)$ and $\sim 10^6 \text{ cm}^{-3}$ for HCN$(1-0)$. Tracers as N_2H^+ or HCN therefore indicate large density regions.

This raises the question of whether the different species used in the analysis coexist spatially. CO and N_2H^+ lines were indeed used together to determine the physical conditions, yet in dense regions, CO may deplete. This has been observed e.g. in dense cores L1544 (Caselli et al., 1999) or B68 (Bergin et al., 2002), where the peak of N_2H^+ emission coincides with the maximum of visual extinction and a “hole” in the CO emission. Yet, in the molecular clouds I studied, the density remains relatively low ($\sim 10^4 \text{ cm}^{-3}$) and CO is unlikely to deplete. In W44, I derived densities up to $\sim 10^5 \text{ cm}^{-3}$, yet there is evidence that CO is not depleted, based on the analysis of the DCO^+/HCO^+ and N_2H^+/HCO^+ abundance ratios (see Chapter 12). On chemical grounds, CO and N_2H^+ are also expected to coexist spatially since one way of forming HCO^+ is through $CO + N_2H^+$. Finally, the main formation route of HCO^+ is through $CO + H_3^+$, which shows that CO and HCO^+ are also expected to coexist spatially.

Second, we also assumed a uniform cloud in the chemical modeling. The code we used, `astrochem`, computes chemical abundances for a gas cell with constant physical parameters, e.g. density, temperature. In other words, this is a single-point calculation. In contrast, other codes are available which can take into account the structure of the cloud. For instance, the `Meudon PDR` code computes the chemical steady-state along a line of sight described by a density and/or temperature profile which may result from constant pressure and thermal balance calculated self-consistently. In previous work, Ceccarelli et al. (2011) used `Meudon PDR` and considered a chemical structure of the cloud in the interpretation of the DCO^+/HCO^+ ratio and the derivation of ζ. Yet, `astrochem` is well suited to the dense interior of molecular clouds, which are shielded regions at high A_V. One advantage of using a single-cell chemical model, which also motived the use of `astrochem`, is that it allows to explore a large parameter space very efficiently. In addition, time-dependent effects need to be explored, such as the time-dependent response of the gas to a sudden increase of the cosmic-ray ionisation rate, which can not be calculated with `PDR` or other steady-state codes.

Still, our modeling approach is only a first step towards a more self-consistent model of the molecular gas in the vicinity of young SNRs. One of our perspectives is to compute the time-dependent chemical state of the gas self-consistently with its temperature, along a line of sight with a prescribed, time-independent, density profile. To do so, the thermal balance between the main heating and cooling processes must be computed. The heating of the gas is driven by the cosmic-rays, directly through the production of the secondary electrons, or indirectly through the energy injected into the ion-neutral chemistry. The time-dependent and depth-dependent evolution of the cosmic-ray spectrum must then be known.

In a recent paper, Morlino and Gabici (2015) considered the propagation of CRs within diffuse clouds of density $\sim 100\ \mathrm{cm}^{-3}$, showing that for particles with energies much larger than 3 MeV, a stationary spectrum establishes over the entire cloud in a timescale of order 1 Myr, shorter than the free-fall time of such a diffuse cloud. However, in a gas at a density of $10^4\ \mathrm{cm}^{-3}$, this argument fails, as the free-fall time is 3×10^5 yr, and the stationarity of the CR spectrum may not be valid. This may be even worse when comparing with the chemical timescales. In fact, although the typical timescale for the formation of molecular hydrogen is of the order of 1 Myr, the ion-neutral chemistry reaches steady-state on timescales comparable or shorter at densities $\sim 10^4\ \mathrm{cm}^{-3}$. This suggests that a self-consistent time-dependent model of cosmic-ray ionisation in dense gas should consider the propagation and evolution of the CR spectrum together with the chemistry. This could be done by assuming a constant density in a first approach, or using a prescribed density profile.

The spatial dependence of the CR spectrum in the cloud (Padovani et al., 2009) results from the energy losses due to ionisation and nuclear interactions. The CR flux can excite Alfvén waves in the process and modify the diffusion properties in the outer layers of the cloud. In particular, Morlino and Gabici (2014) showed that CRs with energies below $10 - 100$ MeV are strongly suppressed in the cloud. The authors are developing a web-tool called CRIME[1], for the calculation of the ionisation produced by CRs, at any depth and depending on the initial CR spectrum. We would like to incorporate their calculation into our chemical code to better take into account the spatial evolution of ζ..

13.2.3 Gas-grain interaction

Finally, except for the formation of H_2 and HD, gas-grains processes are ignored. Electron attachment on grains yet produces charged grains which can play a role on the charge equilibrium in the cloud, mainly through ion recombination. These two processes are listed in the OSU chemical network (Table 13.1) and can be enabled in `astrochem`. Nevertheless, assuming a gas-to-dust mass ratio of 100, which corresponds to a grain abundance from $x(\mathrm{gr}) = 10^{-12}$ to 10^{-10} for olivine grains, depending on their size distribution, calculations in `astrochem` show that these charge exchange reactions have a negligible effect on the predicted chemical abundances (see Figure 13.1). For the calculations, I assumed $n_\mathrm{H} = 10^4\ \mathrm{cm}^{-3}$, $T = 10$ K and $\zeta = 10^{-17}$ to $4 \times 10^{-14}\ \mathrm{s}^{-1}$.

13.2.4 Contamination of observations

In some cases, the observations might be contaminated by the presence of a close protostar. The beam pattern of the antenna spans beyond the width of the main beam FWHM (29"at 3 mm). Yet, the efficiency of the transmission decreases sharply (Greve et al., 1998), down at 3 mm to 25dB (or 0.3%) at twice the FWHM and 40dB (or 0.01%) at 10 times the FWHM. The proximity of a very strong source might then significantly contaminate the signal.

In the most unfavorable situation in our observations, the emission at W28-N2 is strong, due to the presence of a protostar, with an integrated intensity in ^{13}CO$(1-0)$ of $W = 59.6$ K km s^{-1} and a peak temperature $T_\mathrm{peak} = 12.6$ K. The closest line of sight we observed is W28-N6 at 50"of N2, i.e. 1.7 times the main beam width at 3 mm. At this distance, emission in N2 contributes up to 0.06 K km s^{-1} in the integrated intensity of N6 $W = 23.9$ K km s^{-1}. The contamination is negligible.

Another unfavorable situation is W51C-E. The presence of a close protostar raised the question of the contamination of observations in DCO$^+$. Doubts were removed by high spatial resolution observations obtained at the IRAM Plateau de Bure Interferometer (Dumas et al., 2014).

13.2.5 ^{13}C isotope fractionation

Isotopic fractionation reactions are responsible for the enrichment of isotopes of molecules in dense clouds (Watson, 1976). Because of these reactions, the isotopic ratios ^{12}CO/^{13}CO, ^{12}CO/C^{18}O, and HCO$^+$/H^{13}CO$^+$ may deviate from the cosmic ratios ^{12}C/^{13}C and ^{16}O/^{18}O.

---

[1] `http://crime.in2p3.fr/`

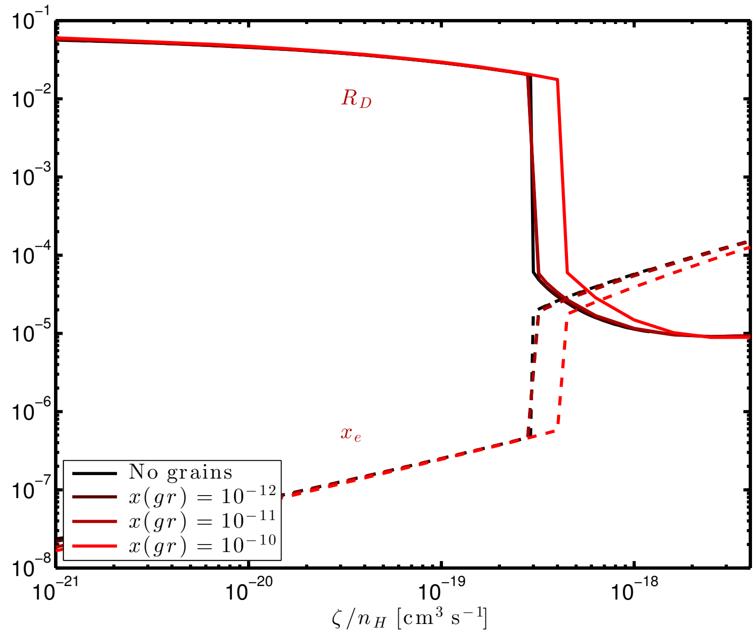

Figure 13.1: Influence of the abundance of grains on the abundance ratio R_D = DCO$^+$/HCO$^+$ and the ionisation fraction $x_e = x(\mathrm{e}^-)$. Reasonable grain abundances span from 10^{-12} to 10^{-10} for a gas-to-dust mass ration of 100, depending on the size distribution of the grains (e.g Le Bourlot et al., 1995b). The effect on the predicted values of R_D and x_e is negligible. The position of the HIP/LIP transition stays within uncertainties (factor of 5).

In my PhD work, I constrained the ^{13}CO/C^{18}O ratio during LVG calculations and found values ^{13}CO/C^{18}O = 10 ± 1 (see Section 7.3.2). To interpret this value, I assumed ^{16}O/^{18}O = 500 and derived ^{12}C/^{13}C ≈ 50, consistent with calculations of the Galactocentric gradient by Milam et al. (2005). I then used this value to derive the column density of HCO$^+$ from observations of the isotope H^{13}CO$^+$, i.e. I assumed HCO$^+$/H^{13}CO$^+$ = ^{12}C/^{13}C = 50.

In a recent paper, Mladenović and Roueff (2014) revisited the exothermicities of fractionation reactions of HCO$^+$ with CO, and derived a new estimation of the ratios of isotopologues of CO, and the HCO$^+$/H^{13}CO$^+$ratio. The authors show an enrichment of H^{13}CO$^+$ with respect to ^{13}CO. Specifically, they assumed ^{12}CO/^{13}CO = 60 and derived HCO$^+$/H^{13}CO$^+$ = 44.2, i.e. a ~ 25 % variation between these two ratios. Applying these results to my work, I may have overestimated the column density of HCO$^+$ (which is derived from H^{13}CO$^+$). Therefore, I may have underestimated the DCO$^+$/HCO$^+$ ratio by up to 25%. This additional uncertainty doesn't change the conclusions of my work.

Table 13.1: Reactions for electron attachment and ion recombination on grains (gr) in the OSU2009 network.

Reaction			Rate constants	
			α	β
e^-+ gr	→	gr^-	6.9 (-15)	0.50
C^+ + gr^-	→	C + gr	4.9 (-17)	0.50
Fe^+ + gr^-	→	Fe + gr	2.3 (-17)	0.50
H^+ + gr^-	→	H + gr	1.7 (-16)	0.50
He^+ + gr^-	→	He + gr	8.5 (-17)	0.50
Mg^+ + gr^-	→	Mg + gr	3.7 (-17)	0.50
N^+ + gr^-	→	N + gr	4.7 (-17)	0.50
Na^+ + gr^-	→	Na + gr	3.6 (-17)	0.50
O^+ + gr^-	→	O + gr	4.4 (-17)	0.50
S^+ + gr^-	→	S + gr	3.0 (-17)	0.50
Si^+ + gr^-	→	Si + gr	3.3 (-17)	0.50
$H_3{}^+$ + gr^-	→	H2 + H + gr	1.0 (-16)	0.50
HCO^+ + gr^-	→	H + CO + gr	3.1 (-17)	0.50

Note - Rate constants are described by an Arrhenius equation:

$$k = \alpha \left(\frac{T}{300}\right)^{\beta} \frac{n_{\mathrm{H}}}{n_{\mathrm{d}}} \ \mathrm{cm}^3 \ \mathrm{s}^{-1},$$

with the gas-to-dust abundance ratio $\frac{n_{\mathrm{H}}}{n_{\mathrm{d}}} = 7.57 \times 10^{11}$ in `astrochem` (see documentation), and we used the notation $a\ (b) = a \times 10^b$.

Summary and perspectives

During my PhD thesis, I investigated the effects of CRs on the ionisation of the gas phase in molecular clouds. In particular, CRs ionise H_2 and subsequently initiate efficient ion-neutral chemical reactions in the cloud. By increasing the ionisation fraction, i.e. the abundance of electrons, CRs also control electronic recombination, hence the abundances of molecular ions. Therefore, CRs govern the abundances of several key species, called tracers of the ionisation. In turn, by studying these tracers, it is possible to constrain the CR ionisation rate ζ in the gas. The adopted standard value of the CR ionisation rate in molecular clouds is $\zeta = 1 \times 10^{-17}$ s^{-1}.

By a combined effort of observation and modeling, I studied the chemical abundances of tracers of the ionisation in molecular clouds next to three supernova remnants: W28, W51C, and W44. Each of these remnants is known to be interacting with the nearby cloud, based on complementary evidence in the gas of the presence of a shock, and the detection of gamma-ray emission from the cloud, probably induced by CR protons.

In the W51C-E region, we obtained high spatial resolution observations with the IRAM PdB interferometer, which brought confirmation of an enhanced ionisation in the cloud, as determined previously by Ceccarelli et al. (2011). These observations also led to the detection of compact SiO emission, which likely traces the passage of the SNR shock through the gas. This gives a consistent picture of a CR ionisation of the gas in the region, due to the presence of low-energy CRs downstream the SNR shock. Complementary IRAM 30m observations were obtained to both recover the missing short-spacings from the interferometer observations and map the surroundings of the W51C-E position, parallel to the SNR shock. It would be interesting to obtain another map, perpendicular to the shock. The detection of compact SiO emission indeed suggests that there might be more SiO emission regions along the propagation axis of the SNR shock. An IRAM 30m map along this direction would thus allow to define new regions to be explored with NOEMA.

In the W28 region, I observed with the IRAM 30m radio telescope several lines of sight close to the SNR shock, where the CR ionisation rate is at least 100 times higher than the standard rate, and one position in the Southern part of the cloud where the rate is “standard”. These observations brought evidence of an enhanced ionisation in a dense cloud next to a SNR, due to the presence of CRs accelerated in the SNR shell. They also brought unprecedented constraints on the diffusion properties of low-energy CRs, in an energy range unaccessible to other observational techniques. In this study, I used the DCO^+/HCO^+ abundance ratio, and I identified the limitations of this method at high ionisation. These limitations suggest to look for alternate tracers of the ionisation.

I then carried out follow-up observations of the W28 region to try to identify such tracers. I selected a series of potential ionisation tracers based on grids of chemical models, which could be observed at the IRAM 30m telescope: CCH, HCN, HNC, $H^{13}CN$, N_2H^+, and CN. I obtained high-spectral resolution and low-noise observations towards known positions in W28 of both high and standard ionisation, in order to compare the chemical abundances of these species at these positions. The presence of several velocity components on the line of sight introduced confusion in the analysis of the hyperfine structure of some transitions, e.g. HCN$(1-0)$. For the moment, there is no definitive identification of new tracers from this analysis. Yet, CN and N_2H^+ seem promising and should be further investigated.

A limitation to this quest for new tracers is that besides the high-ionisation positions in the W28 northern cloud, there is only one position in the southern region where the CR ionisation rate could be determined, which is also the only position with a “standard” ζ. To get a better understanding of the southern region and observe additional low-ionisation sight lines, we obtained follow-up observations at the IRAM 30m telescope to map the southern cloud and study a possible ionisation gradient toward the shell of the SNR. I will carry out these observations at the end of May 2015, and their analysis will come after the end of this thesis.

In parallel of the search for new tracers, I also studied another source, in the SNR W44 region, where we also expect the CR ionisation to be enhanced. However, there is neither a clear DCO^+ emission gradient, nor conclusive evidence of enhanced ionisation from the DCO^+/HCO^+ abundance ratio. Constraints on the CR ionisation rate from DCO^+/HCO^+ and N_2H^+/HCO^+ seem to be inconsistent, as N_2H^+/HCO^+ ratios are similar within all sight lines, regardless of whether DCO^+ is detected or not. Yet, the combined study of DCO^+/HCO^+ and N_2H^+/HCO^+ gives unexpected constraints on the volatile content of carbon and nitrogen in the gas-phase, and points towards high ζ values. We conclude that the carbon abundance is likely higher than previously assumed in our calculations, i.e. CO is likely un-depleted in this region. A time-dependent analysis of the LIP/HIP transition is consistent with the estimated age of the W44 SNR. Results in this region are still preliminary, and need to be properly understood.

Now, we expect to obtain high spatial resolution observations to further explore the northern cloud in W28. Despite the high ionisation, we determined temperatures as low as 8 K toward some of the sight lines. At these positions, a possible alternative explanation to CR ionisation of the non-detection of DCO^+ could be that deuterium is locally depleted. A proposal for ALMA observations was submitted to study the possible deuterium depletion in the W28 region.

It would also be necessary to improve our chemical modeling, by taking into account a self-consistent calculation of the thermal balance. The temperature in a molecular cloud irradiated by a large CR flux is indeed expected to increase with respect to temperatures in passive molecular clouds, although the temperatures we observed in the three sources we studied remain low.

Finally, the H^+/H_3^+ ratio was early recognized to be very different in the LIP and HIP (Le Bourlot et al., 1993), which may have observable consequences on the ortho/para ratio of other species such as nitrogen hydrides. This may provide new diagnostics of the chemical conditions in the HIP, and requires dedicated investigation.

During these three years, I have studied how the abundances of several species are affected by the CR ionisation rate in molecular clouds, and confronted chemical model predictions to radio observations. This research brought valuable insight into the CR induced chemistry in the interstellar medium. CRs are of tremendous importance in the dynamical and chemical evolution of the ISM, and the study of their effect on the chemistry can lead to precious information unaccessible to other observational means, and complementary to high-energy observations. This work indeed brought new perspectives of interdisciplinary research towards the understanding of CRs, from millimeter to gamma-ray observations. Finally, this work is to be extended to observations of the CR ionisation in extragalactic giant molecular clouds, beyond our own Galaxy.

Résumé et perspectives

Durant cette thèse, j'ai étudié les effets des RCs sur l'ionisation de la phase gazeuse dans les nuages moléculaires. Notamment, les RCs ionisent H_2 et initient une série de réactions chimiques entre des ions moléculaires et des espèces neutres dans le nuage. Parce qu'ils augmentent l'abondance des électrons, les RCs contrôlent aussi les processus de recombinaison électronique et donc les abondances des ions moléculaires. Ainsi, les RCs contrôlent l'abondance de certaines espèces caractéristiques, appelées traceurs de l'ionisation. Alors, en étudiant ces traceurs, il est possible de donner des contraintes sur la valeur du taux d'ionisation par les RCs ζ. La valeur considérée comme standard dans les nuages moléculaires est $\zeta = 1 \times 10^{-17}$ s^{-1}.

En associant observations et modélisation, j'ai étudié les abondances chimiques des traceurs de l'ionisation dans les nuages moléculaires proches de trois rémanents de supernova : W28, W51C et W44. Pour chacun de ces rémanents, des preuves observationnelles complémentaires de la présence de gaz choqué, ainsi que la détection d'émission gamma en provenance du nuage – probablement induite par des protons relativistes – démontrent l'existence d'une interaction avec le nuage à proximité.

Dans la région du SNR W51C, des observations à haute résolution spatiale avec l'interféromètre du Plateau de Bure (IRAM) ont apporté la confirmation d'un fort taux d'ionisation, comme proposé par Ceccarelli et al. (2011). Elles ont également permis la détection d'émission compacte de SiO, qui révèle probablement le passage de l'onde de choc du SNR dans le gaz. Ces observations donnent ainsi une image cohérente d'une forte ionisation dans la région, dûe à la présence de RCs de basse énergie en aval du choc. Des observations complémentaires avec le télescope de 30m de l'IRAM ont permis d'une part de fournir les observations manquantes à courte base, et d'autre part de cartographier une zone autour de la position W51C-E, parallèlement au choc. Il serait profitable d'obtenir également une carte perpendiculaire au choc. En effet, nos observations de SiO suggèrent qu'il pourrait y avoir davantage de régions d'émission compacte le long de l'axe de propagation du choc. Une carte obtenue avec le 30m nous permettrait alors de définir d'autres régions à explorer avec NOEMA.

Dans la région du SNR W28, j'ai détecté à l'aide du télescope de 30m de l'IRAM plusieurs lignes de visée proches de l'onde de choc avec des taux d'ionisation par les RCs au moins 100 fois supérieurs à la valeur standard. J'ai également identifié une position dans la région Sud, loin du choc, où l'ionisation est standard. Ces observations apportent la preuve de l'existence d'un très fort taux d'ionisation dans un nuage dense à proximité d'un SNR, qui peut être expliqué par la présence de RCs accélérés dans l'enveloppe du SNR. Elles apportent également des contraintes inédites sur les propriétés de diffusion des RCs, dans un domaine d'énergie inaccessible aux autres techniques d'observation. Dans cette étude, j'ai utilisé le rapport d'abondances DCO^+/HCO^+ et identifié les limites de cette méthode à haute ionisation. À cause de ces limites, il serait nécessaire d'identifier des traceurs de l'ionisation alternatifs.

J'ai alors mené des observations complémentaires dans la région de W28 pour tenter d'identifier de tels traceurs. En m'appuyant sur une grille de modèles chimiques, j'ai sélectionné une liste d'espèces sensibles au taux d'ionisation ζ et pouvant être observées au 30m : CCH, HCN, HNC, $H^{13}CN$, N_2H^+ et CN. J'ai obtenu des observations à haute résolution spectrale avec un bruit très réduit, sur des lignes de visée déjà étudiées précédemment et où les conditions d'ionisation sont très différentes, afin d'y comparer les abondances de cette série d'espèces chimiques. La présence de plusieurs composantes de vitesse du gaz sur une même ligne de visée a parfois rendu l'analyse des structures hyperfines compliquée, comme par exemple celle de $HCN(1-0)$. Jusqu'à présent, l'analyse n'a pas permis d'identifier avec certitude de nouveaux traceurs. Cependant, CN et N_2H^+ semblent des traceurs potentiels. Cette piste nécessiterait d'être davantage approfondie.

Cette quête de nouveaux traceurs est limitée par le faible nombre de positions observées pour l'instant dans la région W28. En effet, une seule position, dans le Sud de la région, présente un taux d'ionisation

ζ “standard”. Nous avons ainsi obtenu des observations complémentaires au 30m de l'IRAM afin de cartographier la région Sud, dans le but de mieux comprendre cette région, d'y observer davantage de lignes de visée et d'étudier un éventuel gradient d'ionisation en direction de l'enveloppe du SNR. Je mènerai ces observations à la fin du mois de mai 2015 et elles seront analysées après la fin de cette thèse.

En parallèle de cette recherche de nouveaux traceurs, j'ai également étudié un nuage moléculaire dans la région du SNR W44, où l'on peut également s'attendre à observer un fort taux d'ionisation. Pourtant, nous n'avons pu détecter ni la présence d'un gradient de l'émission de DCO^+, ni de preuve indiscutable d'une forte ionisation à partir du rapport d'abondances DCO^+/HCO^+. En effet, les contraintes apportées par DCO^+/HCO^+et N_2H^+/HCO^+ semblent contradictoires et les valeurs mesurées de N_2H^+/HCO^+ sont similaires pour chaque ligne de visée, que DCO^+ soit ou non détecté. Néanmoins, l'étude simultanée de ces deux rapports d'abondance a permis d'apporter des contraintes inattendues sur les abondances volatiles de carbone et d'azote dans la phase gazeuse et semble indiquer de fortes valeurs de ζ. De cette étude, nous pouvons conclure que l'abondance de carbone dans la phase gazeuse est probablement supérieure à celle supposée précédemment. En d'autres termes, CO est probablement non déplété dans cette région. La modélisation de l'évolution temporelle de la transition HIP/LIP est cohérente avec l'âge estimé du SNR W44. Ces résultats sont encore préliminaires et nécessitent d'être proprement interprétés.

Nous espérons désormais obtenir des observations à haute résolution spatiale dans la région Nord de W28. Pour certaines lignes de visée, les températures que nous avons déterminées dans la phase gazeuse sont parfois très basses ($\sim$ 8 K) malgré le fort taux d'ionisation observé. Il se pourrait alors que la non-détection de DCO^+ puisse être expliquée localement non par l'ionisation des RCs, mais par la déplétion du deuterium. Nous avons proposé un projet d'observations ALMA pour étudier une possible déplétion du deuterium dans cette région.

D'autre part, il serait nécessaire de développer davantage le modèle de chimie, en introduisant un calcul cohérent de l'équilibre thermique. En effet, on s'attend à ce que la température dans des nuages moléculaires soumis à un flux intense de RCs augmente par rapport à celle des nuages isolés, alors même que les températures mesurées dans les trois nuages présentés ici restent basses.

Enfin, Le Bourlot et al. (1993) ont montré que le rapport H^+/H_3^+ devrait être très différent entre la LIP et la HIP. Cela pourrait avoir des conséquences observables sur le rapport ortho/para d'autres espèces, comme par exemple les hydrures d'azote. Cela pourrait alors fournir de nouveaux outils de détermination des conditions chimiques dans la HIP, et nécessite un travail d'investigation spécifique.

Durant ces trois années, j'ai cherché à comprendre de quelle manière le taux d'ionisation par les RCs influence les abondances chimiques de certaines espèces dans les nuages moléculaires, en comparant les prédictions des modèles chimiques aux observations radio. Ces recherches ont apporté une meilleure compréhension de la chimie induite par les RCs dans le milieu interstellaire. Les RCs ont un rôle primordial dans la dynamique et l'évolution chimique du milieu interstellaire et l'étude de leurs effets sur la chimie fournit des informations cruciales, inaccessibles aux autres techniques d'observation et complémentaires aux observations à haute énergie. Ce travail a ainsi apporté des perspectives de projets de recherche interdisciplinaires pour la compréhension des RCs, des observations millimétriques jusqu'aux observations gamma. Enfin, ce travail peut s'étendre aux observations de l'ionisation par les RCs dans les nuages moléculaires géants, au-delà de notre propre Galaxie.

Bibliography

Abdo, A. A. and Collaboration, F.-L. (2011). Observations of the Young Supernova Remnant RX J1713.7-3946 with the Fermi Large Area Telescope. *The Astrophysical Journal*, 734:28.

Abramowski, A. and Collaboration, H. (2015a). Discovery of the VHE gamma-ray source HESS J1832-093 in the vicinity of SNR G22.7-0.2. *Monthly Notices of the Royal Astronomical Society*, 446:1163–1169.

Abramowski, A. and Collaboration, H. (2015b). H.E.S.S. detection of TeV emission from the interaction region between the supernova remnant G349.7+0.2 and a molecular cloud. *Astronomy and Astrophysics*, 574:A100.

Abramowski, A. and Collaboration, H. (2015c). Probing the gamma-ray emission from HESS J1834-087 using H.E.S.S. and Fermi LAT observations. *Astronomy and Astrophysics*, 574:A27.

Ackermann, M. and Collaboration, F.-L. (2013). Detection of the Characteristic Pion-Decay Signature in Supernova Remnants. *Science*, 339:807–811.

Adams, W. S. (1949). Observations of Interstellar H and k, Molecular Lines, and Radial Velocities in the Spectra of 300 O and B Stars. *The Astrophysical Journal*, 109:354.

Aharonian, F. and Collaboration, H. (2008a). Discovery of very high energy gamma-ray emission coincident with molecular clouds in the W 28 (G6.4-0.1) field. *Astronomy and Astrophysics*, 481(2):401–410.

Aharonian, F. and Collaboration, H. (2008b). Energy Spectrum of Cosmic-Ray Electrons at TeV Energies. *Annual Review of Astronomy & Astrophysics*, 101(2):261104.

Aleksić, J. and Collaboration, M. (2012). Morphological and spectral properties of the W51 region measured with the MAGIC telescopes. *Astronomy and Astrophysics*, 541:13.

André, P., Di Francesco, J., Ward-Thompson, D., Inutsuka, S. I., Pudritz, R. E., and Pineda, J. E. (2014). From Filamentary Networks to Dense Cores in Molecular Clouds: Toward a New Paradigm for Star Formation. *Protostars and Planets VI*, pages 27–51.

Arce, H. G., Shepherd, D., Gueth, F., Lee, C.-F., Bachiller, R., Rosen, A., and Beuther, H. (2008). Molecular Outflow in Low- and High-Mass Star Forming Regions. *PPV*, pages 1–16.

Asplund, M., Grevesse, N., Sauval, A. J., and Scott, P. (2009). The Chemical Composition of the Sun. *Annual Review of Astronomy & Astrophysics*, 47(1):481–522.

Balbus, S. A. and Hawley, J. F. (1998). Instability, turbulence, and enhanced transport in accretion disks. *Reviews of Modern Physics*, 70(1):1–53.

Bell, A. R. (1978). The acceleration of cosmic rays in shock fronts. I. *Monthly Notices of the Royal Astronomical Society*, 182:147–156.

Bergin, E. A., Alves, J., Huard, T., and Lada, C. J. (2002). N2H+ and C18O Depletion in a Cold Dark Cloud. *The Astrophysical Journal*, 570(2):L101–L104.

Bergin, E. A. and Tafalla, M. (2007). Cold Dark Clouds: The Initial Conditions for Star Formation. *Annual Review of Astronomy & Astrophysics*, 45(1):339–396.

Bevington, P. R. and Robinson, D. K. (1992). *Data reduction and error analysis for the physical sciences.* WCB McGraw-Hill, 2^e edition.

Black, J. H. and Dalgarno, A. (1973). The Cosmic Abundance of Deuterium. *The Astrophysical Journal*, 184:L101.

Black, J. H. and Dalgarno, A. (1977). Models of interstellar clouds. I - The Zeta Ophiuchi cloud. *The Astrophysical Journal Supplement Series*, 34:405–423.

Blandford, R., Simeon, P., and Yuan, Y. (2014). Cosmic Ray Origins: An Introduction. In *Nuclear Physics B (Proceedings Supplements)*, pages 9–22. KIPAC, Stanford University.

Blasi, P. (2013). The origin of galactic cosmic rays. *The Astronomy and Astrophysics Review*, 21:70.

Blondin, J. M., Wright, E. B., Borkowski, K. J., and Reynolds, S. P. (1998). Transition to the Radiative Phase in Supernova Remnants. *The Astrophysical Journal*, 500(1):342–354.

Boger, G. I. and Sternberg, A. (2005). CN and HCN in Dense Interstellar Clouds. *The Astrophysical Journal*, 632:302–315.

Boger, G. I. and Sternberg, A. (2006). Bistability in Interstellar Gas-Phase Chemistry. *The Astrophysical Journal*, 645:314–323.

Bohlin, R. C., Savage, B. D., and Drake, J. F. (1978). A survey of interstellar H I from L-alpha absorption measurements. II. *The Astrophysical Journal*, 224:132–142.

Bolatto, A. D., Wolfire, M., and Leroy, A. K. (2013). The CO-to-H2 Conversion Factor. *Annual Review of Astronomy & Astrophysics*, 51:207–268.

Brogan, C. L., Gelfand, J. D., Gaensler, B. M., Kassim, N. E., and Lazio, T. J. (2006). Discovery of 35 New Supernova Remnants in the Inner Galaxy. *The Astrophysical Journal Letters*, 639:L25–L29.

Carigi, L., Peimbert, M., Esteban, C., and García-Rojas, J. (2005). Carbon, Nitrogen, and Oxygen Galactic Gradients: A Solution to the Carbon Enrichment Problem. *The Astrophysical Journal*, 623:213–224.

Carter, M., Lazareff, B., Maier, D., Chenu, J. Y., Fontana, A. L., Bortolotti, Y., Boucher, C., Navarrini, A., Blanchet, S., Greve, A., John, D., Kramer, C., Morel, F., Navarro, S., Peñalver, J., Schuster, K. F., and Thum, C. (2012). The EMIR multi-band mm-wave receiver for the IRAM 30-m telescope. *Astronomy and Astrophysics*, 538:A89.

Caselli, P. and Ceccarelli, C. (2012). Our astrochemical heritage. *The Astronomy and Astrophysics Review*, 20:56.

Caselli, P., Walmsley, C. M., Tafalla, M., Dore, L., and Myers, P. C. (1999). CO Depletion in the Starless Cloud Core L1544. *The Astrophysical Journal*, 523(2):L165–L169.

Caselli, P., Walmsley, C. M., Terzieva, R., and Herbst, E. (1998). The Ionization Fraction in Dense Cloud Cores. *The Astrophysical Journal*, 499:234.

Ceccarelli, C., Hily-Blant, P., Montmerle, T., Dubus, G., Gallant, Y., and Fiasson, A. (2011). Supernova-enhanced Cosmic-Ray Ionization and Induced Chemistry in a Molecular Cloud of W51C. *The Astrophysical Journal*, 740:L4.

Ceccarelli, C., Maret, S., Tielens, A. G. G. M., Castets, A., and Caux, E. (2003). Theoretical H_2CO emission from protostellar envelopes. *Astronomy and Astrophysics*, 410:587–595.

Chevalier, R. A. (1982). Self-similar solutions for the interaction of stellar ejecta with an external medium. *The Astrophysical Journal*, 258:790–797.

Claussen, M. J., Frail, D. A., Goss, W. M., and Gaume, R. A. (1997). Polarization Observations of 1720 MHz OH Masers toward the Three Supernova Remnants W28, W44, and IC443. *The Astrophysical Journal*, 489:143–159.

Codella, C., Bachiller, R., and Reipurth, B. (1999). Low and high velocity SiO emission around young stellar objects. *Astronomy and Astrophysics*, 343:585–598.

Cyganowski, C. J., Brogan, C. L., Hunter, T. R., and Churchwell, E. (2011). Deep Very Large Array Radio Continuum Surveys of GLIMPSE Extended Green Objects (EGOs). *The Astrophysical Journal*, 743(1):56.

Dalgarno, A. (2006). Interstellar Chemistry Special Feature: The galactic cosmic ray ionization rate. *Proceedings of the National Academy of Science*, 103:12269–12273.

Dalgarno, A., Yan, M., and Liu, W. (1999). Electron Energy Deposition in a Gas Mixture of Atomic and Molecular Hydrogen and Helium. *The Astrophysical Journal Supplement Series*, 125(1):237–256.

Dame, T. M., Hartmann, D., and Thaddeus, P. (2001). The Milky Way in Molecular Clouds: A New Complete CO Survey. *The Astrophysical Journal*, 547(2):792–813.

Daniel, F., Cernicharo, J., and Dubernet, M. L. (2006). The Excitation of N_2H^+ in Interstellar Molecular Clouds. I. Models. *The Astrophysical Journal*, 648(1):461–471.

Daniel, F., Dubernet, M. L., Meuwly, M., Cernicharo, J., and Pagani, L. (2005). Collisional excitation rate coefficients of N_2H^+ by He. *Monthly Notices of the Royal Astronomical Society*, 363(4):1083–1091.

de Jong, T., Boland, W., and Dalgarno, A. (1980). Hydrostatic models of molecular clouds. *Astronomy and Astrophysics*, 91:68–84.

Dumas, G., Vaupré, S., Ceccarelli, C., Hily-Blant, P., Dubus, G., Montmerle, T., and Gabici, S. (2014). Localized SiO Emission Triggered by the Passage of the W51C Supernova Remnant Shock. *The Astrophysical Journal Letters*, 786(2):L24.

Dumouchel, F., Faure, A., and Lique, F. (2010). The rotational excitation of HCN and HNC by He: temperature dependence of the collisional rate coefficients. *Monthly Notices of the Royal Astronomical Society*, 406(4):2488–2492.

Elitzur, M. (1976). Inversion of the OH 1720-MHz Line. *The Astrophysical Journal*, 203:124–131.

Elitzur, M. (1992). *Astronomical Masers*. Klower Academic Publishers.

Ellison, D. C., Patnaude, D. J., Slane, P., and Raymond, J. (2010). Efficient Cosmic Ray Acceleration, Hydrodynamics, and Self-Consistent Thermal X-Ray Emission Applied to Supernova Remnant RX J1713.7-3946. *The Astrophysical Journal*, 712(1):287–293.

Faure, A. (2011). Electron fraction and the excitation of interstellar HCO^+. *Memorie della Societa Astronomica Italiana*, 82:929.

Federman, S. R., Lambert, D. L., Sheffer, Y., Cardelli, J. A., Andersson, B.-G., van Dishoeck, E. F., and Zsargo, J. (2003). Further Evidence for Chemical Fractionation from Ultraviolet Observations of Carbon Monoxide. *The Astrophysical Journal*, 591:986–999.

Ferrière, K. M. (2001). The interstellar environment of our galaxy. *Reviews of Modern Physics*, 73:1031–1066.

Flower, D. R. (1999). Rotational excitation of HCO^+ by H_2. *Monthly Notices of the Royal Astronomical Society*, 305(3):651–653.

Frerking, M. A., Langer, W. D., and Wilson, R. W. (1982). The relationship between carbon monoxide abundance and visual extinction in interstellar clouds. *The Astrophysical Journal*, 262:590–605.

Gabici, S., Aharonian, F. A., and Casanova, S. (2009). Broad-band non-thermal emission from molecular clouds illuminated by cosmic rays from nearby supernova remnants. *Monthly Notices of the Royal Astronomical Society*, 396(3):1629–1639.

Garrod, R. T. and Herbst, E. (2006). Formation of methyl formate and other organic species in the warm-up phase of hot molecular cores. *Astronomy and Astrophysics*, 457:927–936.

Gerin, M., , and Collaboration, H. (2010). Interstellar OH^+, H_2O^+ and H_3O^+ along the sight-line to G10.6-0.4. *Astronomy and Astrophysics*, 518:L110.

Giuliani, A. and Collaboration, A. (2011). Neutral Pion Emission from Accelerated Protons in the Supernova Remnant W44. *The Astrophysical Journal Letters*, 742(2):L30.

Giuliani, A., Tavani, M., Bulgarelli, A., Striani, E., Sabatini, S., Cardillo, M., Fukui, Y., Kawamura, A., Ohama, A., Furukawa, N., Torii, K., Sano, H., Aharonian, F. A., Verrecchia, F., Argan, A., Barbiellini, G., Caraveo, P. A., Cattaneo, P. W., Chen, A. W., Cocco, V., Costa, E., D'Ammando, F., Del Monte, E., de Paris, G., Di Cocco, G., Donnarumma, I., Evangelista, Y., Feroci, M., Fiorini, M., Froysland, T., Fuschino, F., Galli, M., Gianotti, F., Labanti, C., Lapshov, Y., Lazzarotto, F., Lipari, P., Longo, F., Marisaldi, M., Mereghetti, S., Morselli, A., Moretti, E., Pacciani, L., Pellizzoni, A., Perotti, F., Picozza, P., Pilia, M., Prest, M., Pucella, G., Rapisarda, M., Rappoldi, A., Soffitta, P., Trifoglio, M., Trois, A., Vallazza, E., Vercellone, S., Vittorini, V., Zambra, A., Zanello, D., Pittori, C., Santolamazza, P., Giommi, P., Colafrancesco, S., and Salotti, L. (2010). AGILE detection of GeV γ-ray emission from the SNR W28. *Astronomy and Astrophysics*, 516:L11.

Glassgold, A. E., Galli, D., and Padovani, M. (2012). Cosmic-ray and X-ray Heating of Interstellar Clouds and Protoplanetary Disks. *The Astrophysical Journal*, 756:157.

Glassgold, A. E. and Langer, W. D. (1974). Model calculations for diffuse molecular clouds. *The Astrophysical Journal*, 193:73–91.

Godard, B. and Cernicharo, J. (2013). A complete model of CH^+ rotational excitation including radiative and chemical pumping processes. *Astronomy and Astrophysics*, 550:A8.

Goldsmith, P. F. (2001). Molecular Depletion and Thermal Balance in Dark Cloud Cores. *The Astrophysical Journal*, 557(2):736–746.

Goldsmith, P. F. and Langer, W. D. (1978). Molecular cooling and thermal balance of dense interstellar clouds. *The Astrophysical Journal*, 222:881–895.

Gómez, G. C. (2006). Errors in Kinematic Distances and Our Image of the Milky Way Galaxy. *The Astronomical Journal*, 132(6):2376–2382.

Graedel, T. E., Langer, W. D., and Frerking, M. A. (1982). The kinetic chemistry of dense interstellar clouds. *The Astrophysical Journal Supplement Series*, 48:321–368.

Green, S. and Thaddeus, P. (1974). Rotational Excitation of HCN by Collisions. *The Astrophysical Journal*, 191:653–658.

Greve, A., Kramer, C., and Wild, W. (1998). The beam pattern of the IRAM 30-m telescope. (a reflector with several surface error distributions). *Astronomy and Astrophysics Supplement*, 133:271–284.

Guélin, M., Langer, W. D., Snell, R. L., and Wootten, H. A. (1977). Observations of DCO/plus/ - The electron abundance in dark clouds. *The Astrophysical Journal Letters*, 217:L165–L168.

Guélin, M., Langer, W. D., and Wilson, R. W. (1982). The state of ionization in dense molecular clouds. *Astronomy and Astrophysics*, 107:107–127.

Gusdorf, A., Pineau des Forets, G., Cabrit, S., and Flower, D. R. (2008). SiO line emission from interstellar jets and outflows: silicon-containing mantles and non-stationary shock waves. *Astronomy and Astrophysics*, 490(2):695–706.

Handa, T., Sofue, Y., Nakai, N., Hirabayashi, H., and Inoue, M. (1987). A radio continuum survey of the Galactic plane at 10 GHz. *Astronomical Society of Japan*, 39:709–753.

Hartmann, J. (1904). Investigations on the spectrum and orbit of delta Orionis. *The Astrophysical Journal*, 19:268–286.

Hasegawa, T. I. and Herbst, E. (1993). New gas-grain chemical models of quiescent dense interstellar clouds - The effects of H2 tunnelling reactions and cosmic ray induced desorption. *Monthly Notices of the Royal Astronomical Society (ISSN 0035-8711)*, 261:83–102.

Helder, E. A., Vink, J., Bykov, A. M., Ohira, Y., Raymond, J. C., and Terrier, R. (2012). Observational Signatures of Particle Acceleration in Supernova Remnants. *Space Science Reviews*, 173(1):369–431.

Hennebelle, P. (2013). On the origin of non-self-gravitating filaments in the ISM. *Astronomy and Astrophysics*, 556:A153.

Herbst, E. (2005). Molecular ions in interstellar reaction networks. *Journal of Physics: Conference Series*, 4(1):17–25.

Hily-Blant, P., Walmsley, M., Pineau des Forêts, G., and Flower, D. (2010). Nitrogen chemistry and depletion in starless cores. *Astronomy and Astrophysics*, 513:41.

Hogerheijde, M. R. and van der Tak, F. F. S. (2000). An accelerated Monte Carlo method to solve two-dimensional radiative transfer and molecular excitation. With applications to axisymmetric models of star formation. *Astronomy and Astrophysics*, 362:697–710.

Hollenbach, D. J. and Tielens, A. G. G. M. (1999). Photodissociation regions in the interstellar medium of galaxies. *Reviews of Modern Physics*, 71(1):173–230.

Indriolo, N., Blake, G. A., Goto, M., Usuda, T., Oka, T., Geballe, T. R., Fields, B. D., and McCall, B. J. (2010). Investigating the Cosmic-ray Ionization Rate Near the Supernova Remnant IC 443 through H+ 3 Observations. *The Astrophysical Journal*, 724(2):1357–1365.

Indriolo, N., Geballe, T. R., Oka, T., and McCall, B. J. (2007). H+3 in Diffuse Interstellar Clouds: A Tracer for the Cosmic-Ray Ionization Rate. *The Astrophysical Journal*, 671(2):1736–1747.

Indriolo, N. and McCall, B. J. (2012). Investigating the Cosmic-Ray Ionization Rate in the Galactic Diffuse Interstellar Medium through Observations of H+ 3. *The Astrophysical Journal*, 745(1):91.

Indriolo, N. and McCall, B. J. (2013). Cosmic-ray astrochemistry. *Chemical Society Reviews*, 42:7763–7773.

Indriolo, N., Neufeld, D. A., Gerin, M., Geballe, T. R., Black, J. H., Menten, K. M., and Goicoechea, J. R. (2012). Chemical Analysis of a Diffuse Cloud along a Line of Sight toward W51: Molecular Fraction and Cosmic-Ray Ionization Rate. *The Astrophysical Journal*, 758(2):83.

Indriolo, N., Neufeld, D. A., Gerin, M., Schilke, P., Benz, A. O., Winkel, B., Menten, K. M., Chambers, E. T., Black, J. H., Bruderer, S., Falgarone, E., Godard, B., Goicoechea, J. R., Gupta, H., Lis, D. C., Ossenkopf, V., Persson, C. M., Sonnentrucker, P., van der Tak, F. F. S., van Dishoeck, E. F., Wolfire, M. G., and Wyrowski, F. (2015). Herschel Survey of Galactic OH+, H2O+, and H3O+: Probing the Molecular Hydrogen Fraction and Cosmic-Ray Ionization Rate. *The Astrophysical Journal*, 800:40.

Jones, A. P. and Williams, D. A. (1985). Time-dependent sticking coefficients and mantle growth on interstellar grains. *Monthly Notices of the Royal Astronomical Society (ISSN 0035-8711)*, 217:413–421.

Katz, B. and Waxman, E. (2008). In which shell-type SNRs should we look for gamma-rays and neutrinos from p-p collisions? *Journal of Cosmology and Astroparticle Physics*, 1:18.

Kerr, F. J. (1962). Galactic velocity models and the interpretation of 21-cm surveys. *Monthly Notices of the Royal Astronomical Society*, 123:327.

Koo, B.-C. and Heiles, C. (1991). A survey of H I 21 centimeter emission lines toward supernova remnants. *The Astrophysical Journal*, 382:204–222.

Le Bourlot, J., Pineau des Forêts, G., and Roueff, E. (1995a). Complex dynamical behaviour in interstellar chemistry. *Astronomy and Astrophysics*, 297:251–260.

Le Bourlot, J., Pineau des Forets, G., Roueff, E., and Flower, D. R. (1995b). On the uniqueness of the solutions to the chemical rate equations in interstellar clouds: the gas-dust interface. *Astronomy and Astrophysics*, 302:870.

Le Bourlot, J., Pineau des Forêts, G., Roueff, E., and Schilke, P. (1993). Bistability in Dark Cloud Chemistry. *The Astrophysical Journal Letters*, 416:L87.

Le Petit, F., Nehmé, C., Le Bourlot, J., and Roueff, E. (2006). A Model for Atomic and Molecular Interstellar Gas: The Meudon PDR Code. *The Astrophysical Journal Supplement Series*, 164:506–529.

Leger, A., Jura, M., and Omont, A. (1985). Desorption from interstellar grains. *Astronomy and Astrophysics (ISSN 0004-6361)*, 144:147–160.

Lesur, G., Kunz, M. W., and Fromang, S. (2014). Thanatology in Protoplanetary Discs: the combined influence of Ohmic, Hall, and ambipolar diffusion on dead zones. *Astronomy and Astrophysics*, 566:A56.

Linsky, J. L., Diplas, A., Wood, B. E., Brown, A., Ayres, T. R., and Savage, B. D. (1995). Deuterium and the Local Interstellar Medium Properties for the Procyon and Capella Lines of Sight. *The Astrophysical Journal*, 451:335.

Maret, S., Bergin, E. A., and Lada, C. J. (2006). A low fraction of nitrogen in molecular form in a dark cloud. *Nature*, 442(7):425–427.

Maret, S., Bergin, E. A., and Tafalla, M. (2013). Chemical modeling of the L1498 and L1517B prestellar cores: CO and HCO^+ depletion. *Astronomy and Astrophysics*, 559:A53.

McCall, B. J., Geballe, T. R., Hinkle, K. H., and Oka, T. (1999). Observations of H_3^+ in Dense Molecular Clouds. *The Astrophysical Journal*, 522(1):338–348.

McCall, B. J., Huneycutt, A. J., Saykally, R. J., Geballe, T. R., Djuric, N., Dunn, G. H., Semaniak, J., Novotny, O., Al-Khalili, A., Ehlerding, A., Hellberg, F., Kalhori, S., Neau, A., Thomas, R., Österdahl, F., and Larsson, M. (2003). An enhanced cosmic-ray flux towards ζ Persei inferred from a laboratory study of the H_3^+-e^- recombination rate. *Nature*, 422(6):500–502.

Milam, S. N., Savage, C., Brewster, M. A., Ziurys, L. M., and Wyckoff, S. (2005). The 12C/13C Isotope Gradient Derived from Millimeter Transitions of CN: The Case for Galactic Chemical Evolution. *The Astrophysical Journal*, 634(2):1126–1132.

Mladenović, M. and Roueff, E. (2014). Ion-molecule reactions involving HCO+ and N2H+: Isotopologue equilibria from new theoretical calculations and consequences for interstellar isotope fractionation. *Astronomy and Astrophysics*, 566:A144.

Morlino, G. and Gabici, S. (2014). Propagation of cosmic rays into diffuse clouds. *arXiv.org*, page 7938.

Morlino, G. and Gabici, S. (2015). Cosmic ray penetration in diffuse clouds. *Monthly Notices of the Royal Astronomical Society: Letters*, 451(1):L100–L104.

Neufeld, D. A. and Collaboration, H. (2010). Herschel/HIFI observations of interstellar OH^+ and H_2O^+ towards W49N: a probe of diffuse clouds with a small molecular fraction. *Astronomy and Astrophysics*, 521:L10.

Nicholas, B. P., Rowell, G., Burton, M. G., Walsh, A. J., Fukui, Y., Kawamura, A., and Maxted, N. I. (2012). A 7 mm line survey of the shocked and disrupted molecular gas towards the W28 field TeV gamma-ray sources. *Annual Review of Astronomy & Astrophysics*, 419:251–266.

Padovani, M. and Galli, D. (2013). Cosmic-Ray Propagation in Molecular Clouds. *Astrophysics and Space Science Proceedings*, 34:61.

Padovani, M., Galli, D., and Glassgold, A. E. (2009). Cosmic-ray ionization of molecular clouds. *Annual Review of Astronomy & Astrophysics*, 501:619–631.

Pineau des Forêts, G., Roueff, E., and Flower, D. R. (1992). The two chemical phases of dark interstellar clouds. *Monthly Notices of the Royal Astronomical Society*, 258:45P–47P.

Radhakrishnan, V., Goss, W. M., Murray, J. D., and Brooks, J. W. (1972). The Parkes Survey of 21-CENTIMETER Absorption in Discrete-Source Spectra. III. 21- Centimeter Absorption Measurements on 41 Galactic Sources North of Declination -48 degrees. *The Astrophysical Journal Supplement Series*, 24:49.

Reynolds, S. P. (2008). Supernova Remnants at High Energy. *Annual Review of Astronomy & Astrophysics*, 46(1):89–126.

Rho, J. and Petre, R. (1998). Mixed-Morphology Supernova Remnants. *The Astrophysical Journal*, 503(2):L167–L170.

Roberts, H. and Millar, T. J. (2000). Modelling of deuterium chemistry and its application to molecular clouds. *Astronomy and Astrophysics*, 361:388–398.

Schilke, P., Walmsley, C. M., Pineau des Forêts, G., and Flower, D. R. (1997). SiO production in interstellar shocks. *Astronomy and Astrophysics*, 321:293–304.

Scoville, N. Z. and Solomon, P. M. (1974). Radiative Transfer, Excitation, and Cooling of Molecular Emission Lines (co and Cs). *The Astrophysical Journal*, 187:L67.

Seo, E.-S. (1991). Measurement of galactic cosmic ray proton and helium spectra during the 1987 solar minimum. *Ph.D. Thesis Louisiana State Univ.*, page 4.

Slane, P., Bykov, A., Ellison, D. C., Dubner, G., and Castro, D. (2014). Supernova Remnants Interacting with Molecular Clouds: X-Ray and Gamma-Ray Signatures. *Space Science Reviews*, -1:26.

Slysh, V. I., Wilson, T. L., Pauls, T., and Henkel, C. (1980). Molecular clouds near supernova remnants. In *In: Interstellar molecules; Proceedings of the Symposium*, pages 473–478. Akademiia Nauk SSSR, Institut Kosmicheskikh Issledovanii, Moscow, USSR.

Snow, T. P. and McCall, B. J. (2006). Diffuse Atomic and Molecular Clouds. *Annual Review of Astronomy & Astrophysics*, 44(1):367–414.

Spielfiedel, A., Feautrier, N., Najar, F., Ben Abdallah, D., Dayou, F., Senent, M. L., and Lique, F. (2012). Fine and hyperfine excitation of C2H by collisions with He at low temperature. *Monthly Notices of the Royal Astronomical Society*, 421(3):1891–1896.

Spitzer, L. J. (1998). *Physical Processes in the Interstellar Medium.* Wiley Interscience, Princeton University Observatory.

Stone, E. C., Cummings, A. C., McDonald, F. B., Heikkila, B. C., Lal, N., and Webber, W. R. (2013). Voyager 1 Observes Low-Energy Galactic Cosmic Rays in a Region Depleted of Heliospheric Ions. *Science*, 341(6):150–153.

Thompson, D. J., Baldini, L., and Uchiyama, Y. (2012). Cosmic ray studies with the Fermi Gamma-ray Space Telescope Large Area Telescope. *Astroparticle Physics*, 39:22–32.

Tielens, A. G. G. M. (2005). *The Physics and Chemistry of the Interstellar Medium* . Cambridge University press.

Trumpler, R. J. (1930). Preliminary results on the distances, dimensions and space distribution of open star clusters. *Lick Observatory bulletin ; no. 420; Lick Observatory bulletins ; no. 420.*, 14:154–188.

Uchiyama, Y., Aharonian, F. A., Tanaka, T., Takahashi, T., and Maeda, Y. (2007). Extremely fast acceleration of cosmic rays in a supernova remnant. *Nature*, 449(7):576–578.

Uchiyama, Y. and Collaboration, F.-L. (2011). GeV Gamma Rays from Supernova Remnants Interacting with Molecular Clouds. *ArXiv e-prints.*

Uchiyama, Y., Funk, S., Katagiri, H., Katsuta, J., Lemoine-Goumard, M., Tajima, H., Tanaka, T., and Torres, D. F. (2012). Fermi Large Area Telescope Discovery of GeV Gamma-Ray Emission from the Vicinity of SNR W44. *The Astrophysical Journal Letters*, 749(2):L35.

Vaupré, S., Hily-Blant, P., Ceccarelli, C., Dubus, G., Gabici, S., and Montmerle, T. (2014). Cosmic ray induced ionisation of a molecular cloud shocked by the W28 supernova remnant. *Astronomy and Astrophysics*, 568:50.

Vink, J. (2013). Supernova Remnants as the Sources of Galactic Cosmic Rays. *370 Years of Astronomy in Utrecht*, 470:269.

Wakelam, V., Herbst, E., Selsis, F., and Massacrier, G. (2006). Chemical sensitivity to the ratio of the cosmic-ray ionization rates of He and H2 in dense clouds. *Astronomy and Astrophysics*, 459:813–820.

Walmsley, C. M., Flower, D. R., and Pineau des For ts, G. (2004). Complete depletion in prestellar cores. *Astronomy and Astrophysics*, 418(3):1035–1043.

Watson, W. D. (1973). Deuterium in Interstellar Molecules. *The Astrophysical Journal*, 181:L129.

Watson, W. D. (1976). Interstellar molecule reactions. *Reviews of Modern Physics*, 48(4):513–552.

Westerhout, G. (1958). A survey of the continuous radiation from the Galactic System at a frequency of 1390 Mc/s. *Bulletin of the Astronomical Institutes of the Netherlands*, 14:215.

Wilson, T. L. and Rood, R. (1994). Abundances in the Interstellar Medium. *Annual Review of Astronomy & Astrophysics*, 32:191–226.

Wolszczan, A., Cordes, J. M., and Dewey, R. J. (1991). Discovery of a young, 267 millisecond pulsar in the supernova remnant W44. *The Astrophysical Journal*, 372:L99–L102.

Wootten, A. (1981). A dense molecular cloud impacted by the W28 supernova remnant. *The Astrophysical Journal*, 245:105–114.

Wootten, H. A. (1977). The molecular cloud associated with the supernova remnant W44. *The Astrophysical Journal*, 216:440–445.

Yamazaki, R., Kohri, K., Bamba, A., Yoshida, T., Tsuribe, T., and Takahara, F. (2006). TeV γ-rays from old supernova remnants. *Monthly Notices of the Royal Astronomical Society*, 371(4):1975–1982.

Yang, B., Stancil, P. C., Balakrishnan, N., and Forrey, R. C. (2010). Rotational Quenching of CO due to H2 Collisions. *The Astrophysical Journal*, 718(2):1062–1069.

Yoshiike, S., Fukuda, T., Sano, H., Ohama, A., Moribe, N., Torii, K., Hayakawa, T., Okuda, T., Yamamoto, H., Tajima, H., Mizuno, N., Nishimura, A., Kimura, K., Maezawa, H., Onishi, T., Mizuno, A., Ogawa, H., Giuliani, A., Koo, B. C., and Fukui, Y. (2013). The Neutral Interstellar Gas toward SNR W44: Candidates for Target Protons in Hadronic γ-Ray Production in a Middle-aged Supernova Remnant. *The Astrophysical Journal*, 768(2):179.

Slides of the PhD defense

Cosmic ray ionisation of molecular clouds

PhD defense by
Solenn Vaupré

Direction
Cecilia Ceccarelli & Pierre Hily-Blant
IPAG, UJF

Start: Sept. 1st, 2012
Defense: July 10th, 2015
Financement Ministériel

UNIVERSITÉ GRENOBLE ALPES

OSUG Observatoire des Sciences de l'Univers de Grenoble

IPAG Institut de Planétologie et d'Astrophysique de Grenoble

Cosmic ray ionisation of molecular clouds

Outline

I. Introduction [French]
II. Tools
III. Results
IV. Perspectives

Introduction

100 years of cosmic rays physics

© VF Hess Gesellschaft

A limited knowledge on cosmic rays

Cosmic rays
= **relativistic charged particles**

Energy	1 MeV	1 GeV	1 TeV
v/c	4%	86%	99.99995%

Low energy CRs (<10 GeV)

- Blocked by Heliosphere
- *Voyager 1* observations (Stone+13)

Higher energy CRs

- Low fluxes
- Direct spatial information is lost

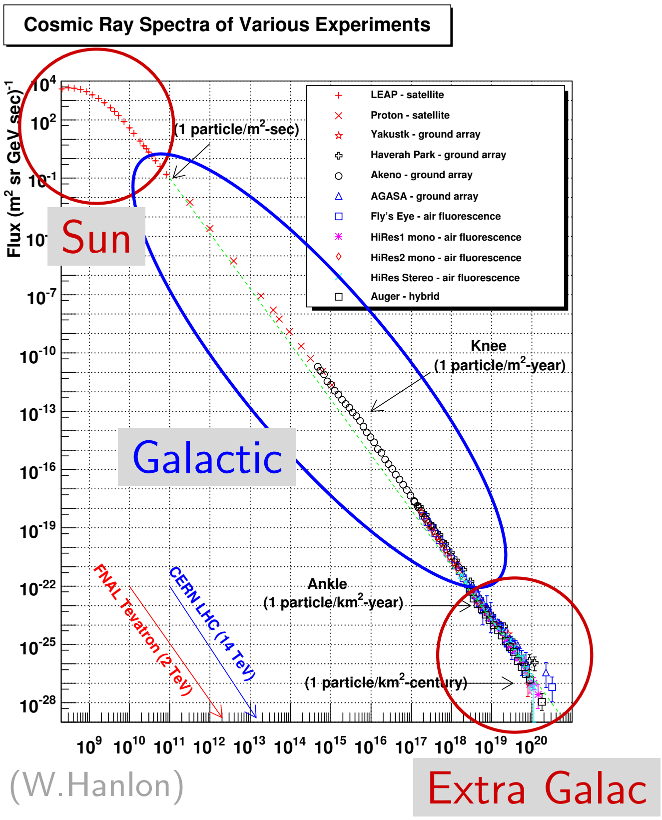

(W.Hanlon)

Role of cosmic rays

CR are omnipresent... (Ferrière'01)

- Travel Galactic & extragalactic distances
- Energy densities ~ 1 eV/ cm^3: CR $\sim$ thermal $\sim$ magnetic
- Travel through gas and dust, and UV-shielded regions

... and influence chemistry and dynamics of ISM

- Induce grain mantle desorption (Léger+85)
- Deposit energy ($\sim 4 - 18$ eV/p), to heat and ionise the gas (Glassgold+12)
- Initiate ionic chemistry (Dalgarno&McCray'72)
- Slow down stellar formation rate up to a factor 200 (Caselli&Ceccarelli'12)
- Maintain turbulence in protoplanetary disks (Lesur+14)

Open questions on CRs

Open questions

- What are the CR sources?
- How are they accelerated?
- What is the initial spectrum?
- How do they propagate?

SNRs as sources of CRs (Baade&Zwicky'34)

- $\sim 10 - 20\%$ kinetic energy $\rightarrow$ CRs (Blasi'13)
- Diffusive shock acceleration process (Bell+78)

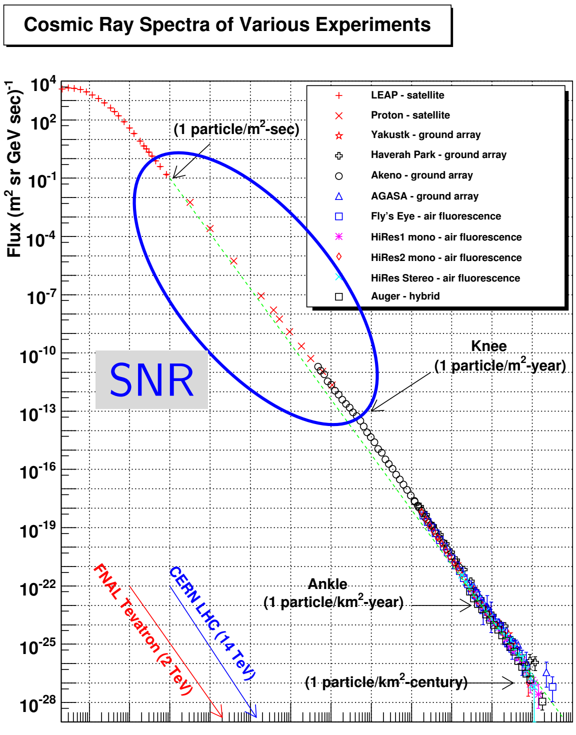

(W.Hanlon)

Radioastronomy to probe low-energy cosmic rays

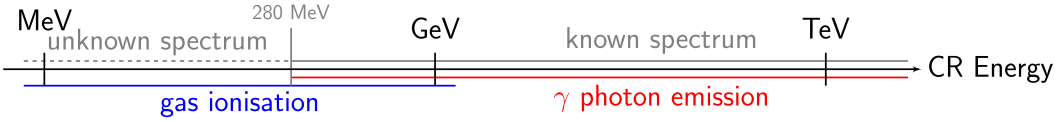

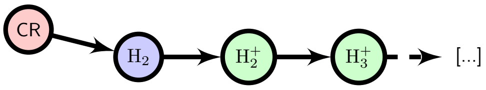

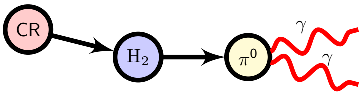

IRAM 30m radiotelescope

FERMI-LAT, AGILE (satellites)

HESS, MAGIC, VERITAS (Cherenkov)

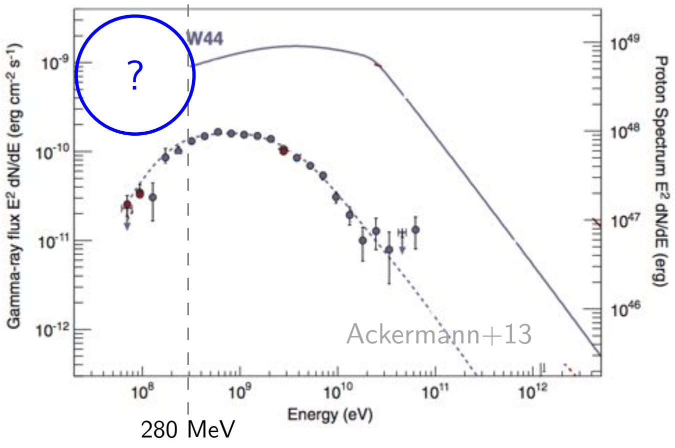

Goal of the thesis

Open questions

- What are the CR sources?
- How are they accelerated?
- What is the initial spectrum?
- How do they propagate?

SNR/MC associations

Can we prove SNRs as CR sources?

- CO emission associated to γ emission: reveals > 280 MeV CR protons (Ackermann+13)
- **Measure ionisation to probe low-energy CRs** (this work)

Situation at the beginning of the thesis

Enhanced ionisation ($\sim 100\times$) in 1 position, in 1 SNR/MC association (Ceccarelli+11)

Goal of the thesis

Systematical study of the ionisation in SNR/MC associations

Outline

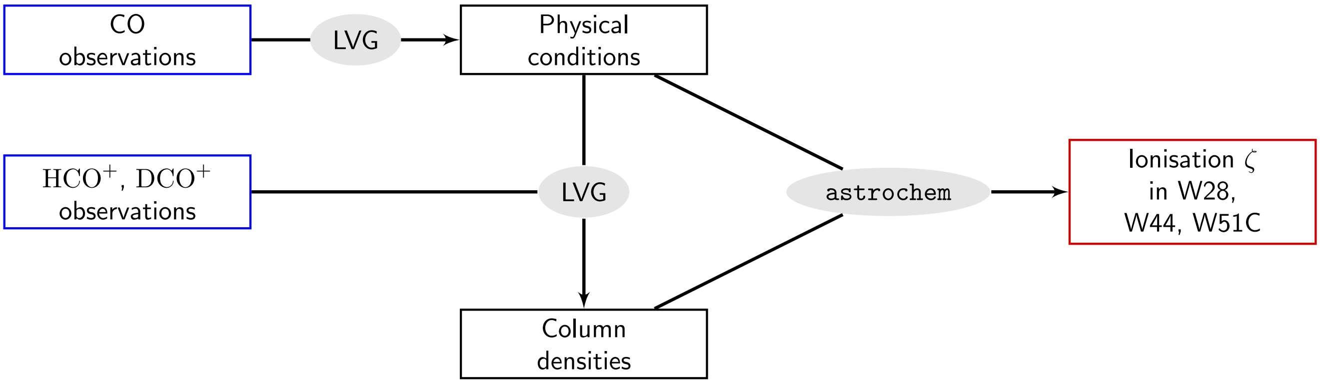
CO observations
LVG
Physical conditions
HCO^+, DCO^+ observations
LVG
astrochem
Ionisation ζ in W28, W44, W51C
Column densities

Definition of the CR ionisation rate ζ

Kinetic rate ζ [s^{-1}]

$H_2 + CR \xrightarrow{\zeta} H_2{}^+ + e^- + CR'$
(or with H or He)

ζ measurements in mol. clouds

- Diffuse clouds
  - H_3^+ absorption
  - OH^+, H_2O^+ absorption
- Dense clouds
  - DCO^+/HCO^+

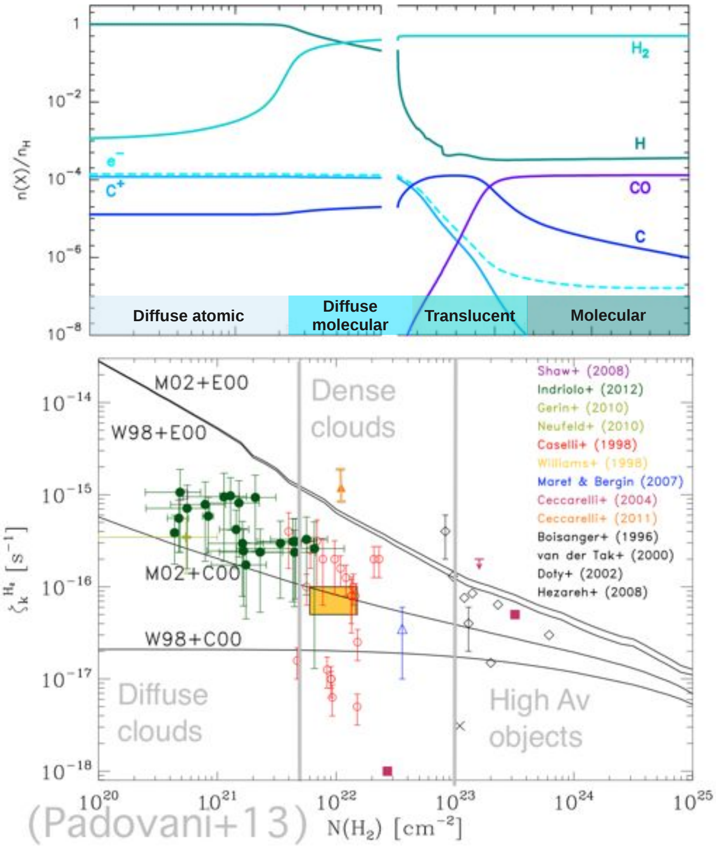

(Padovani+13)

The DCO^+/HCO^+ method

$$\frac{DCO^+}{HCO^+} \approx \frac{1}{3}\frac{H_2D^+}{H_3^+} > \frac{1}{3}\frac{D}{H}$$

$D/H = 1.6 \times 10^{-5}$

fractionation reaction

$$H_3^+ + HD \rightleftharpoons H_2D^+ + H_2 + 220K$$

$T < 30K$

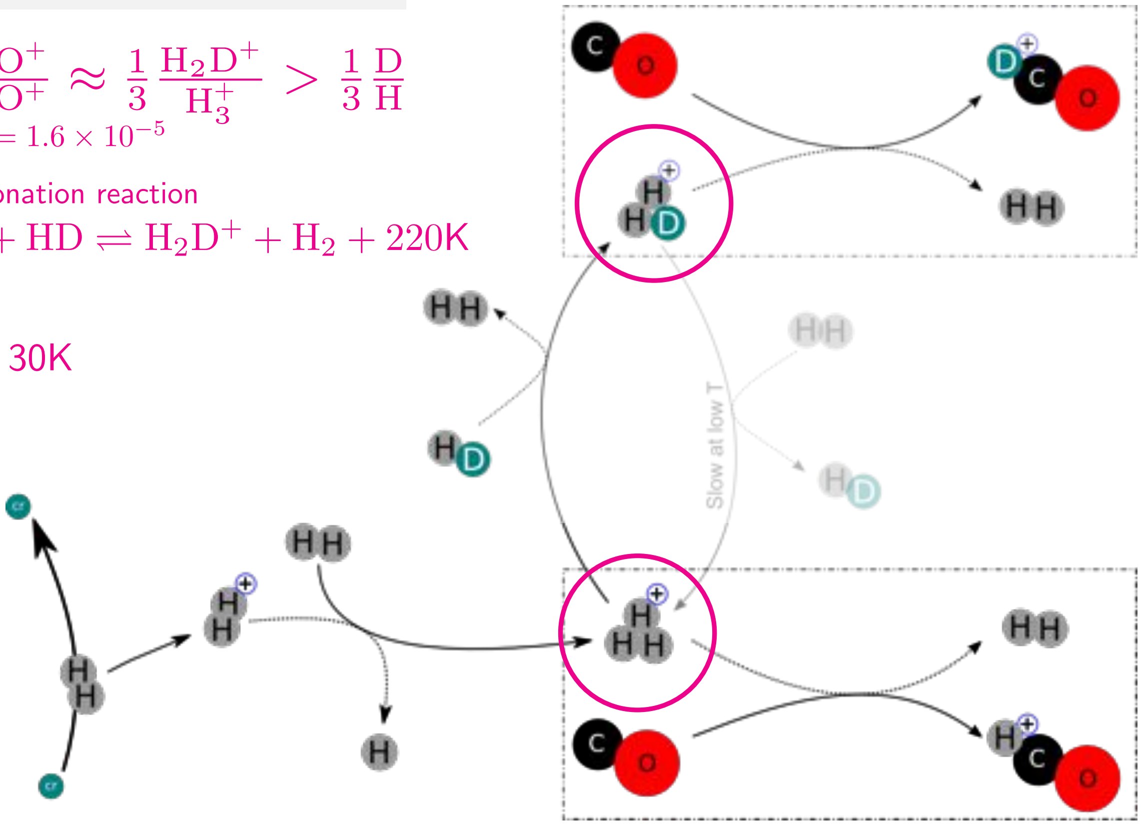

The DCO^+/HCO^+ method

T dependent

observations

$$\frac{DCO^+}{HCO^+} \approx \frac{1}{3}\frac{H_2D^+}{H_3^+} \approx \frac{1}{3}\frac{\alpha x(HD)}{\beta x_e + \gamma x(CO) + \delta e^{-220/T}}$$

e^- abundance

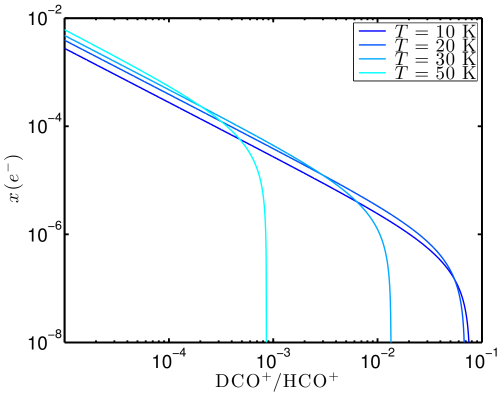

Analytical method

(Guélin+77, Caselli+98)

- Assume $x(HD)$ and $x(CO)$ constant
- $DCO^+/HCO^+ = f(T, x_e)$

The DCO$^+$/HCO$^+$ method

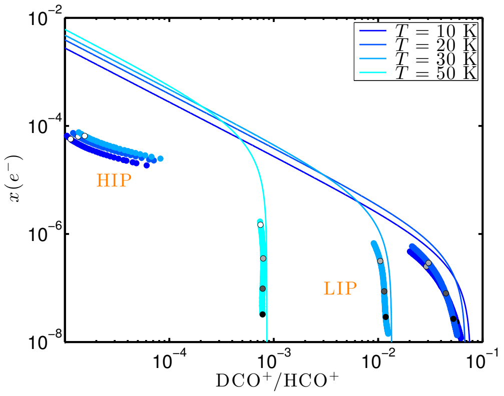

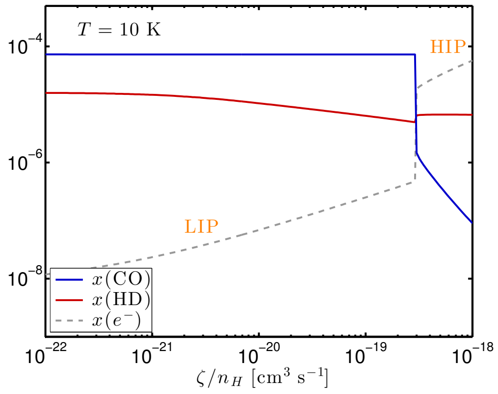

Numerical method (astrochem)

- HD destroyed by H_3^+
- Chemical instability LIP → HIP
  (Pineau des Forêts+72)
- CO destroyed by He^+ in the HIP

Limits (Vaupré et al. 2014, A&A 568:50)

- ζ and x_e in the LIP: relatively large error bars. Example at $T = 20$ K, 40% on DCO$^+$/HCO$^+$ $\Rightarrow$ factor 6 on x_e and 20 on ζ
- In the HIP: DCO$^+$ not detected
  $\Rightarrow$ lower limits on ζ

Position of the transition within a factor 5

- Depends on T, metals abundances, ...

Observations of isotopologue optically thin lines

Objective

- HCO$^+$ and DCO$^+$
- CO multi-line for phys. cond.

Thick transitions

Use heavier isotopologues
$\Rightarrow$ assume isotopic ratio

Species	Line	Frequency [GHz]	E_{up} [K]	n_{crit} [cm^{-3}]
H^{13}CO$^+$	(1-0)	86.754	4.16	2×10^5
C^{18}O	(1-0)	109.782	5.27	2×10^3
^{13}CO	(1-0)	110.201	5.29	2×10^3
DCO$^+$	(2-1)	144.077	10.37	9×10^5
C^{18}O	(2-1)	219.560	15.81	2×10^4
^{13}CO	(2-1)	220.399	15.87	2×10^4

Typical values in W28, $n_H = 10^4$ cm^{-3}, $T = 10$ K

	CO(1-0)	^{13}CO(1-0)	C^{18}O(1-0)	HCO$^+$(1-0)	H^{13}CO$^+$(1-0)	DCO$^+$(2-1)
N [cm^{-2}]	$\sim 3 \times 10^{18}$	$\sim 5 \times 10^{16}$	$\sim 5 \times 10^{15}$	$\sim 5 \times 10^{13}$	$\sim 1 \times 10^{12}$	$\lesssim 1 \times 10^{12}$
τ	~ 100	~ 2	~ 0.2	~ 10	~ 0.2	$\lesssim 0.2$

Observations performed at the IRAM 30m telescope

Date of observations	Objects	Telescope	Nb. of hrs
Dec. 2011, Mar. 2012	W51C / W28	30m	22
July 2012	W51C	PdBi	20
January 2013	W51C	30m	16
July 2014	W44	30m	41
October 2014	W28	30m	19
May 2015	W28	30m	42
Total			160 h

Non-automatic analysis

Analysis with `GILDAS` (Pety'05)

Gaussian fits, HFS

⇒ Integrated intensity W, linewidth

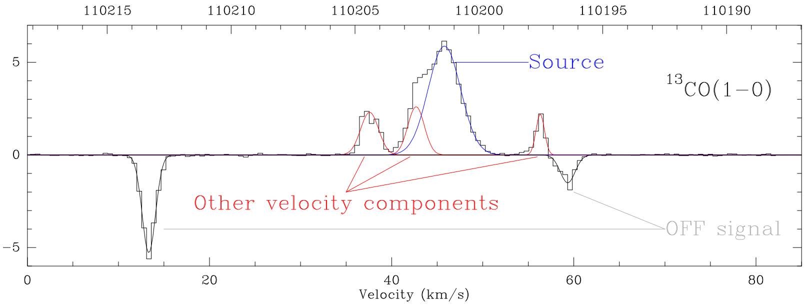

Complex regions...

- Sources in Galactic plane
- W28 close to Galactic center

⇒ Several clouds on line of sight and in field of view

... complex analysis

- No clear reference position (OFF)
- Merged lines
- $< 0.2\%$ contamination from close objects (Greve+98)

⇒ **semi-automatic** analysis only

Total uncertainty

$\sim$ 20-30% on W: calibration, baselines, merged lines

Next step: radiative transfer

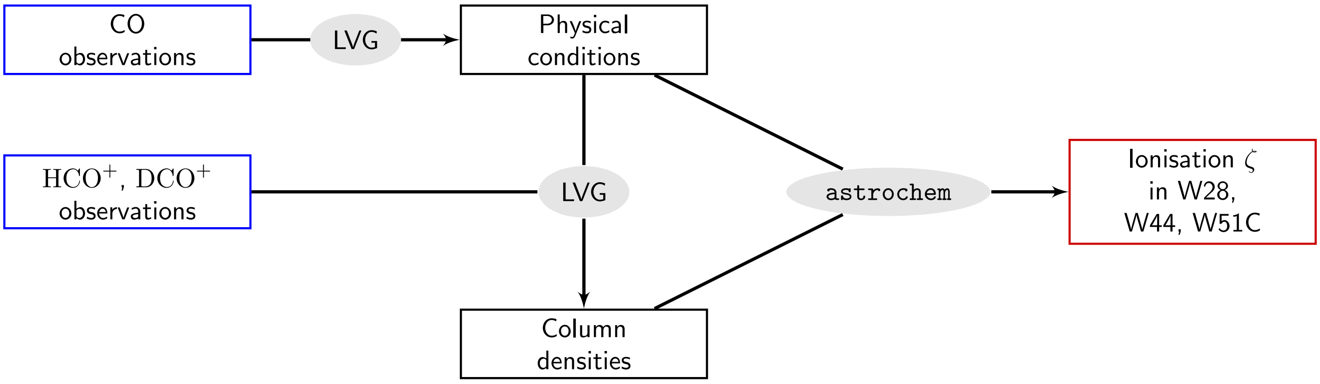

CO observations

LVG

Physical conditions

HCO^+, DCO^+ observations

LVG

astrochem

Ionisation ζ in W28, W44, W51C

Column densities

The LVG tool

Large Velocity Gradient hypothesis

- local escape proba: $\beta = \frac{1-e^{-3\tau}}{3\tau}$
- typical gradient: 0.15 km s^{-1} pc^{-1}
- thermal width: $0.05\sqrt{\frac{T}{10}\frac{m_{\rm CO}}{m}}$ km s^{-1}

$\Rightarrow \sim$ 60 decoupled regions

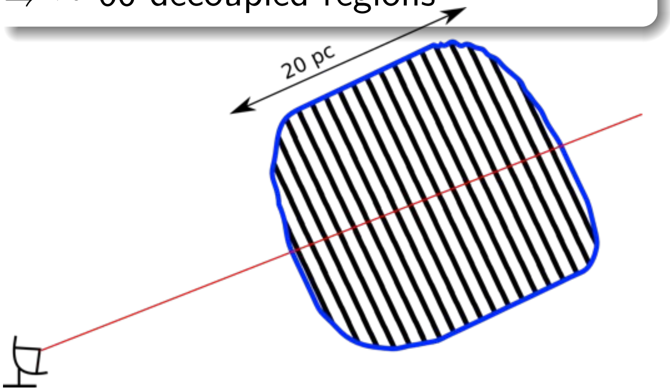

LVG_gre code (based on Ceccarelli+03)

- non-LTE populations
- collisional excitation with H_2
- uniform density, temperature
- successful convergence at high τ
- IDL front-end interface
- benchmark with `RADEX`
- public release

Determination of physical conditions and column densities

#1 Physical conditions

^{13}CO(1-0) C^{18}O(1-0)
^{13}CO(2-1) C^{18}O(2-1)

(Collisional coeff: Yang+10)

Parameters:
$N_{\rm CO}$, $n_{\rm H_2}$, T, Ω, $^{13}{\rm CO}/{\rm C}^{18}{\rm O}$

#2 Column densities

Constrain $N({\rm H}^{13}{\rm CO}^+)$ and $N({\rm DCO}^+)$ with physical conditions

(Collisional coeff: Flower+99)

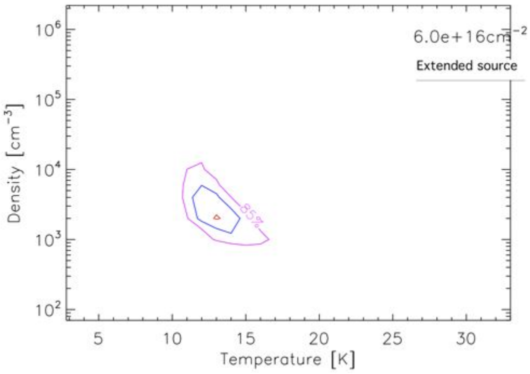

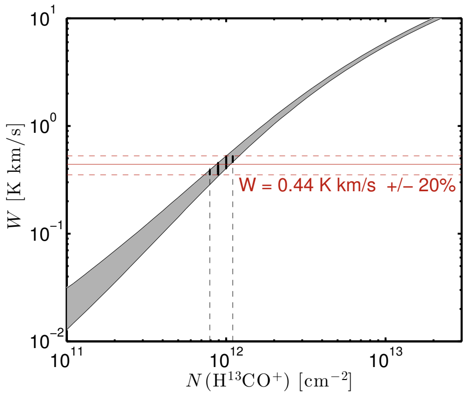

$^{13}{\rm CO}/{\rm C}^{18}{\rm O}$ from the LVG code consistent with Galactocentric gradient

Variation of the isotopic ratio

- Galactocentric gradient (Milam+05)
- Fractionation reactions (Mladenović+14)
  $\frac{{\rm H}^{12}{\rm CO}^+}{{\rm H}^{13}{\rm CO}^+} \approx 0.75 \times \frac{^{12}{\rm CO}}{^{13}{\rm CO}}$

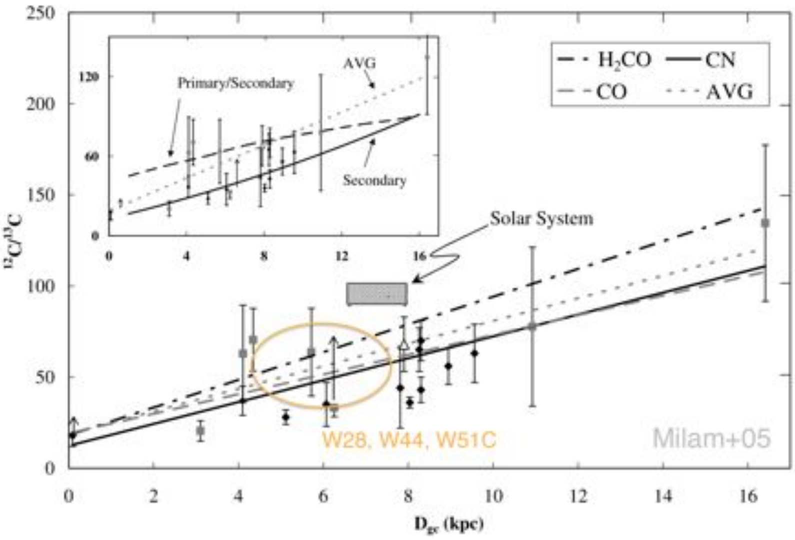

$^{13}{\rm CO}/{\rm C}^{18}{\rm O} = 10 \pm 1$ constrained in LVG
⇒ consistent with Galactic gradient $^{12}{\rm C}/^{13}{\rm C} = 50$ at $D_{gc} = 6$ kpc, assuming $^{16}{\rm O}/^{18}{\rm O} = 500$

Next step: comparison to chemical modeling

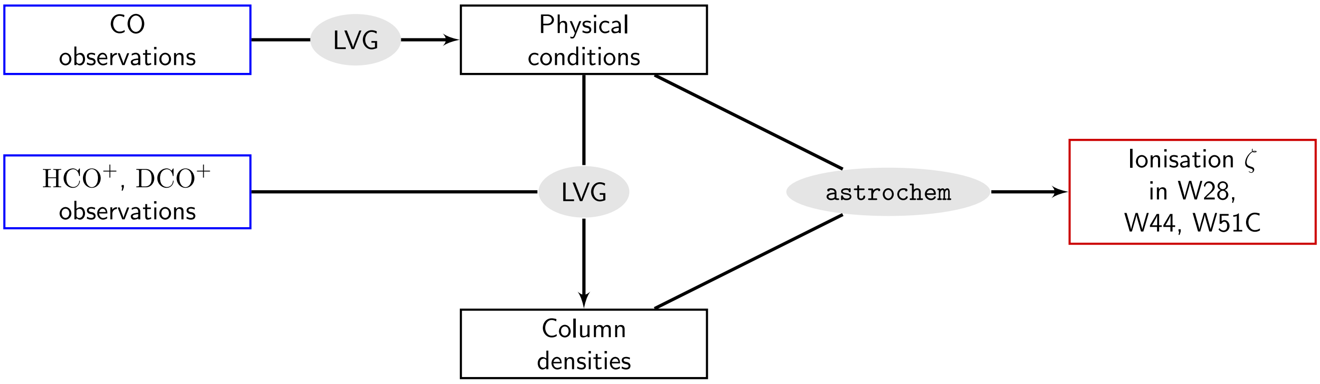

CO observations

LVG

Physical conditions

HCO^+, DCO^+ observations

LVG

Column densities

astrochem

Ionisation ζ in W28, W44, W51C

Chemical modeling with astrochem

The `astrochem` code (Maret+13)

- "One-point" model: $n_{\rm H}$, T, A_V
  → focus on UV shielded regions
- **Time-dependent**
  → use steady-state
- Gas-grain interactions neglected

Chemical network

- OSU2009: $>$ 6000 gas-phase reactions
- $+$ $\mathrm{DCO^+}$ network (Taquet+14)

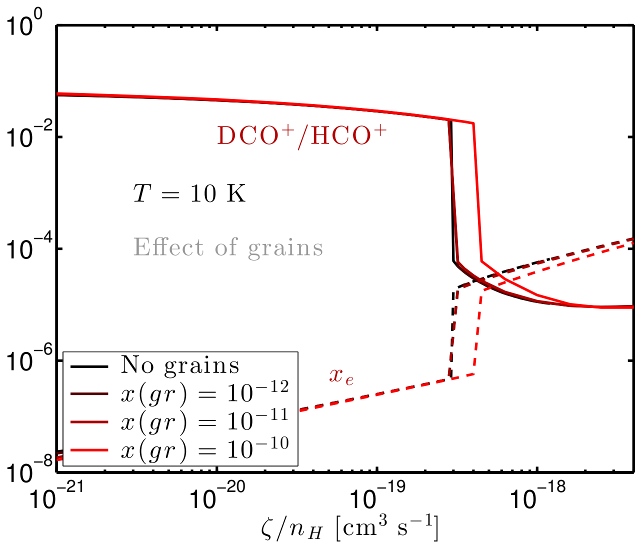

Relevant parameter: $\zeta/n_{\rm H}$ (Lee+98)

Summary of the methods

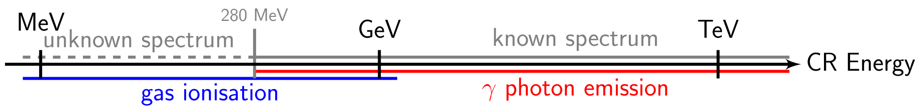

- Observe molecular emission to measure CR ionisation
- Targets: dense molecular clouds close to SNRs

⇒ **Unprecedented observations in such regions**

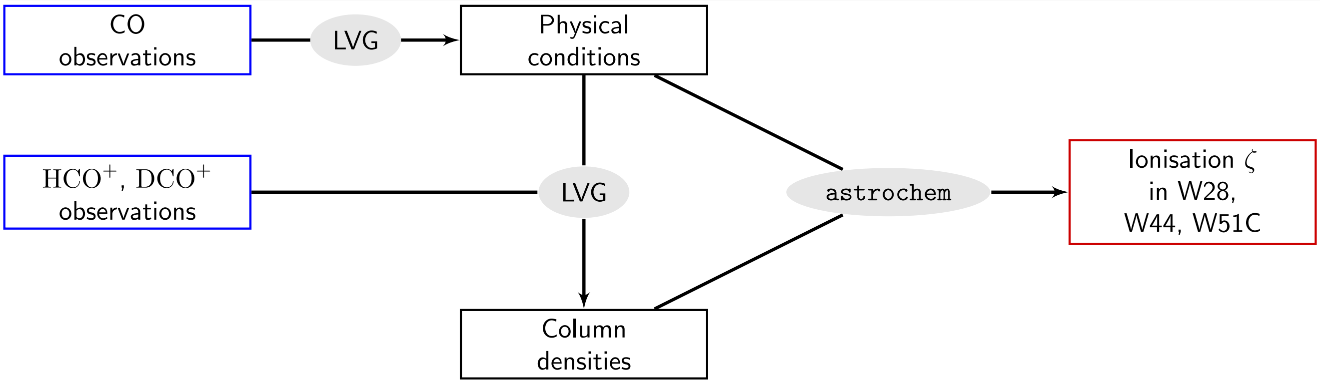

Selection criteria

Selection of 3 SNR/MC associations: W28, W51C, W44

- γ emission from the cloud: presence of $>$ 280 MeV CR protons
- SNR old enough to interact with the cloud (expansion, particle acceleration)
- Evidence of an interaction in the gas: broadened lines, OH masers, ...
- Favorable geometry

Presentation of the regions

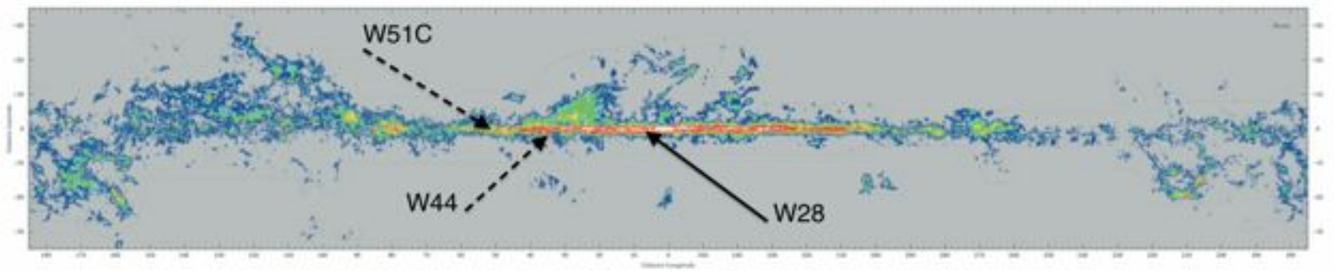

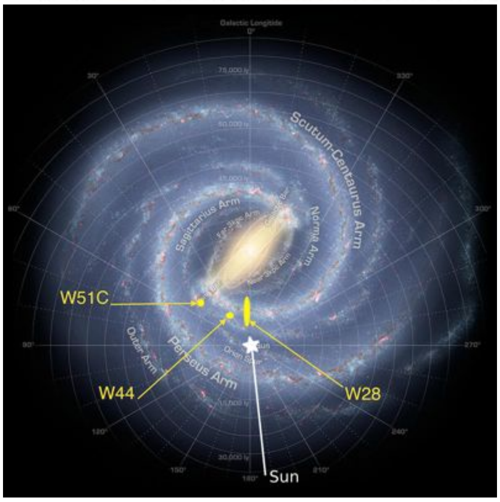

		W51C	W44	W28
	Galactic coordinates	(49.3, 0.3)	(34.6, -0.5)	(6.3, 0)
SNR	**Age** [yr]	$\sim 3 \times 10^4$	$\sim 2 \times 10^4$	$\gtrsim 10^4$
	Heliocentric distance [kpc]	~ 5.5	~ 3	$2 - 4$
	Galactic distance [kpc]	~ 6.9	~ 6.3	$4.5 - 6.5$
	Width [']	~ 30	~ 30	~ 42
	Width [pc]	~ 48	~ 26	$10 - 24$
Cloud	**Density** n_{H} [cm^{-3}]	$\sim 10^4$	$10^4 - 10^5$	$10^3 - 10^4$
	Temperature [K]	$21 - 24$	$7 - 17$	$8 - 20$

The SNR W28 region (Vaupré et al. 2014, A&A 568:50)

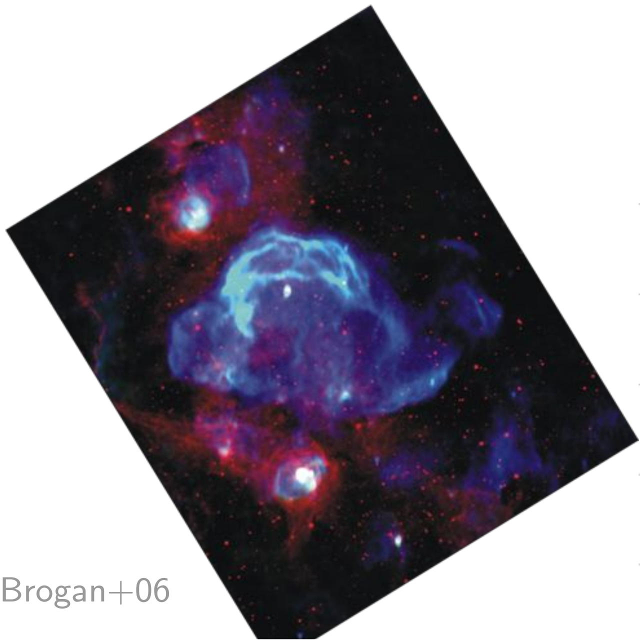

Brogan+06

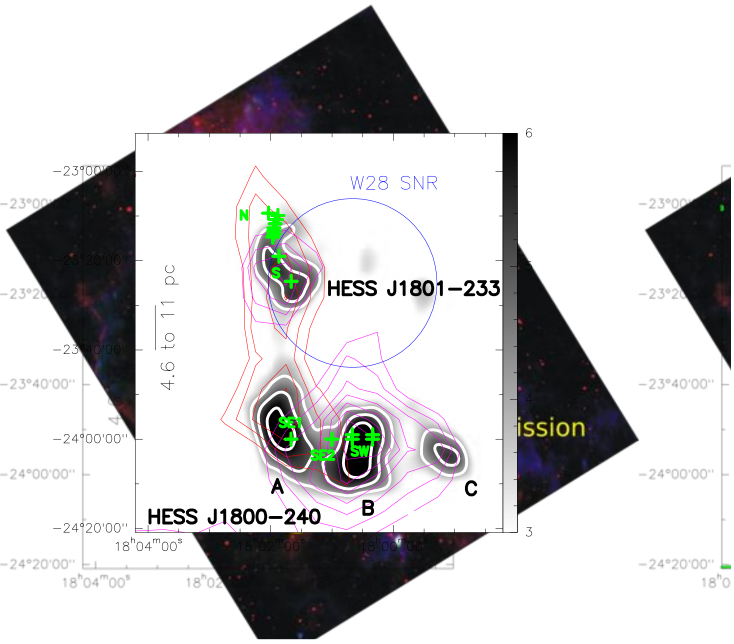

CO(1-0) survey (Dame+01), Radio boundary (Yusef-Zadeh+00), HESS (TeV) (Aharonian+08), AGILE (GeV) (Giulani+10), *Fermi*-LAT (GeV) (Abdo+10), shocked gas (Wootten+81, Nicholas+11,12), OH masers (Claussen+97)...

Observations in W28 (Vaupré et al. 2014, A&A 568:50)

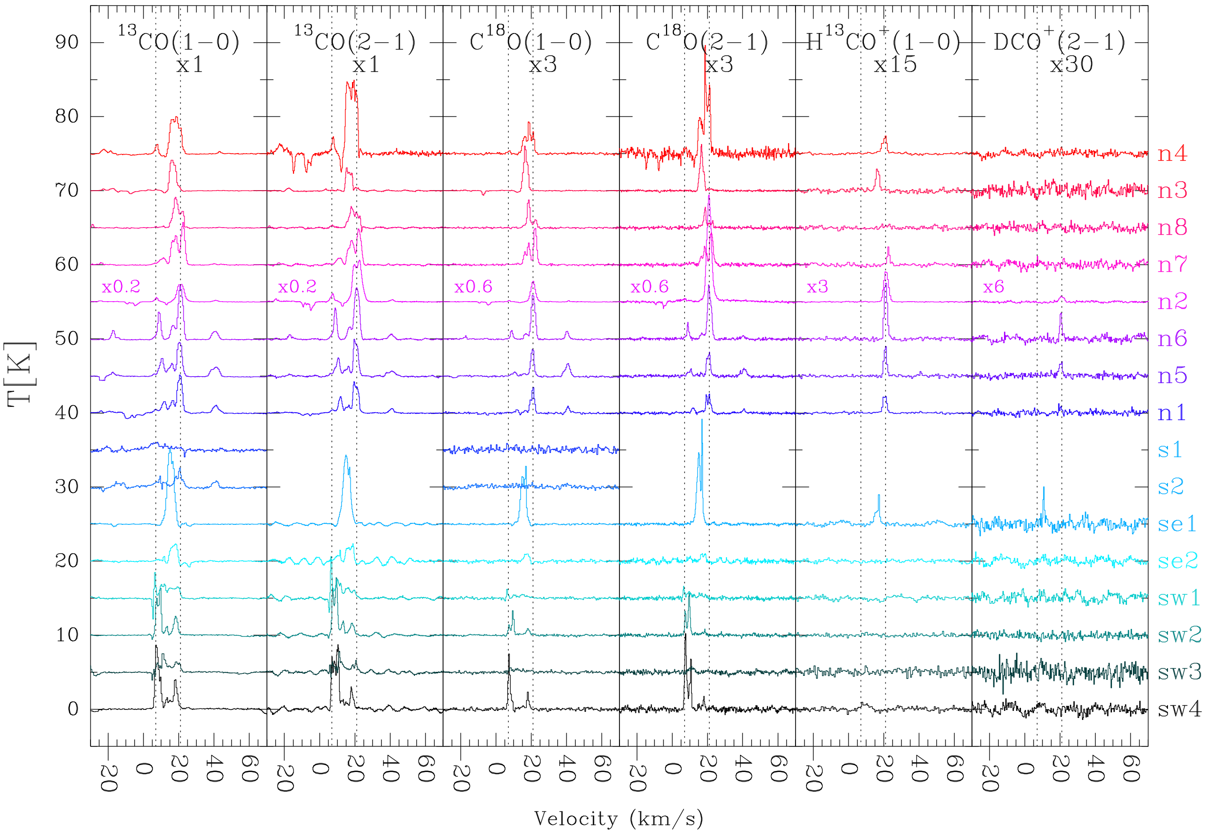

CR ionisation in W28 (Vaupré et al. 2014, A&A 568:50)

Pos.	Δv [km s^{-1}]	n_{H_2} [10^3 cm^{-3}]	T_{kin} [K]	N(C^{18}O) [10^{15} cm^{-2}]	A_V [mag]	N(H^{13}CO$^+$) [10^{12} cm^{-2}]	N(DCO$^+$) [10^{12} cm^{-2}]	$R_D = \frac{[\mathrm{DCO}^+]}{[\mathrm{HCO}^+]}$	ζ [10^{-17} s^{-1}]
N1	3.5	0.6 {0.2 – 1}	15 ± 5	4 {2 – 6}	21 {11 – 32}	0.8 – 1.3	< 0.22	< 0.005	> 13
N5	3.0	4 {2 – 5}	10 ± 2	3 {2 – 8}	16 {11 – 32}	1.1 – 1.4	0.89 – 1.30	0.014 – 0.020	130 - 330
N6	3.0	4 {2 – 6}	13 ± 3	6 {4 – 20}	32 {21 – 105}	1.8 – 2.5	0.79 – 1.30	0.008 – 0.012	130 - 400
N2[†]	5.0	> 2	16 ± 2	20 {15 – 30}	105 {79 – 158}	5.6 – 8.9	1.10 – 2.00	0.003 – 0.006	-
N7	2.5	2 {2 – 5}	10 ± 2	4 {3 – 10}	21 {16 – 53}	0.6 – 0.9	< 0.25	< 0.007	> 130
N8	3.5	1 {0.6 – 2}	8 ± 1	3 {2 – 4}	16 {11 – 21}	< 0.2	< 0.35	-	-
N3	3.5	6 {4 – 10}	8 ± 1	6 {5 – 7}	32 {26 – 37}	1.0 – 1.4	< 0.35	< 0.006	> 260
N4	3.0	2 {0.6 – 4}	12 ± 3	2 {2 – 3}	11 {5 – 16}	1.0 – 1.4	< 0.35	< 0.006	> 40
SE1	4.0	2 {1 – 5}	19 ± 5	6 {5 – 20}	32 {26 – 105}	0.4 – 0.56	0.79 - 1.0	0.032 - 0.05	0.2 - 20
SE2	3.0	4 {2 – 10}	8 ± 2	0.9 {0.4 – 20}	5 {2 – 105}	< 0.2	< 0.28	-	-
SW2	1.5	2 {1 – 4}	20 ± 4	4 {3 – 10}	21 {16 – 53}	< 0.1	< 0.22	-	-
SW4[†]	1.5	6 {4 – 10}	16 ± 2	1.5 {1 – 3}	5 {5 – 16}	0.5 – 0.8	< 0.25	< 0.009	-

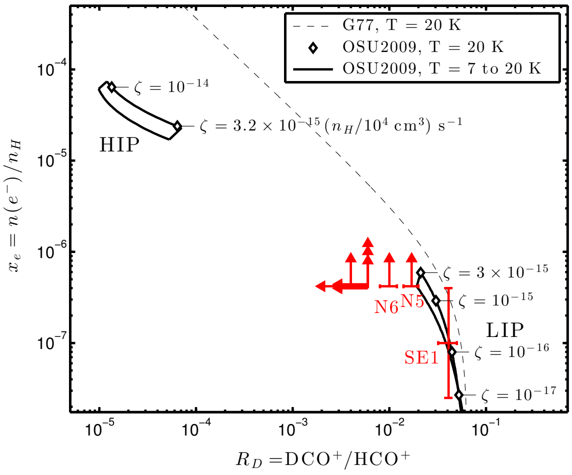

Enhanced ionisation and CR properties

(Vaupré et al. 2014, A&A 568:50)

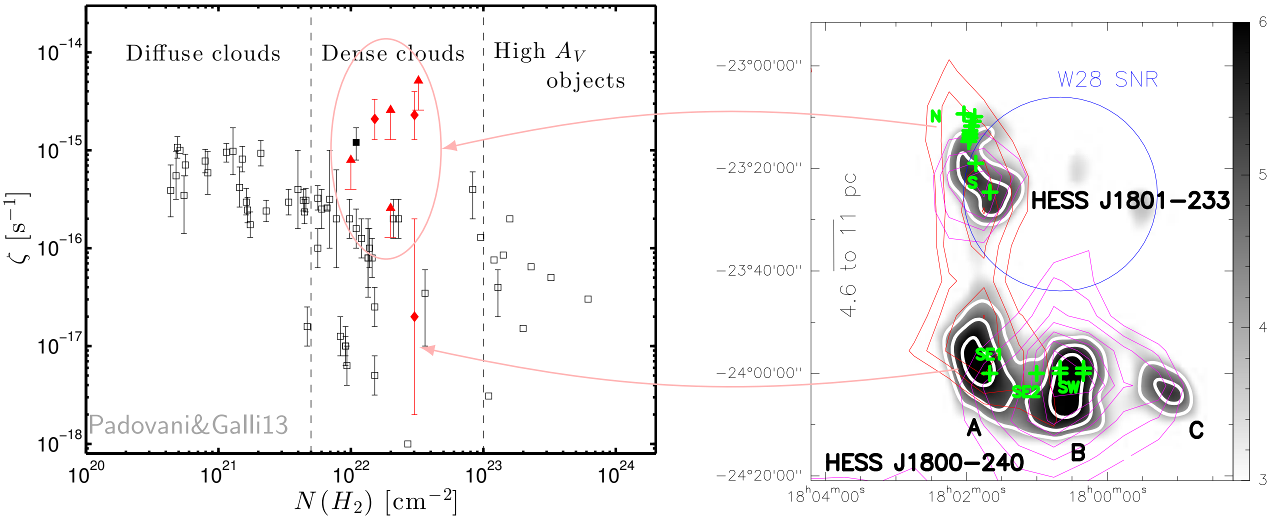

Energy dependent CR escape (Vaupré et al. 2014, A&A 568:50)

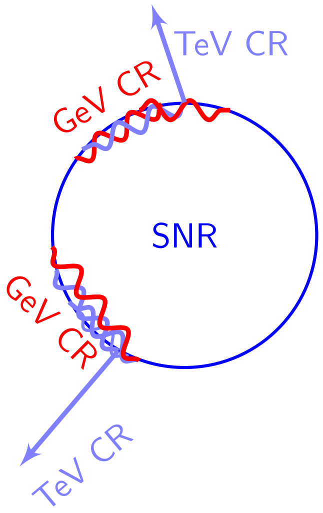

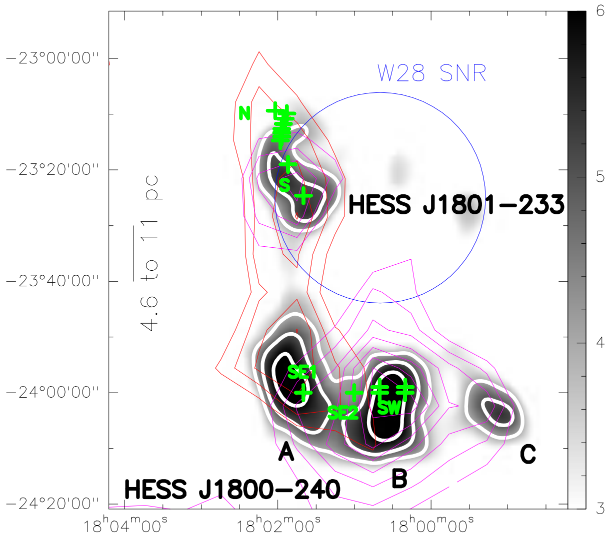

- GeV CR still bound to SNR shell ⇒ no ionising CRs in the South
- TeV CR have escaped and reached the South

⇒ Determination of the CR diffusion coefficient

CR propagation (Vaupré et al. 2014, A&A 568:50)

Diffusion coefficient

$$D_{(\approx 10\ \mathrm{GeV})} \gtrsim 3 \times 10^{27} \left(\frac{R}{10\ \mathrm{pc}}\right)^{2} \left(\frac{t}{10^{4}\ \mathrm{yr}}\right)^{-1}\ \mathrm{cm}^2/\mathrm{s}$$

1 GeV γ photon → 10 GeV CR

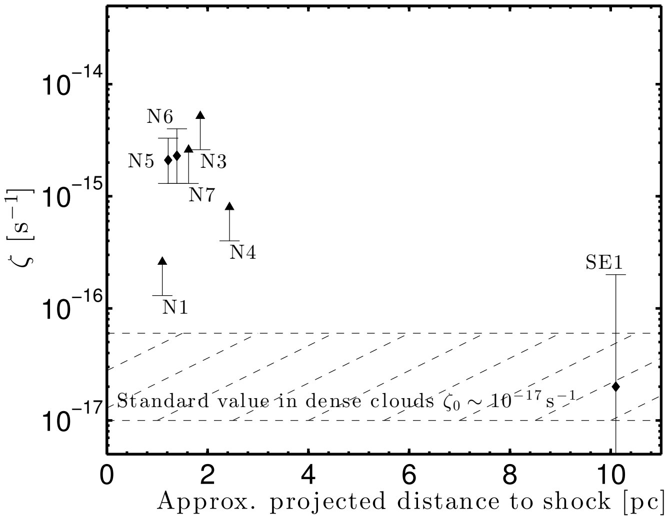

The SNR W44 region (Vaupré et al. 2015, in prep.)

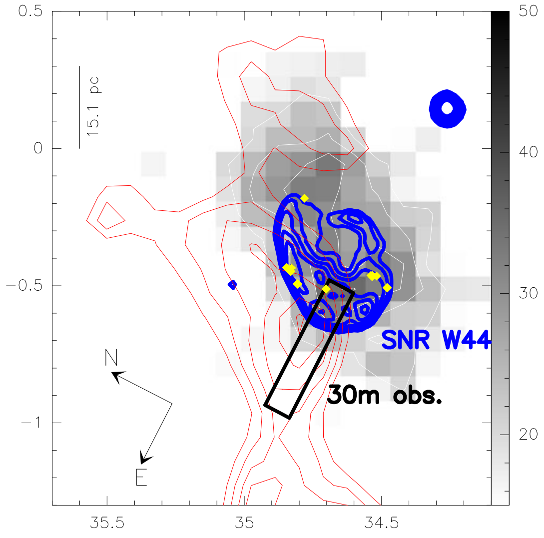

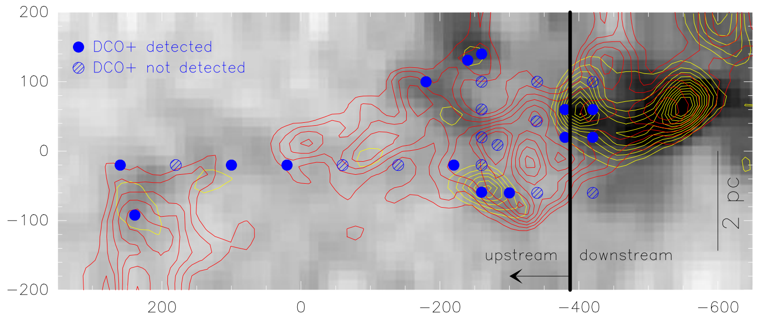

- $\sim 10\times$ denser region than W28
- Use $\mathrm{N_2H^+}$ to help constrain physical conditions: 3 HFS components and higher critical density than CO $n_{\mathrm{crit}} \sim 2 \times 10^5\ \mathrm{cm}^{-3}$
- No clear trend with projected distance

CO(1-0) survey (Dame+01), Radio boundary (Handa+87), *Fermi*-LAT (GeV) (Uchiyama+12), AGILE (Giuliani+11), shocked gas (Wootten+77), OH masers (Claussen+97) ... Signature of hadronic processes (Ackermann+13)

Results in W44 (Vaupré et al. 2015, in prep.)

Ionisation from $\mathrm{DCO^+/HCO^+}$

With $n_{\mathrm{H}} \sim 10^5$ cm^{-3}:

- 11 positions compatible with LIP: $\zeta < 3 \times 10^{-14}$ s^{-1}
- 4 upper limits: $\zeta > 3 \times 10^{-14}$ s^{-1}

For 13 positions, $\zeta \gtrsim 10^{-15}$ s^{-1}?

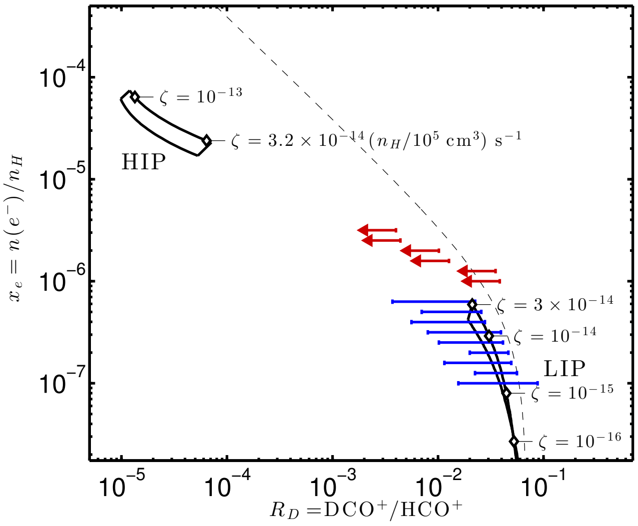

Few constraints on ζ

⇒ motivation to look for additional information from other species: $\mathrm{N_2H^+}$?

The SNR W51C region (Dumas, Vaupré et al. 2014, ApJ 786:L24)

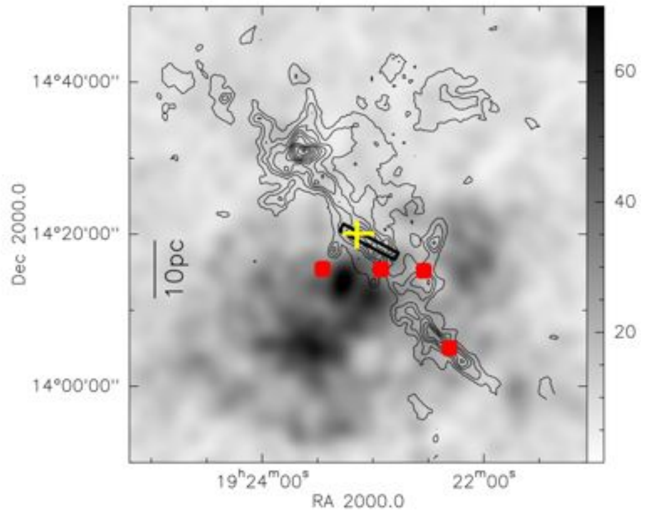

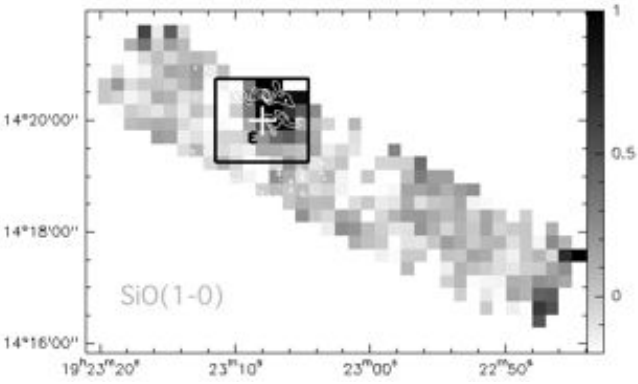

$^{13}\mathrm{CO}(2\text{-}1)$ (Jackson+06), ROSAT (X-ray) (Koo+95), *Fermi*-LAT (Uchiyama+09), MAGIC (0.3-1 TeV) (Aleksic+12), OH masers (Koo+95), shocked gas (Koo&Moon'97), ...

Enhanced ionisation

- Ceccarelli+11: W51C-E
- PdBI observations to look for possible contamination by protostar

Compact SiO emission: shock (Dumas, Vaupré et al. 2014, ApJ786)

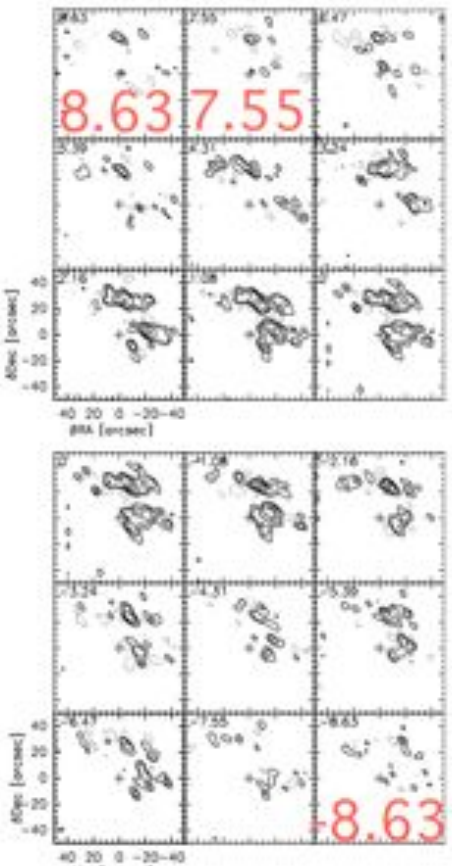

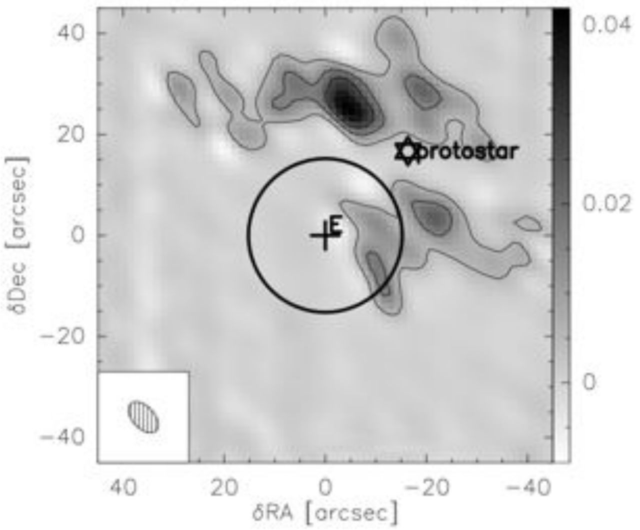

Not associated to outflow
⇒ Trace low-velocity shock induced by passage of SNR shock
⇒ Coherent picture of a region
filled with ionising CRs

Conclusions

Open questions at the beginning of the thesis and my contribution

1. What are the CR sources?
   Enhanced CR ionisation in three SNR/MC associations (W51C, W28 and W44) ⇒ SNRs are likely CR sources
2. How are they accelerated?
   Shock in the W51C region likely traces passage of the SNR blast wave, where CR accelerated
3. What is the initial spectrum?
   Comparing [MeV-GeV] CR flux from ζ to [$>$ 280 MeV] CR flux from γ-rays, possible constraint ⇒ could be used by modelers (e.g. CRIME)
4. How do they propagate?
   Ionisation gradient in the W28 region
   ⇒ Strong constraint on the CR diffusion coefficient

In addition: Much better understanding of the classical $\mathrm{DCO^+/HCO^+}$ method and it limits to measure ionisation in dense molecular clouds

Perspectives

Perspectives on observations

- Alternative tracers to DCO$^+$/HCO$^+$ to measure CR ionisation in the HIP
- Trace CR diffusion through ionisation gradient

Perspectives on modeling

- Constraints from time-dependent analysis of the HIP/LIP transition
- Include consistent thermal balance calculation
- Include CR spectrum propagation (Padovani+09), CRIME project (Morlino&Gabici'14), also as a function of time

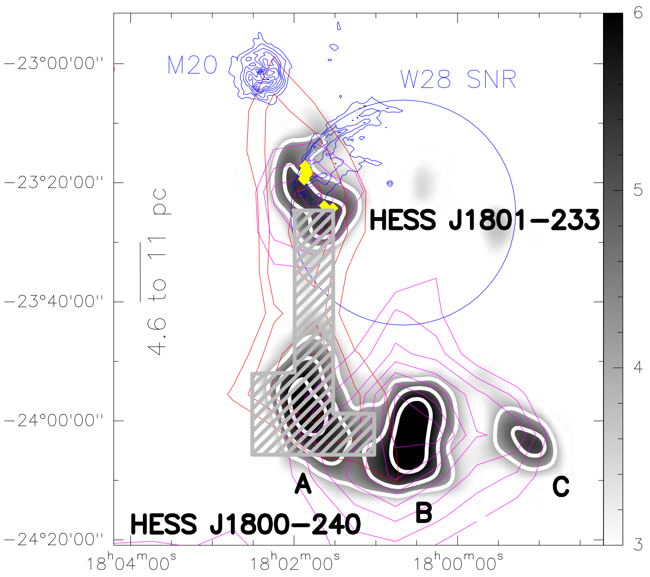

Trace CR diffusion through ionisation gradient

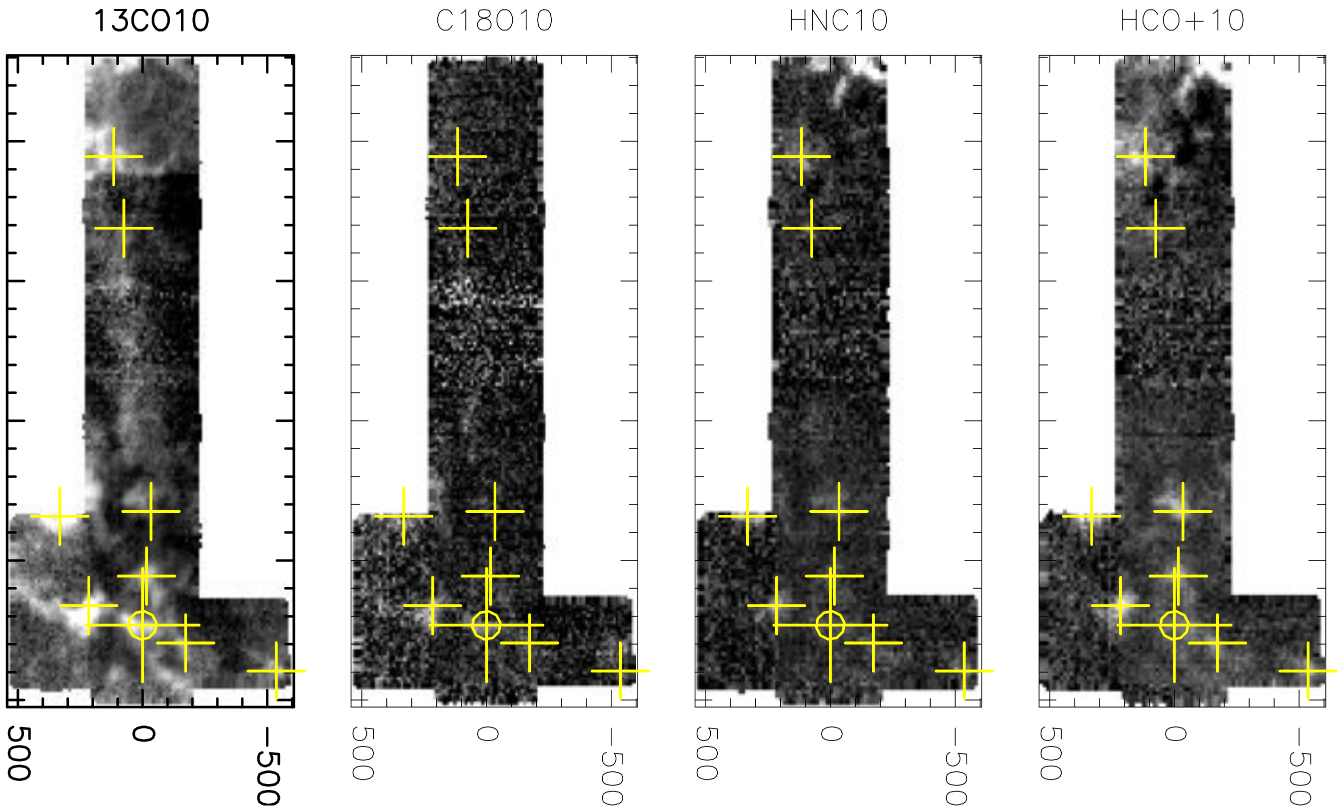

Looking for alternative tracers of CR ionisation

Predictions with `astrochem`...

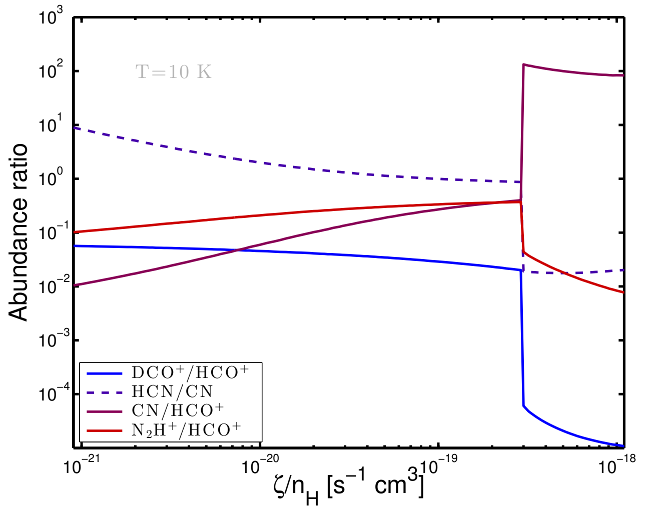

... and observations in W28

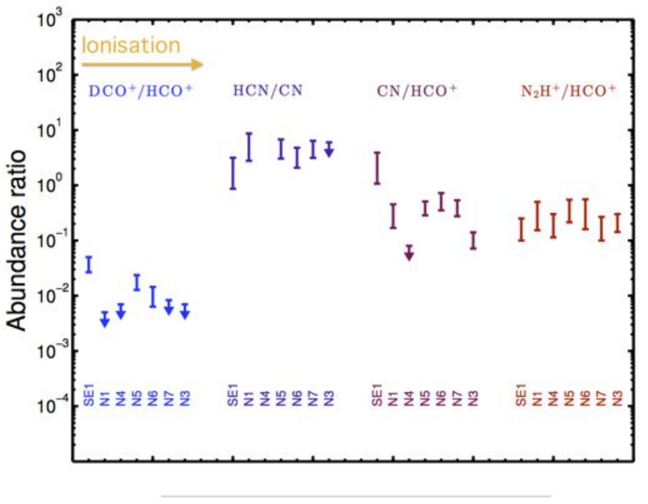

Objective

- Measure in HIP
- More precise in LIP

- Merged CN observations in SE1: tentative value
  $\Rightarrow$ need additional "standard" positions
- Surprisingly, N_2H^+/HCO^+ gives no information

Chemical network of the N_2H^+/HCO^+ ratio

Main formation route		Destruction routes	
$H_3^+ + N_2$	$\rightarrow N_2H^+ + H_2$	(1) $N_2H^+ + CO$	$\rightarrow HCO^+ + N_2$
		(2) $N_2H^+ + e^-$	$\rightarrow N_2 + H$
$H_3^+ + CO$	$\rightarrow HCO^+ + H_2$	(1) $HCO^+ + CO$	$\rightarrow HCO^+ + CO$
		(2) $HCO^+ + e^-$	$\rightarrow CO + H$

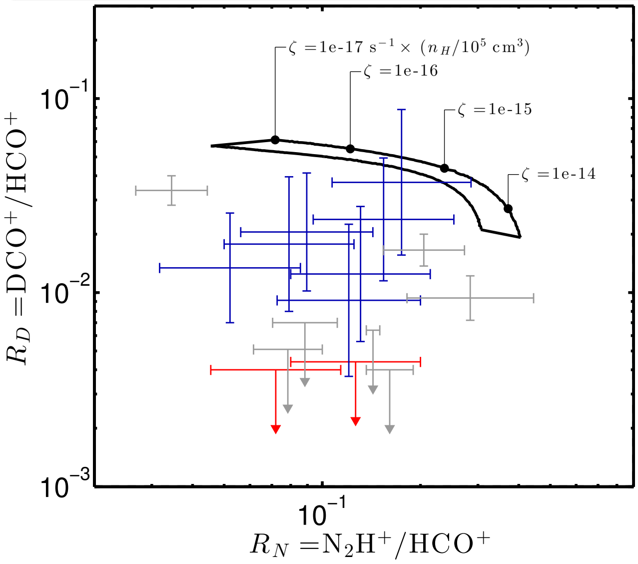

Expectations

- (1) dominates at low x_e:
  $\Rightarrow N_2H^+/HCO^+ \ll N_2/CO$
- (2) dominates at high x_e:
  $\Rightarrow N_2H^+/HCO^+ \rightarrow N_2/CO$

(Ceccarelli+14, Morales+14)

The N_2H^+/HCO^+ ratio gives constraints on volatile abundances and CR ionisation (χ^2 maps)

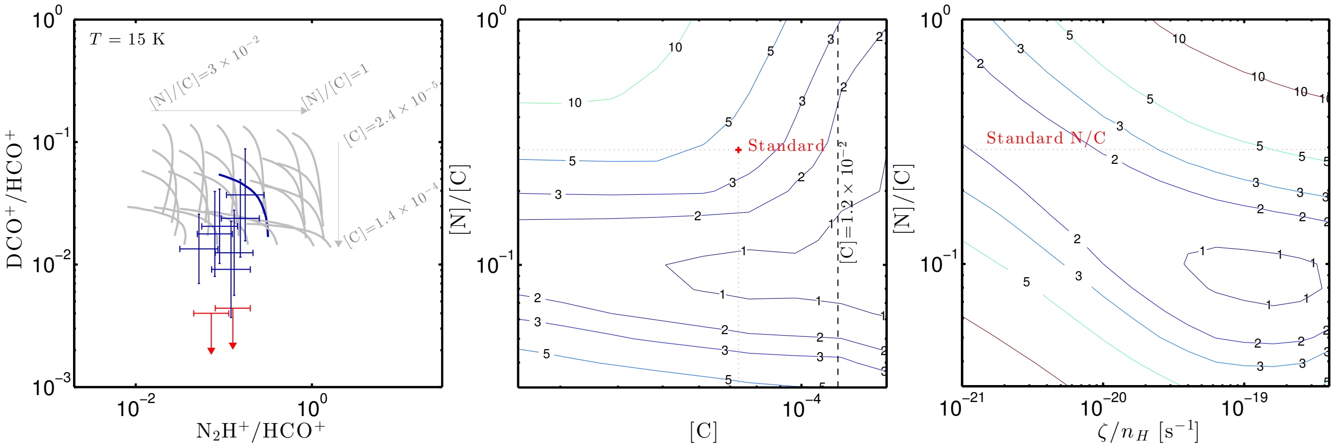

Parameters

No significant effect of T, metals, or $^{12}C/^{13}C$ → volatile abundances C, N

Volatiles

$0.07 \lesssim N/C \lesssim 0.2$
$[C] \gtrsim 5 \times 10^{-5}$

Ionisation

$4 \times 10^{-15} \lesssim \zeta \lesssim 4 \times 10^{-14}$ s^{-1} at $n_H = 10^5$ cm^{-3}

Is the LIP/HIP transition time dependent?

Method

- Starting point: molecular cloud at steady-state and standard ionisation $\zeta = 10^{-17}$ s^{-1}
- At $t = 0$, increase ζ

Conclusions on the timescale of transition

- Simultaneous for both ratios
- Timescale ↘ as C abundance ↗
- Timescale slightly shorter than age of SNR for standard abundance [C]= 7.3×10^{-5}
  ⇒ steady-state ok

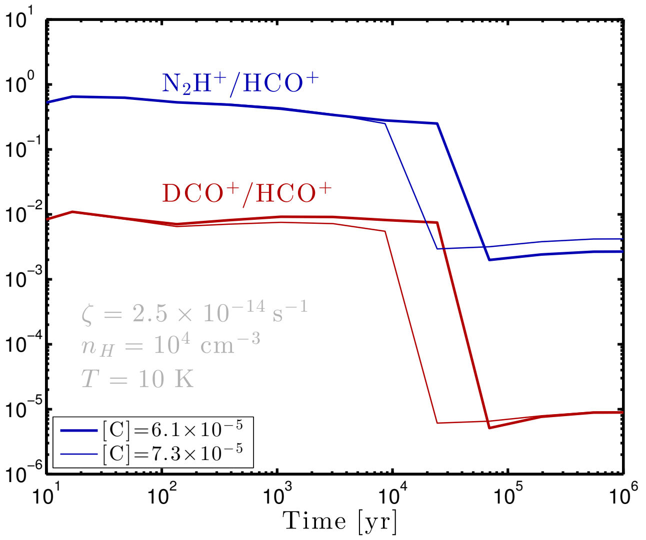

Acknowledgments

Interdisciplinary research

Molecular astrophysics	High energy astrophysics
G.Dumas (IRAM)	G.Dubus (IPAG)
C.Ceccarelli (IPAG)	S.Gabici (APC)
P.Hily-Blant (IPAG)	T.Montmerle (IAP)
S.Vaupré (IPAG)	J.Krause (APC)
-	M.Padovani (LUPM)

Financial support from the Programme National Hautes Énergies (PNHE)

Personal perspectives

Higher education teaching in Dijon, starting September 1st